LAPP-T-98/06

Thèse de doctorat de l'Université Paris VII – Denis Diderot
Spécialité : Physique des Particules

présentée par

Viatcheslav VALUEV

pour obtenir le titre de

Docteur de l'Université Paris VII – Denis Diderot

Recherches des oscillations de neutrinos $\nu_\mu \rightarrow \nu_e$ dans l'expérience NOMAD.

Soutenue le 07 juillet 1998 devant le jury composé de:

M. R. D. COUSINS
M. Y. DECLAIS
M. A. RUBBIA
M. D. SILLOU
M. F. VANNUCCI

Thèse préparée dans le cadre du **Réseau de Formation et de Recherche JINR (Dubna) – LAPP (Annecy-le-Vieux) – LPNHE (Paris)**

Acknowledgements

First of all, I would like to thank Patrick Nédélec and Daniel Sillou for the very idea of writing French thesis and for their constant help for many years, no matter which problems – in physics, in life or financial – could occur. It was (and I hope it will be) a pleasure to work together and to have such friends!

I would like to thank the members of "PADS" group – Patrick Nédélec, André Rubbia, Daniel Sillou, Antonio Bueno, Robert Cousins, Yuri Nefedov and Tatiana Vinogradova – whose contributions to the particle identification and energy flow reconstruction algorithms, together with numerous discussions and exchange of ideas, made this work possible. Special thanks go to André, for his invaluable help and a lot of support and encouragement during many years. I am very grateful to Alexey Krasnoperov for his wonderful "ratio" package (able to compare any data with any Monte Carlo) and to Yuri Nefedov for taking such a good care of limit calculations.

I am greatly indebted to Prof. S. A. Bunyatov for letting me spend extensive periods of time at CERN and at LAPP, which has been of immense worth to me. Many thanks to other people who made my work in NOMAD possible – Leslie Camilleri, Luigi Di Lella, Jean-Marc Gaillard, Patrick Nédélec, Daniel Sillou and François Vannucci.

I would like to thank the members of the jury for the amazingly careful reading of this manuscript and for many critical comments provided. I'm specially indebted to Prof. François Vannucci for offering me a possibility to perform a thesis at the University of Paris VII and for taking a good care of all the formalities required.

Finally, I would like to thank the members of the $\nu_\mu \rightarrow \nu_e$ working group for their assistance and usuful discussions. I am especially grateful to Frederick Weber for his comments on the manuscript.

Contents

Chapter 1

Introduction

The existence of neutrino was proposed by W. Pauli in 1930 as an attempt to explain the continuous spectrum of electrons emitted in nuclear β-decay [1]. The idea was considered at that time almost as revolutionary as an alternative explanation, the violation of energy conservation. The experimental confirmation came only 25 years later, when the first neutrino (electron antineutrino $\bar{\nu}_e$) was observed in the Savannah River reactor experiment [2].

Pauli postulated the existence of a new neutral light fermion. Even if we know now that neutrinos exist, are neutral and come in three species (flavours)[1] as charged leptons do [3], the question about their masses remains open. The neutrinos are exactly massless in the Standard Model of electroweak interactions. However, the masslessness of neutrinos is not ensured by any basic principle (as is the case for the masslessness of the photon, ensured by gauge invariance). Non-zero neutrino masses arise in many extensions of the Standard Model, too numerous to be described here (for a recent review see, e.g., [4] and references therin). The discovery of neutrino mass would be of extreme importance, since many significant effects in physics, astrophysics and cosmology depend on neutrino properties, all associated with their mass [5]:

- the theory of nucleosynthesis as well as the dark matter problem and its related issue of structure formation in the Universe would be greatly affected by new neutrino properties;
- the deficit of observed neutrinos emitted from the Sun with respect to the expected amount – the so-called "solar neutrino problem" – could be explained by new neutrino physics (as opposed to a modification of standard solar model);
- atmospheric neutrinos produced by cosmic rays hitting the Earth atmosphere show a deficit of ν_μ relative to ν_e with respect to the expected ratio, the effect which could be accounted for by massive neutrinos;

---

[1] Unless the additional ones are "sterile", i.e. they do not have weak interactions, or they are heavier than $M_Z/2 \simeq 45$ GeV.

- finally, non-zero neutrino mass would be an indication of physics beyond the Standard Model and therefore would be extremely welcome.

At present we only know upper bounds on neutrino masses obtained in direct mass searches:

$$m_{\nu_e} \ < \ O(10 \text{ eV}), \ \ m_{\nu_\mu} \ < \ 170 \text{ keV}, \ \ m_{\nu_\tau} \ < \ 18.2 \text{ MeV} \tag{1.1}$$

These bounds show that neutrinos are much lighter than their corresponding charged fermions, $m_e = 0.5$ MeV, $m_\mu = 105.7$ MeV and $m_\tau = 1.78$ GeV. However, due to experimental difficulties and limitations, all direct mass measurements performed so far provide upper bounds on neutrino masses which are less stringent than the values favoured by different models and other types of experiments (mainly solar and atmospheric neutrino flux measurements) by several orders of magnitude. Nowadays, the only possible technique[1] to detect neutrino masses below ~1 eV is to search for neutrino oscillations.

In this chapter we describe briefly the phenomenology of neutrino oscillations in vacuum, the one relevant for the oscillation searches at accelerators, and review the basic principles of neutrino oscillation experiments.

1.1 Neutrino oscillations in vacuum

The hypothesis of neutrino mixing has been first proposed by B. Pontecorvo by analogy with the K^0 - $\bar{K}^0$ process, originally for the $\nu_e \to \bar{\nu}_e$ transitions [6]. After the discovery of ν_μ the concept of neutrino mixing has been adapted to oscillations between different neutrino flavours [7]. According to this hypothesis, the three known neutrino flavours which take part into the weak interactions, $\nu_\alpha \equiv \nu_e,\ \nu_\mu,\ \nu_\tau$, are quantum-mechanical superpositions of three mass eigenstates ν_i which describe the propagation of neutrinos in space-time:

$$\nu_\alpha = \sum_{i=1} U_{\alpha i} \nu_i \tag{1.2}$$

where $U_{\alpha i}$ is the unitary 3×3 matrix analogous to the Cabibbo-Kobayashi-Maskawa matrix for quarks.

From Eq. (1.2) it follows that the space-time evolution of a neutrino with momentum $\vec{p}$ produced in the state ν_α at $t = x = 0$ is given by

$$\nu(t) = e^{i\vec{p}\vec{x}} \sum_i U_{\alpha i} e^{-iE_i t} \nu_i \tag{1.3}$$

where $E_i = \sqrt{p^2 + m_i^2}$. If the masses m_i are not equal (and non-zero), the three terms of the sum in Eq. (1.3) get out of phase and the state $\nu(t)$ acquires a component ν_β with $\beta \neq \alpha$.

In an accelerator-based oscillation experiment one creates a neutrino beam of defined weak eigenstate ν_α (usually ν_μ) and tries to detect at a different point of space-time the

---

[1] With the exception of neutrinoless double beta decay search to probe Majorana neutrino masses.

weak eigenstate ν_β (not necessarily $\beta \neq \alpha$). The probability of its detection is

$$P_{\nu_\alpha \to \nu_\beta}(t) \;=\; |\langle \nu_\beta \mid \nu(t)\rangle|^2 \;= \left|\sum_i U_{\beta i}\; e^{-i(E_i t - \vec{p}\vec{x})}\; U^*_{\alpha i}\right|^2 \tag{1.4}$$

The details of the formalism of neutrino oscillations depend on the number of neutrino flavours. So far most of the experimental data were analysed in the simplest approach when only two neutrino flavours are taken into account. At present it is recommended [3] that the experimental results should be analysed in the complete three-flavour mixing approach. We describe first the two-flavour formalism, still preferred by many experimentalists for its simplicity and for compatibility with the results of the past experiments, and then proceed to the complete three-flavour approach.

1.1.1 Two-flavour formalism

In the case of two-neutrino mixing, the mixing matrix U is described by only one real parameter θ (the mixing angle). Then, the probability of neutrino oscillations simplifies to[1]

$$P_{\nu_\alpha \to \nu_\beta} \;=\; \left|\delta_{\alpha\beta} - \sin^2(2\theta) \cdot \sin^2\left(\Delta m^2 \frac{L}{4E}\right)\right| \tag{1.5}$$

Eq. (1.5) is expressed in natural units. In more familiar units we can write

$$P_{\nu_\alpha \to \nu_\beta} \;=\; \left|\delta_{\alpha\beta} - \sin^2(2\theta) \cdot \sin^2(1.27\Delta m^2 L/E)\right| \tag{1.6}$$

where $\Delta m^2 = |m_2^2 - m_1^2|$ [eV^2] is the difference of the squares of the mass eigenvalues, L [km] is the source-detector distance, E [GeV] is the energy of the neutrino. An important consequence of the expression (1.5) is that neutrino oscillation experiments cannot measure individual neutrino masses, but only difference of their squares.

Eq. (1.5) and (1.6) describe neutrino oscillations with an amplitude equal to $\sin^2(2\theta)$ and the oscillation length λ given by

$$\lambda = \frac{4\pi E}{\Delta m^2} = \frac{2.48 E \text{ [GeV]}}{\Delta m^2 \text{ [eV}^2\text{]}} \text{ [km]}. \tag{1.7}$$

Therefore, to observe neutrino oscillations, three conditions have to be fulfilled:

- at least one of three neutrinos is massive; the masses of neutrinos of different flavours are not equal;
- the mixing angle is large enough to be probed by a given experiment;
- the oscillation length λ is less or of the order of the source-detector distance, which can be rewritten as $\Delta m^2 \geq E/L$. Thus, to search for low mass differences the distance L should be large and/or the energy of the neutrino beam E should be small.

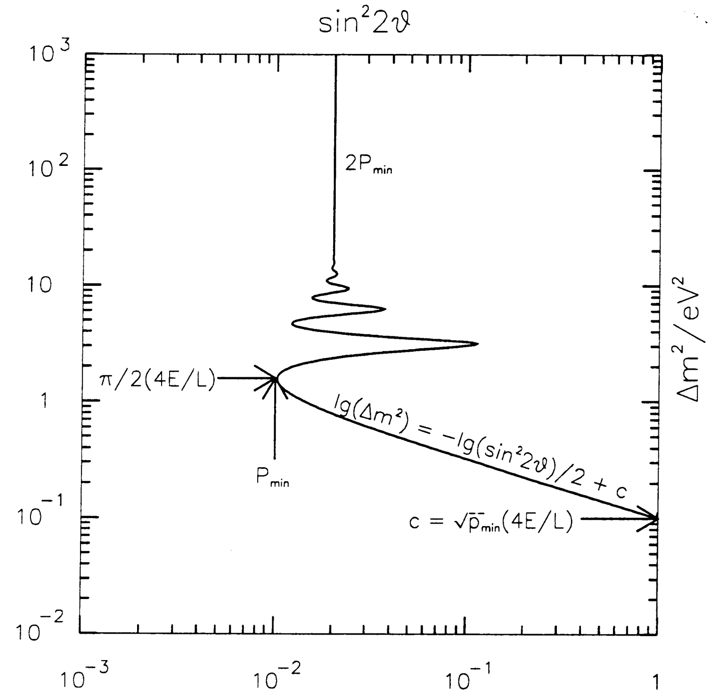

Figure 1.1: Sensitivity of a typical neutrino oscillation experiment: minimal excluded oscillation probability $P_{min} = 0.01$, mean value of $4E/L = 1$ eV^2 (e.g., neutrino energy of 1.27 GeV and source-detector distance of 1 km), width of the L/E distribution is 10% of the mean L/E value, assuming a Gaussian L/E distribution.

The results of oscillation experiments in two-flavour formalism are usually presented in a two-parameter space of $\sin^2(2\theta)$ and Δm^2. Fig. 1.1 illustrates how the experiment-related parameters P_{min}, L and E and the oscillation-related parameters $\sin^2(2\theta)$ and Δm^2 are correlated:

- For small Δm^2, corresponding to $\lambda \gg L$, the phase term $\sin^2(\pi L/\lambda)$ can be approximated by $(\pi L/\lambda)^2$. This results in a vanishing sensitivity of the experiment and in a straight line of experiment-independent slope in a double-logarithmic plot, see Fig. 1.1.
- The value of Δm^2, for which the sensitivity in $\sin^2(2\theta)$ is maximal, is reached for $L = \lambda/2$, independently of P_{min}.
- For large Δm^2, corresponding to small oscillation length, the $\sin^2(\pi L/\lambda)$ is averaged as 1/2 and $\sin^2(2\theta) = 2P_{min}$.

In case of a negative result (no oscillation signal observed) the parameter region on the

---

[1] in the assumption of relativistic neutrinos ($m_i \ll p$).

right side of the curve shown in Fig. 1.1 would be excluded. Observation of an oscillation signal would instead result in a preferred parameter region within a band along this curve.

1.1.2 Three-flavour formalism

In the complete three-flavour approach, the probability of neutrino oscillations (1.4) can be written as

$$P_{\nu_\alpha \to \nu_\beta} = \delta_{\alpha\beta} - 4 \sum_i \sum_{j>i} U_{\alpha i} U^*_{\beta i} U^*_{\alpha j} U_{\beta j} \sin^2(\Delta_{ij}/2) \tag{1.8}$$

with $\Delta_{ij} = \Delta m^2_{ij} L/2E$. If we ignore possible CP violation, the U matrix is real and can be parametrized as

$$U = \begin{pmatrix} c_{12}c_{13} & s_{12}c_{13} & s_{13} \\ -s_{12}c_{23} - c_{12}s_{23}s_{13} & c_{12}c_{23} - s_{12}s_{23}s_{13} & s_{23}c_{13} \\ s_{12}c_{23} - c_{12}c_{23}s_{13} & -c_{12}s_{23} - s_{12}c_{23}s_{13} & c_{23}c_{13} \end{pmatrix} \tag{1.9}$$

with $c_{ij} = \cos\theta_{ij}$ and $s_{ij} = \sin\theta_{ij}$, where θ_{12}, θ_{13} and θ_{23} are three independent real mixing angles lying in the first quadrant.

Of the three Δm^2_{ij} appearing in Eq. (1.8) only two are independent, since $\Delta m^2_{21} + \Delta m^2_{32} = \Delta m^2_{31}$. The complete solution of the problem consists therefore in determining five unknowns: two Δm^2_{ij}'s and the three θ_{ij}'s.

Assuming a mass hierarchy like the one in the quark (or charged lepton) sector, the condition $m_1 \ll m_2 \ll m_3$ (predicted by the so-called "see-saw" model [8]) implies $\Delta m^2_{21} \ll \Delta m^2_{31} \approx \Delta m^2_{32}$. This hierarchy generates two kinds of oscillations, one "short" (i.e. with oscillation length $\lambda_{short} \sim E/\Delta m^2_{31}$) and one "long" (i.e. with $\lambda_{long} \sim E/\Delta m^2_{21}$). Thus, each transition probability contains a "short" (or "fast") and a "long" (or "slow") components:

$$\begin{aligned} P(\nu_\alpha \to \nu_\beta) &= P_{short}(\nu_\alpha \to \nu_\beta) + P_{long}(\nu_\alpha \to \nu_\beta); \\ P_{short}(\nu_\alpha \to \nu_\beta) &\approx 4U^2_{\alpha 3} U^2_{\beta 3} \sin^2(\Delta_{31}/2); \\ P_{long}(\nu_\alpha \to \nu_\beta) &= -4U_{\alpha 1} U_{\beta 1} U_{\alpha 2} U_{\beta 2} \sin^2(\Delta_{21}/2). \end{aligned} \tag{1.10}$$

Any given neutrino oscillation experiment may be sensitive to either only the "short" or both the "short" and "long" oscillations, depending on the L/E range under study. Two L/E ranges are usually discerned: the so-called "short baseline" experiments with $1/\Delta m^2_{13} \ll L/E \ll 1/\Delta m^2_{12}$ are sensitive only to "short" oscillations, whereas the "long baseline" experiments with $L/E \gg 1/\Delta m^2_{12}$ are sensitive to both the "fast" and "slow" oscillation components. Historically, short, medium and long baseline experiments correspond to $\Delta m^2 > 10$ eV^2, $\Delta m^2 \approx 1$ eV^2 and $\Delta m^2 \approx 10^{-2}$ eV^2, respectively.

If, in addition to the mass hierarchy, we assume the mixing matrix to be "almost diagonal" like the CKM matrix ($\cos\theta_{ij} \gg \sin\theta_{ij}$), then $P(\nu_e \to \nu_\tau)$ and $P(\nu_\mu \to \nu_\tau)$ are dominated by the "short" component ($\propto U^2_{\tau 3}$) and are expected to be governed by m_3, whereas $P(\nu_\mu \to \nu_e)$ is dominated by the "long" component ($\propto U_{e1}U_{\mu 2}$) and is expected to be governed by m_2.

1.2 Principles of neutrino oscillation experiments

Experiments searching for neutrino oscillations are numerous; they have been carried out using both man-made (nuclear reactors, low and high energy accelerators) and natural (cosmic rays and even the Sun) neutrino sources. However, from the experimental point of view, all neutrino oscillation experiments can be subdivided into two categories:

- **Appearance (or exclusive) experiments.** In these experiments the flux of a given neutrino flavour $\beta \neq \alpha$ is measured at a certain distance from the source where mainly ν_α are produced. The beam energy must be high enough to allow the creation of l_β (the charged lepton of flavour β); then the oscillation probability $P(\nu_\alpha \to \nu_\beta)$ is measured directly.

  This method is sensitive to small mixing angles, since it is sufficient to detect a small number of ν_β interactions, provided the fraction of prompt ν_β is small. The sensitivity of these experiments is, however, often limited by the systematic uncertainty on the knowledge of the beam contamination by ν_β. For example, in a typical ν_μ beam from a high energy accelerator the ν_e contamination is of the order of 1% with an ~10% uncertainty.

  Searches for ν_e and ν_τ appearance in a beam containing predominantly ν_μ neutrinos have been performed at accelerators. In these experiments the presence of ν_e (ν_τ) neutrinos is detected by observing the interactions ν_e (ν_τ) + nucleon $\to e^-$ (τ^-) + hadrons.

- **Disappearance (or inclusive) experiments**. These experiments try to measure deviations from the expected ν_α flux at a certain distance from the source. The probability measured is

  $$P(\nu_\alpha \to \nu_\alpha) = 1 - \sum_{\beta \neq \alpha} P(\nu_\alpha \to \nu_\beta). \tag{1.11}$$

  The sensitivity of disappearance experiments is limited by the systematic uncertainty on the knowledge of the neutrino flux from the source. However, these experiments are the only way to search for neutrino oscillations when the neutrino energy is below the kinematical threshold of producing l_β and it is impossible to perform an appearance experiment. In addition, disappearance search is sensitive to the oscillations into exotic flavours such as "sterile" neutrinos (neutrinos that do not take part in the standard weak interactions).

  Disappearance experiments with man-made neutrino sources have been performed at nuclear reactors and at accelerators. The core of a nuclear reactor is an intense source of $\bar{\nu}_e$ with an average energy of ~3 MeV, which can be detected by observing the reaction $\bar{\nu}_e + p \to e^- + n$. If a $\bar{\nu}_e$ turns into a $\bar{\nu}_\mu$ or a $\bar{\nu}_\tau$, it becomes invisible for detectors because μ^+ or τ^+ production is energetically forbidden. Proton accelerators produce ν_μ neutrinos with energies between ~30 MeV and ~200 GeV. In disappearance experiments the ν_μ flux is measured by detecting the reaction ν_μ + nucleon $\rightarrow \mu^-$ + hadrons.

To reduce beam-induced systematic uncertainties, several **two-detector disappearance experiments** have been performed (see Chapter 2). They measured the neutrino flux of flavour α at two different distances from the source. The sensitivity in Δm^2 in such experiments is limited to a small range corresponding to the condition $L_1 < \lambda < L_2$, where L_1 and L_2 denote the distances of the near and far detectors from the neutrino source.

The results of different oscillation experiments in various channels – $\nu_e \leftrightarrow \nu_\mu$, $\nu_e \leftrightarrow \nu_\tau$, $\nu_\mu \leftrightarrow \nu_\tau$ for appearance searches, $\nu_e \not\rightarrow \nu_e$, $\bar{\nu}_e \not\rightarrow \bar{\nu}_e$, $\nu_\mu \not\rightarrow \nu_\mu$, etc. for disappearance ones – are compared. No distinction is usually made between $\nu_\alpha \rightarrow \nu_\beta$ and $\nu_\beta \rightarrow \nu_\alpha$ and between results in neutrino and antineutrino channels, which means neglecting CP-violating effects (which could occur in a three-flavour scheme).

The main subject of this document is the appearance search for $\nu_\mu \rightarrow \nu_e$ oscillations performed in a short baseline experiment at a high energy accelerator. In the next chapter we present the review of the experimental results on $\nu_\mu \rightarrow \nu_e$ oscillation searches obtained in the experiments which explored the region of oscillation parameters similar to that of our study.

Chapter 2

Search for $\nu_\mu \rightarrow \nu_e$ oscillations at accelerators

2.1 Introduction

The search for $\nu_\mu \rightarrow \nu_e$ oscillations at accelerators has been an extremely active field for the past 20 years. First experiments were performed in early 80's using bubble chambers as neutrino detectors. They were mostly motivated by a non-zero $\bar{\nu}_e$ mass evidence ($14 \leq m_{\bar{\nu}_e} \leq 46$ eV) in the measurements of the end point of the electron energy spectrum in tritium β-decay at ITEP (Troitsk) [9]. No oscillation signal was found, but the sensitivity of the experiments was limited by large systematic uncertainties in the knowledge of the beam and low statistics. To increase the number of neutrino interactions, bubble chambers were replaced by massive calorimetric detectors. A series of experiments was conducted at CERN, Fermilab and BNL, first comparing the ν_μ rates in two simultaneously operating detectors (in order to reduce beam-induced uncertainties) and later, when the composition of neutrino beams became better known, performing a ν_e appearance search using fine granularity of the calorimeters. The results of these oscillation searches were negative.

The interest for the $\nu_\mu \rightarrow \nu_e$ oscillation search has highly increased again in 1996, when the LSND collaboration claimed for evidence for $\bar{\nu}_\mu \rightarrow \bar{\nu}_e$ oscillations with a central value of the oscillation probability $P(\bar{\nu}_\mu \rightarrow \bar{\nu}_e) = 3.1 \cdot 10^{-3}$ (90% C.L.) and an allowed region on the oscillation parameter plane partially unexplored before. This result was later supported by an excess of events consistent with an oscillation probability of $2.6 \cdot 10^{-3}$ (90% C.L.) observed by the LSND in $\nu_\mu \rightarrow \nu_e$ oscillation search, with backgrounds and systematic errors different from those of $\bar{\nu}_\mu \rightarrow \bar{\nu}_e$. Recent results from KARMEN and CCFR experiments exclude a part of the oscillation parameter space favoured by the LSND results, but the question still remains open and more data are needed in order to deduce a definitive conclusion.

In this chapter we review the experimental results of the search for $\nu_\mu \rightarrow \nu_e$ oscillations at high and medium energy accelerators. We will not discuss here the results of oscillation search at reactors and the possible interpretation of the atmospheric neutrino anomaly in terms of $\nu_\mu \to \nu_e$ oscillations [5], which involve the region of oscillation parameters different from that explored in this study.

2.2 Bubble chambers experiments

Bubble chambers could provide an excellent identification of the ν_e charged current interactions and precise measurements of the neutrino energy, thus making possible a ν_e appearance search in beams consisting predominantly of ν_μ neutrinos. However, these early experiments suffered from large uncertainties in the knowledge of ν_e component of neutrino beams and from small detector masses leading to relatively low statistics of recorded neutrino interactions.

2.2.1 Gargamelle

The heavy liquid bubble chamber Gargamelle filled with heavy freon was exposed to both the CERN PS and the CERN SPS neutrino beams, with a mean neutrino energy of 1.5 GeV and 25 GeV respectively.

At the PS beam, about 200 (60) candidates for electron neutrino (antineutrino) interactions found in a 1973–1977 exposure of $1.1 \cdot 10^{18}$ ($4.5 \cdot 10^{18}$) protons on target have been analyzed with the main purpose to study the total cross-sections of ν_e and $\bar{\nu}_e$ interactions [10]. No excess of electron (positron) events with respect to those expected from the ν_e ($\bar{\nu}_e$) component of the beam was found. The upper limits of $\sin(2\theta) = 0.064$ (i.e. $\sin^2(2\theta) = 4 \cdot 10^{-3}$) for $\Delta m^2 \geq 50$ eV^2 and of $\Delta m^2 \approx 1$ eV^2 at full mixing were set at 95% C.L., assuming energy dependent ν_e flux uncertainty between 15% and 30%. Such a stringent limit on $\nu_\mu \to \nu_e$ oscillations published 20 years ago could be obtained, first of all, due to a very small ($\approx$0.4%) ν_e contamination in a ν_μ PS beam.

In 1980 the Gargamelle chamber was installed at the newly constructed CERN SPS wide-band neutrino beam with a mean ν_μ energy of 25 GeV and ν_e contamination of about 1%, at a distance of $\sim$500 m from the center of decay region. Two-prong events consisting of an e^- (μ^-) and a proton stopping in the chamber were searched for as ν_e (ν_μ) quasielastic (QE) candidates [11]. There were 4 e^-p and 534 μ^-p events found above the cut of $E_{vis} > 10$ GeV and 4.0 ± 0.8 e^-p events expected (assuming 20% uncertainty on the calculated ν_e spectrum). The limit on oscillation probability $P(\nu_\mu \to \nu_e) < 0.004$ was set at 68% C.L., excluding $\Delta m^2 > 1.4$ eV^2 at full mixing.

2.2.2 BEBC

The BEBC chamber filled with a Ne-H$_2$ mixture was installed at the same SPS neutrino beam, 150 m closer to the target compared to Gargamelle. The 93 ν_e charged current (CC) candidate events with a total visible energy above 10 GeV and an electron momentum above 1 GeV/c were found, yielding the ratio of seen to expected events of 1.21 ± 0.19 [12]. Combining the results from the kinematic distributions with those from the rates, the limits of $\sin^2(2\theta) < 0.01$ at large Δm^2 and $\Delta m^2 < 1.7$ eV^2 at full mixing were set, similar to Gargamelle SPS results.

A few years later the BEBC chamber was used as a neutrino detector to search for $\nu_\mu \rightarrow \nu_e$ oscillations at the PS beam [13]. The low energy of ν_μ neutrinos ($\langle E_{\nu_\mu} \rangle = 1.5$ GeV) and the large distance between the detector and neutrino source (L = 800 m from the center of decay region) made the experiment sensitive to low values of Δm^2 ($\sim$0.1 eV^2 at full mixing). The background ν_e flux in the PS beam was estimated to be only 0.4% of the ν_μ flux. 470 ν_μ CC and 4 ν_e CC candidate events have been observed in an exposure of $9.1{\cdot}10^{18}$ protons on target, with an expected background of 3 ν_e CC events, indicating no evidence for $\nu_\mu \rightarrow \nu_e$ oscillations. The lowest values of the oscillation parameters excluded at 90% C.L. were $\Delta m^2 = 0.09$ eV^2 for $\sin^2(2\theta) = 1$ and $\sin^2(2\theta) = 0.013$ for $\Delta m^2 = 2.2$ eV^2. The L/E ratio in this experiment (and, consequently, Δm^2 region explored) was similar to that of the LSND, but the limit set on $\sin^2(2\theta)$ was less stringent than the LSND allowed region on oscillation parameters space (discussed later in this chapter).

2.2.3 15-ft bubble chamber

The 15-ft bubble chamber filled with a heavy Ne-H_2 mixture was installed at a distance of 1.2 km from the center of decay region at the wide-band neutrino beam at Fermilab [14]. The average energy of ν_μ events was 18.5 GeV, the number of ν_e CC interactions relative to the total number of ν_μ CC events was calculated to be (1.5 ± 0.3)%. Requiring the momentum of e^- to be larger than 1 GeV/c, a sample of 595 ν_e CC candidates was selected. These events were corrected for background and efficiencies to yield a number of 942 ± 85 ν_e CC interactions, in agreement with expected 1027 ± 210 events. Comparing measured and predicted ratios of ν_e CC to ν_μ CC interactions, the limit on oscillation probability of $P(\nu_\mu \rightarrow \nu_e) \leq 3{\cdot}10^{-3}$ was set at 90% C.L., excluding the values of $\sin^2(2\theta) > 6{\cdot}10^{-3}$ at large Δm^2 and $\Delta m^2 > 0.6$ eV^2 at full mixing.

2.2.4 SKAT

The ratio of ν_e to ν_μ induced charged current interactions has been studied with the SKAT heavy liquid bubble chamber exposed to the wide-band neutrino beam of the Serpukhov accelerator with neutrino energies between 3 and 30 GeV [15]. The neutrino beam produced by the interactions of 70 GeV protons on an aluminium target consisted predominantly of ν_μ neutrinos (with the mean energy of 8 GeV) with only about 0.6% of ν_e admixture. The bubble chamber SKAT filled with 6.5 m^3 of heavy freon was located at a distance of 270 m from the target.

A sample of 83 events – ν_e CC candidates – with electron and no other lepton in the final state has been selected. The non-prompt background in the sample was estimated to be 1.5 ± 0.5 events. Comparing the observed ratio of electron to muon neutrino charged current candidates with that expected, the value of R = $(N_{e^-}/N_{\mu^-})_{obs}/(N_{e^-}/N_{\mu^-})_{exp}$ = 0.98 ± 0.15 was found, where the error includes the estimated uncertainty of the ν_e/ν_μ flux ratio. The regions of $\sin^2(2\theta) > 2.5{\cdot}10^{-3}$ at large Δm^2 and $\Delta m^2 > 1.3$ eV^2 at full mixing were excluded at 90% C.L. The combination of low ν_e beam contamination, excellent electron identification capabilities and a high-statistics data sample allowed the SKAT experiment to set the limit on the mixing angle $\sin^2(2\theta)$ which remained the world best value [3] at large Δm^2 until the CCFR results published in 1997.

2.3 Experiments with two detectors

The sensitivity of large statistics neutrino oscillation experiments is usually limited by the systematic uncertainties in the knowledge of the initial flux of the neutrino beam. To minimize these systematic uncertainties associated with neutrino flux monitoring, several experiments operated simultaneously two similar detectors at different distances from the neutrino source. The ν_μ rates observed in two detectors, properly corrected for beam angular divergence, acceptance, etc., are compared and a difference could be attributed to $\nu_\mu \to \nu_e$ oscillations displayed through ν_μ disappearance.

2.3.1 CHARM experiment

The CHARM collaboration recorded data corresponding to about $9.8{\cdot}10^{18}$ protons on target with “close” and “far” detectors installed at the CERN PS beam [16]. Both detectors consisted of marble plates (18 and 60 plates for close and far detectors respectively) interleaved with layers of scintillation counters and proportional drift tubes [17]; the target-calorimeter part was supplemented by muon spectrometers. The close detector was located at the distance of about 120 m from the target and had a fiducial mass of 27 t; the far detector was at 900 m from the target and weighed about 122 t.

Charged current quasielastic interactions of muon neutrinos were selected in both detectors (2 043 events in the close detector and 268 events in the far detector). The ratio of the observed rates r_{obs} in the two detectors was properly corrected for the different dead-times, cosmic background and selection efficiencies and then compared to the expected ratio r_{exp}, computed with Monte Carlo program simulating the beam and the response of the detectors. The total error on r_{exp} was estimated to be less than 5%. The ratio of the observed event rates to that expected assuming no oscillations was found to be

$$r_{obs}/r_{exp} = 0.96 \pm 0.06 \pm 0.05 \quad \text{for short tracks (4-15 planes)} \tag{2.1}$$

and

$$r_{obs}/r_{exp} = 1.21 \pm 0.20 \pm 0.04 \quad \text{for long tracks (16-49 planes)} \tag{2.2}$$

yielding no evidence for oscillations. The most restrictive limit for the mass difference was $\Delta m^2 \leq 0.19$ eV^2 at full mixing; the most stringent value for the mixing angle was $\sin^2(2\theta) < 0.17$ at $\Delta m^2 \approx 1.5$ eV^2 (at 90% C.L.).

2.3.2 CDHS experiment

The CDHS collaboration operated close and far detectors at the CERN PS beam [18] simultaneously with the CHARM collaboration. Both close and far detectors consisted of iron plates interleaved with plastic scintillator hodoscopes [19] (6 and 21 modules respectively) and were installed at the distances from the target very similar to those of the CHARM close and far detectors. The accumulated data corresponded to $7.0 \cdot 10^{18}$ protons on target.

Charged current interactions of muon neutrinos were selected in both detectors by requiring a minimal projected event range of 40 cm and imposing fiducial volume cuts. About 22 000 events in the close detector and 3 300 events in the far detector were found. The ratio of close/far events multiplied by the ratio of the square of the distances from the target and by the ratio of the detector masses was then computed, with other relevant effects (such as differences in the neutrino spectra in the two detectors due to different angular acceptancies, minor differences in the design of the detectors, etc.) corrected for by a Monte Carlo simulation. The corrected ratio of the total rates in the two detectors was found to be

$$R_{corr} = 1.044 \pm 0.023 \tag{2.3}$$

showing no evidence for oscillations within the sensitivity of the experiment.

The overall systematic error in the ratio of event rates in the two detectors was estimated to be 2.5%. Taking this uncertainty into account, exclusion limits on the oscillation parameter plane were computed. At the 90% C.L., Δm^2 values between 0.26 and 90 eV^2 were excluded for maximum mixing; the most restrictive value for the mixing angle was $\sin^2(2\theta) = 0.053$ at $\Delta m^2 \approx 2.5$ eV^2, consistent with the CHARM results.

2.3.3 CCFR experiment

The CCFR collaboration used the Fermilab narrow-band neutrino beam as a neutrino source [20]. The integrated proton flux was $3.4 \cdot 10^{18}$ incident on the production target. Data were taken at five different momentum settings for π^+ and K^+ mesons, yielding neutrinos with E_ν between 40 and 230 GeV, and at a single setting for antineutrinos. Both close and far neutrino detectors consisted of a target calorimeter (steel plates instrumented with scintillation counters and spark chambers), followed by a muon spectrometer. The detectors were located at 715 and 1116 m from the mid-point of the decay pipe and had the fiducial masses of 108 and 444 t respectively.

The number of charged current interactions of muon neutrinos in the two detectors was compared as a function of neutrino energy, obtained from the dichromatic beam properties and the radial vertex position. The ratio of close/far events in each energy bin has been corrected for different lifetimes, reconstruction efficiencies, angular divergence, etc. A comparison of the corrected ratio with the hypothesis of no oscillations yielded a χ^2 of 15.7/18 d.o.f., and the data were therefore found consistent with no oscillations. Assuming CP invariance, the analysis of combined neutrino-antineutrino data ruled out Δm^2 values between 15 and 1000 eV^2 for $\sin^2(2\theta) > 0.02$-0.40 at 90% C.L. The CCFR experiment was sensitive to the region of Δm^2 higher than that of the CHARM and CDHS due to a higher energy of neutrino beam.

2.4 Appearance experiments at CERN

2.4.1 CHARM PS ν_e appearance analysis

A sample of events selected by the CHARM collaboration at the CERN PS beam exposure (Sec. 2.3.1) has been analyzed for the appearance search of electron neutrino quasielastic interactions in the close and far detectors [16]. For this purpose, the capability of the CHARM fine-grained calorimeter to detect and identify electromagnetic showers down to ~0.5 GeV has been used.

The subsample of quasielastic events in which a muon could not be identified (124 "0μ events" in the close and 15 in the far detector) was analyzed by estimators tuned to identify electromagnetic showers with the help of low energy electron and pion test beam data. This event selection yielded 17 events in the close and 1 event in the far detector. After subtracting the estimated backgrounds from hadronic showers and from the admixture of electron neutrinos in the beam, and after correcting for efficiencies, the ratios r_{CD} and r_{FD} of electron to muon quasielastic events in the close and far detector respectively were computed:

$$\begin{aligned} r_{CD} &= (-0.5 \pm 1.1)\% \\ r_{FD} &= (-3.1 \, {}^{+\,4.8}_{-\,2.2})\% \end{aligned} \tag{2.4}$$

where the quoted errors are both statistical and systematic (7%, mostly due to uncertainties in the efficiency calculations). The obtained limit on the mixing angle for large Δm^2 (the close detector measurement) was:

$$\sin^2(2\theta) < 0.03 \quad (90\% \text{ C.L.}) \tag{2.5}$$

2.4.2 CHARM SPS ν_e appearance analysis

Another data sample collected with the CHARM detector was analyzed using similar procedures [16]. This data sample was recorded in 1983 when the detector was exposed to the wide-band neutrino beam of the CERN 400 GeV SPS with the main purpose to measure the cross-sections of ν_μ and $\bar{\nu}_\mu$ scattering on electrons. The total integrated fluxes were $1.2 \cdot 10^{18}$ and $2.3 \cdot 10^{18}$ protons on target in the neutrino and antineutrino beams respectively. The detector was located at a distance of ~820 m from the neutrino source.

As in the case of the analysis described in the previous section, any appearance of an unexpected number of electromagnetic showers could be interpreted as an indication for $\nu_\mu \to \nu_e$ oscillations. Combining neutrino and antineutrino data and comparing the measured number of ν_e quasielastic candidates with the expected number showed an excess of 55 ± 84 events in the data sample, yielding no evidence for oscillations. An upper limit on the mixing angle for large Δm^2 was set:

$$\sin^2(2\theta) < 8.0 \cdot 10^{-3} \quad (90\% \text{ C.L.}) \tag{2.6}$$

2.4.3 CHARM II ν_e and $\bar{\nu}_e$ appearance search

The search for $\nu_\mu \to \nu_e$ and $\bar{\nu}_\mu \to \bar{\nu}_e$ oscillations at CERN has been continued with the CHARM II detector exposed to the CERN wide-band neutrino beam in 1987-1991 [21]. The CHARM II detector [22], located at about 650 m from the average neutrino production point, consisted of a massive (~700 t weight, 35 m long) and low-density fine-grained calorimeter (420 glass plates of 0.5 X_0 each, interspersed with plastic streamer tubes and scintillation counters) and of a muon spectrometer. A search for quasielastic neutrino and antineutrino interactions $\nu_e\ n \to e^-\ p$ and $\bar{\nu}_e\ n \to e^+\ n$ was performed based on an exposure of $2.6{\cdot}10^{19}$ protons on target (corresponding to more than 10^7 neutrino charged current interactions) collected over 5 years.

The ν_e and $\bar{\nu}_e$ quasielastic events were selected by requiring a single electromagnetic shower in the detector. The main background due to single π^0 production in neutral current interactions was evaluated by making use of the difference in the signal released by an electron and a π^0 in a scintillation counter at the beginning of the shower development and subtracted. The observed number of ν_e and $\bar{\nu}_e$ QE candidates was compared to that expected from flux calculations (which was normalized to the number of observed ν_μ and $\bar{\nu}_\mu$ quasielastic events). An excess of 265 ± 178 observed over expected events was found, consistent with no evidence for oscillations. An upper limit set on the mixing angle $\sin^2(2\theta)$ for large mass differences ($\Delta m^2 > 200$ eV^2) was:

$$\sin^2(2\theta) \ < \ 5.6 \cdot 10^{-3} \quad (90\% \text{ C.L.}) \tag{2.7}$$

The total systematic uncertainty on the ν_e/ν_μ flux ratio estimated to be 15% was taken into account in the calculations of the limit.

2.4.4 CDHS and CHARM narrow-band beam analysis

The data on neutrino scattering collected in 1986 by the CDHS and CHARM collaborations at the CERN SPS narrow-band neutrino beam were re-analyzed in 1995 to search for $\nu_\mu \to \nu_e$ oscillations [23]. This analysis made use of the high precision measurements of R, the ratio of 0μ to 1μ events in $\nu_\mu N$ deep inelastic scattering, performed by the CDHS and CHARM collaborations to measure the value of the electroweak mixing angle.

The analysis performed was similar to that of the CCFR collaboration described in Sec. 2.7. The world average value of $\sin^2\theta_W$ was used to predict the ratio R and any deviation in the measured R from the predicted value would be attributed to $\nu_\mu \to \nu_e$ oscillations. The mean values of neutrino energy E_ν and source-detector distance L of the narrow-band neutrino beam were $E_\nu \sim 50$ GeV and $L \sim 600$ m.

No evidence of a discrepancy between the predicted and the measured values of R was found. The oscillation parameter region of $\sin^2(2\theta) > 3{\cdot}10^{-3}$ at large Δm^2 and $\Delta m^2 > 2.4$ eV^2 at full mixing was excluded.

2.5 BNL experiments

Three experiments have searched for $\nu_\mu \to \nu_e$ oscillations using the BNL wide-band neutrino beam. They were: an experiment primarily designed to measure neutrino-electron scattering E734 [24], a follow-up of a previous indication of neutrino oscillations at the CERN PS E816 [25], and a specially designed neutrino oscillation experiment E776 [26].

The AGS (Alternating Gradient Synchrotron) at Brookhaven National Laboratory produced about $1.3{\cdot}10^{13}$ protons with the energy 28.3 GeV every 1.4 s. The neutrinos were produced in decays in flight of the secondary pions and kaons originating from proton interactions on titanium target. The polarity of the focusing device ("horn") could be changed to produce wide-band neutrino or antineutrino beams. Because mainly pions were produced in the target, the neutrino beam consisted predominantly of ν_μ ($\bar{\nu}_\mu$ in the negative focusing mode) neutrinos. The mean ν_μ energy was 1.5 GeV. A small expected ν_e ($\bar{\nu}_e$) contamination of 0.68% (0.63%) from kaon and muon decays made possible the search for $\nu_\mu \to \nu_e$ ($\bar{\nu}_\mu \to \bar{\nu}_e$) oscillations in appearance mode.

2.5.1 E734 experiment

The E734 detector [27], located at a mean distance of 96 m from a neutrino source, consisted of 112 planes of liquid scintillator and 224 planes of proportional drift cells uniformely interspersed, followed by a 12 X_0 shower counter and a magnet. The fiducial mass of the detector was 75 tons. A search for quasielastic neutrino interactions $\nu_e\ n \to e^-\ p$ and $\nu_\mu\ n \to \mu^-\ p$ in the detector was performed based on an exposure of $8.8{\cdot}10^{18}$ protons on target collected in 1983.

The ν_e quasielastic interactions were selected by requiring a single electromagnetic shower with $\theta_{e\nu} < 240$ mrad relative to the mean neutrino beam direction. The shower angle was reconstructed by a fit to all hits in the drift cells with a resolution of $\Delta\theta_{e\nu}$ = 30 mrad. The shower energy was measured by summing the deposited energy in the scintillator cells and the energy resolution was found to be $\Delta E_e/E_e = 12\%/\sqrt{E_e}$.

The main background to ν_e QE interactions was due to π^0 production in ν_μ-induced neutral current processes, deep inelastic ν_e interactions and neutrino-electron scattering. The photons from π^0 decays were rejected by observing the primary vertex and using the spatial separation of the photon conversion vertex (V^0) from the primary vertex. All the background sources were suppressed by the requirement $E_e > 0.9$ GeV; the remaining background events were estimated using a data sample of identified V^0 and Monte Carlo simulation and subtracted bin-by-bin in the shower energy distribution. The final ν_e QE sample contained 418 events in the region $0.9 < E_e < 5.1$ GeV.

The ν_μ QE interactions were selected by requiring two prong events, one prong being identified as a proton (by range and ionization) and the other prong exiting the detector (muon). The main background in this data sample consisted of charged-current single π^+ production. The final $\nu_\mu\ n \to \mu^-\ p$ sample (background subtracted) contained 1370 events.

The flux and spectra of ν_e and ν_μ neutrinos were obtained from the two described data sets using Monte Carlo calculated event acceptances and the known quasielastic cross-sections. The measured ratio of neutrino fluxes $[\Phi(E_{\nu_e})/\Phi(E_{\nu_\mu})]_{obs}$ was compared with the expected ratio $[\Phi(E_{\nu_e})/\Phi(E_{\nu_\mu})]_{exp}$ as a function of the neutrino energy. No disagreement between the observed and expected flux ratios was found, showing no evidence for $\nu_\mu \rightarrow \nu_e$ oscillations. Using the data with electron energy E_e between 0.9 and 2.1 GeV, an upper limit on the oscillation probability was set [24]:

$$P(\nu_\mu \rightarrow \nu_e) < 1.7 \cdot 10^{-3} \quad (90\% \text{ C.L.}) \tag{2.8}$$

The region in the oscillation parameter space excluded at 90% confidence level is shown in Fig. 2.1. A systematic uncertainty of 20%, comprised mainly of contributions from the acceptance functions and flux calculation, was taken into account in the limit calculations.

The E734 detector was used a few years later for a $\nu_\mu \rightarrow \nu_e$ oscillation search with a 3 GeV narrow-band neutrino beam at AGS [28]. Less stringent limit of $\sin^2(2\theta) < 1.0 \cdot 10^{-2}$ for large Δm^2 (at 90% C.L.) was obtained for an exposure of $9.0 \cdot 10^{18}$ protons on target. The difference in the results was attributed to a more than two times larger prompt ν_e contamination in the narrow-band neutrino beam.

2.5.2 E816 experiment

The E816 detector [29], located at a distance of 130 m from the mid-point of the decay tunnel, consisted of 25 modules designed for the fine-grained calorimeter of Fréjus proton decay experiment. One such module was made of two flash-tube planes with a 3 mm thick iron plate (17% X_0) between them. The first 10 modules (2.5 X_0 in total, with fiducial mass of 7 tons) were used as the interaction target, the other 15 modules were designed to contain the electromagnetic showers and the amount of matter was increased by additional lead plates.

The search for ν_μ and ν_e quasielastic interactions has been performed based on an exposure of $1.14 \cdot 10^{19}$ protons on target recorded in 1986. QE interactions of ν_μ were defined as "two-track" events with a non-interacting track crossing more than 10 modules (at least 3 cm of iron). The neutral current background in ν_μ data sample was estimated to be 5%. To select ν_e QE interactions, "one-track – one-shower" event topology was required. The energy of electromagnetic showers was measured by counting the number of hit tubes. The detector was calibrated using the test beam of electrons and positrons in the energy range 0.3–2 GeV, the shower energy resolution was found to be $\Delta E_e/E_e = (18 \pm 4)\%/\sqrt{E_e}$.

The main background to ν_e QE interactions was due to π^0s produced in inelastic reactions. A cut on the shower energy $E_e > 300$ MeV was imposed; Monte Carlo simulation showed that this cut eliminates about 70% of π^0 while keeping 90% of the ν_e events. The fine structure of the detector allowed a good spatial separation between electrons and π^0-induced photons; an additional π^0 rejection factor was obtained by a detailed analysis of the vertex-shower distance (called "disconnection"). The residual background consisted of "one-track – one-π^0" events, where the latter appeared as a single shower beginning right after the primary vertex. To evaluate the remaining background and its error, both the Monte Carlo simulation and π^0 events with both photons seen in the data were used.

In total, 178 e-like events were observed in the data. The estimated background amounted to 101 ± 10.8 events from π^0s close to the vertex and 34 ± 4.7 ± 9 events due to ν_e beam contamination (20% systematic uncertainty due to K/π ratio assumed), giving the electron excess of 43 ± 17.8 ± 9 events. The statistical significance of the excess is about two standard deviations. The corresponding ratio of the number of ν_e relative to ν_μ to its expectation from ν_e beam contamination was [25]:

$$\frac{(N(\nu_e)/N(\nu_\mu))_{observed}}{(N(\nu_e)/N(\nu_\mu))_{expected}} = 2.3 \pm 0.6 \quad (1\sigma) \tag{2.9}$$

An observed excess of electron events was attributed to possible problems in a flux prediction by a Monte Carlo beam simulation, in particular, at the low energy part of the spectrum ($300 < E_e < 900$ MeV), where the validity of the Monte Carlo simulation program was not verified. Unfortunately, the energy distribution of excess events was not reported. No claim of neutrino oscillations was made and no limit deduced. The E816 experiment can serve as a good example of how difficult the neutrino experiments are.

2.5.3 E776 experiment

The E776 detector [30], located at a distance of about 1 km from a neutrino source, consisted of 90 planes of proportional drift tubes interleaved with 2.5 cm thick concrete absorber (30% X_0), followed by a muon spectrometer. The total mass of the calorimetric part was 230 tons. The average muon energy resolution was 15%; the electron energy resolution was $\Delta E/E = 20\%/\sqrt{E}$.

A search for quasielastic ν_μ ($\bar{\nu}_\mu$) and ν_e ($\bar{\nu}_e$) interaction candidates was performed based on an exposure of $1.4 \cdot 10^{19}$ ($1.5 \cdot 10^{19}$) protons on target collected with the horn at positive (negative) polarity in 1986.

The containment, length and angle cuts were applied to select ν_μ ($\bar{\nu}_\mu$) QE events. The final sample consisted of 6 676 (3 065) events for positive (negative) horn polarity, the selection efficiency was estimated to be 29% for ν_μ and 40% for $\bar{\nu}_\mu$ interactions. The neutrino energy was reconstructed using the muon energy and angle; the spectra for the Monte Carlo simulation and the data agreed well for both sets.

To select ν_e ($\bar{\nu}_e$) QE events, well-collimated electromagnetic showers with a discontinuous hit pattern due to e-γ energy exchange were separated from hadronic showers with the help of criteria based on test beam data and Monte Carlo simulation. The cuts applied were 99% efficient in rejecting charged pions with energies above 1 GeV, while retaining 85% of electrons in test beam. The remaining sample consisted of electron events with a significant contamination of events with a π^0 in a final state. About 70% of the π^0-induced showers above 1 GeV were rejected by an analysis of shower profile (π^0-induced showers are wider and exhibit greater asymmetry than electron ones). The corresponding electron efficiency was estimated by the test beam measurements to be 80%. The remaining π^0

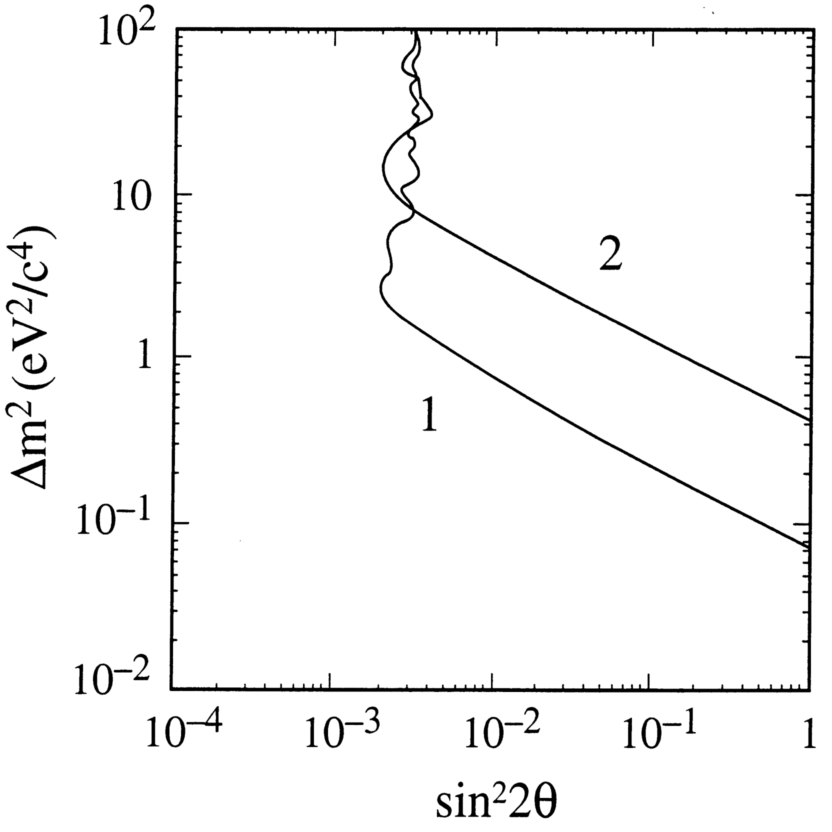

Figure 2.1: The 90% C.L. exclusion limits for $\bar{\nu}_\mu \rightarrow \bar{\nu}_e$ and $\nu_\mu \rightarrow \nu_e$ oscillations from the 1) E776 and 2) E734 appearance experiments at BNL.

contamination in the electron sample was estimated using π^0-induced showers found in the data and scaled, as a function of energy, by a Monte Carlo estimated probability for a π^0 to be misidentified as an electron. The expected π^0 background was 94 (41) events for the positive (negative) polarity sample. The systematic uncertainty in π^0 background prediction was estimated to be 20%.

The ν_e ($\bar{\nu}_e$) beam contamination was computed by a detailed Monte Carlo simulation program. The predicted background, normalized to the number of ν_μ ($\bar{\nu}_\mu$) events in the data, is 32.0 (7.7) from ν_e and 3.5 (12.2) from $\bar{\nu}_e$ for the positive (negative) horn polarity sample. The estimated error in the ν_e beam background was 11%.

The final positive polarity (ν_e) sample contained 136 events consistent with a total expected background of 131 ± 23 ± 19 events. The corresponding numbers for negative polarity ($\bar{\nu}_e$) sample were 47 data events with 62 ± 15 ± 9 events of expected background. No excess of electron-neutrino events was found indicating no evidence for $\nu_\mu \rightarrow \nu_e$ or $\bar{\nu}_\mu \rightarrow \bar{\nu}_e$ oscillations. Moreover, both sets of data were consistent with the expected background as a function of electron energy. Using the whole energy spectrum between 0 and 10 GeV and combining two limits for the positive and negative polarity data samples, an upper limit on the oscillation probability was set [26]:

$$P(\nu_\mu\ (\bar{\nu}_\mu)\ \to\ \nu_e\ (\bar{\nu}_e))\ <\ 1.5\cdot 10^{-3}\quad (90\%\ \text{C.L.}) \tag{2.10}$$

The region of the oscillation parameter space excluded by E776 at 90% confidence level is shown in Fig. 2.1. The difference in limits set by E734 and E776 experiments is almost completely accounted for by the difference in distances from neutrino source.

2.6 Medium energy accelerator experiments

2.6.1 LSND experiment

The Liquid Scintillator Neutrino Detector (LSND) was designed to detect neutrinos originating in a proton beam stop at the Los Alamos Meson Physics Facility (LAMPF)[1], and to search for $\bar{\nu}_\mu \to \bar{\nu}_e$ and $\nu_\mu \to \nu_e$ oscillations with a high sensitivity. Both channels have yielded evidence for neutrino oscillations.

The 800 MeV/c protons from the LAMPF linear accelerator sent to a 30 cm long water target produce mainly pions. Most of them (~97% of π^+ and ~95% of π^-) are stopped in the copper beam stop, situated 1.5 m downstream. Neutrinos are then produced by the following decay processes:

$$\begin{array}{lll} \pi^+ & \to\ \mu^+\ \nu_\mu & \text{(in flight or at rest)} \\ \mu^+ & \to\ e^+\ \nu_e\ \bar{\nu}_\mu & \text{(at rest)} \\ \pi^- & \to\ \mu^-\ \bar{\nu}_\mu & \text{(in flight)} \\ \mu^- & \to\ e^-\ \bar{\nu}_e\ \nu_\mu & \text{(at rest)} \end{array} \tag{2.11}$$

The detector [31] is a cylindrical tank containing 167 tons of liquid scintillator, located at about 30 m from the neutrino source. The use of doped mineral oil (CH_2) allows the detection of both Čerenkov and scintillator light in 1220 8" photomultiplier tubes, covering ~25% of the tank surface. The detector needs to distinguish $\bar{\nu}_e$ interactions from the events induced by ν_e and ν_μ, as well as cosmic rays.

Search for $\bar{\nu}_\mu \to \bar{\nu}_e$ oscillations from muon decay at rest

The positive pions which come to rest in the beam stop decay through the sequence

$$\begin{array}{l} \pi^+ \to \mu^+\ \nu_\mu \\ \mu^+ \to e^+\ \nu_e\ \bar{\nu}_\mu \end{array} \tag{2.12}$$

with a maximum energy of produced $\bar{\nu}_\mu$ and ν_e of 52.8 MeV (~$m_\mu/2$).

A search for $\bar{\nu}_\mu \to \bar{\nu}_e$ oscillations of $\bar{\nu}_\mu$ from μ^+ decay at rest can be performed in appearance mode due to very low $\bar{\nu}_e$ contamination in the beam. The only source of $\bar{\nu}_e$

---

[1] The accelerator name was changed in October 1995 to LANSCE (Los Alamos Neutron Scattering Center).

is $\pi^- \rightarrow \mu^- \ \bar{\nu}_\mu$ decay in flight (5% of all π^-) followed by a $\mu^- \rightarrow e^- \ \bar{\nu}_e \ \nu_\mu$ decay (only 12% of μ^- stopping in the high Z material). In addition, the production of positive pions in the LSND setup exceeds that of negative pions by a factor of about eight, so that the relative yield of $\bar{\nu}_e$ compared to $\bar{\nu}_\mu$ is $\sim(1/8)\times 0.05\times 0.12 \approx 7.5{\cdot}10^{-4}$ (a detailed Monte Carlo simulation gives a value of $7.8{\cdot}10^{-4}$).

For the $\bar{\nu}_e$ detection the inverse beta decay reaction followed by neutron capture (a usual way to detect reactor $\bar{\nu}_e$) is used:

$$\begin{aligned} \bar{\nu}_e \, p &\rightarrow e^+ \, n \\ n \, p &\rightarrow d \, \gamma \end{aligned} \tag{2.13}$$

Thus, the signature for the $\bar{\nu}_\mu \rightarrow \bar{\nu}_e$ oscillation search is two-fold and consists of a prompt electron-like signal, followed by a delayed 2.2 MeV photon correlated with the first signal in both position and time.

There are three main categories of background to be rejected:

- **Beam-unrelated background induced by cosmic rays.** It is suppressed at the trigger level by use of the passive and active (veto) shields; however, the trigger rate is dominated by this background (neutrino-induced events constitute less than 10^{-5} of all triggers). Cosmic ray induced neutrons are strongly suppressed by use of electron identification criteria based on the quality of the position and Čerenkov angle fits and the relative amount of early light.[1] A set of additional cuts based on the time to the previous and subsequent triggered events is applied to reject Michel $e^\pm$ from muon decay [32]. Because of the large duration of the proton pulses (600 μs), the precise relative timing of the event with respect to the pulse could not be applied, so that the remaining beam-unrelated background was measured from the beam-off sample and subtracted from beam-on sample.

- **Beam-related events with a primary particle identified as an electron and an accidental γ signal.** An approximate likelihood ratio R is defined using measured distributions of (a) the time of the γ after the primary event; (b) the number of hit photomultipliers for the reconstructed γ; (c) the distance of the reconstructed γ from the primary event. The obtained R distributions are then used to separate correlated neutron-capture photons from accidental signals.[2] This cut also discriminates against cosmic ray particles other than neutrons.

  One needs also to distinguish events induced by $\bar{\nu}_e$ (oscillation candidates) from the events produced by ν_e (it is not possible to distinguish an e^+ from an e^-). The requirement of a minimum positron energy E_{e^+} of 36 MeV eliminates most of the

---

[1] The identification efficiency was studied on the sample of electrons from decays of stopping cosmic ray muons and was found to be (84 ± 2)% in the $36 < E_e < 60$ MeV energy range with a typical neutron rejection of $\sim 10^3$.

[2] Measured on cosmic ray beam-off events, the efficiency that an accidental γ satisfies $R > 30$ is 0.6%, while the efficiency for a correlated γ is 23%.

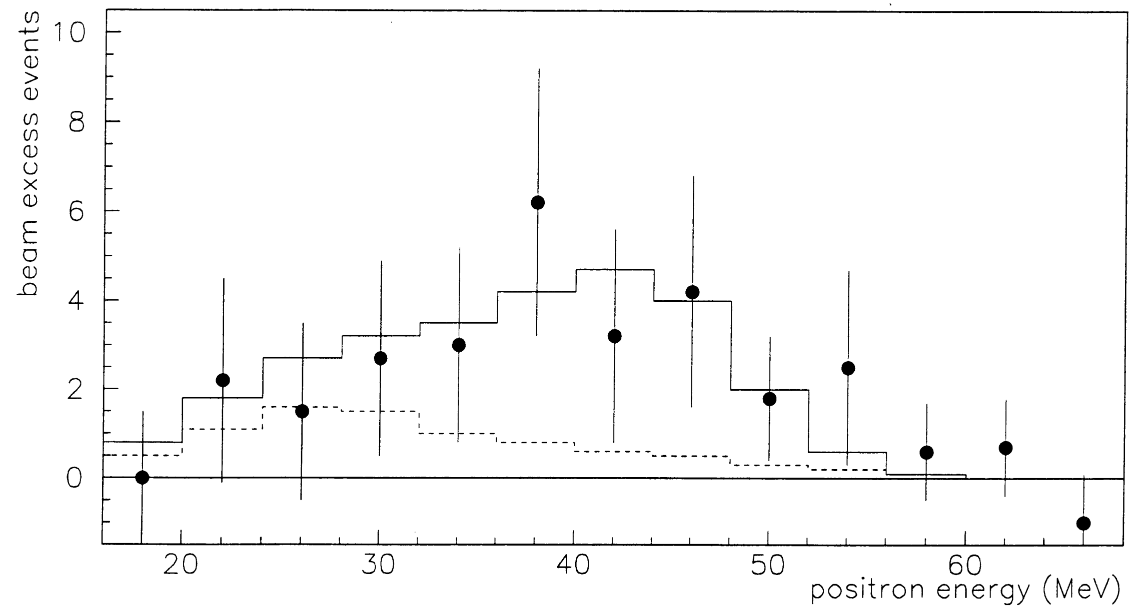

Figure 2.2: The energy distribution of the LSND beam-excess $\bar{\nu}_e$ events (data points) compared with the estimated neutrino background in the absence of oscillations (dashed line) and with the expected distribution for neutrino oscillations at large Δm^2 plus estimated beam-related background (solid line).

ν_e background due to $\nu_e\ ^{12}C \to e^-\ ^{12}N$ ($E_e < 36$ MeV) and $\nu_e\ ^{12}C \to e^-\ n\ ^{11}N$ ($E_e < 20$ MeV) reactions.

- **Beam-related events with a primary $e^\pm$ and a correlated neutron-capture signal.** This background is mainly due to $\bar{\nu}_e$ produced in the beam stop by μ^- at rest and the misidentification of $\bar{\nu}_\mu$ charged-current interactions as $\bar{\nu}_e$ events. As was already discussed, a dangerous $\bar{\nu}_e$ background (with the positron spectrum similar to that expected from oscillations) is suppressed by more than three orders of magnitude compared to $\bar{\nu}_\mu$ flux. Both $\bar{\nu}_e$ background and the background from a misidentification of $\bar{\nu}_\mu\ p \to \mu^+\ n$ events were estimated using the detailed beam and detector Monte Carlo simulation [33].

Requiring $R > 30$ and $36 < E_e < 60$ MeV, 22 events were observed in the beam-on data collected between 1993 and 1995. The beam-off background is measured to be 2.5 events. The estimated beam-related background amounts to 1.72 ± 0.41 events with correlated neutrons and 0.41 ± 0.06 without. The probability that the 22 or more beam-on events are entirely due to a statistical fluctuation of the 4.6 ± 0.6 events of total expected background is $4.1 \cdot 10^{-8}$. Fig. 2.2 shows the energy distribution of beam-on minus beam-off events over an extended energy range in comparison with the total estimated beam-related background (dashed line) and an oscillation signal plus estimated background (solid line).

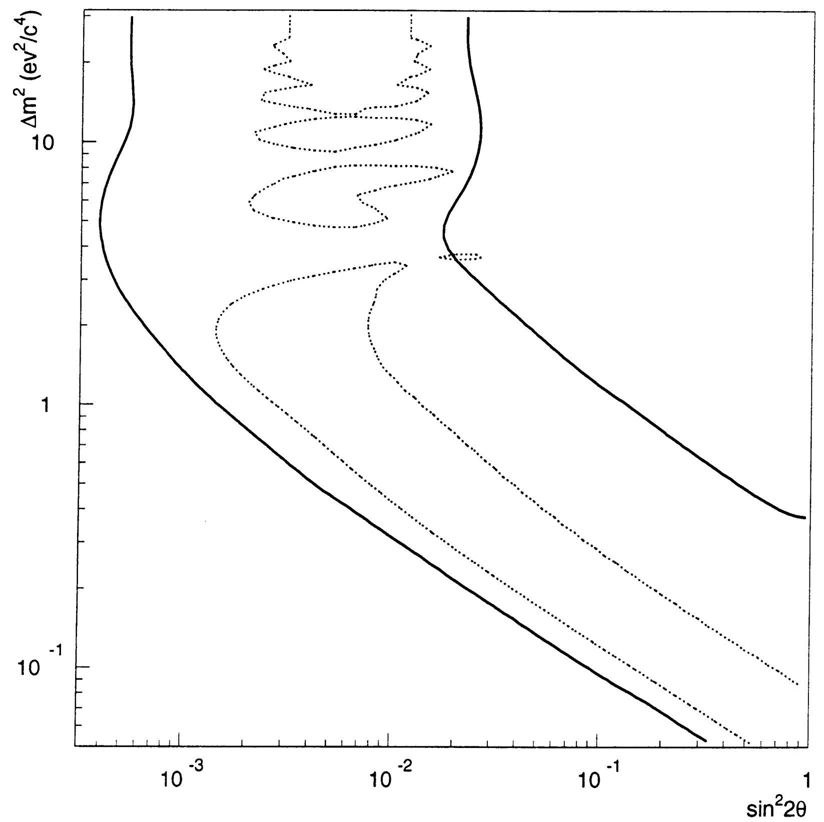

Figure 2.3: The 99% likelihood LSND favored regions for the decay at rest $\bar{\nu}_\mu \rightarrow \bar{\nu}_e$ oscillations (dashed contours) and the 95% confidence region for the decay in flight $\nu_\mu \rightarrow \nu_e$ oscillations (solid contour).

Accepting positron energies between 20 and 60 MeV, the total excess over background is $51.0\ ^{+20.2}_{-19.5} \pm 8.0$ events. If this excess is attributed to $\bar{\nu}_\mu \rightarrow \bar{\nu}_e$ neutrino oscillations, one obtains [34]:

$$P(\bar{\nu}_\mu \rightarrow \bar{\nu}_e) = (3.1 \pm 1.2 \pm 0.5) \cdot 10^{-3} \quad (90\% \text{ C.L.}) \tag{2.14}$$

The favored regions in the oscillation parameter plane have been calculated taking into account the systematic effects by varying the inputs to reflect uncertainties in background estimation, neutrino fluxes, and the R distribution shape. These allowed regions are shown in Fig. 2.3 (dashed contours).

Preliminary (not yet published) LSND results based on the data collected between 1993 and 1997 yield 29 beam-on events with 5.2 ± 0.6 beam-off and 3.0 ± 0.6 beam-related estimated background events (for $R > 30$ and $36 < E_e < 60$ MeV). The total excess over background for positron energies between 20 and 60 MeV is 82.8 ± 23.7 events, giving the probability for $\bar{\nu}_\mu \rightarrow \bar{\nu}_e$ neutrino oscillations of $(3.1 \pm 0.9 \pm 0.5)\cdot 10^{-3}$ at 90% C.L. [35].

Search for $\nu_\mu \to \nu_e$ oscillations from pion decay in flight

If neutrino oscillations of the type $\bar{\nu}_\mu \to \bar{\nu}_e$ occur, then $\nu_\mu \to \nu_e$ oscillations must occur also. A search for $\nu_\mu \to \nu_e$ oscillations has been conducted by the LSND collaboration using ν_μ from π^+ decay in flight. The signature for this oscillation search is the presence of an isolated electron in the energy range $60 < E_e < 200$ MeV from the inclusive charged-current reaction $\nu_e\ C \to e^-\ X$. The analysis has to rely solely on electron identification without any additional correlations which could help to improve the detection of the signal. Therefore, much more sophisticated electron identification algorithm compared with that used for the decay at rest analysis has been developed which was based on the relative likelihood of the measured photomultiplier charges and times [36].

The major irreducible beam-induced background is due to small ν_e contamination in the beam from $\mu^+ \to e^+\ \nu_e\ \bar{\nu}_\mu$ decay in flight (about 10^{-5} of μ^+) and $\pi^+ \to e^+\ \nu_e$ decay (with branching ratio of $1.24 \cdot 10^{-4}$). The number of beam-induced background events was calculated using the beam Monte Carlo neutrino fluxes and the $\nu_e\ C$ cross-section [33, 37].

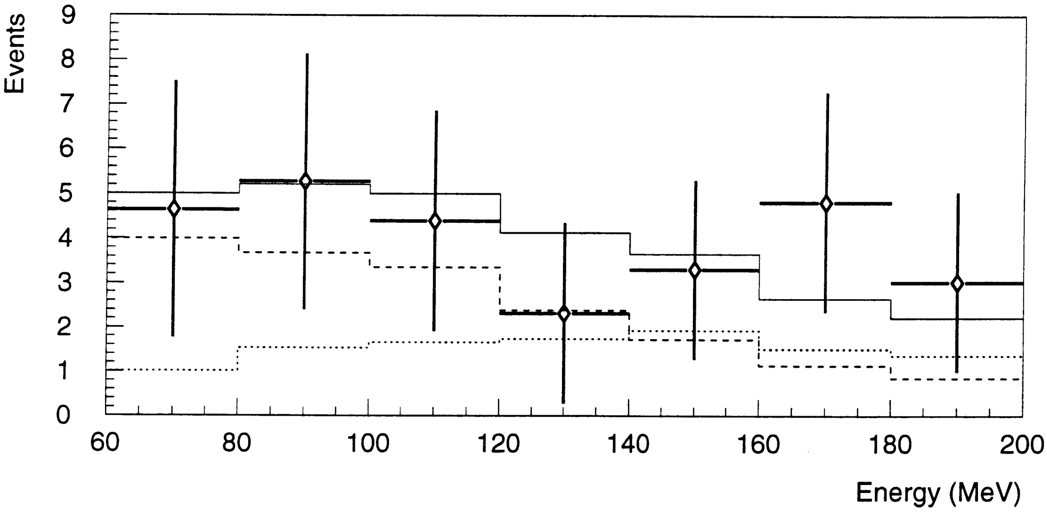

Figure 2.4: The energy distribution of the LSND beam-excess ν_e events (data points) compared with the estimated neutrino background (dotted histogram), the oscillation signal for large values of Δm^2 (dashed histogram), and the sum of the two (solid line).

An excess of beam-on events above the expected number from the sum of beam-related background and cosmic-ray beam-off events was observed. The "or" of two independent analyses gives 40 beam-on events selected[1] with the beam-off and ν-induced background of 12.3 ± 0.9 and 9.6 ± 1.9 events respectively. The probability that the 21.9 ± 2.1 estimated background events fluctuate into 40 or more observed events is $1.1 \cdot 10^{-3}$. The energy distribution of the beam-excess events is shown in Fig. 2.4 together with the energy distribution of the beam-induced background and that expected from a $\nu_\mu \to \nu_e$ oscillation

---

[1] Monte Carlo estimated efficiency of selection is ~16.5%.

signal for large values of Δm^2. The excess events are consistent with $\nu_\mu \to \nu_e$ oscillations with an oscillation probability of [38]:

$$P(\nu_\mu \to \nu_e) = (2.6 \pm 1.0 \pm 0.5) \cdot 10^{-3} \quad (90\% \text{ C.L.}) \tag{2.15}$$

A fit to the energy distribution, including systematic uncertainties and assuming neutrino oscillations as the source of ν_e excess, yields the allowed region in the oscillation parameter plane shown in Fig. 2.3 (solid contour). This region is consistent with the allowed region from the decay at rest $\bar{\nu}_\mu \to \bar{\nu}_e$ oscillation search. Since $\nu_\mu \to \nu_e$ oscillation search has different backgrounds and systematic errors from the $\bar{\nu}_\mu \to \bar{\nu}_e$ oscillation search, it provides additional evidence that both effects observed by LSND are due to neutrino oscillations.

2.6.2 KARMEN experiment

The KARMEN (KArlsruhe Rutherford Medium Energy Neutrino) experiment is being performed at the neutron spallation facility ISIS of the Rutherford Appleton Laboratory and is searching for $\bar{\nu}_\mu \to \bar{\nu}_e$ and $\nu_\mu \to \nu_e$ oscillations.

The ISIS neutrino beam is similar to the LAMPF one. However, an important difference is that the ISIS beam is pulsed with a time structure consisting of two 100 ns long proton pulses separated by 225 ns (this sequence has a repetition frequency of 50 Hz). Thus it is possible (Eq. (2.12)) to separate the ν_μ from "fast" pion decays (τ = 26 ns) and the $\bar{\nu}_\mu$ and ν_e from the "slow" muon decay (τ = 2.2 μs) by their different time distributions with respect to the beam pulse (syncronization beam-detector is better than ± 2 ns). This feature is important for $\nu_\mu \to \nu_e$ oscillation search.

The detector [39] is a 56 t segmented liquid scintillator calorimeter, located at a mean distance of 17.6 m from the beam stop. It is subdivided into 512 independent 3.5 m long boxes viewed by two 3" photomultipliers at each end. The event position is determined by the individual module and the time difference of the photomultiplier signals at each end of the module; the energy deposited in a module is given by the sum of the light output from either end. A Gd_2O_3 coated paper placed between adjacent modules allows neutron detection by neutron capture in Gadolinium followed by γ emission with a total energy of ~8 MeV and characterized by a large cross-section for fast neutrons.

Search for $\nu_\mu \to \nu_e$ oscillations

The KARMEN detector is installed at almost 90° with respect to the proton beamline, so the ν_μ flux from pion decay in flight is greatly suppressed and cannot be used for oscillation searches. However, due to the precise timing, the search for $\nu_\mu \to \nu_e$ oscillations from isotropic pion decay at rest (2.12) is possible, which LSND cannot perform.

Monoenergetic ν_e neutrinos (E_ν = 29.8 MeV) in the pion time window are searched for. The detection reaction is $\nu_e\ {}^{12}C \to e^-\ {}^{12}N_{g.s.}$ with the subsequent β-decay of the ground state ${}^{12}N_{g.s.} \to {}^{12}C\ e^+\ \nu_e$. Its signature consists of a prompt e^- signal with an energy

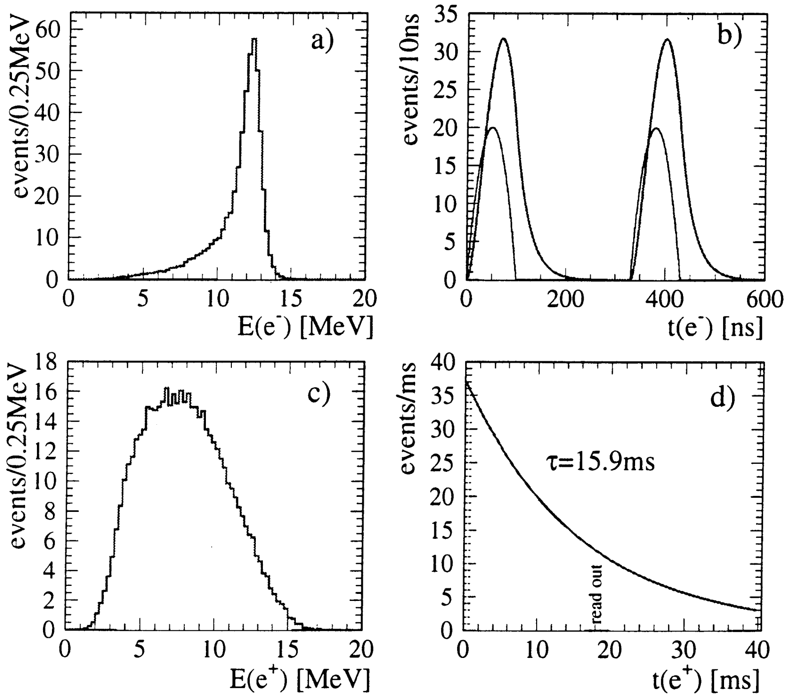

Figure 2.5: Expected signature of $\nu_\mu \to \nu_e$ oscillations (large Δm^2): a) energy distribution of prompt e^-; b) time of prompt signal relative to ISIS beam pulse; c) energy distribution of e^+; d) time difference between prompt and sequential signal. Shaded areas show the allowed regions of applied cuts.

spectrum peaked at 12.5 MeV followed by the spatially correlated e^+. After the cuts that maximize the signal (illustrated in Fig. 2.5), 2 events were observed in the data taken between 1992 and 1995. The beam-related background was estimated to be 1.76 ± 0.20 events and the cosmic ray induced background was 0.50 ± 0.20 events. With the total expected background of 2.26 ± 0.3 events, no evidence for $\nu_\mu \to \nu_e$ oscillations is found and an upper limit on the oscillation probability was set [40]:

$$P(\nu_\mu \to \nu_e) < 2.0 \cdot 10^{-2} \quad (90\% \text{ C.L.}) \tag{2.16}$$

The search for $\nu_\mu \to \nu_e$ oscillations from pion decay at rest in KARMEN has small background, so the sensitivity for this oscillation channel is essentially limited by the statistics.

Search for $\bar{\nu}_\mu \to \bar{\nu}_e$ oscillations

A search for $\bar{\nu}_\mu \to \bar{\nu}_e$ oscillations of $\bar{\nu}_\mu$ from μ^+ decay at rest gives the maximum sensitivity for the oscillation searches in KARMEN. The $\bar{\nu}_e$ contamination of the beam is very small ($\bar{\nu}_e/\nu_\mu \sim 6.2 \cdot 10^{-4}$) and the interactions of $\bar{\nu}_e$ have about 20 times larger cross-section compared to that of ν_e ($\nu_e\ {}^{12}C \to e^-\ {}^{12}N_{g.s.}$). The detection reaction is the

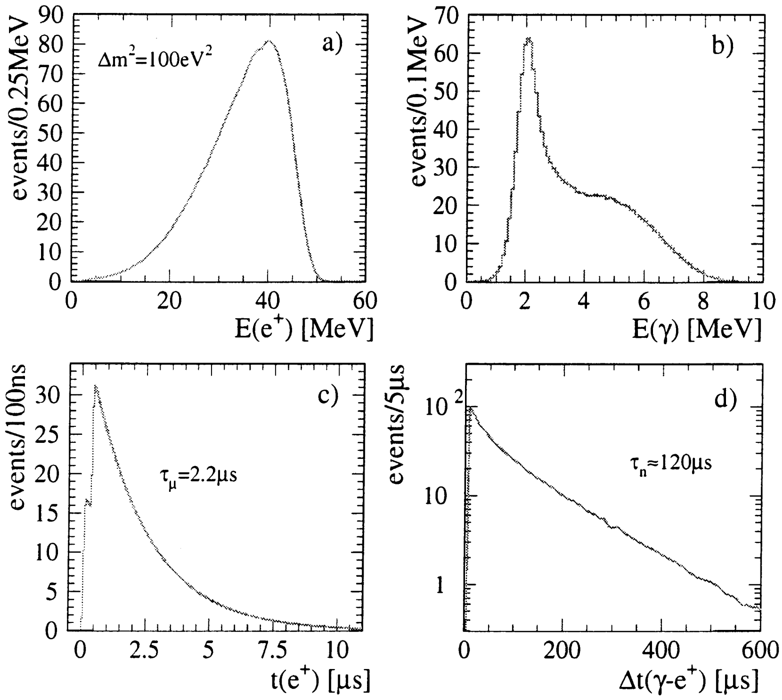

Figure 2.6: Expected signature of $\bar{\nu}_\mu \to \bar{\nu}_e$ oscillations (large Δm^2): a) energy distribution of prompt e^+; b) energy distribution of sequential γ's; c) time of prompt signal relative to ISIS beam pulse; d) time difference between prompt e^+ and sequential γ's. Shaded areas show the allowed regions of applied cuts.

inverse β-decay $\bar{\nu}_e\ p \to e^+\ n$ with a subsequent capture of the neutron by Gadolinium $n\ Gd \to Gd\ \gamma$ (8 MeV) or by protons $n\ p \to d\ \gamma$ (2.2 MeV). The signature (illustrated in Fig. 2.6) is a prompt positron signal with energies up to 51 MeV followed by the spatially correlated γ signal with energies of 2.2 MeV or up to 8 MeV. The positrons are expected in a time window of 0.5 to 10.5 μs after beam pulse, the neutrons are captured typically with $\tau = 120\ \mu$s.

In the data sample accumulated in 1990-1995, KARMEN found 16.4 ± 1.3 events per μs in a 10 μs window after the beam pulse. The expected background rate was 12.2 ± 0.2 events/μs (mainly cosmic ray induced events). Therefore, an excess of 2.4σ was observed; the sequential signal was found to be consistent with neutron capture but the time and energy distributions of the prompt signal did not follow the expectation from oscillations. On the basis of no evidence for oscillations, an upper limit on the $\bar{\nu}_\mu \to \bar{\nu}_e$ oscillation probability was set [40]:

$$P(\bar{\nu}_\mu \to \bar{\nu}_e) < 4.25 \cdot 10^{-3} \quad (90\% \text{ C.L.}) \tag{2.17}$$

Fig. 2.7 shows the 90% C.L. KARMEN exclusion limits for $\bar{\nu}_\mu \to \bar{\nu}_e$ and $\nu_\mu \to \nu_e$ oscillation channels in the parameter space of Δm^2 and $\sin^2(2\theta)$, in a two neutrino flavour calculation.

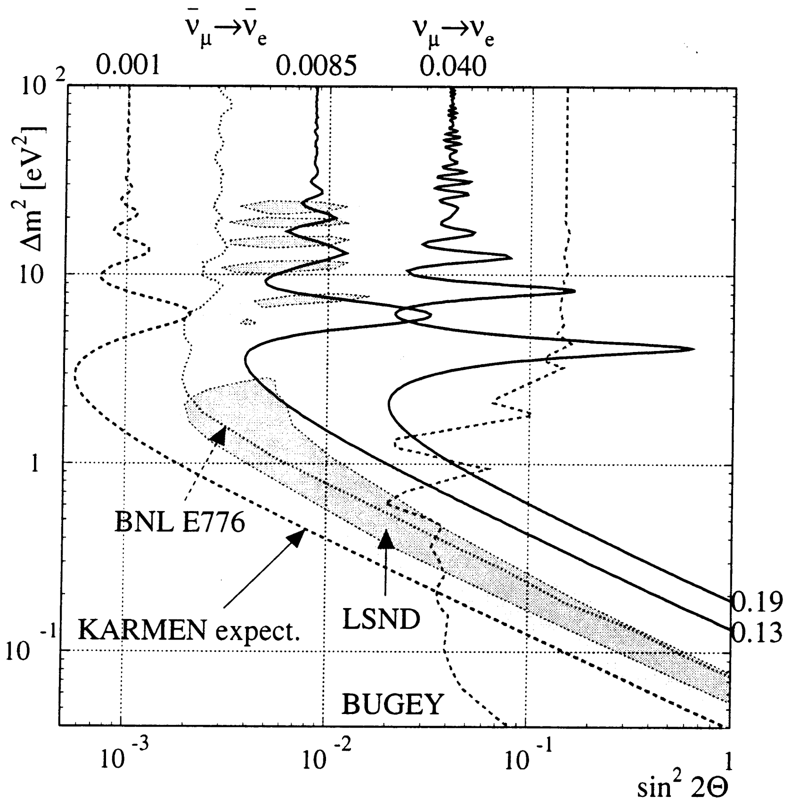

Figure 2.7: The 90% C.L. exclusion limits for $\bar{\nu}_\mu \to \bar{\nu}_e$ and $\nu_\mu \to \nu_e$ oscillations from KARMEN (solid lines), as well as the expected sensitivity for $\bar{\nu}_\mu \to \bar{\nu}_e$ oscillations after the upgrade (dashed line). Also shown are 90% and 99% likelihood LSND favored regions for muon decay at rest $\bar{\nu}_\mu \to \bar{\nu}_e$ oscillations (shaded areas) and oscillation limits from BNL E776 and Bugey experiments.

2.6.3 Comparison of LSND and KARMEN experiments

The main features of two experiments are compared in Table 2.1.

One of the main advantages of LSND over KARMEN is statistics: the beam intensity is 5 times higher at LAMPF than at ISIS and the mass of LSND detector is 3 times that of KARMEN. However, longer data taking period and smaller distance to neutrino source result in only 50% more statistics in LSND with respect to KARMEN [41].

The neutron capture by Gadolinium in KARMEN is a clear advantage over LSND. The photons emitted in the neutron capture by Gadolinium have energies up to 8 MeV (with an average energy of 6 MeV). In the neutron capture by proton, as in LSND, the total photon energy is only 2.2 MeV, which makes more difficult the separation of the signal over background.

Another KARMEN advantage is the time structure of the proton beam which, in particular, makes possible the search for oscillations of ν_μ from pion decay at rest.

The angle between the beam line and the detector is only 17° in LSND which allows to study $\nu_\mu \to \nu_e$ oscillations from pion decay in flight. However, this process is also a source

	LSND	KARMEN
Beam:		
Accelerator	LAMPF	ISIS
Energy	800 MeV	800 MeV
Proton beam current	1 mA	0.2 mA
Beam pulse	600 μs	2×100 ns
Repetition rate	120 Hz	50 Hz
Detector:		
Mass	180 t	56 t
Detection principle	Liquid scintillator + Čerenkov light	Liquid scintillator
σ_E/E	$6.6\%/\sqrt{E}$	$11.5\%/\sqrt{E}$
Position resolution	11 cm	11.5 cm
Neutron capture	Protons	Gd + protons
Oscillation search:		
Energy	20-300 MeV	10-50 MeV
Distance	~29 m	~17 m
Angle w.r.t. beam	17°	90°
Data taking:		
Years	1993-1995	1990-1995
Integrated charge	14 772 C	9 122 C

Table 2.1: The comparison between LSND and KARMEN experimental setups.

of beam-releated background for $\bar{\nu}_\mu \to \bar{\nu}_e$ oscillation search, and it is highly suppressed in KARMEN, situated at 90° with respect to the beam axis.

The detection of Čerenkov light in LSND provides a much better electron identification than that in KARMEN. Direct and isotropic scattered Čerenkov light emitted by relativistic electrons (about 2/3 of the total amount of light) have different emission time distributions compared to that of isotropic scintillation light, the only one occuring for non-relativistic particles such as neutrons and protons. Likelihood analysis of the differences between scintillation and Čerenkov light provides robust particle identification for $e^\pm$ in LSND [36].

At present, KARMEN sensitivity for $\bar{\nu}_\mu \to \bar{\nu}_e$ oscillation channel is limited by the background from cosmic muons stopping or scattered in the iron shielding surrounding the detector. Energetic neutrons emitted in these processes can penetrate into the detector without being vetoed, producing an event sequence of prompt recoil proton (misidentified as positron) followed by the capture of thermalized neutron. With an additional veto system installed in 1996, an upgraded KARMEN (KARMEN2) should either confirm or disprove the LSND result within three years (1997-1999) of data taking, reaching a sensitivity for $\bar{\nu}_\mu \to \bar{\nu}_e$ oscillations of $\sin^2(2\theta) < 1.6 \cdot 10^{-3}$ at 90% C.L. for large Δm^2 (dashed line in Fig. 2.7).

Recent (not yet published) KARMEN2 results on $\bar{\nu}_\mu \to \bar{\nu}_e$ oscillation search based on the data collected in February – September 1997 (1412 C protons on target corresponding to ~15% of the total KARMEN1 statistics) yield no measured events with 1.77 events of total expected background. Event selection criteria are very similar to those used by KARMEN1, but the cosmic background is reduced by more than a factor of 40. The limit on $\sin^2(2\theta) < 6.2 \cdot 10^{-3}$ at 90% C.L. for large Δm^2 (≥ 100 eV^2) is set [42].

2.6.4 Search for $\bar{\nu}_e$ appearance at LAMPF

We should mention for completeness that an appearance search of $\bar{\nu}_e$ has also been conducted in 1987–1989 at the Los Alamos Meson Physics Facility using a 20-ton detector consisting of liquid scintillation counters and proportional drift tubes (LAMPF experiment E645) [43]. The principle of the oscillation search was similar to that of the LSND search from muon decay at rest (see Sec. 2.6.1).

The total accumulated proton flux on the beam stop was 13 780 Coulombs. The selection of $\bar{\nu}_e$ events resulted in 11 beam-on events and the beam excess of 8.3 ± 3.4 events. The Monte Carlo calculations predicted a beam excess of 5.2 ± 0.5 events (8% systematic error assumed). The limits on $\bar{\nu}_\mu \to \bar{\nu}_e$ oscillation parameters of $\sin^2(2\theta) < 0.024$ at large Δm^2 and $\Delta m^2 < 0.14$ eV^2 at full mixing were set, less stringent than those of the KARMEN experiment.

2.7 CCFR experiment

The results of $\nu_\mu \to \nu_e$ oscillation search using the CCFR massive coarse-grained detector in the FNAL Tevatron neutrino beam have been recently reported [44, 45].

The Fermilab neutrino beam is created by decays of pions and kaons produced in interactions of the 800 GeV protons with a beryllium target. The FNAL Tevatron Quadrupole Triplet beam line, which had no sign-selecting magnets, was used to transport the secondary hadrons. This resulted in a wide-band neutrino beam which contains predominantly ν_μ neutrinos with energies up to 600 GeV (the average ν_μ energy is 165 GeV). The fraction of ν_e in the beam is 2.3%, the average energy is 160 GeV, 82% of ν_e neutrinos are produced from $K^+ \to \pi^0 e^+ \nu_e$.

The CCFR detector, located at a distance of about 1.2 km from the mid-point of the decay tunnel, consists of an 18 m long, 690 ton target calorimeter, followed by a 10 m long iron toroidal spectrometer. The target calorimeter is made of 168 steel plates, 3 m × 3 m × 5.15 cm each. The active elements are liquid scintillation counters placed every two steel plates and drift chambers placed every four plates. The separation between scintillation counters corresponds to 6 radiation lengths; the energy resolution of electromagnetic showers is $\sigma_E/E_e = 25\%/\sqrt{E_e}$.

The neutrino interactions observed in the detector can be divided into three classes depending on the type of the incoming neutrino and on the interaction type:

1. ν_μ charged current (CC) events $\nu_\mu N \rightarrow \mu^- X$;
2. $\nu_{\mu,e}$ neutral current (NC) events $\nu_{\mu,e} N \rightarrow \nu_{\mu,e} X$;
3. ν_e charged current events $\nu_e N \rightarrow e^- X$.

The ν_μ CC events (class 1) are identified by the presence of a primary muon which deposits energy characteristic of a minimum ionizing particle in a large number of consecutive scintillation counters. Neutral current events (class 2) and ν_e CC events (class 3) have no primary muon and deposit all the energy over a range of counters typical of a hadronic shower (5 to 20 counters). Moreover, the electron produced in ν_e CC events deposits energy in a few counters downstream of the interaction vertex which changes the energy profile of the shower.

Two different methods were used for $\nu_\mu \rightarrow \nu_e$ oscillation search: the first one was based on the difference in the longitudinal energy deposition pattern [44], the second one made use of a statistical separation of ν_e CC interactions by a shower profile analysis [45].

For the first method, all neutrino interactions were subdivided into "short" and "long" events, short events (mainly class 2 and class 3) being defined as those which deposit energy over an interval of 30 or fewer scintillation counters. The ratio R_{30} was defined to be the number of short events divided by the number of long events. Its value depends strongly on the ratio of neutral current to charged current events and was studied earlier by the CCFR collaboration to determine the value of electroweak mixing angle $\sin^2\theta_W$ [46]. In the study of $\nu_\mu \rightarrow \nu_e$ oscillations, the world average value of $\sin^2\theta_W$ was used to predict the R_{30} ratio. Any deviation in the measured R_{30} from the predicted value could be attributed to $\nu_\mu \rightarrow \nu_e$ oscillations, since interactions of additional ν_e in the neutrino beam would be registered as short events and thus would cause the measured R_{30} to be larger than its calculated value.

The ratio R_{30} was measured as a function of the energy deposited in the first 20 counters following the interaction vertex, E_{cal}. Requiring $E_{cal} > 30$ GeV (to suppress the contributions from quasielastic and resonance production) and imposing fiducial cuts to ensure event containment, the resulting data sample consisted of about 450 000 events. Fig. 2.8 shows the R_{30} distribution as a function of E_{cal} for the data and for the detailed Monte Carlo simulation.

All the systematic uncertainties in the comparison of $R_{30}(E_{cal})$ in the Monte Carlo and in the data were thoroughly studied in the weak mixing angle measurement and well-known. The largest systematic error is induced by the 4.2% uncertainty in the ν_e flux, dominated by a 20% production uncertainty in the K_L content of the secondary beam which produces 16% of ν_e neutrinos. The majority of the ν_e flux comes from $K_{e3}^{\pm}$ decays, which were constrained by the observed ν_μ spectrum from $K \rightarrow \mu\ \nu$ decays.

The data were fit by minimizing a χ^2 which incorporates the possible effect of oscillations, statistical and systematical uncertainties. At all values of Δm^2 the data were

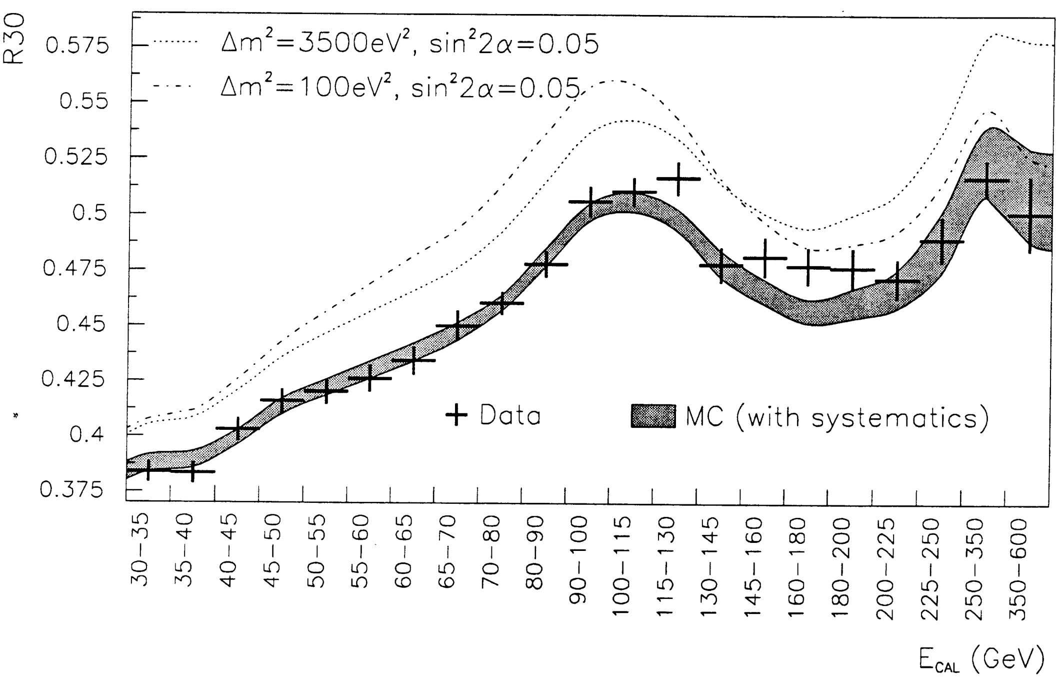

Figure 2.8: The ratio R_{30} as a function of E_{cal} for the data (points with error bars) compared to Monte Carlo prediction with 1σ systematic uncertainty assuming no oscillations (filled band).

found consistent with no observed $\nu_\mu \to \nu_e$ oscillations. The 90% confidence upper limit is shown in Fig. 2.10 (dashed line). The limit on the mixing angle for large ($>$ 1000 eV^2) Δm^2 is [44]:

$$\sin^2(2\theta) \; < \; 3.8 \cdot 10^{-3} \quad (90\% \text{ C.L.}) \tag{2.18}$$

For the second method, the absolute flux of ν_e neutrinos at the detector is compared to the flux predicted by a detailed beam line simulation. To identify statistically ν_e CC events, shower energy profile of short and long events is compared and the difference is attributed to the presence of ν_e CC interactions in the short sample.

The shower energy deposition profile is characterized by the ratio of the sum of the energies deposited in the first three scintillation counters to the total visible energy E_{vis} deposited in the calorimeter:

$$r_3 \; = \; 1 \; - \; \frac{E_1 \; + \; E_2 \; + \; E_3}{E_{vis}} \tag{2.19}$$

To compare directly short, long and ν_e CC events, a muon track from the data was added to the short events and a GEANT [47] generated electromagnetic shower of the appropriate energy was added to the long data events. Then the shape of the observed r_3 distribution for the short sample was fitted to a combination of ν_μ CC and ν_e CC distributions (with appropriate muon additions):

$$\nu_\mu NC(+\mu) \; = \; \alpha \cdot \nu_\mu CC \; + \; \beta \cdot \nu_e CC(+\mu) \tag{2.20}$$

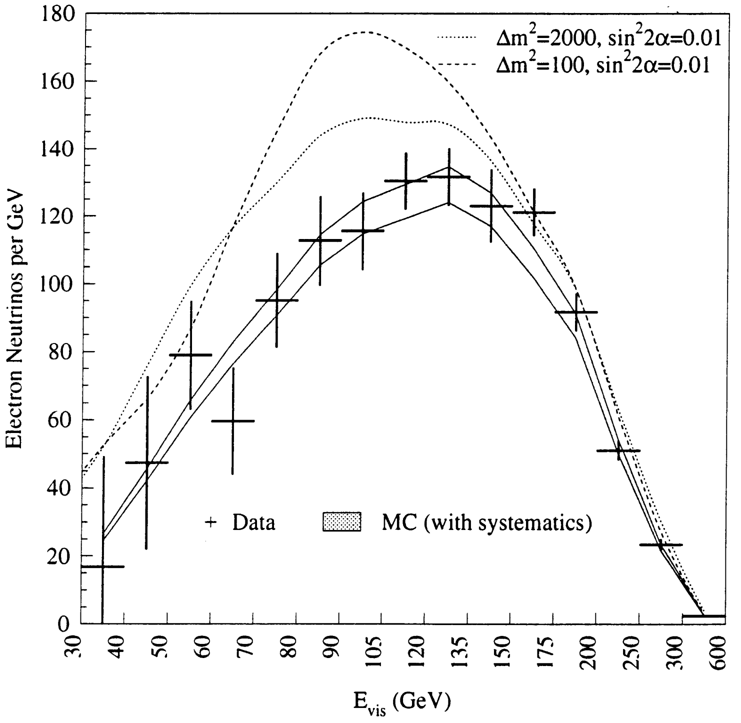

Figure 2.9: Number of electron neutrinos as a function of E_{vis} for the data (points with error bars) compared to Monte Carlo prediction with 1σ systematic uncertainty assuming no oscillations (filled band).

The final data samples (after $E_{vis} > 30$ GeV and fiducial cuts) consisted of 630 000 long and 290 000 short events. The fit performed in different E_{vis} bins yielded the number of ν_e CC events as a function of E_{vis} shown in Fig. 2.9. The measured number of ν_e CC interactions agrees with the Monte Carlo prediction in each energy bin.

The major sources of systematic uncertainties in the comparison of the electron flux extracted from the data to that predicted by the Monte Carlo were the 4.1% uncertainty in the incident flux of ν_e (discussed above) and the error in the shower shape modeling, estimated by extracting the ν_e flux using two different definitions of r. A χ^2 fit of the data was performed; at all Δm^2 the data were found consistent with no observed $\nu_\mu \rightarrow \nu_e$ oscillations. The 90% confidence upper limit is shown in Fig. 2.10 (solid line). The limit on the mixing angle for large (> 1000 eV^2) Δm^2 is [45]:

$$\sin^2(2\theta) < 1.8 \cdot 10^{-3} \quad (90\% \text{ C.L.}) \tag{2.21}$$

2.8 Conclusion

The summary of the present experimental situation in $\nu_\mu \rightarrow \nu_e$ oscillation search in the region of $\Delta m^2 > 0.1$ eV^2 is shown in Table 2.2 and Fig. 2.10. The LSND muon decay at rest allowed region in the oscillation parameter plane (filled band) with the central

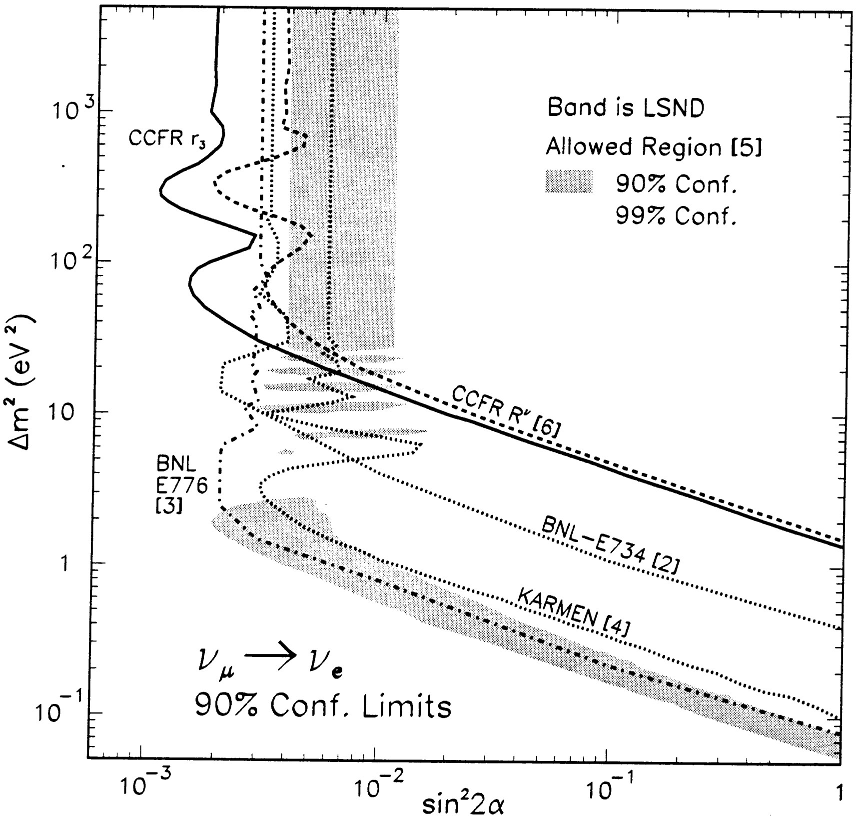

Figure 2.10: The regions of $\sin^2 2\alpha$ and Δm^2 parameters (two-flavour mixing scheme) of $\nu_\mu \rightarrow \nu_e$ oscillations allowed by the LSND analysis of muon decays at rest (filled band) and excluded by the KARMEN, BNL E776, BNL E734 and CCFR R_{30} (dashed line) and r_3 (solid line) analyses (see text).

value of oscillation probability $P(\bar{\nu}_\mu \rightarrow \bar{\nu}_e) = 3.1 \cdot 10^{-3}$ (90% C.L.) is not fully excluded by the ensemble of the negative results from other experiments. The most stringent limits at different values of Δm^2 are set by the measurements of Bugey [48] (not shown), KARMEN, BNL E776 and CCFR collaborations. More data are needed to clarify the situation and any new competitive result on $\nu_\mu \rightarrow \nu_e$ oscillation search is important.

Experiment	Year	Method	$\langle E_{\nu_\mu}\rangle$, GeV	$\sin^2(2\theta)$ $\Delta m^2 \to \infty$	Δm^2, eV^2 $\sin^2(2\theta) = 1$
Gargamelle @ PS	1978	$\nu_\mu \to \nu_e$	1.5	$4 \cdot 10^{-3}$	1.0
Gargamelle @ SPS	1981	$\nu_\mu \to \nu_e$	25	$8 \cdot 10^{-3}$	1.4
BEBC @ SPS	1981	$\nu_\mu \to \nu_e$	25	$10 \cdot 10^{-3}$	1.7
BEBC @ PS	1986	$\nu_\mu \to \nu_e$	1.5	$13 \cdot 10^{-3}$	0.09
15-ft	1981	$\nu_\mu \to \nu_e$	18.5	$6 \cdot 10^{-3}$	0.6
SKAT	1988	$\nu_\mu \to \nu_e$	8	$2.5 \cdot 10^{-3}$	1.3
CHARM	1988	$\nu_\mu \to \nu_x$	1.5	0.17 @ 1.5 eV^2	0.19 - 50
CDHS	1984	$\nu_\mu \to \nu_x$	1.5	0.05 @ 2.5 eV^2	0.26 - 90
CCFR	1985	$\nu_\mu \to \nu_x$	40-230	0.02 @ 100 eV^2	15 - 1000
CHARM @ PS	1988	$\nu_\mu \to \nu_e$	1.5	$30 \cdot 10^{-3}$	0.8
CHARM @ SPS	1988	$\nu_\mu \to \nu_e$	25	$8.0 \cdot 10^{-3}$	1.0
CHARM II @ SPS	1994	$\nu_\mu \to \nu_e$	25	$5.6 \cdot 10^{-3}$	0.85
CDHS + CHARM	1996	$\nu_\mu \to \nu_x$	50	$3.0 \cdot 10^{-3}$	2.4
BNL-E734	1985	$\nu_\mu \to \nu_e$	1.5	$3.4 \cdot 10^{-3}$	0.43
BNL-E776	1992	$\nu_\mu \to \nu_e$	1.5	$3.0 \cdot 10^{-3}$	0.075
KARMEN	1997	$\nu_\mu \to \nu_e$	0.0298	$40 \cdot 10^{-3}$	0.19
KARMEN	1998	$\bar{\nu}_\mu \to \bar{\nu}_e$	0.01-0.05	$6.2 \cdot 10^{-3}$	0.10
LAMPF-E645	1993	$\bar{\nu}_\mu \to \bar{\nu}_e$	0.02-0.06	$24 \cdot 10^{-3}$	0.14
CCFR	1995	$\nu_\mu \to \nu_x$	140	$3.8 \cdot 10^{-3}$	1.6
CCFR	1997	$\nu_\mu \to \nu_e$	140	$1.8 \cdot 10^{-3}$	1.6

Table 2.2: Summary of negative searches for $\nu_\mu \to \nu_e$, $\bar{\nu}_\mu \to \bar{\nu}_e$ and $\nu_\mu \to \nu_x$ neutrino oscillations from various accelerator experiments.

Chapter 3

The NOMAD experiment

3.1 Introduction

The Neutrino Oscillation MAgnetic Detector (NOMAD) experiment [49] was designed to search for ν_τ appearing from $\nu_\mu \rightarrow \nu_\tau$ oscillations in the CERN SPS wide-band neutrino beam, which consists primarily of ν_μ neutrinos with a negligible ($< 5 \cdot 10^{-6}$) contamination of prompt ν_τ [50]. If $\nu_\mu \rightarrow \nu_\tau$ oscillations occur, ν_τ neutrinos could be detected via their charged current interactions $\nu_\tau N \rightarrow \tau^- X$ in an active target using the kinematical characteristics of the subsequent τ^- decays. Located at a distance of 620 m from the average neutrino production point, NOMAD is sensitive to the cosmologically interesting ν_τ mass range $\Delta m^2 > 1$ eV^2 and is expected to reach a sensitivity of $\sin^2 2\theta_{\mu\tau} < 3.8 \cdot 10^{-4}$ for $\Delta m^2 \geq 40$ eV^2.

The $\tau^- \rightarrow e^- \nu_\tau \bar{\nu}_e$ decay channel has the smallest background because of the low ν_e contamination (less than 1%) in the beam. Therefore, the detector has been optimized to efficiently detect electrons, in particular ν_e CC interactions. Their analysis is relevant for the search for $\nu_\mu \rightarrow \nu_e$ oscillations, since an oscillation signal would manifest itself both as an excess of events in the ν_e CC sample and as a change in the shape of the ν_e energy spectrum. The interest for this kind of study has recently highly increased, following the LSND claim for evidence for $\nu_\mu \rightarrow \nu_e$ oscillations [34, 38]. In case of $\nu_\mu \rightarrow \nu_e$ oscillations with $\Delta m^2 > 10$ eV^2 and with the probability of $3 \cdot 10^{-3}$ observed by LSND, a signal should be seen in the NOMAD data.

Since the NOMAD detector has a granularity and a target density similar to that of a bubble chamber, the experiment can also study conventional neutrino physics processes which require the tracking and identification of individual particles together with the large statistics of neutrino interactions.

In this chapter we briefly review the design of the CERN wide-band neutrino beam, the principles of $\nu_\mu \rightarrow \nu_\tau$ oscillation search with NOMAD and describe the detector design, optimized for the efficient detection of various τ^- decay modes. A detailed discussion of $\nu_\mu \rightarrow \nu_e$ oscillation search is deferred until chapter 6.

3.2 The CERN neutrino beam

The NOMAD detector is located at the CERN West Area Neutrino Facility (WANF) and is exposed to the SPS wide-band neutrino beam. This beam line has been operating for nearly 20 years either in the wide-band beam or in the narrow-band beam mode. In the wide-band beam the neutrino parent particles are focused over a wide range of momenta, which provides a high intensity neutrino beam required for the $\nu_\mu \rightarrow \nu_\tau$ oscillation search.

Fig. 3.1 shows a schematic layout of the WANF beam line, which has been optimized in 1992 and 1993 [51] and realigned [52] for the NOMAD and CHORUS experiments.

The neutrinos are primarily produced from the decays in flight of the secondary π and K mesons originating from 450 GeV protons impinging on a beryllium target. The protons are extracted from the SPS in two 4 ms long spills (fast/slow extraction cycle) separated by 2.6 s with a 2.0 s "flat top". The proton beam has a Gaussian shape with $\sigma \approx 0.5$ mm at the target. Two Beam Current Transformers (BCTs) upstream of the target measure the flux of incident protons. The delivered intensity extends up to $1.5{\cdot}10^{13}$ protons in each of the two spills. The SPS cycle repeats every 14.4 s.

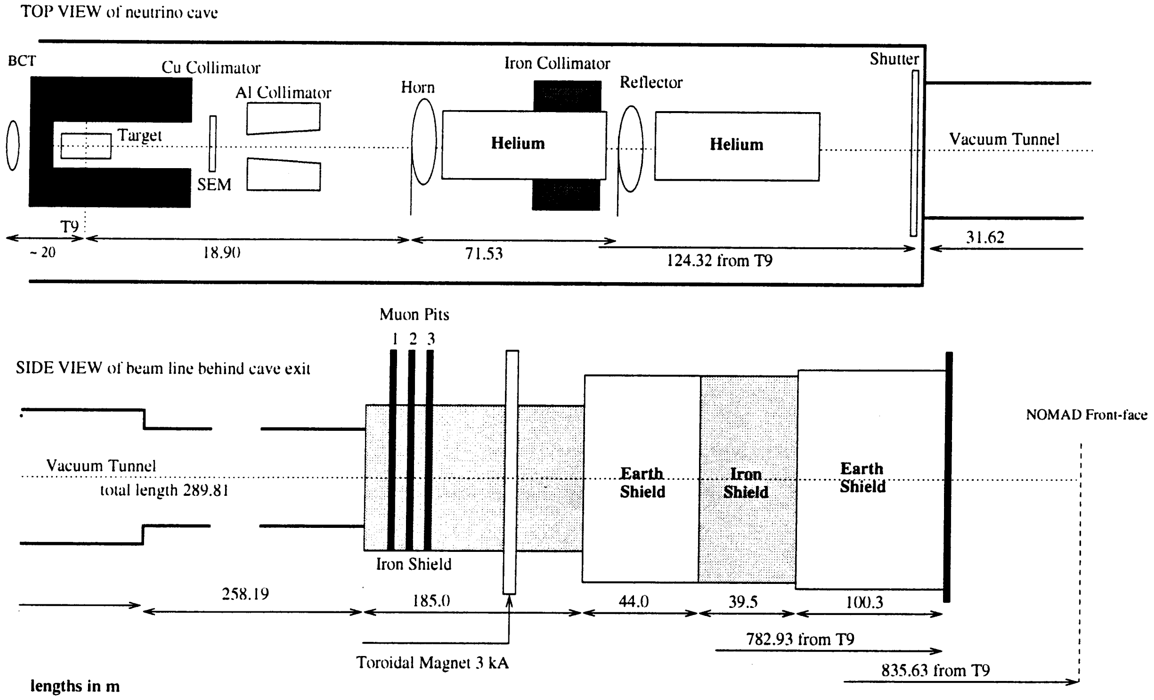

Figure 3.1: Schematic layout of the WANF beam line pointing out its main elements (not drawn to scale).

The target station consists of 11 beryllium rods positioned longitudinally along the proton beam line and separated by 9 cm gaps. Each rod is 10 cm long and 3 mm in diameter. A small-angle collimator is installed immediately after the target station to provide a better matching of the secondary particle beam to the entrance apertures of the magnetic elements downstream. The Secondary Emission Chamber (SEM) measures the total flux of secondary particles in the forward direction.

The secondary pions and kaons are focused by a pair of coaxial magnetic lenses – the horn and the reflector. In such a system charged particles are deflected by the toroidal field between two coaxial conductors carrying equal and opposite currents, so that the focusing of particles of one charge sign implies defocusing of particles of the opposite sign. The polarity of the currents can be changed to provide neutrino or antineutrino beams. The sections between the horn and reflector and between the reflector and decay tunnel are enclosed in helium tubes in order to reduce the absorption of the secondary particles. A large-angle collimator has been installed between the horn and the reflector to reduce the $\bar{\nu}_\mu$ contamination in neutrino beam by intercepting the defocused negative secondaries before they decay.

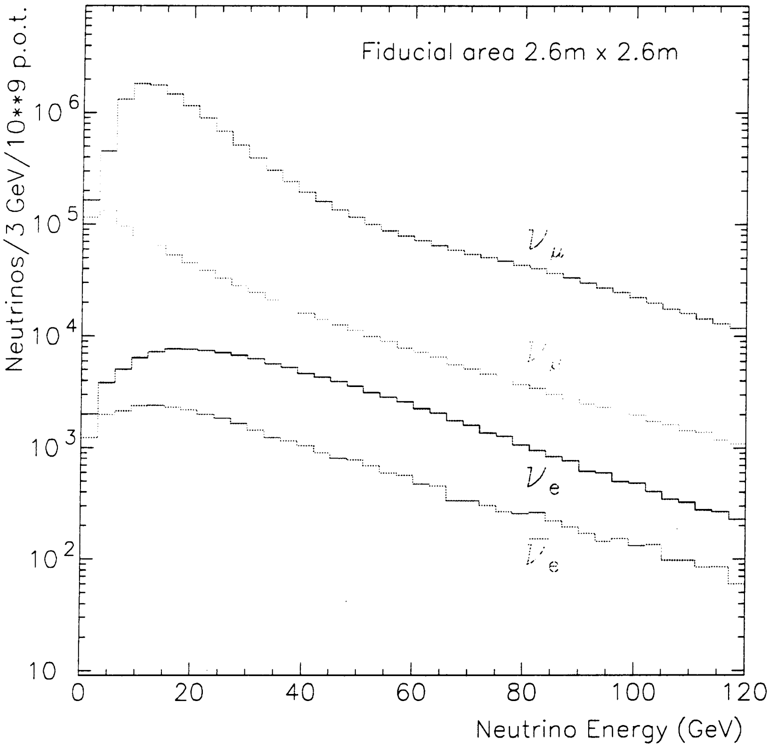

Figure 3.2: The predicted energy spectra of neutrinos at NOMAD. The spectra are calculated for a fiducial area of 2.6×2.6 m^2 and for 10^9 protons on target.

The focused mesons decay in a 290 m long vacuum tunnel. The decay tunnel is followed by shielding made of iron and earth to range out the muons and absorb the hadrons. A toroidal magnet located at the entrance of the iron shielding defocuses the residual muons. A neutrino beam monitoring system, based on the detection of muon yields at several depths in the iron shield (the "muon pits"), is built into the line. The silicon detectors in these muon pits provide an absolute flux measurement. The calibration of the silicon detectors is performed periodically using emulsion measurements in the pits.

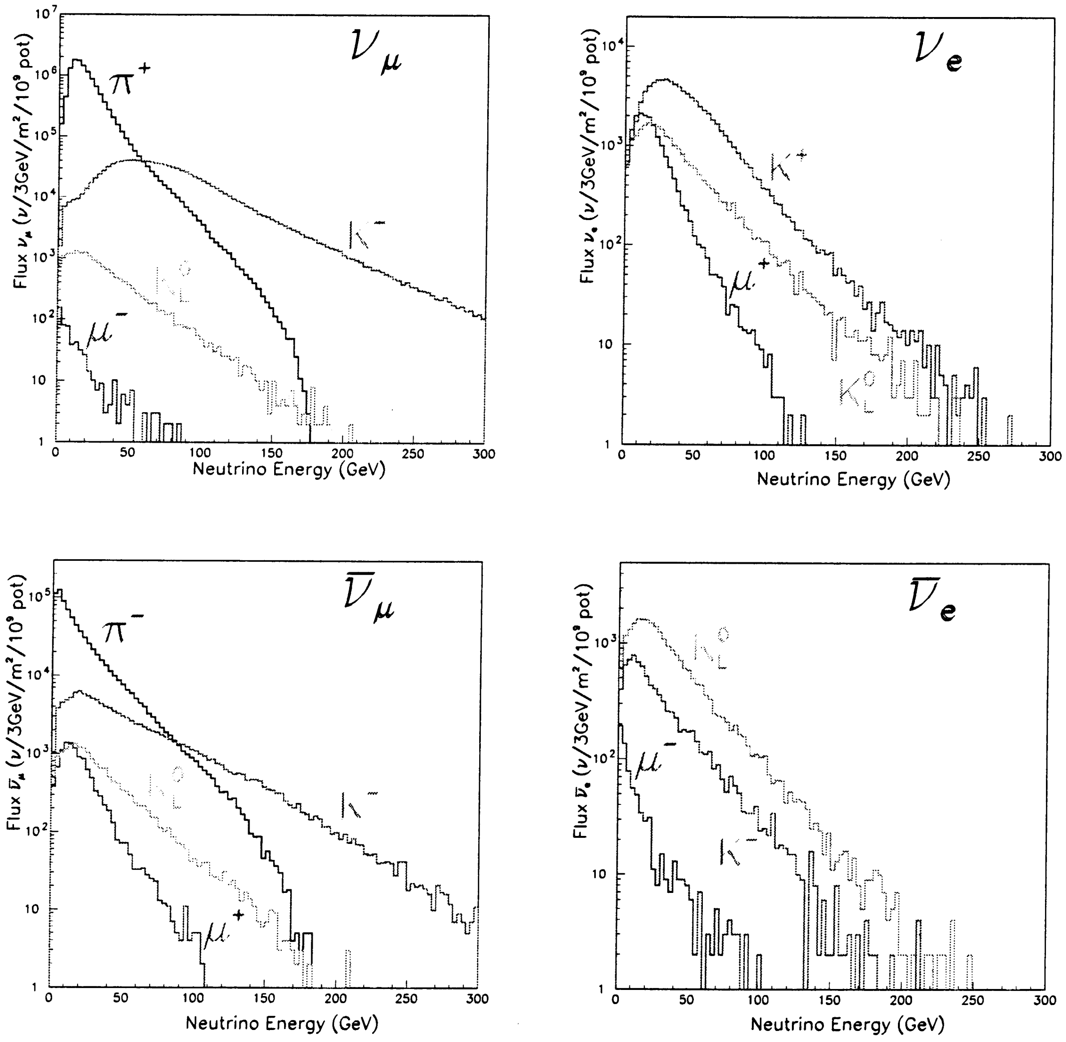

Figure 3.3: Predicted compositions of the ν_μ, $\bar{\nu}_\mu$, ν_e and $\bar{\nu}_e$ spectra at NOMAD [53].

As a result, the CERN neutrino beam (normally operated in the positive focusing mode) consists predominantly of ν_μ neutrinos with an about 5.5% $\bar{\nu}_\mu$ admixture, a small ν_e component (less than 1%) and a negligible ($< 5 \cdot 10^{-6}$) contamination of prompt ν_τ. The spectra of the principal four neutrino species, ν_μ, $\bar{\nu}_\mu$, ν_e and $\bar{\nu}_e$, are shown in Fig. 3.2. The average ν_μ energy is about 24 GeV, that of the ν_e is about 39 GeV.

The NOMAD and CHORUS detectors are located at about 835 m and 823 m from the target respectively. The average distance between the meson decay point and NOMAD is 620 m. The predicted compositions of the ν_μ, $\bar{\nu}_\mu$, ν_e and $\bar{\nu}_e$ spectra at NOMAD are shown in Fig. 3.3 [53]:

- The ν_μ neutrinos (top left) are primarily produced via two body decays of π^+ ($\approx 91\%$ of ν_μ) and K^+ ($\approx 8\%$), plus much smaller contributions from other sources (K^0_L, μ^-, charmed hadrons, etc.). The upper limit of the ν_μ energy is set by the mass of the parent particle: the neutrinos from the pion decay dominate the ν_μ spectrum up to ~50 GeV, these from K^+ decays are the main ν_μ component above ~75 GeV.

- Analogous to ν_μ, the $\bar{\nu}_\mu$ neutrinos (bottom left) are primarily produced via decays of π^- ($\approx 85\%$ of $\bar{\nu}_\mu$) and K^- ($\approx 11\%$). Compared to ν_μ, a larger fraction of $\bar{\nu}_\mu$ comes from K^0_L, μ^+, and charmed hadron decays. The K^-/π^- ratio smaller than that of the K^+/π^+ causes the $\bar{\nu}_\mu$ from π^- to dominate the $\bar{\nu}_\mu$ spectrum till about 100 GeV. The $\bar{\nu}_\mu$ flux relative to ν_μ is about 5.5%.

- Four sources contribute to the ν_e flux (top right): the contribution from $K^+ \to \pi^0\ e^+\ \nu_e$ is dominant (about 66% of ν_e); the muons ($\approx 16\%$) and $K^0_L \to \pi^-\ e^+\ \nu_e$ ($\approx 15\%$) contribute next; finally, the charmed hadrons and hyperons contribute at the 3% level to the total ν_e. The ν_e flux relative to ν_μ in the absence of $\nu_\mu \to \nu_e$ oscillations is expected to be about 0.9%.

- The principal source of $\bar{\nu}_e$ (bottom right) is the $K^0_L \to \pi^+\ e^-\ \bar{\nu}_e$ decay, accounting for about 67% of $\bar{\nu}_e$. The other sources of $\bar{\nu}_e$ are: $K^- \to \pi^0\ e^-\ \bar{\nu}_e$ ($\approx 18\%$), charmed hadron decays ($\approx 13\%$, not plotted), and a small contribution from μ^-. The $\bar{\nu}_e$ flux relative to ν_μ is only about 0.3%.

The knowledge of the neutrino fluxes – in particular, the relative abundance of ν_e to ν_μ neutrinos at various energies – is crucial for the $\nu_\mu \to \nu_e$ oscillation search in NOMAD. The various simulations of the neutrino beam, predicted neutrino fluxes and uncertainties of the predictions will be discussed in detail in chapter 7.

3.3 Search for $\nu_\mu \to \nu_\tau$ oscillations with NOMAD

The design of the NOMAD detector has been optimized to use the kinematic selection methods for the search for $\nu_\mu \to \nu_\tau$ oscillations. A potential ν_τ candidate is detected by means of its charged current interaction and the subsequent τ^- decay:

$$\nu_\tau\ +\ N\ \to\ \tau^-\ +\ X\ \ ;\ \ \tau^-\ \to\ \textit{decay products}\ +\ \nu_\tau \qquad (3.1)$$

NOMAD was designed to detect both the leptonic ($e^-\nu_\tau\bar{\nu}_e$ or $\mu^-\nu_\tau\bar{\nu}_\mu$) and hadronic ($\pi^-\nu_\tau$, $K^-\nu_\tau$, $\rho^-\nu_\tau$ or $\pi^-\pi^-\pi^+(n\pi^0)\nu_\tau$) decay modes of the produced τ^-, i.e. about 88% of the τ decays. The identification of ν_τ interactions in NOMAD relies on kinematic criteria. The isolation of the τ decay products from the remainder of the event, and the momentum imbalance in the transverse plane (missing p_T) induced by the momentum carried away by the final state neutrino(s) from τ decay, allows one to distinguish the ν_τ CC interactions from ν_μ and ν_e CC or neutral current background events. This kinematical method was proposed long ago [54], but neutrino detectors of previous generations never had the required resolution to make use of it.

The basic concept of the oscillation search in each τ^- decay channel is to use various Monte Carlo and data samples to define a set of cuts that optimize the sensitivity to $\nu_\mu \rightarrow \nu_\tau$ oscillations and reduce the background to an acceptable level. The principles of the analysis are briefly described below.

3.3.1 Hadronic τ decay channels

The analysis of the hadronic τ^- decays relies mainly on isolation criteria. Particle identification is used only to reject charged current events containing primary muons or electrons. The largest background are neutral current interactions and charged current events where the leading lepton (muon or electron) is not identified.

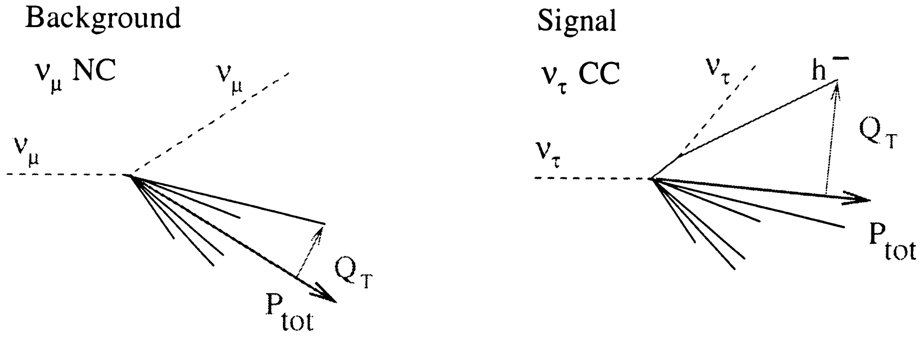

Figure 3.4: Isolation variable Q_T for ν_μ NC background (left) and $\tau^- \rightarrow h^- \; \nu_\tau$ signal (right).

The generic hadron candidate h^- (where h^- is π^-, ρ^- or $\pi^+\pi^-\pi^-$) is searched for as a leading negatively charged primary particle. The Q_T, component of the momentum of the hadron system $\vec{p}_{h^-}$ perpendicular to the total visible momentum $\vec{p}_{tot}$ (see Fig. 3.4), is computed for each event:

$$Q_T = \sqrt{(\vec{p}_{h^-})^2 - (\vec{p}_{h^-} \cdot \vec{p}_{tot})^2 / p_{tot}^2}. \tag{3.2}$$

Since hadrons in the background events are produced in the fragmentation of the hit quark and the nucleon remnants, they have a limited transverse momentum with respect to the total system, while the expected signal exhibits a long Q_T tail. A cut on this variable is used to efficiently separate signal from the background.

3.3.2 Leptonic τ decay channels

Fig. 3.5 illustrates the main kinematic criteria used in the selection of the leptonic τ decay modes. The missing momentum in the plane transverse to the incoming neutrino

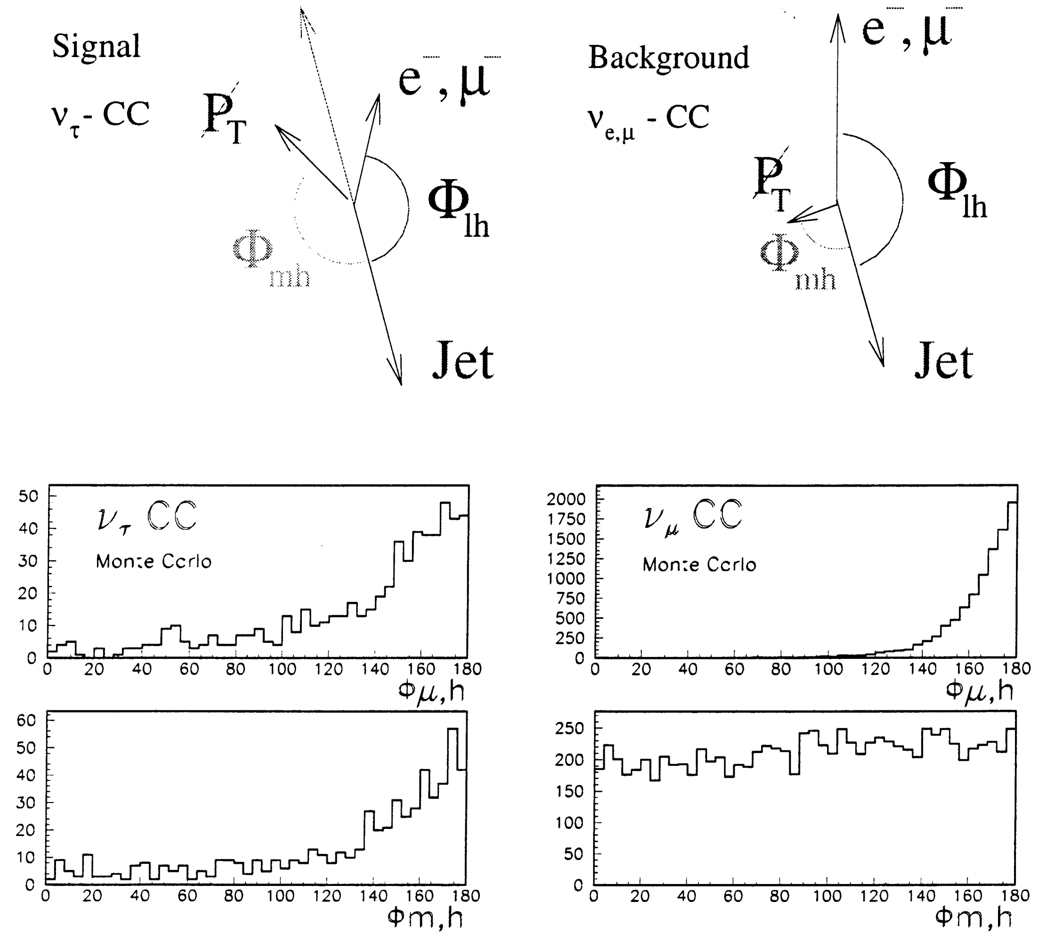

Figure 3.5: Transverse plane variables used to distinguish ν_τ CC signal (left) from $\nu_{e,\mu}$ CC background interactions (right): definition of the variables (top) and their Monte Carlo simulated distributions (bottom).

direction ($\not{p}_T$) can be calculated and interpreted as a measurement of the transverse momentum of the neutrinos from τ decay. The angles Φ_{lh} and Φ_{mh} are then formed between the transverse momentum vectors of the outgoing lepton l (where l is e^- or μ^-), the hadron jet resultant h and missing $\not{p}_T$, as shown in Fig. 3.5, top. The angle Φ_{lh} is peaked strongly towards 180° in ν_e and ν_μ CC events (Fig. 3.5, bottom), whereas in ν_τ events this correlation is much weaker due to the escaping neutrinos from τ decay. Similarly, the direction of the $\vec{\not{p}}_T$ in the ν_e and ν_μ CC interactions is determined by resolution and has no particular direction, making the Φ_{mh} distribution flat. In contrast, the Φ_{mh} distribution in ν_τ CC events is peaked towards 180°, reflecting the fact that the τ^- and the hadron jet are produced back-to-back in the transverse plane. The separation between signal and background is enhanced by combining these angular variables in the Φ_{lh} - Φ_{mh} plane, see Fig. 3.6.

The electronic $\tau^- \to e^- \nu_\tau \bar{\nu}_e$ decay channel is particularly attractive because of a

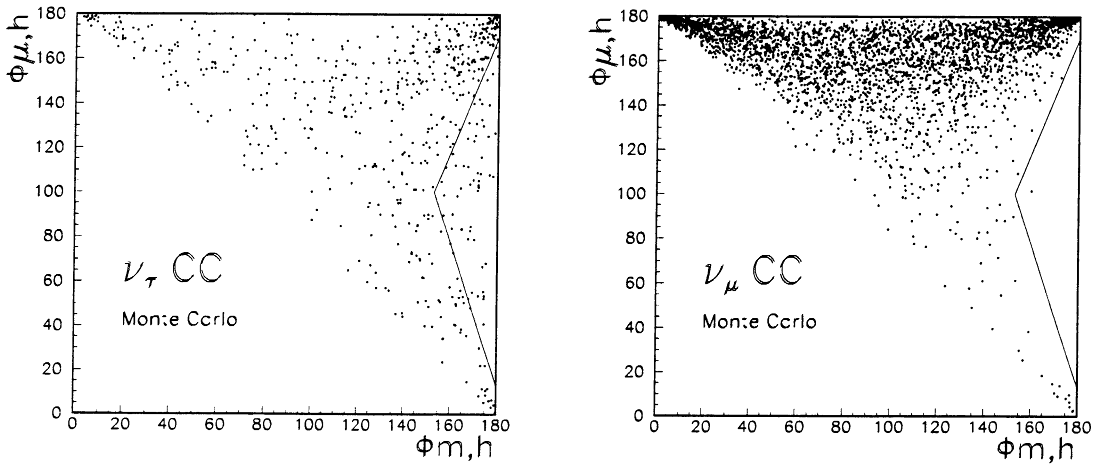

Figure 3.6: Distributions of Φ_{mh} versus $\Phi_{\mu h}$ for ν_τ CC signal (left) and ν_μ CC background interactions (right), Monte Carlo simulation.

small background. The signal detection in this channel relies on excellent identification capabilities and precise energy and direction measurements of electrons. The dominant background arises from mismeasured ν_e CC events which must be reduced by the kinematic cuts described above. The additional ν_e CC rejection factor comes from larger energy of primary ν_e neutrinos compared to that of ν_μ.

Besides ν_e CC interactions, the following background sources are present:

- photon conversions and Dalitz decays of π^0s in neutral current events or in ν_μ CC interactions with a lost muon;
- misidentified isolated pions simulating electrons;
- $\mu^- \to e^- \bar{\nu}_e \nu_\mu$ and $K^- \to e^- \pi^0 \nu_e$ decays, Compton scattering;

These backgrounds are removed by tight electron identification and electron isolation cuts. All of them can be measured with great accuracy in the data, especially in the large sample of ν_μ CC events.

It is important to note that the large statistics of ν_μ CC interactions offers the possibility to study detector and physics effects on the resolution of kinematic variables and on the oscillation search. A comparison of the ν_μ CC data to the Monte Carlo generated sample gives a direct measure of the effect of the differences in the hadronic system between the data and the MC.

3.3.3 Requirements on the detector design

The kinematic selection methods described above impose stringent requirements on the design of the NOMAD detector:

- electrons and muons need to be well identified to search for τ leptonic decay modes, as well as for rejecting CC background as efficiently as possible in the $\tau \to$ hadrons search;
- the energy of neutral particles and the momentum of charged particles need to be measured as precisely as possible in order to have good resolution of kinematic variables;
- large statistics of neutrino interactions should be accumulated, for the experiment to be sensitive to low oscillation probability and to study the tails of the background distributions on ν_μ CC data sample.

The next section of this chapter describes the NOMAD subdetectors and the way these goals were achieved.

3.4 The NOMAD Detector

The NOMAD detector [55] is shown schematically in Fig. 3.7. It consists of a number of subdetectors, most of which are located in a dipole magnet [56] with a field volume of $7.5 \times 3.5 \times 3.5$ m^3. The magnetic field is horizontal, perpendicular to the neutrino beam direction, and has the value of 0.4 T. The active target with a mass of $\sim$2.7 t is a set of drift chambers used to reconstruct charged particle tracks and to measure their momenta in a magnetic field. The active target is followed by a transition radiation detector to identify electrons and a system of preshower and electromagnetic calorimeter used to improve the electron identification and to provide the measurement of electron energy together with the reconstruction of electromagnetic showers induced by photons. Large drift chambers located outside the magnet are used for the muon identification. The detector is complemented by iron-scintillator hadronic and front calorimeters. The upstream veto and the two trigger planes are used to select neutrino interactions in the detector.

The various NOMAD subdetectors are described in the following sections of this chapter. The transition radiation detector will be discussed in more detail in the next chapter.

3.4.1 Veto counters

The veto system consists of an arrangement of 59 scintillation counters covering an area of 5×5 m^2 at the upstream end of the NOMAD detector. The scintillators have a thickness of 2 cm, a width of 21 cm, and are of two lengths, 300 cm and 210 cm. Most (56) of the counters are viewed at both ends by photomultipliers; the remaining three counters have single–ended readout. The counters are arranged in a geometry which provides an optimal rejection of charged particles produced upstream of NOMAD, of those produced in neutrino interactions in the iron detector support and of cosmic rays. Interactions in the lateral part of the support structure of the detector and in the magnet coil are not vetoed,

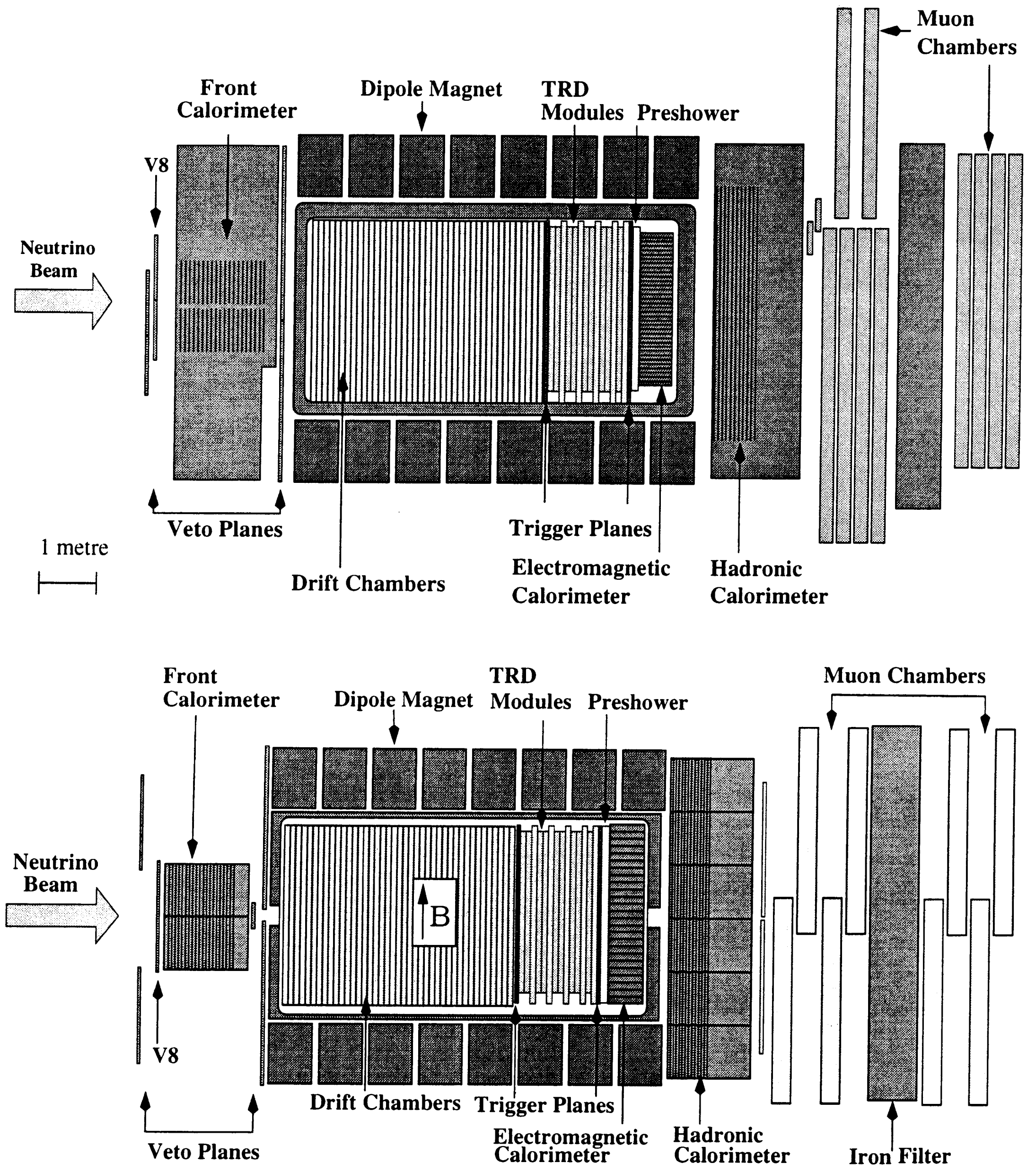

Figure 3.7: A sideview (top) and a topview (bottom) of the NOMAD detector.

but are easily distinguished from the interactions in the active target by the reconstruction of the event vertex.

The two photomultiplier outputs connected to each scintillation counter are fed via discriminators to the inputs of mean-timer modules [57]. For central detector triggers, the veto signal is formed by logical OR of all mean-timer modules; for triggers in the front calorimeter, the veto is formed from the subset of ten counters (denoted V_8) mounted on the front face of the support (see Fig. 3.7). The charged particle rejection efficiency of the

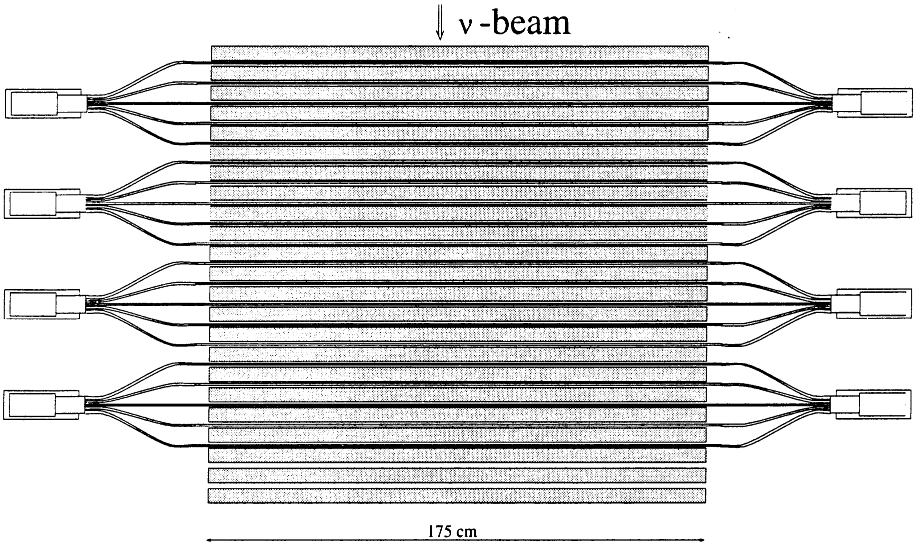

Figure 3.8: Top view of the FCAL.

NOMAD veto is constantly monitored and is at a level of 96-97%.

3.4.2 Front calorimeter

The central part of the NOMAD detector is suspended from iron pillars at the two ends of the magnet. The front pillar was instrumented with scintillators to provide an additional massive active target for neutrino interactions. The expected number of ν_μ CC events in this front calorimeter (FCAL), which has a depth of about 5 nuclear interaction lengths and a total mass of ~17.7 tons, is about ten times more than that in the drift chamber target. Physics topics to be addressed by the FCAL include [58]:

- **Multi-muons.** The study of opposite sign dimuons is of special interest. About 70 000 of such events in ν_μ CC interactions in FCAL is expected. This large sample may allow a compelling determination of the Cabibbo-Kobayashi-Maskawa matrix element V_{cd}, the strange quark sea content k and the mass of the charm quark m_c.
- **Neutral heavy particle search.** If a neutral heavy particle is induced by a neutrino interaction, it may subsequently decay. With a combination of the FCAL and other NOMAD subdetectors one can explore a large region of masses and mixing of such a particle.

The FCAL consists of 23 iron plates which are 4.9 cm thick and separated by 1.8 cm gaps. In order to measure the energy and centroid of hadronic showers in neutrino induced interactions, 20 out of the 22 gaps are instrumented with long scintillators which are read out on both ends by 3" photomultipliers.[1] The dimensions of the scintillators are

---

[1] The scintillators and photomultipliers were previously used in the CDHS experiment [59]; test measurements showed that the quality of the material is still satisfactory to be reused in the NOMAD.

$175 \times 18.5 \times 0.6$ cm^3. As a compromize between optimal light collection and the number of electronic channels, five consecutive scintillators along the beam axis are ganged together by means of twisted light guides and form a module. Ten such modules are placed above each other and form a stack. Along the beam axis are four such stacks, as shown in Fig. 3.8. The area of the FCAL "seen" by the neutrino beam is 175×190 cm^2.

Since the FCAL is part of the structural components of the NOMAD detector, it cannot be easily calibrated in a test beam of known hadronic energy. The FCAL calibration has been performed using highly relativistic muons, a reasonable approximation of minimally ionizing particles (m.i.p.). The hadronic energy equivalent of a m.i.p. has been determined by a Monte Carlo simulation and by a study of the shape of Y_{bj} distribution, which is well known for neutrino charged current interactions. A detailed description of the calibration procedure can be found in [60].

3.4.3 Drift chambers

The drift chambers provide at the same time the target material and the tracking of particles. They were designed with the conflicting requirements that their walls should be as heavy as possible in order to maximise the number of neutrino interactions and as light as possible in order to minimise multiple scattering of particles, secondary particle interactions and photon conversions. To minimise the total number of radiation lengths for a given target mass, the chambers are made of low density and low atomic number materials; there is less than 1% of a radiation length between 2 consecutive measurements.

The transverse dimensions of the chambers are approximately 3×3 m^2 and they fully occupy the available transverse space inside the magnet coil. There are 49 chambers in the complete detector corresponding to 147 sense wire planes. The 44 target chambers are mounted in 11 modules of four chambers each in the front part of the detector; five chambers are installed individually in the TRD region and are used for a better extrapolation of the tracks to the rest of the subdetectors. The total fiducial mass of the chambers is 2.7 t over an area of 2.6×2.6 m^2.

The layout of the drift chambers is sketched in Fig. 3.9. They are built on panels made of aramid fibres in a honeycomb structure. These panels are sandwiched between two Kevlar-epoxy resin skins, which maintain the mechanical rigidity and flatness over the large surface area. Each drift chamber consists of four panels (Fig. 3.9, top). The three 8 mm gaps between the panels are filled with an argon (40%) – ethane (60%) mixture at atmospheric pressure. These gaps are equipped with sense wires at angles of +5, 0 and −5 degrees with respect to the magnetic field direction. Potential wires are interleaved with the sense wires (Fig. 3.9, bottom). These wires are equally spaced vertically to provide drift cells of ± 3.2 cm around each sense wire. Field shaping aluminum strips, 2.8 mm wide and separated by 1.2 mm, are printed on mylar glued to the panels. The 3 m long wires are glued to support rods at 3 points to keep the anode-cathode gap constant. The potential wires are held at −3200 V and the anode wires at +1750 V. The potentials on the strips provide a drift field of 1 kV/cm. With this electric field and the gas mixture

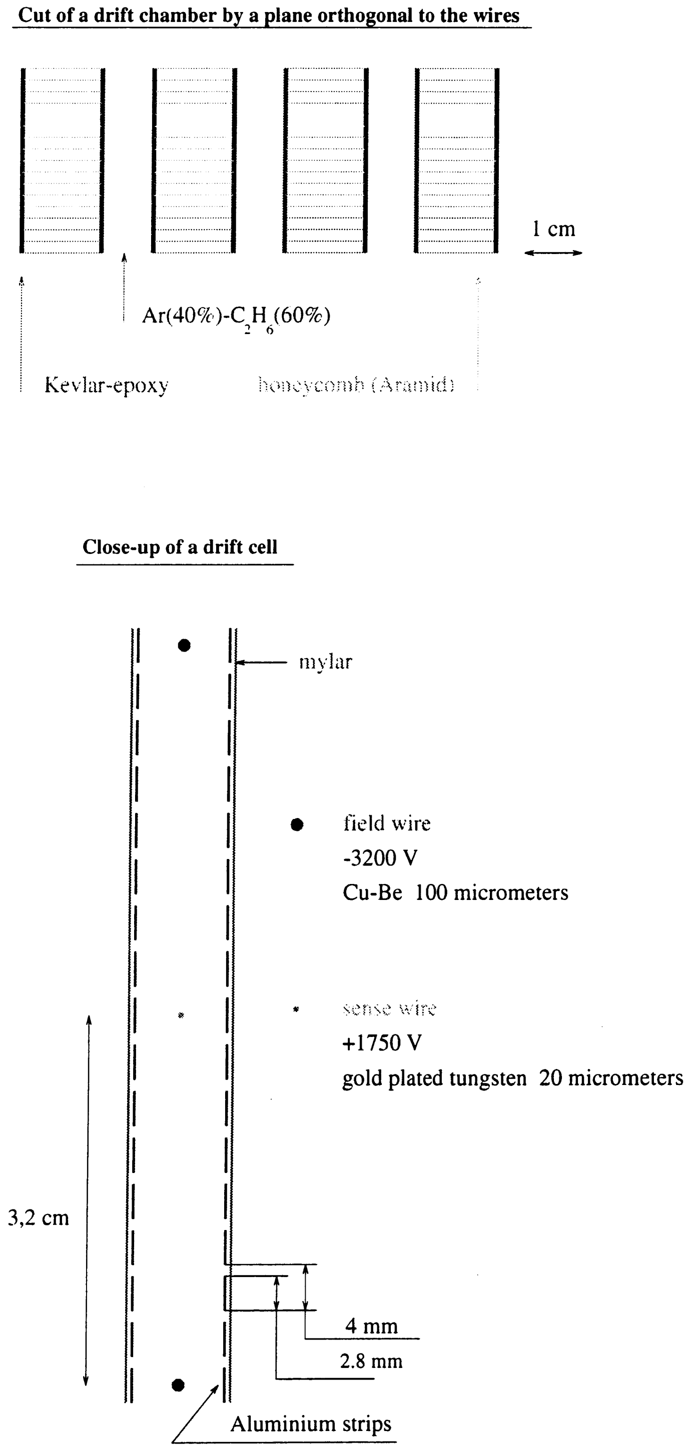

Figure 3.9: Schematic view of the drift chamber layout.

used, the ionization electrons drift with a velocity of about 50 mm/μs.

The space resolution has been studied using straight tracks (muons) crossing the detector. The distribution of residuals with a sigma of about 150 μm has been obtained after a careful alignment of all wires and a detailed description of the time-to-distance relation. The dependence of the track residuals on drift distance and polar angle is shown in Fig. 3.10. One can see that for large incident angles, deformations of the electric field significantly deteriorate the resolution. The resolution along the wires, with the 5° stereo angles, is 1.5 mm.

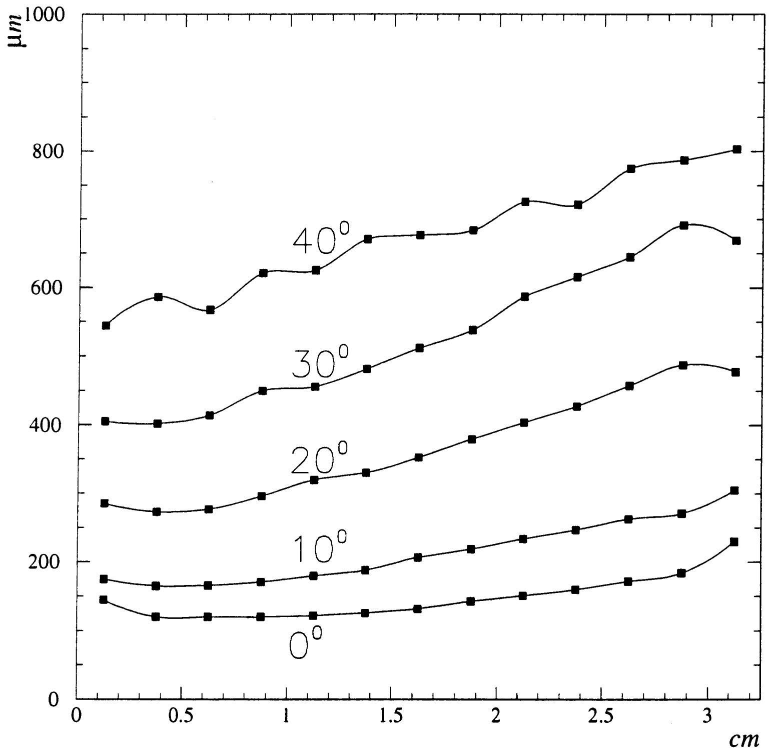

Figure 3.10: The dependence of the track residuals on drift distance and angle.

The momentum resolution provided by the drift chambers is a function of particle momentum and track length. For charged hadrons and muons travelling normal to the plane of the chambers, it can be parametrized as:

$$\frac{\sigma_p}{p} \approx \frac{0.05}{\sqrt{L}} \oplus \frac{0.008p}{\sqrt{L^5}} \tag{3.3}$$

where the momentum p is in GeV/c and the track length L is in metres. The first term is the contribution from multiple scattering and the second term comes from the single hit resolution of the chambers. For a momentum of 10 GeV/c, multiple scattering is the dominant contribution for track lengths larger than 1.3 m. Typical values of the momentum resolution σ_p/p as a function of the track length L and momentum p are shown in Table 3.1.

Track length L, m	σ_p/p, %, for tracks of		
	1 GeV/c	10 GeV/c	50 GeV/c
1.5	4.1	5.0	15.1
3.5	2.7	2.7	3.2

Table 3.1: Momentum resolution σ_p/p obtained in the NOMAD drift chambers for various momenta p and track lengths L.

The tracking is less precise for electrons due to bremsstrahlung in the tracking system. The electron energies are measured by combining information from the drift chambers and the electromagnetic calorimeter (see chapter 6 for further discussion).

3.4.4 Trigger counters

Two trigger planes are installed in the NOMAD detector; the first plane follows the active target and the second plane is positioned behind the TRD region. Each of them covers a fiducial area of 280×286 cm^2 and consists of 32 scintillation counters with single-ended photomultiplier readout. The scintillators have a thickness of 0.5 cm and a width of 19.9 cm and are connected by adiabatic lightguides to 16-dynode photomultipliers of the proximity mesh type, which are oriented parallel to the magnetic field. The field of 0.4 T reduces the response of these photomultipliers by only 30%. A coincidence between the signals in two planes is required for a valid trigger.

The average efficiency of the trigger counters for single tracks has been determined with data and found to be $(97.5 \pm 0.1)\%$.

3.4.5 Preshower detector

The preshower (PRS), which is located just in front of the electromagnetic calorimeter, is composed of two planes of proportional tubes (286 horizontal and 288 vertical) preceded by a 9 mm lead(96%) - antimony(4%) converter of 1.6 X_0.

The proportional tubes are made from extruded aluminium profiles (see Fig. 3.11) and are glued to two aluminium end plates of 0.5 mm thickness. Each tube has a square cross-section of 9×9 mm^2 and the walls are 1 mm thick. The proportional tubes have gold-plated tungsten wires and operate with a mixture of Ar(80%) – CO_2(20%) at a voltage of 1500 V. Signals from each tube are fed into charge preamplifiers. The output signals of opposite polarity are sent via Delaying and Pulse Shaping Amplifiers to charge ADCs.

The preshower serves mainly for two purposes:

- The finer granularity of the PRS compared to that of the electromagnetic calorimeter (ECAL) allows to determine the impact point of converted photons with a spatial resolution of about 1 cm and helps to separate overlapping ECAL clusters caused by adjacent charged particles.

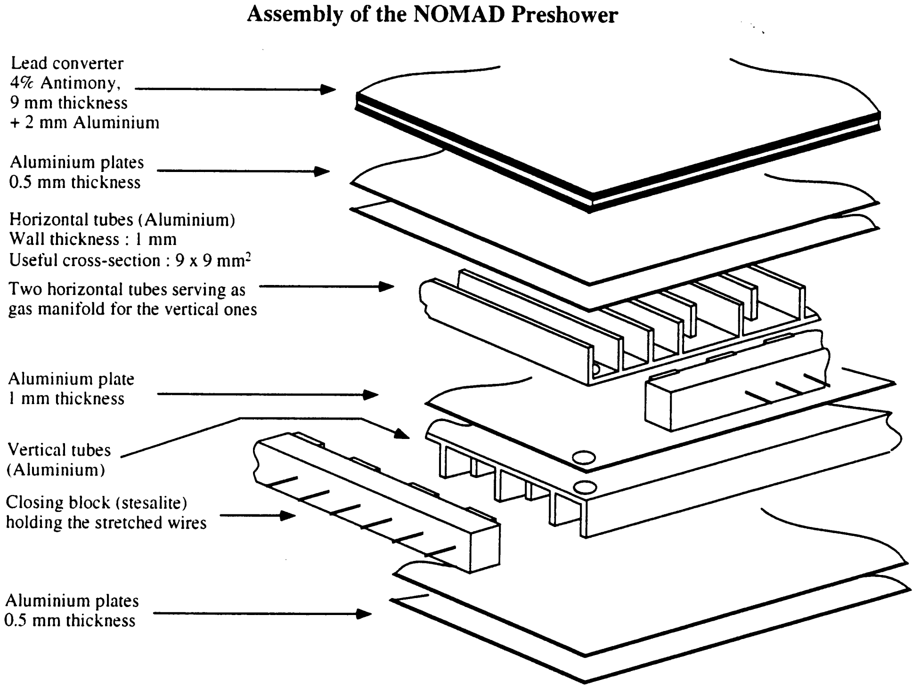

Figure 3.11: An exploded view of the preshower.

- The pulse height measurements allow to improve electron-pion discrimination provided by the TRD. A pion contamination of less than 10% for a 90% electron efficiency has been measured in test beam for particles with energies larger than 4 GeV.

3.4.6 Electromagnetic calorimeter

The electromagnetic calorimeter (ECAL) has been designed for two purposes:

- To provide the measurements of electron energy together with the reconstruction of electromagnetic showers induced by photons.
- Used in conjunction with the preshower, to improve the electron identification provided by the TRD.

The need to accurately measure electromagnetic showers induced by electrons and photons with energies ranging from about 100 MeV up to 100 GeV requires a large dynamic range in the ECAL response and in the associated electronics. A lead-glass detector was chosen for its excellent energy resolution and uniformity of response.

The ECAL consists of 875 lead-glass Čerenkov counters of TF1-000 type arranged in a matrix of 35 rows and 25 columns. Each counter is a 19 radiation lengths deep block with a rectangular cross-section of 79 × 112 mm^2 (Fig. 3.12). The light detectors are two-stage photomultipliers, tetrodes, with a typical gain of 40 in the operating conditions of NOMAD. They are coupled to the back face of the lead-glass blocks cut at 45° with respect to the block axis, in such a way that the symmetry axis of the tetrodes forms an

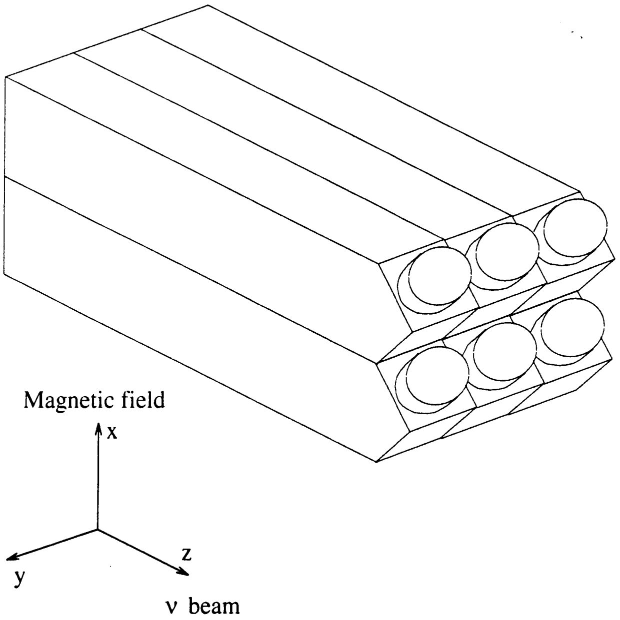

Figure 3.12: Schematic view of lead-glass counters with phototetrodes.

angle of 45° with respect to the field direction, thus keeping the signal reduction caused by the magnetic field to less than 20%. A low-noise electronic chain, composed of a charge preamplifier followed by a shaper and a peak sensing ADC, provides a calorimeter response in a dynamic range larger than $4 \cdot 10^3$.

A fast signal is also provided for time measurements, in order to reject energy depositions not associated to the triggered event and for using the ECAL at the trigger level. The obtained time resolution is a few ns for energy depositions larger than 1 GeV.

The monitoring of the lead-glass response is performed using two blue Light Emitting Diodes (LED) per counter mounted on the same face of the block on which the tetrodes are positioned. A complementary check on the stability of the calorimeter response is obtained with muons. The calorimeter response to muons corresponds to a peak value for the energy deposition of (0.566 ± 0.003) GeV.

Before the final assembling in NOMAD, each lead-glass block was calibrated using a 10 GeV/c electron beam having a small momentum spread ($\Delta p/p = 1\%$). The effect of the magnetic field on the calibration was taken into account by LED measurements performed with and without magnetic field. The linearity of the calorimeter response to electrons was verified at the test beam in the energy range 1.5–80 GeV; the deviation from linearity is less than 1%.

After the deconvolution of the electronic noise from the data, the energy resolution was found to be:

$$\frac{\Delta E}{E} = \frac{(3.22 \pm 0.07)\%}{\sqrt{E(\mathrm{GeV})}} \oplus (1.04 \pm 0.01)\% \tag{3.4}$$

The uniformity of the ECAL response as a function of the impact point of the incoming electrons has been measured to be within ±0.5%. The dependence of the energy release on the incident angle of the incoming electrons θ has been studied and is empirically well parametrized as $E(\theta) = E\sqrt{\cos(\theta)}$. Both the impact point and the incidence angle do not affect the energy resolution. The average resolution of the shower position of about 4 mm has been found.

Using a test beam setup comprising PRS and ECAL prototypes, the response to both electrons and pions was measured. Combining preshower and ECAL energy measurements, a pion rejection factor of about 10^3 is obtained in the energy range 2–10 GeV with an efficiency of 90% to detect electrons.

A detailed description of ECAL can be found in [61]; its performance when exposed to test beams of electrons, pions and muons is reported in [62].

3.4.7 Hadron calorimeter

The hadron calorimeter (HCAL) is intended to detect neutral hadrons and to provide a measurement of the energy of charged hadrons complementary to that derived from momentum measurements in the drift chambers. Knowledge of neutral hadrons is important when constructing kinematic quantities such as missing transverse momentum, and calorimetric measurements of charged particles can be used both as a consistency check on the momentum measurement and as an aid in distinguishing between muons and charged hadrons.

The HCAL is an iron-scintillator sampling calorimeter. For its construction the downstream pillar, which serves as a support for the central detector as well as a filter for the muon chambers, was instrumented with scintillators. This downstream pillar (as well as the upstream one used for the FCAL) consists of 23 iron plates 4.9 cm thick separated by 1.8 cm gaps. The active elements of the hadron calorimeter are scintillator paddles 3.6 m long, 1 cm thick, and 18.3 cm wide. Tapered acrylic light pipes are glued to each end of the scintillator paddle to form an assembly 5.5 m long. Eleven of these assemblies are threaded horizontally through the first 11 gaps in the pillar to form a calorimeter module, the depth of which is approximately 3.1 interaction lengths (λ_{int}). Scintillation light is directed through adiabatic light guides to a 5" phototube at each end of the module. Eighteen of these modules are stacked vertically to form a calorimeter with an active area of 3.6×3.5 m^2. A schematic front view of the HCAL, showing the scintillators and tapered acrylic light pipes, is given in Fig. 3.13.

The output from each phototube is split: one signal is delayed and sent to a charge-integrating ADC, while the second is discriminated and sent to a multihit TDC. The ADC signals are used for energy and position measurements, while the TDC signals are used to determine event timing.

The energy deposited in a given module is obtained from the geometric mean of the two phototube signals, and the horizontal position of the energy deposit is determined from the attenuation length of the scintillator and the ratio of the phototube signals. The difference between the predicted and the measured horizontal position has been studied on a sample of muons passing through a single module; typical position resolutions are of

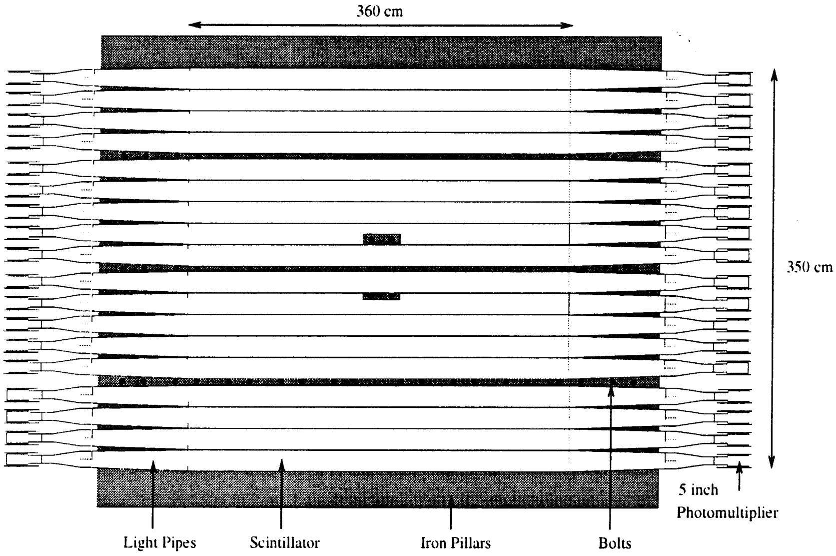

Figure 3.13: A front view of the HCAL; see the text for details.

the order of 20 cm. Vertical positions are determined from the pattern of energy sharing between the modules.

The energy resolution of HCAL is about $120\%/\sqrt{E(\mathrm{GeV})}$. Since there is a high probability that hadrons will begin to shower in the approximately 2.1 λ_{int} of material upstream of the hadron calorimeter, the total hadronic energy is taken to be a weighted sum of the energies deposited in the hadron and electromagnetic calorimeters.

3.4.8 Muon chambers

The muon detector consists of 10 drift chambers previously used in the UA1 experiment [63]. Each chamber has an active area of 3.75 × 5.55 m^2 with two planes of drift tubes in the horizontal and two in the vertical directions. The chambers are arranged in pairs (modules) for track segment reconstruction. The first muon station consists of three modules and is placed behind the hadron calorimeter. It is followed by an 80 cm thick iron absorber and a second muon station of two modules (cf. Fig. 3.7).

A drift chamber is made of aluminium tubes with external dimensions of 45 × 150 mm^2 and with variable length. A single stainless steel wire is placed in the center. The maximum drift time is 1.4 μs. In total there are 1210 drift tubes, each with a maximum drift distance of 7 cm. The signals are preamplified and after discrimination passed to a TDC module with a time resolution of 1 ns.

The chambers are operated with an argon(40%) – ethane(60%) gas mixture. Their performance is monitored continuously using high energy muons passing through the detector. The average position resolution for hits is 430 μm. The average hit efficiency is 92.5% and the dominant source of the inefficiency is due to the dead areas between the drift tubes.

Track segments are reconstructed separately for each station from (typically) 3 or 4 hits per projection. The measured efficiency for the reconstruction of track segments is 97%.

In 1995 there was a small gap between the muon chambers in station 1. For the 1996 run this gap was closed with several scintillation counters, see Fig. 3.7.

3.4.9 Data acquisition system

NOMAD operates in the burst mode, where triggers arrive in short intervals (spills) separated by relatively long intervals without beam. In order to minimize the dead time, the digitized information is buffered internally on FASTBUS electronics and read-out immediately after the end of each spill.

Signals from each subdetector arrive at some combination of three types of FASTBUS modules: twelve-bit charge-integrating ADCs, twelve-bit peak-sensing ADCs, and sixteen-bit TDCs. Both types of ADCs were designed at CERN, accomodating sixty-four channels and a 256 event memory. The LeCroy 1876 Model 100 TDCs have a time resolution of 1 ns and provide input for ninety-six channels with a 64 kilobyte buffer as well as internal zero-suppression. There are a maximum of 11 648 channels to read-out per event.

Five VME-based boards (FIC 8234) with Motorola 68040 processors control the read-out of the front-end electronics through an extended VME Subsystem Bus (VSB) connected to slave controllers (F68B7) in each of twelve FASTBUS crates. Each FASTBUS controller card provides four megabytes of additional memory for event buffering. The VME controllers perform block transfers of the available data to local buffers, assemble the data into subevents and check for consistency and integrity. They then pass the subevents through a VME interconnect bus (VIC) to the "event builder", a sixth VME processor, which assembles all the pieces into complete events and writes them, together with information about the beam extraction, to one of two nine gigabyte disks. Twice daily, a separate process transfers the data to a tape vault for storage on high capacity DLT tapes. Several Sun Sparc workstations monitor the quality of the data and the status of the detectors.

The data-acquisition software centers around elements known as "stages". These stages use the CERN-designed CASCADE [64] software which provides a well-organized framework for DAQ development including scheduling, buffer management and event access facilities. The event-builder stage also asynchronously receives beam calibration data, summaries of monitoring information, and detector status information whenever they change. The standard configuration for NOMAD DAQ software is shown in Fig. 3.14.

The slow control system consists of a Sun workstation and several Apple Macintosh computers running the LabView graphical software [65]. The Macintoshes monitor all high and low voltages, gas systems and temperature probes in the experiment, and pass slow control data to the Sun workstation, which generates alarms when needed. Periodic samples of slow control data, along with all alarm records, are passed from the Sun to the event builder stage and saved for offline use.

Monitoring programs for each of the nine subdetectors as well as for beam, scaler

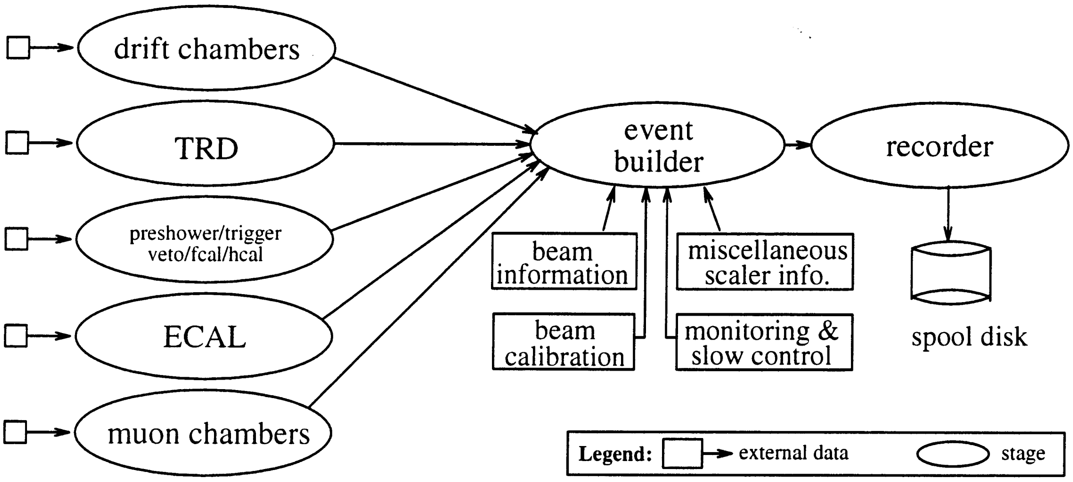

Figure 3.14: Data-acquisition software configuration.

and trigger information connect to the stages and generate summary histograms used to verify the quality of the data. Additionally, a separate monitoring program reconstructs muon events received during the flat-top of each SPS cycle for calibration and alignment purposes and records them in a separate data stream.

The system records over 1.5 megabytes of data per minute, with a typical assembled neutrino event containing around 2000 32-bit words before reconstruction. Additionally, approximately six times this quantity flows through the acquisition in the form of calibration events which are not recorded. In the neutrino spills, the data-acquisition has a typical deadtime of 10% arising from digitizations. The data-taking time lost due to down-time and inter-run transitions is less than 3%.

3.4.10 Triggering

Compared to other high energy physics experiments, the event rate is low and different trigger levels are not required. However, several targets for neutrino interactions and different trigger types such as neutrino or muon triggers are to be used in conjunction with the beam cycle. In order to have a computer-controlled trigger selection and the information of the trigger source recorded, a VME-based module called MOTRINO (MOdular TRIgger for NOmad) with a wide range of functionalities has been especially designed for NOMAD. The detailed description of MOTRINO is given in [66].

Various triggers were set up. The $\overline{V} \times T_1 \times T_2$ trigger is the main one and allows a study of neutrino interactions in the drift chamber target region. At least one hit in both trigger planes T_1 and T_2 is required. To prevent triggering on through-going muons, no hit should have occured in the veto counters V. The livetime of this trigger is $(86 \pm 4)\%$, its rate is $\sim 5.0/10^{13}$ p.o.t. Of these triggers, about 0.5 are potentially interesting candidates for neutrino interactions in the drift chambers. The remaining triggers consist of cosmic rays (about 1), non-vetoed muons (1.5) and neutrino interactions in the magnet (2.0).

In addition, several different triggers are set up for the study of neutrino interactions in the front and electromagnetic calorimeters. In total, approximately 15 neutrino candidate triggers are taken in each neutrino spill. Furthemore, various triggers are used in the 2.6 s long flat-top between the two neutrino bursts. These triggers serve mainly for the calibration, alignment and efficiency measurement purposes. One of the triggers is a selection of electrons, from muon decay or delta rays, which allows a study of the behaviour of electrons in the detector. In total, about 60 triggers are taken in each flat-top.

Chapter 4

Transition Radiation Detector

4.1 Introduction

The NOMAD transition radiation detector (TRD) has been designed to separate electrons from pions with a pion rejection factor greater than 10^3 for a 90% electron efficiency in the momentum range from 1 to 50 GeV/c. This electron-pion separation factor, together with the additional pion rejection provided by the preshower and electromagnetic calorimeter, is required in the search of the following oscillation processes:

- in the $\nu_\mu \rightarrow \nu_\tau$ oscillation search in $\tau^- \rightarrow e^- \nu_\tau \bar{\nu}_e$ decay channel, in order to eliminate neutral current (NC) neutrino interaction events in which an isolated pion track fakes an electron [67];
- in the $\nu_\mu \rightarrow \nu_e$ oscillation search, in order to efficiently identify ν_e charged current (CC) interactions $\nu_e\, N \rightarrow e^-\, X$, while keeping background from ν_μ CC and ν_μ NC interactions small [68];
- in the $\nu_\mu \rightarrow \nu_\tau$ oscillation search in hadronic decay channels $\tau^- \rightarrow h^-(n\pi^0)\nu_\tau$ ($h^- \equiv \pi^-$, K^-) and $\tau^- \rightarrow \pi^-\pi^+\pi^-(n\pi^0)\nu_\tau$, to ensure that the hadrons – candidates for τ-decay products – are not misidentified electrons [67].

In this chapter we describe the design of the NOMAD TRD, its calibration, monitoring, slow-control system and the test beam results. A discussion of the electron-pion discrimination algorithms and their performance is deferred until chapter 5.

4.2 General principles of the TRD

The theory of transition radiation is well known [69] and numerous detectors using this effect for particle identification have been built [70].

Transition radiation (TR) is produced by charged particles crossing boundaries between media of different dielectric constants. The TR energy radiated at an interface of two media is proportional to the Lorentz factor $\gamma = E/m$ of the particle, and therefore can be used to distinguish particles of known energies. The energy of the TR photons emitted by ultrarelativistic particles extends to the keV region and can be measured by X-ray detectors. The ensemble of these two factors makes the TR effect well suited for particle identification at high values of γ, where other identification methods (e.g. Čerenkov detectors) become inefficient.

The emission probability of a photon at an interface is, however, small (of the order of $\alpha = 1/137$), so that in practice a "radiator" with many interfaces should be used to increase the radiation yield cumulatively. On the other hand, the detectable amount of TR energy is reduced by the absorption of the TR photons in the radiator material and the coherent effect is limited by dispersions in the regular spacing of the interfaces [71, 72].

To efficiently detect the emitted X-rays while affecting minimally the incident particle, gaseous detectors (proportional or drift chambers) are usually used with heavy Z filling, mostly Xe. The radiation is forward peaked with an emission angle with respect to the particle direction of the order of $1/\gamma$, so that the TR energy deposition is superimposed with the simultaneous ionization losses of the parent particle in the detector gas.

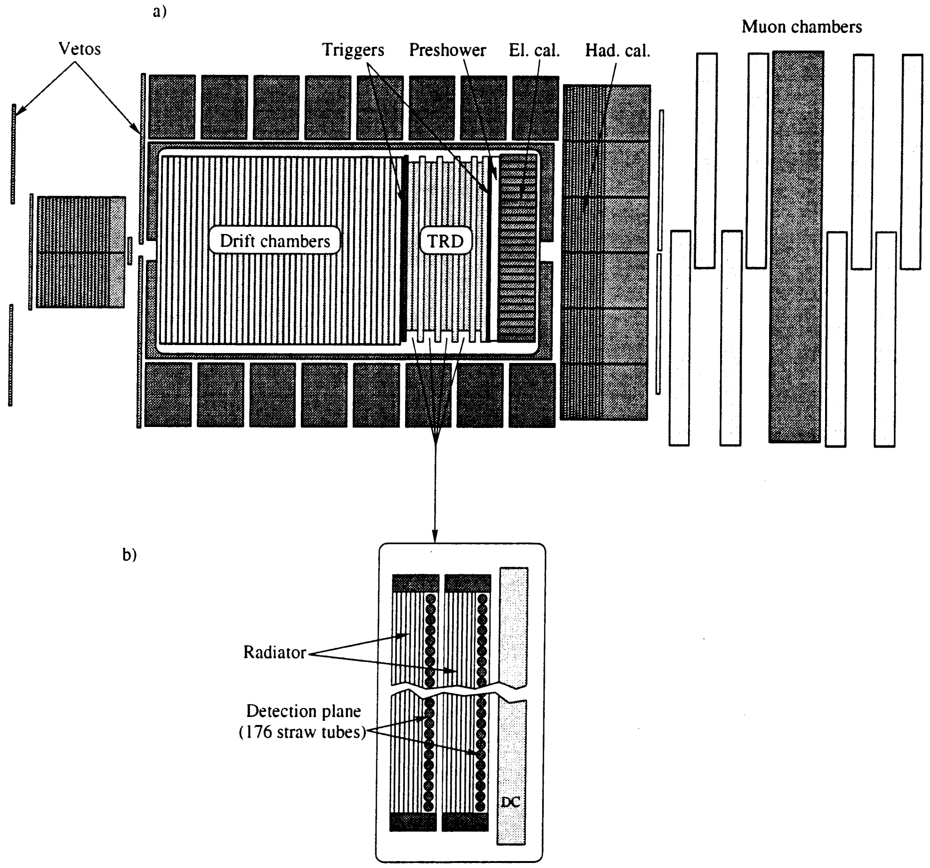

Figure 4.1: a) Top view of NOMAD detector and b) schematic top view of a TRD doublet.

The transition radiation effect provides an efficient way to separate electrons from other charged particles in the NOMAD momentum range.

4.3 Design of the NOMAD TRD

The design of the transition radiation detector was optimised using a complete simulation cross-checked with a series of test beam measurements [73]. The detector had to satisfy two experimental constraints: the limited longitudinal space available inside the NOMAD magnet and the requirement that there be less than 2% of a radiation length between two consecutive measurements of the particle trajectory in the drift chambers.

The TRD is located after the drift chamber target (see Fig. 4.1, a)) and consists of 9 identical modules. The first 8 modules are paired into 4 doublets, as shown in Fig. 4.1, b). Five drift chambers used for tracking and momentum measurements are imbedded in the TRD, one after each doublet and one after the last module, in order to provide an accurate track extrapolation from the active target to the electromagnetic calorimeter.

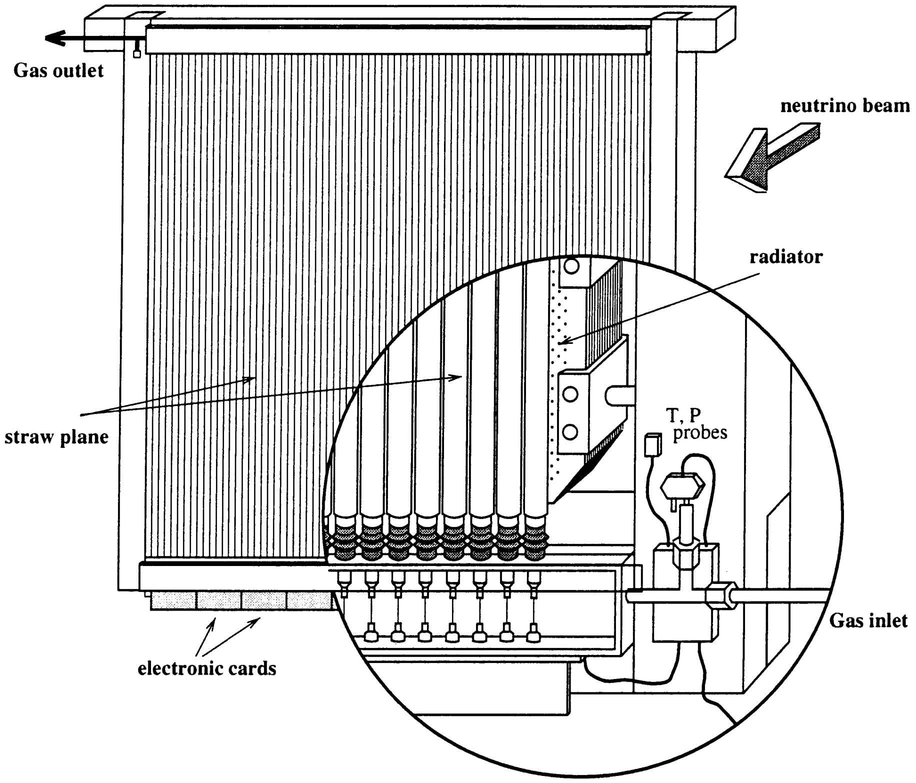

Figure 4.2: Schematic view of a TRD module, as seen from the detection plane side.

Each TRD module comprises a radiator followed by a detection plane (Fig. 4.2):

- The radiator is a set of 315 polypropylene foils, each 15 μm thick and 2.85×2.85 m^2 in area, separated by 250 μm nitrogen gaps.
- The detection plane consists of 176 vertical straw tubes, each 3 m long and 16 mm in diameter, positioned with a 16.2 mm pitch. The straw tubes are fed in parallel with a 80% xenon – 20% methane gas mixture.

The number of modules and the large effective area of a module make the NOMAD TRD one of the largest transition radiation detectors ever built.

4.3.1 The TRD radiators

Radiator materials

The best candidates are high density low Z materials, since photon reabsorption in the radiator is proportional to Z^4. The best choice would be lithium, but it is difficult to use in practice. Plastics $(CH_2)_n$ are the most convenient to manufacture radiators of large dimensions. They can be used in the form of foam or fiber blocks (mechanically preferable as a strong supporting frame is not needed) or, alternatively, as a thin foil structure. Studies made in the past [70] to compare the transition radiation produced in different forms of radiators have shown that thin foil radiators are more efficient for a given radiator thickness.

We have performed several measurements with test beams and reached the same conclusions. Fig. 4.3 is an example of such a measurement where a polyethylene foam block of 3.1% radiation length and 235 mm thick was compared to a 500 foil test radiator containing less matter (2.3% radiation length and 210 mm thick). The result, 30% more energy detected in the second case, clearly favours the foil radiator. We have finally chosen polypropylene foils (mechanically easier to stretch than polyethylene foils).

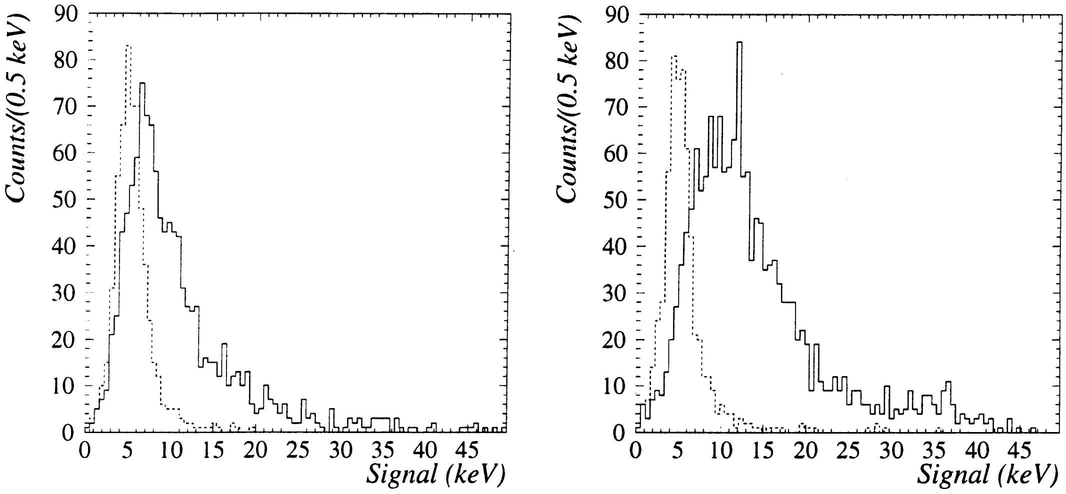

Figure 4.3: Detected response to electrons in a 2 GeV/c test beam with a foam radiator (left) and with a foil radiator (right). Dotted lines show the response to pions. The photon detection was not optimal due to gas impurities in the X-ray detector.

In between foils, vacuum would be the best but is not practicable. We use nitrogen which is easier to use than helium for gas-tightness reasons.

Radiator structure and TRD modularity

For the optimization of the detector and identification algortihms, the Monte Carlo simulation of ionization losses in thin gas layers and of the transition radiation emission and absorption has been developed [73, 74]. The simulation package included:

- the parametrization from Ermilova et al. [75] of the dE/dx in thin layers of gas;
- the dependence of the ionization losses and transition radiation yield on the Lorentz factor and the angle of the incident particle;
- the dependence of the TR yield on the dispersion of both foil and gap thickness;
- the Auger and fluorescence effects in the process of photoabsorption in xenon [76];
- the effect of the cylindrical shape of the straw tubes;
- the space charge corrections for the response of the straw tubes as a function of the energy of the detected photons (see discussion in Sec. 4.6.1).

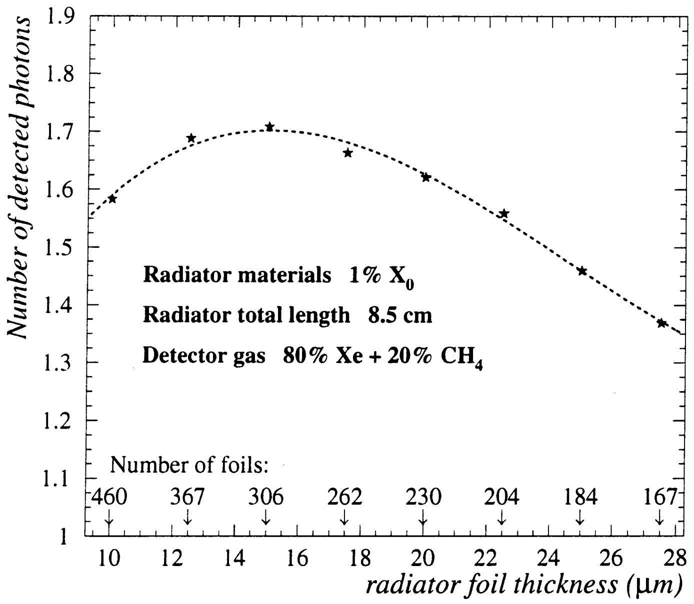

Figure 4.4: Expected number of detected TR photons as a function of the radiator foil thickness, for given radiator length and allowed amount of material. The curve shown is a result of a smoothing.

This simulation package was used, in particular, to compute the number of detected TR photons emerging from radiators up to 1% X_0 thick with uniformly spaced foils and a given length [77]. The number of foils, their thickness and the gap were varied. The result of such a calculation is shown in Fig. 4.4. The effects of foil thickness and gap dispersions were included in the computations and the results were checked by test beam measurements. For the total radiator lenght of 8.5 cm, the maximal TR yield is expected for about 310 polypropylene foils, each ~15 μm thick.

As a result of simulation and test beam studies, the detector consists of 9 modules, with radiators made of 315 polypropylene foils, each 15 μm thick, spaced by 250 μm.

The spacing of radiator foils should be as regular as possible in order not to decrease the amount of emitted transition radiation (the effect could be as large as 10% for the 50% dispersion of the gap thickness). To maintain a uniform gap between foils on their whole area in spite of electrostatic effects, the polypropylene film was first embossed with 250 μm bumps. The bumps were made every 20 mm; their shifted lines are distant by 50 mm. The embossed foils were then stretched on an aluminium frame.

4.3.2 The detection planes

Choice of a straw detector for the TRD

Since a large planar detector filled with xenon gas would require a thick window which would absorb low-energy transition radiation photons, the X-ray detector was made of vertical cylindrical tubes ("straws") with 28 μm aluminized mylar walls, placed side by side (see Fig. 4.2). The straw diameter, 16 mm, was chosen as a compromize between the probability of capturing transition radiation photons and the amount of ionization losses of the particle crossing the tube. The straw tubes are made of two shifted 12.5 μm thick ribbons of aluminised (115 nm of aluminium) mylar rolled and glued along a 16 mm diameter helix. The sensitive anode is a 50 μm diameter gold-plated tungsten wire stretched with a tension of 100 g.

As a consequence of the cylindrical shape of the straws, the gas thickness traversed by a particle depends on the track position with respect to the axis of the straw tube. The mean efficiency of a TRD straw plane has been estimated to ~98.5% for minimum ionizing particle tracks [78]. The inefficiency is mainly due to ~0.2 mm gap between the straws. The detector response as a function of the track position will be further discussed in chapter 5.

A horizontal orientation of the straws would have been preferable in NOMAD due to the magnetic field direction. However, the vertical orientation was chosen to avoid problems of deformation of the straws because of gravitational sagging. Since the anode wire should be kept within close distance from the straw axis for electrical stability, a horizontal orientation would have required spacers, thus introducing dead zones within the active area of the detector.

Two methods of the signal processing could be used: the "cluster counting" [79] and the measurement of the total energy deposition. The methods of "cluster counting" reach essentially the same rejection power as the total energy deposition method [70] but make use of a defined threshold, whereas charge integration leaves more flexibility in the offline treatment. We have chosen to measure the total energy deposition in the straw tubes and to operate the detector in proportional mode.

Detector gas mixture

The X-ray detector of the TRD uses an 80% Xe – 20% CH_4 gas mixture:

- xenon offers the largest photoabsorption cross-section for the transition radiation photons in the keV range, as shown in Fig. 4.5.
- methane, at the level of 20%, gives a much shorter drift time than carbon dioxide [80], that leads to a lesser sensitivity to impurities such as oxygen or water.

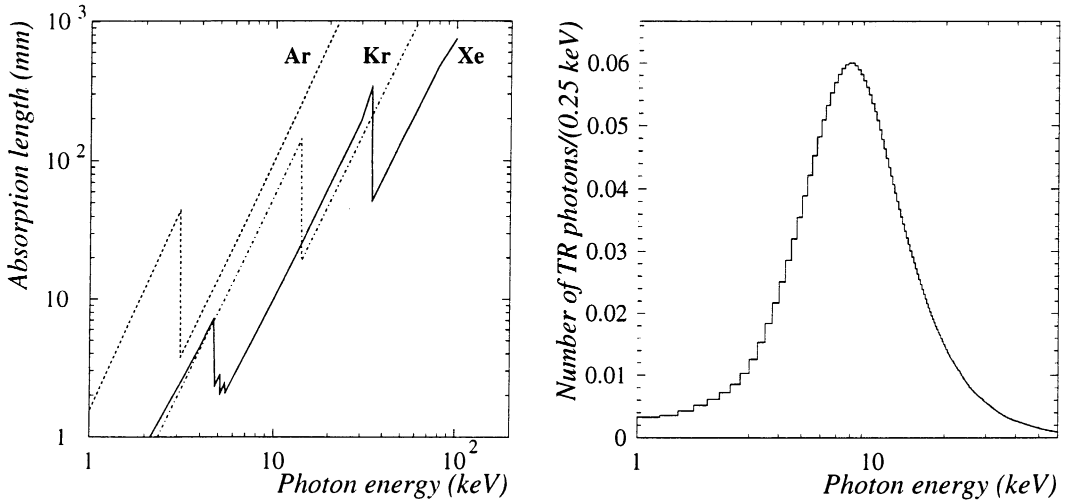

Figure 4.5: Left: absorption length of photons in various rare gases as a function of the photon energy. Right: transition radiation spectrum expected for 5 GeV/c electrons at normal incidence in a NOMAD TRD radiator.

Our simulations have shown [77] that electron-pion discrimination is not significantly influenced by CH_4 percentage variations between 10% and 40%, at a constant gain. The CH_4 percentage of 20% was chosen to keep the high voltage at a relatively low value. The stability and uniformity of the Xe-CH_4 proportions within the whole detector and a low level contamination of the gas mixture were provided by a specially developed closed circuit system with continuous purification of the gas [81].

In order to protect the gas mixture in the straw tubes from water and oxygen contamination, each TRD module is covered by two aluminised mylar skins with a permanent flow of dry N_2 between them. The typical increase in a contamination between the input and output of the detector is by 20 ppm for O_2 and 100 ppm for H_2O.

4.3.3 Electronics

A detailed description of the NOMAD TRD electronics can be found elsewhere [81, 82]. In order to accurately measure the signal with energies ranging from about 100 eV up to 100 keV, a 10^3 linear dynamic range is required. The signals from the 1584 straw tubes are fed into preamplifiers. Their differential output signals are transmitted via 32 twisted-pair cables to differential drivers located outside the magnet. The charge ADCs are read-out by a VME system. A test pulse calibration system is used to check the entire electronic chain and to control its linearity.

4.4 The calibration and monitoring of the detector

The TRD electron-pion separation is based on the difference in the total amount of energy deposited in the detector gas by different particles. The measurement of this deposited energy should bring the smallest possible additional uncertainties to its intrinsic fluctuations, and needs precise calibration and control systems.

The signal S_{ADC} read-out from the charge ADC connected to each straw tube depends not only upon the total energy deposition Q_{tot}, but also on the response functions of the straw tube F_{straw} and of the electronic chain G_{el}:

$$S_{\mathrm{ADC}} = S_{\mathrm{ped}} + Q_{\mathrm{tot}}(p, \theta, \vec{x}) \times F_{\mathrm{straw}}(\mathrm{HV}, \%\mathrm{CH}_4, \mathrm{T}, \mathrm{P}, ...) \times G_{\mathrm{el}} \qquad (4.1)$$

The deposited energy Q_{tot} depends upon the momentum p, track angle θ and position $\vec{x}$ of a given particle. Complex processes like space charge effect could also influence the charge collected at the anode. The tube response F_{straw} varies with the straw tube gain, which is a function of the gas composition, high voltage, oxygen, water and nitrogen contaminations, pressure and temperature in the straw, etc. The electronic chain response G_{el} depends mainly on the gain and linearity of the preamplifiers and of the receivers.

In order to take into account the possible variations of both F and G, the calibration system has been implemented for the TRD. The electronic response function G is monitored by a test-pulse system [82], used to measure periodically the linearity of the electronic chain as well as the cross-talk between channels. The global detector response S is calibrated permanently during data taking by a system using ^{55}Fe radioactive sources. The way the ^{55}Fe calibration is performed, the decoding of the calibration information, its storage and its use are described below.

4.4.1 The calibration method

The main purpose of the TRD calibration is to provide a way to convert the ADC counts into the units of energy (keV). This absolute calibration of the detector is based on the measurements of the energy deposited by 5.89 keV X-rays emitted by ^{55}Fe radioactive sources.

Mylar ribbons impregnated by a ^{55}Fe sulfate solution are attached horizontally across the middle of each straw plane, on the external envelope facing the straws. The ^{55}Fe source emits 5.89 keV monoenergetic photons absorbed by the gas in the straw tube (about 20 counts/s per straw) and give a narrow gaussian-like distribution well suited for the calibration purpose. The measured position of the peak expressed in ADC counts varies with time reflecting all the changes in the detector conditions (high voltage, temperature, pressure, gas mixture composition, etc.) and is used as a reference for energy measurements.

Two reference points for the calibration of the energy scale are necessary:

- The value of the pedestal expressed in ADC counts, S_{ped}, corresponds to null energy deposition;
- The value of the ^{55}Fe signal peak expressed in ADC counts, S_{Fe}, corresponds to 5.89 keV.

With the help of these reference points the ADC → keV conversion for any energy deposition in TRD straw tube, S_{ADC}, can be performed:

$$E(\text{keV}) = \frac{S_{\text{ADC}} - S_{\text{ped}}}{S_{\text{Fe}} - S_{\text{ped}}} \times 5.89(\text{keV}) \tag{4.2}$$

The linearity of the straw tube response is monitored by the measurements of the ^{109}Cd peak ($E_\gamma = 22.1$ keV) attached in the middle of eight straw tubes at both edges of every TRD module.

4.4.2 The calibration procedure

During data taking periods, the TRD is continuously calibrated. Calibration triggers are enabled at each accelerator cycle during off-spill time and 256 calibration events are recorded in each ADC card, filling the memory depth of all the 64 ADC channels. The online acquisition controller reads out each event and separates the values corresponding to the hit straw from the 63 pedestal values. These calibration data are recorded onto tapes every 50 000 calibration events (about once an hour).

For each straw tube a gaussian fit is performed on the ^{55}Fe distributions at the end of a run. An example of the ^{55}Fe and ^{109}Cd distributions and their fits is shown in Fig. 4.6. The mean and sigma of the fit of ^{55}Fe signal in each tube (Fig. 4.7, a) and b)) are saved in a database [83] and define the ^{55}Fe calibration run per run which is used later on in the offline analysis. The distributions of the ^{55}Fe source activity and the χ^2 of the fits (Fig. 4.7, c) and d) respectively) reflect the level of noise and are used for the TRD monitoring. For example, the χ^2 distribution of Fig. 4.7, d) shows that 1) the fits of all the ^{55}Fe signals are good; 2) the first ADC card (digitizing the signals in the first 64 straw tubes of the module) is less noisy the the two others. The increase in χ^2 at the edges of the module is due to an additional activity of the ^{109}Cd sources installed there.

Further details of the calibration procedure are described in [84].

4.4.3 Pedestals

The pedestal means μ_{Ped} and widths σ_{Ped} used for the TRD calibration are obtained in the following way. During normal data acquisition, only events with the deposited energy above a threshold of $\mu^0_{\text{Ped}} + 5\sigma^0_{\text{Ped}}$ are recorded. Every 100th burst, this zero-suppression is not carried out and recorded events contain pedestal data from all the straw tubes. The fits performed on these data determine μ_{Ped} and σ_{Ped}. An example of the pedestal

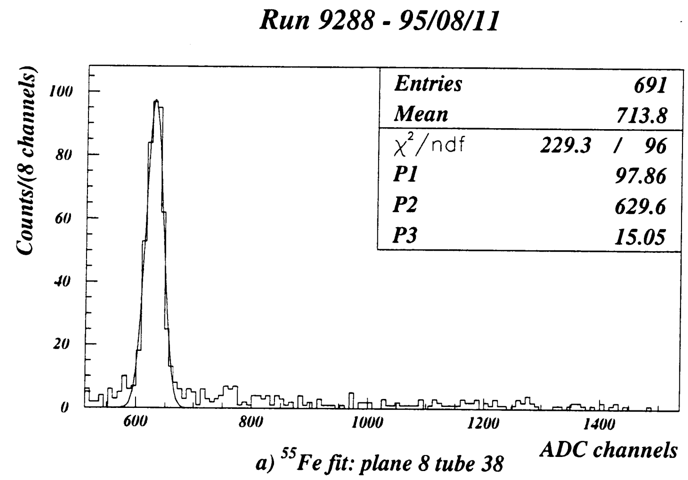

a) ^{55}Fe fit: plane 8 tube 38

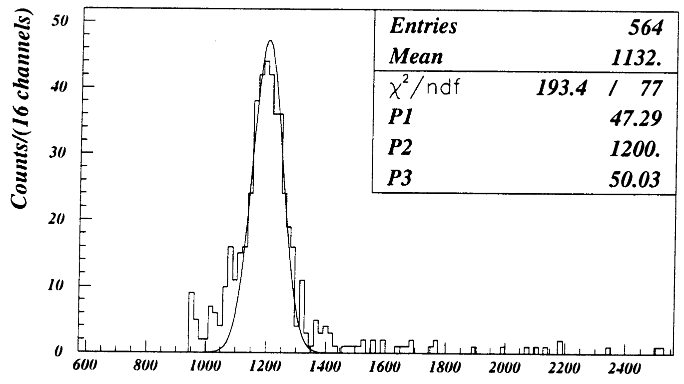

b) ^{109}Cd fit: plane 8 tube 1

Figure 4.6: Example of the ^{55}Fe and ^{109}Cd distributions with the gaussain fit. The value of the pedestal corresponds to about 450 ADC channels.

distribution and its fit, as well as pedestal mean and sigma distributions as a function of the straw tube number, is shown in Fig. 4.8.

4.4.4 ^{55}Fe monitoring

The ^{55}Fe distributions from calibration events as well as the distributions of means and widths of the pedestals are sent periodically to the TRD online monitoring program. Every several hours it produces summary histograms of the calibration parameters for online controls. Online (and offline) checks have shown that pedestals are remarkably stable (fluctuations are less than ±1 ADC count/month). The main variations of the ^{55}Fe values are due to the global parameter changes, such as gas composition or ambient air temperature.

Based on the ^{55}Fe online and offline monitoring information, a map of the TRD out-of-order channels – too noisy, disconnected, unstable, etc. – is produced for each run and stored in the database. The channels marked in the map (if any) are ignored in the data

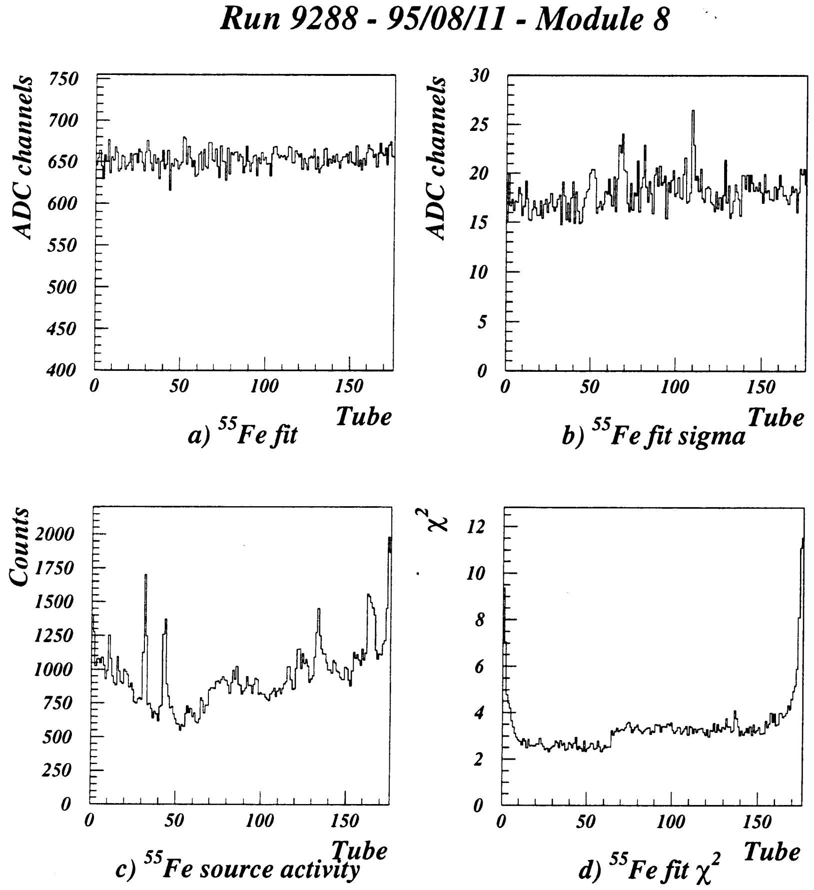

a) ^{55}Fe fit

b) ^{55}Fe fit sigma

c) ^{55}Fe source activity

d) ^{55}Fe fit χ^2

Figure 4.7: Example of the distributions obtained as a result of the TRD ^{55}Fe calibration: a) mean of the fit; b) sigma of the fit; c) source activity (number of counts) and d) χ^2 of the fit, all as a function of the straw tube number (module 8, run 9288, 1995 data).

processing.[1]

4.5 The Slow Control system

The Slow Control system [85] surveys the relevant parameters of the detector. It generates alarms and records information for offline corrections every hour and for each alarm.

The differential pressure and temperature are measured at the bottom and top of each TRD plane (see Fig. 4.2), and the absolute pressure is measured in the surround of the detector. By combining these measurements, the absolute pressure in each TRD plane can be determined with an accuracy of about 2 mbars. The temperature measurements

---

[1] For more than four years of operation, only a single straw tube, out of a total of 1584, has become fully inefficient. With this exception, the average number of malfunctioning channels is well below one straw tube per run.

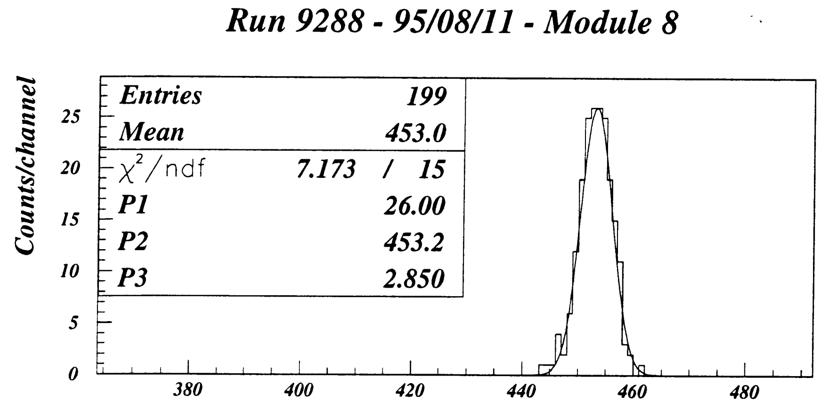

a) Pedestal fit: plane 8 tube 30

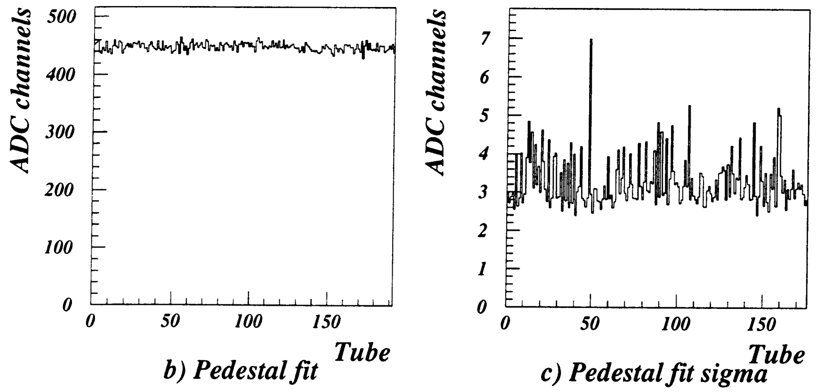

b) Pedestal fit

c) Pedestal fit sigma

Figure 4.8: Examples of: a) pedestal distribution in the individual straw tube with the gaussain fit; b) mean of the fit; c) sigma of the fit, both as a function of the straw tube number for the module 8 (run 9288, 1995 data).

have an accuracy of 0.1°C. In addition, the high voltage applied to each half-plane of the detector is measured with an accuracy of 10 V by a simple resistive divider. The front-end electronics low voltage supply is also monitored. On each side of a TRD plane, slow-control cards collect the probe signals and transmit them through CAMAC Data Loggers to a dedicated computer. An interfacing program converts the probe signals and displays the results.

In the gas station, an hygrometer and an oxygen detector measure the water vapour and oxygen contamination which are kept below acceptable thresholds (about 400 ppm for water and 40 ppm for oxygen). A specific device measures the proportion of methane. Mass flowmeters measure the flow of xenon and methane.

The averaged parameters of the working conditions of the detector for each run are stored in the database.

4.6 Studies of detector response

4.6.1 Saturation effects

The linearity of the output signal as a function of the deposited energy has been measured with a short (10 cm long) straw tube prototype using low rate X-ray sources at seven discrete energy values between 5.89 and 44.2 keV. Fig. 4.9 shows the measured signal as a function of the photon energy (at 2250 V, 30°C, 1019 mbar and 18% CH_4). The deviation from linearity is about 35% at 22 keV, if one takes as the unsaturated response function the tangent at the origin of the fitted exponential curve. The saturation at the ^{55}Fe photon energy is 8.7%.

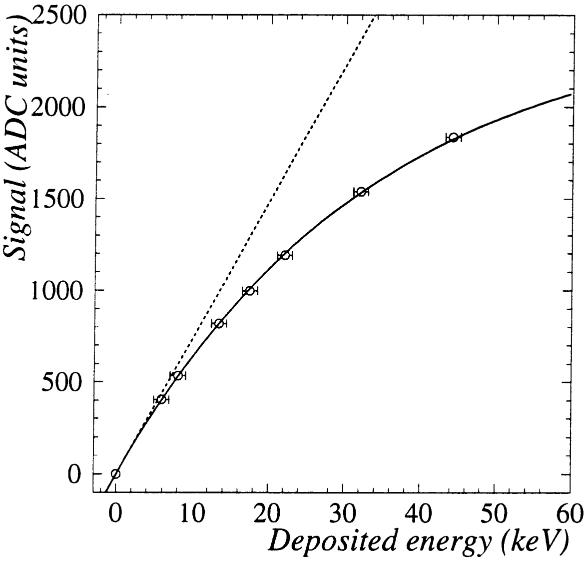

Figure 4.9: Measured response to a single photon fitted by an exponential as a function of the photon energy.

The observed saturation effect could not be reproduced by the simulation of the photoabsorption process in xenon which includes both Auger and fluorescence effects [76]. On the other hand, the dependence of the effect on the working detector parameters, high voltage in particular, was observed. This saturation effect was attributed mainly to space charge effects on single photon absorption process. The working conditions were chosen such as to minimize the observed non-linearity. The results of the measurements were parametrized and used in the Monte Carlo simulation programs.

4.6.2 Response of the detector to test beam particles

Test beams of electrons, pions and muons at various particle momenta between 1 and 100 GeV/c were used to test prototypes and later on modules of the final detector, to estimate the production of transition radiation by different radiators and the response of the detector. Fig. 4.10 shows the signal obtained during the early test beam measurements using a single TRD module with 10 GeV/c electrons and pions at normal incidence.

Parameters such as the particle angle of incidence and impact point were also varied. Numerous results of test beam measurements, some of them already mentioned in this chapter and some discussed in the next one, ensured the excellent performance of the detector and the stability of its operation in-situ. The test beam results were also used to cross-check the simulation of the detector and to establish the particle identification algorithms described in the next chapter.

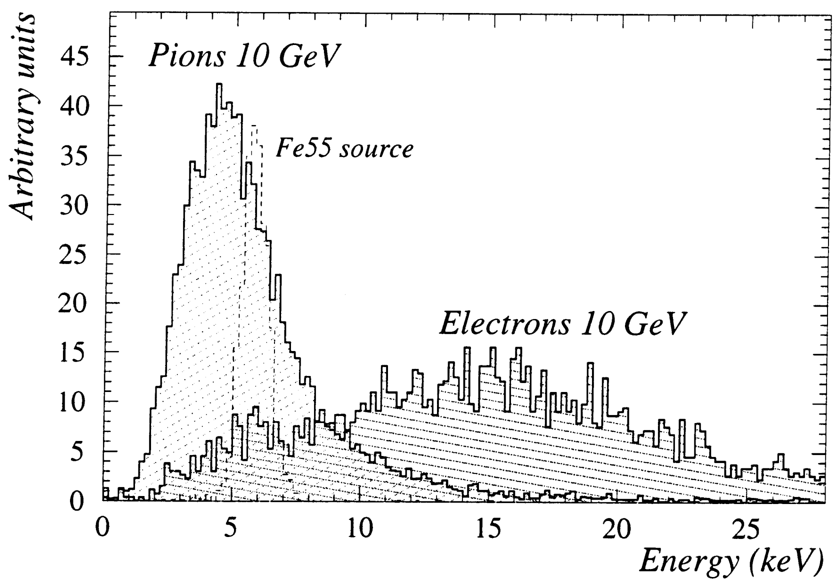

Figure 4.10: Response of a full-size TRD module to test beam particles.

4.7 Conclusion

A large area transition radiation detector has been designed and constructed for the NOMAD experiment, to identify electrons at 90% efficiency with a rejection factor against pions of 10^3. Although made of very thin material extending over large dimensions, the detector has proven to be robust. The TRD has now been operating for more than four years and works with excellent stability.

In the next chapter we describe the algorithms developed for electron identification, and the tests on real data which demonstrate that the expected identification performances have been achieved.

Chapter 5

Performance of the TRD

5.1 Introduction

As already mentioned, excellent electron identification is required in NOMAD, both for $\nu_\mu \to \nu_\tau$ and $\nu_\mu \to \nu_e$ oscillation searches. The overall π rejection achieved by the NOMAD subdetectors has to be larger than 10^5. A major part of the electron identification is performed by the transition radiation detector, which was designed to discriminate between isolated electron and pion tracks with a rejection factor greater than 10^3 for a 90% electron efficiency in a 1 to 50 GeV/c momentum range.

In this chapter we describe the algorithms developed for the electron-pion discrimination by the TRD and their performance. The principles of the electron identification are reviewed in Sec. 5.2. The algorithms developed for the recognition of electrons are described in Sec. 5.3 and discussed in Sec. 5.4. The identification performance obtained on the data are described in Sec. 5.5.

5.2 Principles of TRD electron identification

Particle identification by the TRD is based on the difference in the total energy deposited in the detection planes by particles with different Lorentz factors ($\gamma = E/m$). All charged particles crossing the detector lose energy by ionization. In addition, highly relativistic ones (mainly electrons in NOMAD) produce transition radiation (TR) X-rays at the interfaces of the radiator foils.

The number of transition radiation photons emitted by a NOMAD radiator as a function of the Lorentz factor is shown in Fig. 5.1. A 10 GeV/c electron at normal incidence emits, on the average, $\simeq 3.1$ photons with a mean energy $\simeq 14$ keV each. About 50% of the photons emitted by a radiator are absorbed in the subsequent detection plane. The average energy of a detected photon is $\simeq 8$ keV, due to the xenon photoabsorption cross-section peak at around 5.5 keV [86]. The energy of the detected TR photons is added to the ionization losses of the parent electron ($\simeq 9$ keV at 10 GeV/c) in the same straw tube, since the photons are emitted at a small mean angle $1/\gamma \ll 1$ mrad with respect to the

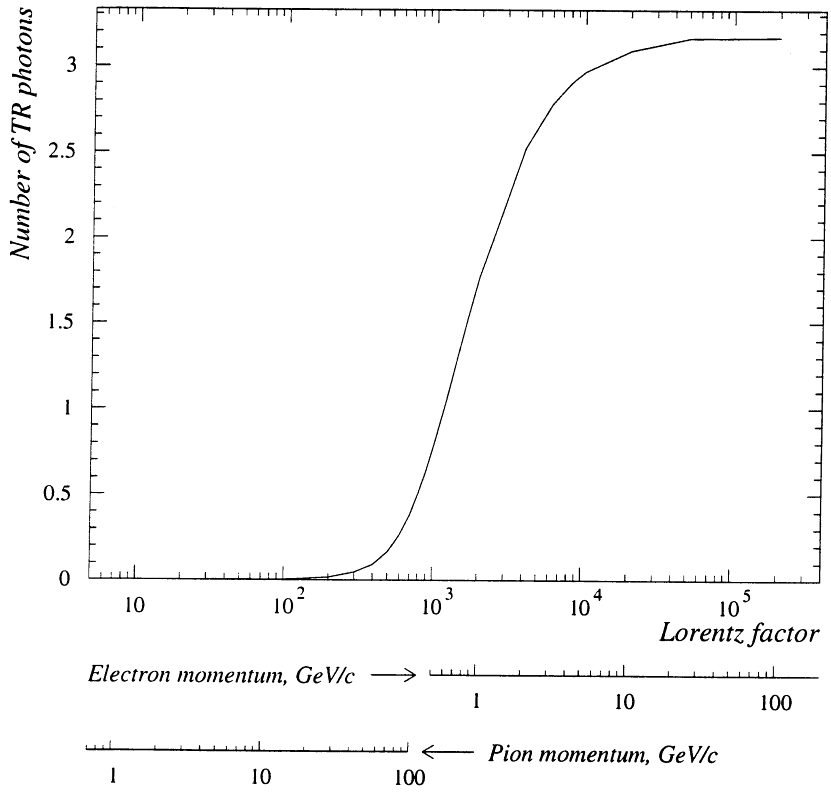

Figure 5.1: The expected number of transition radiation photons emitted by a NOMAD TRD radiator as a function of the Lorentz factor.

electron direction. The 20 keV total average energy deposited by a 10 GeV/c electron is large compared to the mean $\simeq$ 7.5 keV energy deposition of a pion of the same momentum. Monte Carlo simulated spectra of the energy deposited by 10 GeV/c electrons and pions are shown in Fig. 5.2.

5.3 Electron identification algorithms

The TRD data acquisition and calibration procedures have been described in chapter 4. The signal processing produces a list of TRD hits (straw tubes with an energy deposition above threshold).

The first step of the identification procedure consists in matching the TRD hits with the tracks reconstructed by the drift chambers. As a result, a set of hits collected along the road of a drift chamber track is assigned to this track. With at most one hit per TRD module allowed to be matched, up to 9 hits can be associated with a track. The energy depositions in the associated hits are then compared to the expectations for the two particle hypotheses, electron e and pion π, taking into account the momentum of the particle as measured by the drift chambers.

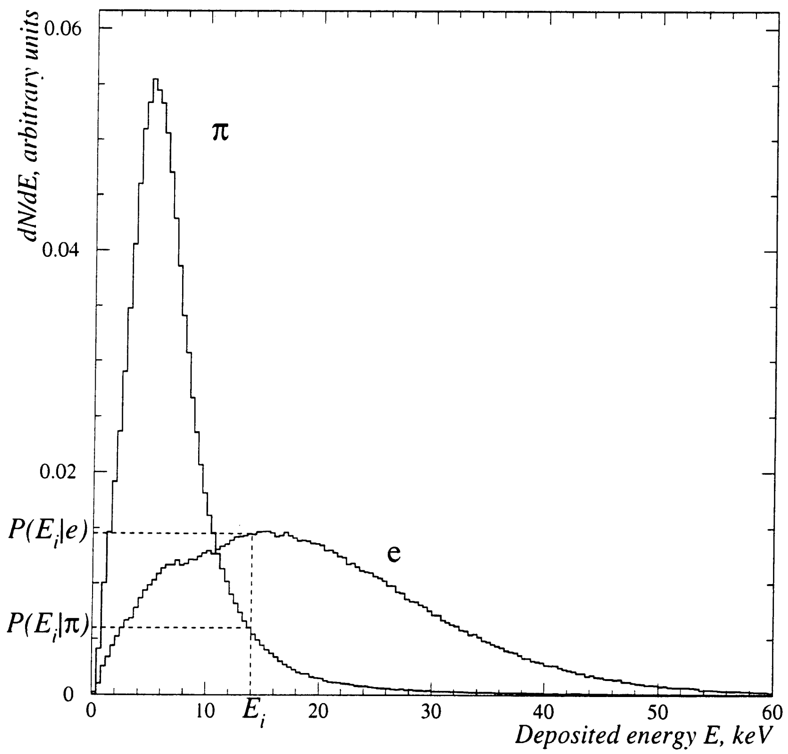

Figure 5.2: Monte Carlo simulated spectra of the energy deposited in the TRD straw tube gas mixture (single detection plane) by 10 GeV/c pions and electrons at normal incidence.

Two complementary identification algorithms have been developed for isolated and non-isolated particles and are applied depending of the topology of the event:

- If all the hits of the set are associated with a single track, the particle is defined as isolated, Fig. 5.3 (a).
- If several particles cross the same straw tubes, their energy depositions are summed up. When such "shared" hits are matched with several tracks, the particles are defined as non-isolated, Fig. 5.3 (b).

5.3.1 Identification of isolated particles

A likelihood ratio estimator $\pounds$ is constructed for each DC track with associated hits in the TRD:[1]

$$\pounds = \sum_{i=1}^{N_h} \log \frac{P(E_i \mid e)}{P(E_i \mid \pi)} \tag{5.1}$$

where

---

[1] A detailed description of the algorithm can be found in [87].

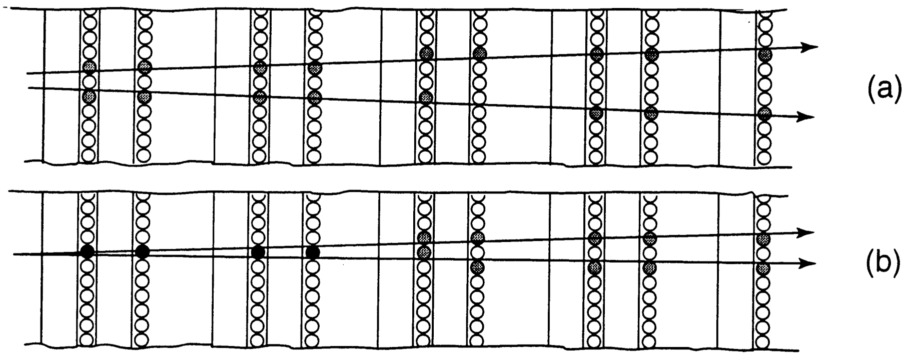

Figure 5.3: Examples of different track topologies in TRD (schematic top view): (a) isolated particles, all the associated hits are "non-shared" (shown in grey); (b) non-isolated particles, hits associated in the first 4 modules are "shared" (shown in black).

- N_h is the number of TRD hits associated with a particle;
- $P(E_i \mid e)$ and $P(E_i \mid \pi)$ are the probability density functions for an electron e and for a pion π to deposit the energy E_i in the ith straw tube (Fig. 5.2).

The probability densities $P(E_i \mid e)$ and $P(E_i \mid \pi)$ are functions of many parameters, such as the particle Lorentz factor, momentum, angles with respect to the straw tube, etc. These functions have been obtained from detailed simulation and extensive test beam measurements and are discussed in the following sections.

Eq. (5.1) assumes uncorrelated signals in different detection planes, though a fraction of the transition radiation photons emitted by electrons in the first radiator of a doublet may be detected in the second module, which leads to a correlation. As discussed in Sec. 5.4, this effect can be neglected in the NOMAD TRD setup.

The distributions of the likelihood ratio (5.1) are computed for the two particle hypotheses (e and π). The fractions of electrons and pions above a certain threshold value $\pounds_{th}$ define, respectively, the efficiency for electron identification (ε_e) and the corresponding pion acceptance (ε_π), see Fig. 5.4. The integration of the likelihood ratio distributions yields the electron efficiency ε_e and the pion acceptance ε_π as a function of the threshold $\pounds_{th}$ (Fig. 5.5). For each track, the decision on the nature of the particle is made by comparing the value of the computed likelihood ratio $\pounds$ with the threshold $\pounds_{th}$. The value of the threshold is determined by the required ε_e or ε_π.

The expected pion acceptance for different electron identification efficiencies is shown as a function of the number of hits N_h in Fig. 5.6 for 1 GeV/c and 10 GeV/c particles. A minimum number of 4 hits is necessary to have a reliable association with a DC track, therefore, we require a signal in at least 4 detection planes to apply the identification algorithm. The pion rejection factor $R = 1/\varepsilon_\pi$ achieved with 9 TRD modules is larger than 10^3 for a 90% electron efficiency.

For a pion acceptance $\varepsilon_\pi = 10^{-3}$ and 9 associated hits, the electron efficiency ε_e as a function of the momentum of the incident particle is shown in Fig. 5.7. It is larger

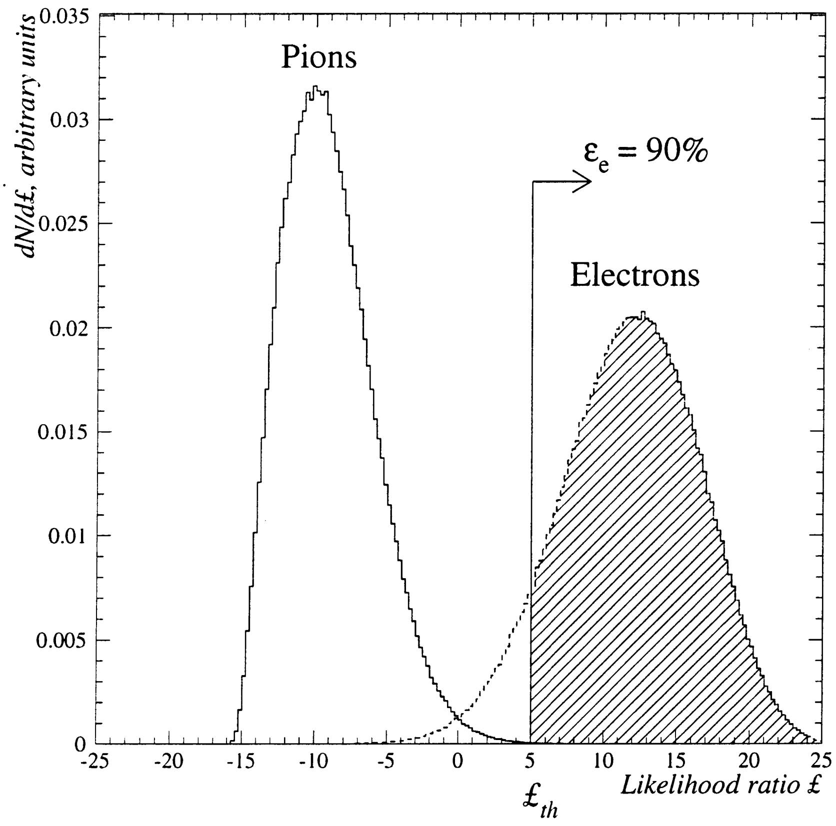

Figure 5.4: The likelihood ratio distributions for 10 GeV/c pions and electrons with 9 associated TRD hits (Monte Carlo simulation). A threshold $£_{th}$ corresponding to a 90% electron identification efficiency is shown.

than 90% in the momentum range from ~1 GeV/c to ~50 GeV/c. Below 1 GeV/c, the TRD identification capability degrades rapidly due to the sharp decrease in the transition radiation yield induced by electrons. Above 50 GeV/c, electron-pion discrimination commences to deteriorate because the TR photon production by pions becomes significant (see Fig. 5.1). In the data analysis, the identification algorithm is applied to particles in the momentum range from 0.5 GeV/c to 50 GeV/c.

Ionization losses of protons in the momentum range of 0.5 to 3 GeV/c significantly exceed energy losses of pions of the same momentum. Therefore, the electron-pion discrimination algorithm described above gives a poor rejection of low momentum (typically less than ~1.5 GeV/c) protons, their large fraction being misidentified as electrons. Positron-proton discrimination by TRD (relevant only for positive charge sign particles) in this momentum range requires a dedicated treatment, the development of which is in progress.

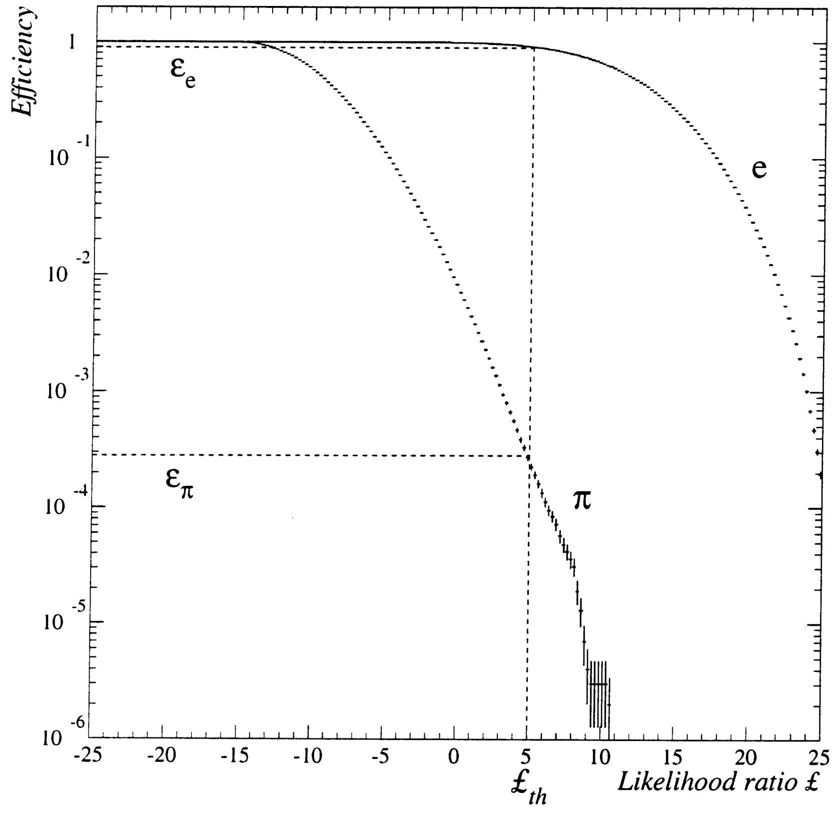

Figure 5.5: Electron identification efficiency ε_e and pion acceptance ε_π as a function of the threshold for 10 GeV/c particles with 9 associated hits (Monte Carlo simulation). The threshold value $\pounds_{th}$ shown corresponds to $\varepsilon_e = 90\%$.

5.3.2 Identification of non-isolated particles

The method

The main task of the TRD is the identification of leading electrons produced in τ decays or in ν_e CC interactions. These electrons are in general well isolated from other tracks in an event. However, the identification of non-isolated particles by the TRD is also possible (though with smaller efficiency), as the number of tracks producing each TRD hit is known from the accurate reconstruction of the track coordinates in the drift chambers. The identification of non-isolated electrons is useful to study the processes where an electron is imbedded in the hadron jet (e.g., decays of charmed particles).

Two tracks whose projections onto the horizontal plane are close to one another cannot be separated in the TRD. For instance, in the case of ν_e CC interactions, about 25% of the events include tracks crossing the same straw tubes, producing so-called "shared" hits. Application of the identification algorithm described in the previous section to "shared" hits where the energies deposited by each of the non-isolated tracks are summed up, would

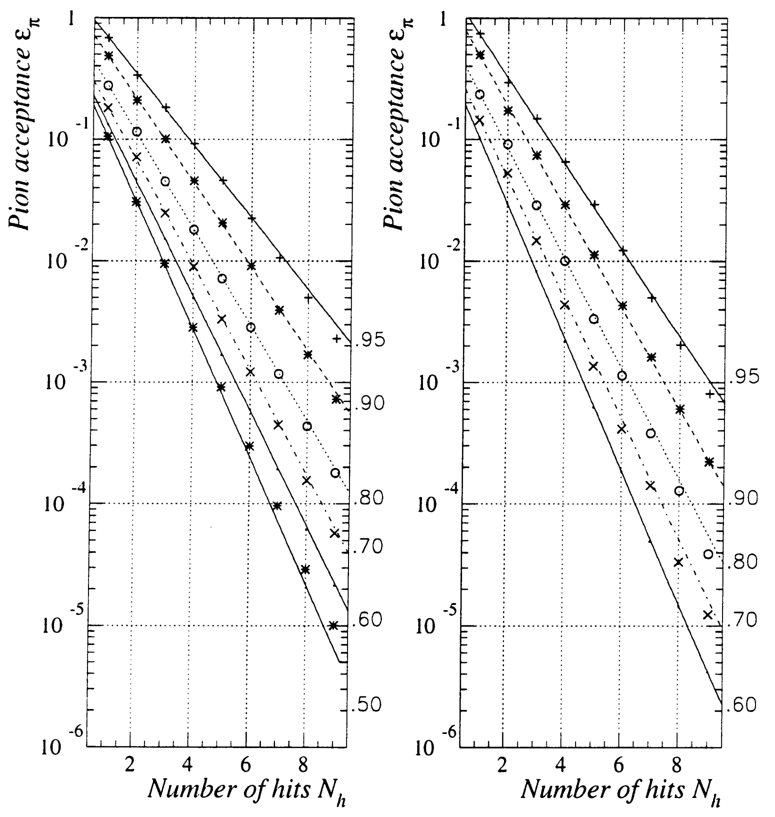

Figure 5.6: Expected pion acceptance, ε_π, corresponding to fixed values of electron identification efficiency, ε_e, as a function of the number of associated hits N_h, for 1 GeV/c (left) and 10 GeV/c (right) particles. Straight lines are drawn to guide the eye; points along each line are computed for the value of ε_e indicated at the end of the line, on the right.

lead to substantial particle misidentification. For example, more than 95% of two pions with all 9 hits "shared" would be identified as electrons.

We have developed a procedure for the identification of non-isolated particles which takes into account the number of tracks associated with each hit as well as the particle momenta.[1] This algorithm is applied to a pair of tracks if the number of "shared" hits is larger than 3. If two tracks share less than 4 hits, they are treated separately by the particle identification procedure for isolated tracks (Sec. 5.3.1) applied to their "non-shared" hits only.

While for an isolated particle of momentum p the decision is made between the two hypotheses $e(p)$ and $\pi(p)$, for two non-isolated particles of momenta p_1 and p_2 one has to consider four hypotheses $\pi(p_1) * \pi(p_2)$, $e(p_1) * \pi(p_2)$, $\pi(p_1) * e(p_2)$ and $e(p_1) * e(p_2)$. Thus, four likelihood estimators are computed from the corresponding probability density distributions for a combination of two particles:

---

[1] A detailed description of the algorithm can be found in [88].

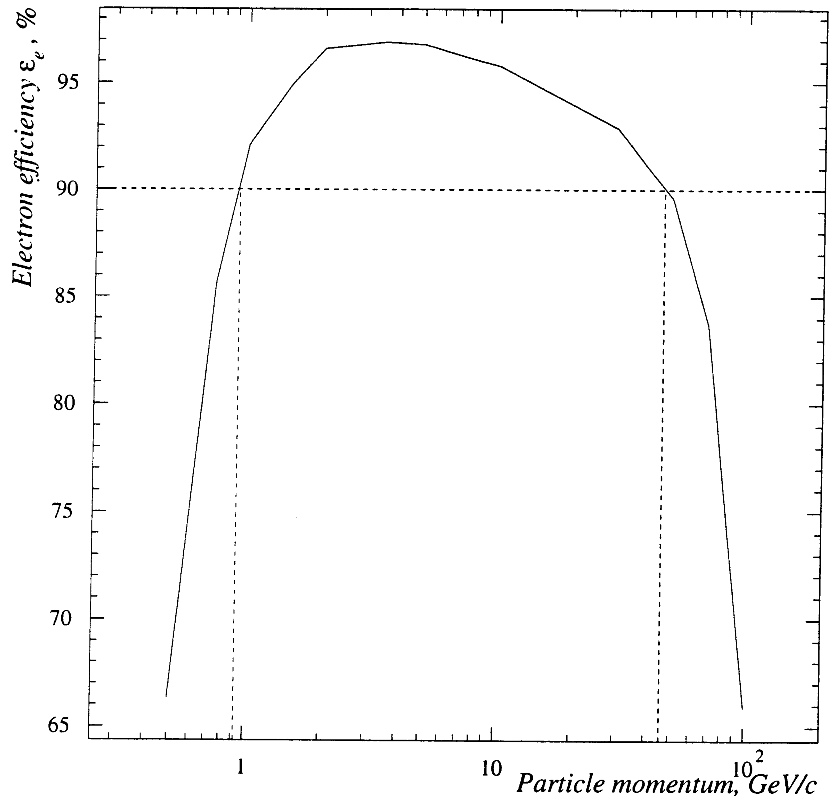

Figure 5.7: Monte Carlo predicted electron efficiency ε_e corresponding to $\varepsilon_\pi = 10^{-3}$ as a function of the momentum of the particle for 9 associated hits.

$$\pounds_{kl} = \log \left[\prod_{i=1}^{N_{sh}} P\left(E_i \mid k(p_1) * l(p_2)\right) \prod_{j=1}^{N_{nsh}} P\left(\left(E_j^1 + E_j^2\right) \mid k(p_1) * l(p_2)\right) \right] \tag{5.2}$$

where

- k, l run each for e, π;
- N_{sh} is the number of modules where the hits are "shared" by the two particles;
- N_{nsh} is the number of modules where the two particles have "non-shared" hits;
- $P(E_i \mid (k(p_1) * l(p_2))$ are the probability densities for the combination of two particles $k(p_1)$ and $l(p_2)$ with momenta p_1 and p_2 to deposit the total energy E_i in the ith straw tube. If, in the jth TRD module, two tracks are associated with different "non-shared" hits, the energy depositions E_j^1 and E_j^2 from these hits are added.

The probability density distributions used in the Eq. (5.2) were obtained by convolution of the distributions of the energies deposited by the isolated particles (see Fig. 5.8). The

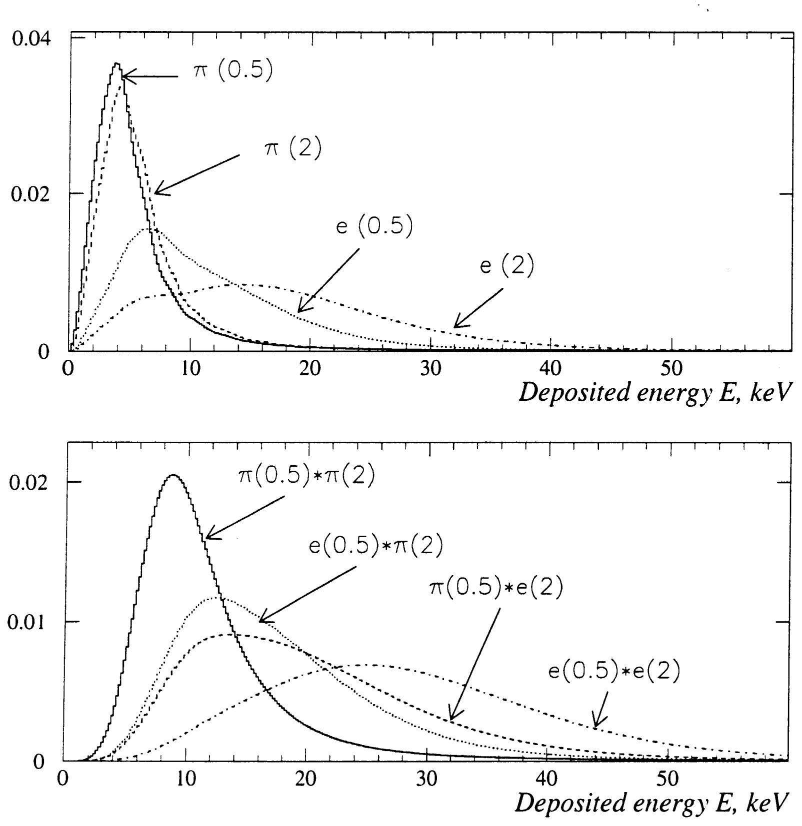

Figure 5.8: TRD response to isolated (top) and non-isolated (bottom) 0.5 GeV/c and 2 GeV/c electrons and pions (Monte Carlo simulation). Particle momentum is shown in brackets.

decision on the nature of each of the two particles is made by selecting the hypothesis corresponding to the largest likelihood value among the four $\mathcal{L}_{kl}$.

The discrimination between $e(p_1) * \pi(p_2)$ and $\pi(p_1) * e(p_2)$ hypotheses on the basis of "shared" hits is not possible when $p_1 \sim p_2$. In such case, energy depositions in "non-shared" hits are treated separately for each track and provide additional information to help to tag the electron and pion.

Monte Carlo tests of the method

The identification procedure for non-isolated particles has been studied for a sample of Monte Carlo events with two tracks generated with a uniform momentum distribution in the range from 0.5 to 50 GeV/c and having 9 "shared" hits in the TRD. The results are presented in Table 5.1. The expected efficiencies of a correct $\pi * \pi$ and $e * e$ identifications are greater than 90%, with contamination from $e * \pi$ and $\pi * e$ combinations limited to a few percent. The expected probability to misidentify an $e * e$ combination as a $\pi * \pi$ pair and vice versa is less than 10^{-3}. On the other hand, a significant fraction (~25%) of $e * \pi$

and $\pi * e$ combinations is expected to be identified as electron pairs.

	Identified as (%)		
Generated as	$\pi * \pi$	$e * \pi$, $\pi * e$	$e * e$
$\pi * \pi$	91.9	8.1	< 0.1
$e * \pi$, $\pi * e$	0.7	74.8	24.5
$e * e$	< 0.1	3.0	97.0

Table 5.1: Monte Carlo expectation of the identification efficiency for different combinations of particles sharing 9 hits in the TRD (uniform momentum distribution).

The identification procedures for both isolated and non-isolated particles have also been applied to a sample of Monte Carlo events simulating ν_e CC interactions in the detector. The results obtained for the identification of particles with more than 3 "shared" hits in ~20 000 generated events are shown in Table 5.2. The improvement due to the identification algorithm for non-isolated particles is clearly seen. Most importantly, the amount of misidentified $\pi * \pi$ combinations is reduced from ~99% to ~17%.

	Identified (%) by					
	Isolated particle ID			Non-isolated particle ID		
Generated as	$\pi * \pi$	$e * \pi$, $\pi * e$	$e * e$	$\pi * \pi$	$e * \pi$, $\pi * e$	$e * e$
$\pi * \pi$	0.9	< 0.1	99.1	83.4	15.2	1.4
$e * \pi$, $\pi * e$	1.6	< 0.1	98.4	9.2	38.4	52.4
$e * e$	0.1	< 0.1	99.9	3.4	12.6	84.0

Table 5.2: Performance of the TRD identification algorithms for non-isolated particles in ν_e CC Monte Carlo simulated events.

5.4 Discussion of the electron identification algorithms

The identification algorithms described in Sec. 5.3 demand an accurate measurement of the energy depositions E_i and a precise knowledge of the probability density distributions $P(E_i \mid e)$ and $P(E_i \mid \pi)$, i.e., of the detector response to both electrons and pions. In this section, we discuss the impact of the characteristics of incident particles and detector parameters on the energy deposition, the way they were taken into account in the electron identification procedure, and the implementation of the identification algorithms.

5.4.1 Experimental studies and algorithm assumptions

The response of each straw tube is continuously calibrated by means of ^{55}Fe radioactive sources, emitting 5.89 keV X-rays. The signals from the ^{55}Fe sources, which vary with the changes in most of the detector parameters (such as high voltage, temperature, pressure, composition of the gas mixture, its H_2O and O_2 contaminations, etc.), allow a precise measurement of the detector response.

With the sources located in the middle of each straw, however, the ^{55}Fe calibration does not take into account possible variations in the gas mixture composition along the straw tubes. A uniform response of the straw tubes along the vertical axis has been obtained by an empirical adjustment of the operating conditions. This uniformity is permanently controlled by measurements of the positions of the minimum ionizing peak of muons over the whole detector area [81]. Therefore, in the identification algorithms we assume the response of all 1584 straw tubes to minimum ionizing particles to be identical and independent of the altitude of the particle impact point.

In order to simplify the identification algorithms, a number of studies have been carried out with the aim of reducing the number of parameters on which the probability density distributions of electrons depend. They have shown that the following parameters can be neglected in the identification procedure:

- **Impact point of the electron.** The transition radiation yield depends on the mean dispersion of the gaps between the foils of the radiator [72] which can vary along the large radiator area because of local inhomogeneities. Consequently, one could expect an X-ray yield dependence of the impact point of the electron on a radiator. A thorough scan of the surface of the radiators by 10 GeV/c electrons in a test beam showed no variation in the X-ray production rate within the 5% accuracy of the measurements.

- **Module position in a doublet.** In the 4 TRD doublets, the second detection plane of a doublet detects about 10% of the X-ray photons emitted in the radiator of the first module which were not absorbed in the first detection plane. Due to this effect, a larger average response of the second module is expected. On the other hand, the regularity of the spacing between the foils was substantially improved during the manufacturing of the radiators. It was decided to install 4 radiators of inferior quality as second radiators of a doublet in order to compensate their lower X-ray yield by a higher detection rate. The signal in the first and second detection planes of a doublet has been studied for a sample of δ electrons from NOMAD data (see Sec. 5.5). No difference in the module responses was observed at a level of a 3% measurement accuracy.

- **Angle with respect to the radiator.** The angle between the incident particle and the radiator surface could affect the transition radiation yield by changing the distance through the foil and spacing traversed by a particle [89]. The simulation showed a compensation between the increase in the transition radiation production and the increased X-ray photon re-absorption in the radiator in the relevant angular range [73].

Based on these studies we assumed in the implementation of the electron identification algorithms that the probability density distributions both for electrons and pions do not vary from one detection plane to another or over the 2.85×2.85 m^2 surface of the detector and depend only on the Lorentz factor of the incident particle.

5.4.2 Implementation of the identification algorithms

To study the detector response to electrons and pions, test beam measurements [81] and a detailed simulation of the detector [73] have been performed. Due to the impossibility of in-situ calibration of the entire detector by electron and pion beams, the TRD simulation package, the results of which were confirmed by test beam measurements, was used to compute the probability density distributions of the energy deposition by isolated and non-isolated particles.

In practice, to identify isolated particles, the probability density distributions were generated for a set of several momenta of electrons and pions and tabulated. The integrated likelihood ratio distributions for electrons and pions (see Fig. 5.5) as a function of their momenta and number of associated hits were also computed and stored. This information allows to tighten (loosen) electron selection criteria according to the goals of different analyses. An interpolation procedure is used to account for the measured momentum of a particle.

For the identification of non-isolated particles, only the probability density distributions for the four possible hypotheses were computed and tabulated as a function of the particle momentum.

The performance of the TRD obtained in the analysis of the real data described below confirms the validity of the assumptions, the excellent steering of the detector, and the correct description of the detector response by the simulation program.

5.5 TRD performance with experimental data

The TRD performance has been studied using experimental data in-situ, with the detector installed as a part of NOMAD. The agreement between the expected and the observed response for isolated particles, as well as the performance of electron identification, were tested on two samples of events selected during NOMAD data taking:

- through-going muons – muons crossing the detector between two neutrino spills (Sec. 5.5.1);

- δ electrons produced by through-going muons (Sec. 5.5.2).

The latter sample has also been used to study the performance of the identification procedure for non-isolated particles (Sec. 5.5.3). Finally, the electron identification algorithm for non-isolated particles has been applied to electron-positron pairs resulting from photon conversions (Sec. 5.5.3).

5.5.1 TRD performance for minimum ionizing particles

A sample of more than 200 000 through-going isolated muons in the momentum range from 2.5 to 50 GeV/c, recorded during the "flat top" period of the SPS accelerator cycle (see chapter 3), has been analysed. The measured and simulated spectra of the ionization losses of muons in the TRD have been compared for various muon momenta. Excellent agreement between data and simulation was found over three orders of magnitude, as shown in Fig. 5.9 for 10 GeV/c muons.

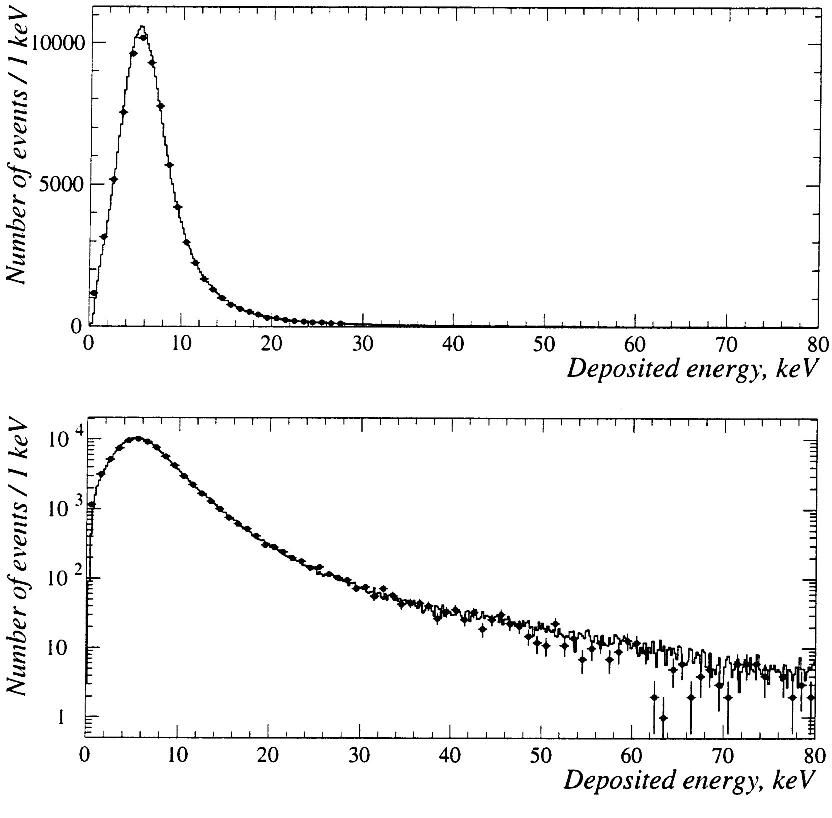

Figure 5.9: Comparison of experimental (points with error bars) and simulated (histogram) energy losses of 10 GeV/c muons (linear and logarithmic scales).

The TRD identification algorithm for isolated particles was applied to a fraction of the muon sample. The probability for a muon to be identified as an electron was found to be $\varepsilon_\mu = (1.17 \pm 0.30)\cdot 10^{-3}$, which is in agreement with the required $R = 10^3$ rejection factor. The distribution of the likelihood ratio probability for muons is shown in Fig. 5.10. The flatness of the histogram confirms the agreement between the input parameters of the identification algorithm and the data. The absence of a peak at low probability values shows also the purity of the selected muon sample and the absence of electron admixture.

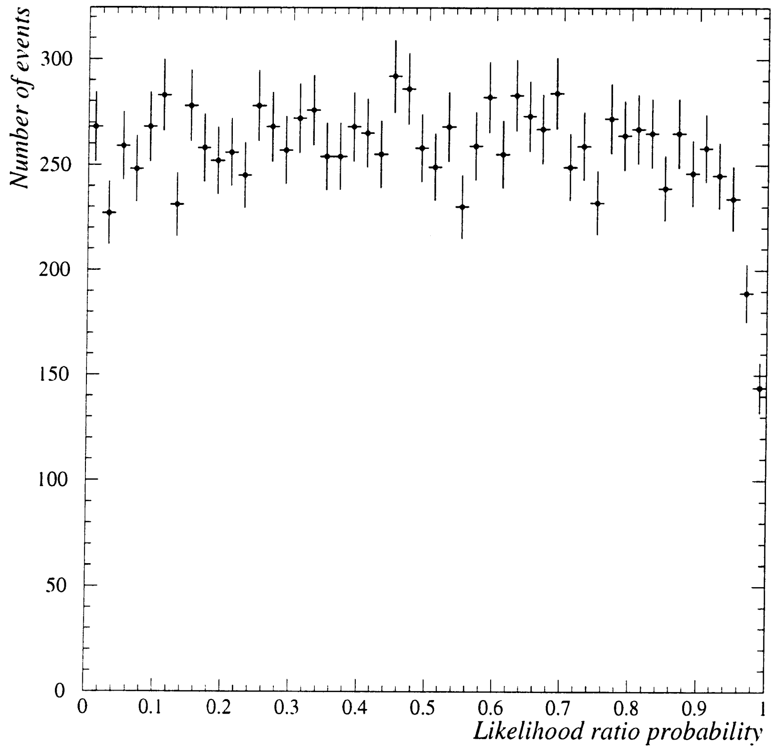

Figure 5.10: Distribution of the likelihood ratio probability for muons.

5.5.2 TRD performance for electrons

As the TRD is an essential tool for electron identification in NOMAD, selecting an unbiased electron sample from neutrino interaction events in order to evaluate the performance of the TRD is problematic. Instead, the in-situ detector response to electrons was studied on a sample of δ-rays emitted by "flat top" muons. Such δ electrons are well suited for the studies of TRD performance due to the following reasons:

- With an average momentum of the "flat top" muons of about 20 GeV/c, the maximum allowed energy of the emitted δ-ray, E_δ^{max}, is about 13 GeV [3], well above the TRD identification threshold of 0.5 GeV.
- The angle of emission of a δ-ray electron with energy E_δ is given by the expression [90]:

$$\cos^2\theta = \frac{E_\delta}{E_\delta^{max}} \tag{5.3}$$

Consequently, a large fraction of δ electrons with E_δ on the order of a few GeV is expected to be spatially well separated from the muon track (see Fig. 5.11).

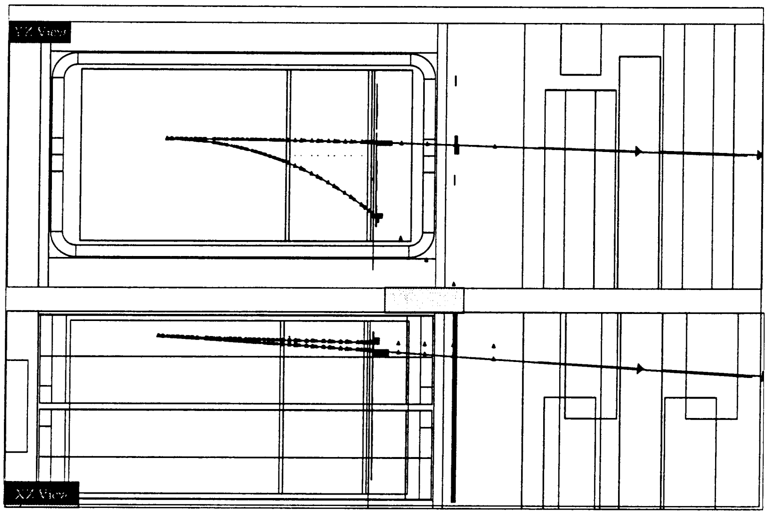

Figure 5.11: An example of a δ-ray event. The muon track (observed in the muon chambers) and the δ electron track (absorbed in the electromagnetic calorimeter) are well separated in both projections.

The criteria for δ-ray event selection, based only on the topology of the event and on the muon identification, are totally independent of the TRD electron identification. A sample of 1216 δ-ray electrons was selected by requiring two track events including a muon (identified in the NOMAD muon chambers) and a second particle (δ-ray) with a momentum above 0.5 GeV/c. An example of a selected event is shown in Fig. 5.11. Fig. 5.12 shows the momentum distribution of the selected δ-rays as measured by the drift chambers, which is in agreement with the expected $1/E_\delta^2$ behaviour [3].

The selected sample of δ-rays allows one to compare the simulated and experimental spectra of energy deposited in the TRD by low momentum electrons. Their excellent agreement is shown in Fig. 5.13. The simulated spectrum was generated by taking into account the measured δ-ray momentum and angular distributions.

The TRD electron identification algorithm for isolated particles has identified 1075 electrons among 1216 δ-rays. The measured value of the electron identification efficiency $\varepsilon_e = (88.4 \pm 0.9\ (\mathrm{stat}))\%$ is in agreement with the expected $(89.9 \pm 1.1)\%$ for the identification of electrons at low momenta, for a pion rejection factor of 10^3.

5.5.3 Performance of the identification of non-isolated particles

Sample of δ-ray electrons

The identification of non-isolated particles has been studied on the sample of muons emitting δ-rays described in Sec. 5.5.2. Non-isolated particles in data were generated by adding, plane by plane, the energy deposition of an isolated muon and an isolated

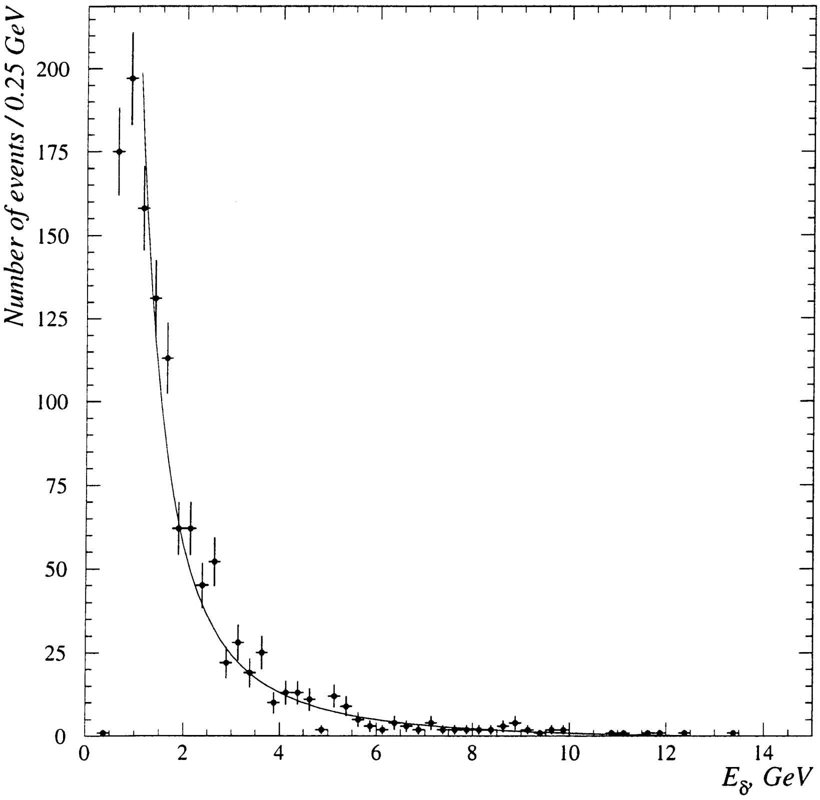

Figure 5.12: Momentum distribution of δ-rays. A $1/E_\delta^2$ fit of the momentum distribution is shown.

electron from two separate events, thus forming 9 "shared" hits. The performance of the identification algorithm on data and simulation is shown in Table 5.3. About 64% of $e*\mu$ combinations are correctly identified, which agrees with the Monte Carlo expectation within large statistical error.

Reconstructed as	Data, %	Simulation, %
$\pi * \pi$	2.9	1.0
$e * \pi$, $\pi * e$	63.9	72.1
$e * e$	33.2	26.9

Table 5.3: The performance of the identification procedure for non-isolated particles applied to the summed energy depositions by muon and δ electron ($\pi * e$ combination).

Photon conversions

Another test of the identification of non-isolated particles was performed on photon conversion pairs. The electron and positron resulting from a photon conversion are pro-

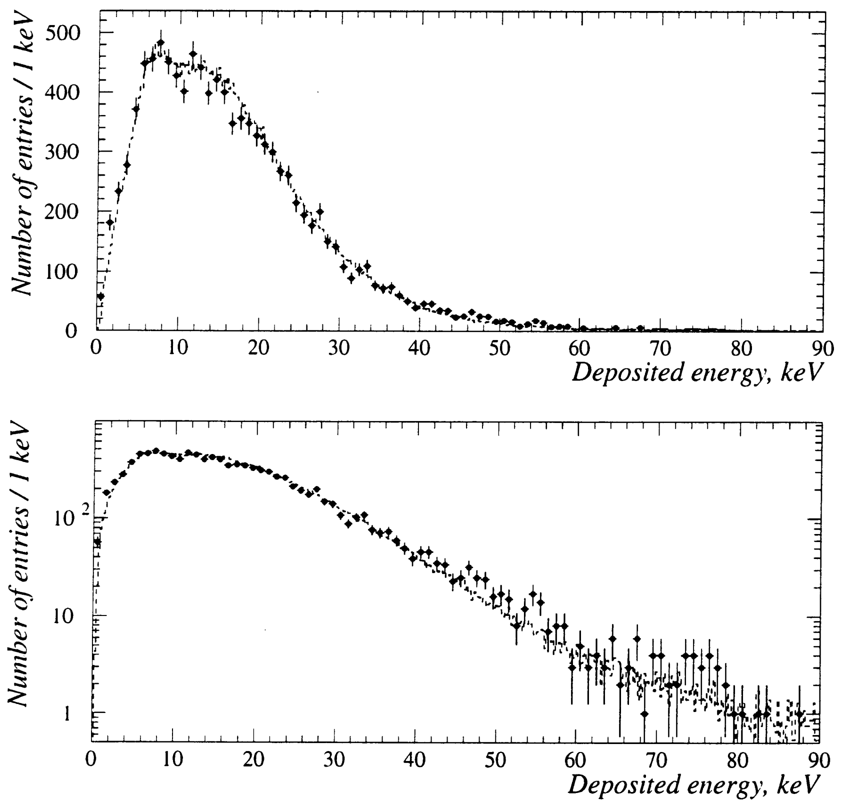

Figure 5.13: Comparison of experimental (points with error bars) and simulated (dashed line) distributions of the energy deposited in the TRD by δ electrons (linear and logarithmic scales).

duced at a small angle with respect to each other and usually lead to "shared" hits in TRD. On the other hand, due to the magnetic field in the detector, the two tracks are opened up in the vertical projection and are reconstructed separately by the drift chambers.

Based on the topology of the conversions and requiring that the invariant mass of a pair be compatible with that of a photon (less than 100 MeV/c^2), we selected about 600 electron-positron pairs from a subsample of ν_μ CC neutrino interaction events recorded in NOMAD. Among them, in 75 cases both tracks had a momentum above the identification threshold and more than 3 "shared" hits in the TRD. Of these, 65 pairs were correctly recognized by the identification procedure for non-isolated particles as an $e{*}e$ combination. The efficiency obtained, $(86.7 \pm 3.9)\%$, is in agreement with the 86.0% Monte Carlo expectation for the identification of $e * e$ combinations with the measured momentum distribution.

5.6 Conclusion

The algorithm developed for the identification of isolated particles in the NOMAD TRD provides a 10^3 pion rejection factor for a 90% electron identification efficiency in the momentum range 1–50 GeV/c. The procedure designed for the identification of non-isolated particles significantly reduces the number of mis-identifications, especially in large multiplicity events.

The simulated and the observed detector response, both to minimum ionizing particles and to electrons, are in excellent agreement. The results obtained for muons and electrons during NOMAD data acquisition confirm the assumptions made in the implementation of the identification algorithms.

The performance of the TRD obtained for the electron-pion discrimination makes possible an appearance search for $\nu_\mu \to \nu_e$ oscillations in NOMAD.

Chapter 6

Analysis of the 1995 and 1996 NOMAD data

6.1 An outline of the $\nu_\mu \to \nu_e$ oscillation search in NOMAD

The NOMAD experiment has been designed to reliably identify and to measure with good precision the charged current (CC) and neutral current (NC) interactions of the four neutrino species, ν_μ, $\bar{\nu}_\mu$, ν_e and $\bar{\nu}_e$. NOMAD's unprecedented ability to efficiently detect ν_e CC events in a high statistics neutrino experiment and the low ν_e contamination in the CERN SPS wide band neutrino beam are the keys to a sensitive search for $\nu_\mu \to \nu_e$ oscillations.

The interest in this kind of study has recently greatly increased, following the LSND experiment claim for evidence for $\bar{\nu}_\mu \to \bar{\nu}_e$ and $\nu_\mu \to \nu_e$ oscillations [34, 38]. In case of $\nu_\mu \to \nu_e$ oscillations with a probability of $3.1 \cdot 10^{-3}$ observed by LSND and with $\Delta m^2 > 10$ eV^2, an oscillation signal should be seen in the NOMAD data.

This signal would manifest itself both as an excess of ν_e CC events and as a change in the shape of the ν_e CC energy spectrum, due to different energy distributions of incident ν_e and ν_μ neutrinos. In addition to ν_e charged current events, electrons are amply produced in ν_μ charged current and neutral current interactions, mostly due to π^0 Dalitz decays and photon conversions. The electron signature can also be simulated by misidentified charged hadrons. An excess of electron events above the predicted background – comprising "prompt" electrons from ν_e-induced CC events and "non-prompt" electrons from the CC and NC interactions of other neutrino species – would be an indication for the $\nu_\mu \to \nu_e$ oscillations.

In order to reduce systematic uncertainties associated with the absolute flux prediction and kinematic selection efficiency, it is preferable to study the ratio $R_{e\mu}$ between the number of ν_e and ν_μ charged current interactions. To compare the observed and the predicted $R_{e\mu}$ ratios and to draw a conclusion on the presence or absence of an oscillation signal in NOMAD, a precise determination of the relative ν_e/ν_μ flux is required. The sensitivity of the analysis can be increased by taking into account the $R_{e\mu}$ dependence on the neutrino energy E_ν and on the radial position of neutrino interaction vertex R^2.

The following algorithm of the analysis is imposed:

- to select events containing either a muon μ^- or an electron e^-;
- to reject as much as possible the non-prompt background in both μ^- and e^- samples, while keeping an efficiency of the selection of the prompt ν_μ and ν_e neutrino-induced charged current events as high as possible;
- to evaluate the remaining non-prompt background;
- to estimate the energy of neutrino and the radial position of its interaction vertex;
- to conclude on the presence or absence of $\nu_\mu \to \nu_e$ oscillations by comparing the ratio of the observed e^- and μ^- events to that expected in the absence of oscillations (Monte Carlo predictions for the e^- and μ^- samples are the sums of prompt and non-prompt background contributions);
- to estimate the systematic uncertainties of the analysis; and
- to compute an allowed (or excluded) region of oscillation parameters.

A negligible contribution from $\bar{\nu}_\mu \to \bar{\nu}_e$ oscillations is expected in the e^+ data sample, given the admixture of $\bar{\nu}_\mu$ in the beam (~5.5% of ν_μ) and the small non-excluded probability of the oscillations ($P < 4{\cdot}10^{-3}$). Therefore, the antineutrino interactions should provide a control sample for the $\nu_\mu \to \nu_e$ oscillation search.

This chapter describes the selection criteria of $\overset{(-)}{\nu}_\mu$ and $\overset{(-)}{\nu}_e$ charged current events in the analysis of 1995 and 1996 NOMAD data. We also discuss the energy flow reconstruction algorithm, the estimations of non-prompt background, the efficiency and the purity of selection. The analysis of the ν_e CC events presented here is of more general interest than for the search for $\nu_\mu \to \nu_e$ oscillations, since it allows also the study of the predominant background source for $\nu_\mu \to \nu_\tau$ oscillation search in $\tau^- \to e^-\bar{\nu}_e\nu_\tau$ channel.

6.2 Data and Monte Carlo samples

The $\nu_\mu \to \nu_e$ oscillation search presented below is based on data collected during the two first NOMAD physics runs in 1995 and 1996, for a total exposure of $0.86{\cdot}10^{19}$ and $1.38{\cdot}10^{19}$ protons on target (p.o.t.) respectively. During the 1995 run, the drift chambers of the detector were being gradually installed, so that the run was divided into 3 almost equal periods when 4, 8, and finally the full 11 modules (cf. 3.4.3) were in place.

The Monte Carlo (MC) events were generated according to the expected neutrino flux [91] using the NEGLIB 5.07 [92] deep inelastic scattering (DIS) event generator based on LEPTO 6.1 [93] and JETSET [94] packages. The response of the NOMAD detector was simulated with the help of GEANT [47]-based GENOM Monte Carlo package [95] (version 5.12) complemented by the TRDSM 203 [74] package for the simulation of the transition radiation emission, the photo-absorption, and the ionization losses in thin gas layers.

The overall data sample used for this analysis is the NOMAD processing of the 1995 data (4, 8 and 11 module data taking periods), 1996 data and the corresponding samples of ν_e, $\bar{\nu}_e$, ν_μ, $\bar{\nu}_\mu$ CC and ν_μ NC Monte Carlo simulated events. The data samples consist of 341 222 (605 571) events reconstructed in the drift chamber target volume of the detector for the 1995 (1996) run. They are composed of both neutrino interactions in the NOMAD active volume (mainly ν_μ CC with smaller admixtures of ν_μ NC events and events produced by other neutrino flavours) and other events (through-going muons, neutrino interactions in the magnet coils, cosmic rays, etc.). The MC statistics used for the present analysis include samples of 1 050 000 ν_μ CC and $\bar{\nu}_\mu$ CC events (twice the expected data statistics), 235 000 ν_e CC and 130 000 $\bar{\nu}_e$ CC events (40 times of the ν_e data statistics) and 590 000 ν_μ NC events (4 times of that expected in the data).

An identical reconstruction chain was applied to both the 1995-1996 data and MC samples. It consisted of three main stages of the processing:

- **phase1:** reconstruction of tracks in the drift chambers. The trajectories of charged particles are reconstructed from the hits in the drift chambers. From these trajectories momenta are estimated using a Kalman filter technique [96] whose transport equations include the magnetic field map and account for the energy loss and multiple scattering in the materials traversed. At this first step energy losses are computed assuming all particles are pions (pion track fit).

- **phase2:** reconstruction of standalone objects in other subdetectors (hits in TRD, track segments in muon chambers, etc.); combination of those objects into higher level ones (the so-called matching process [97]); TRD-based particle identification. The trajectories of the particles identified as electrons or positrons are re-fitted to account for bremsstrahlung (electron track fit). All tracks not identified as muons or electrons are assumed to be hadrons. Vertices are formed from charged tracks emerging from the same region in space.

- **dst:** filling of ZEBRA [98]-based data summary tapes (DST) on the basis of phase1 and phase2 information.[1]

6.3 Selection of ν_μ and ν_e charged current interactions

The general analysis procedure is the following:

- first, the so-called "event quality" cuts are applied to all data and Monte Carlo samples in order to select well-reconstructed neutrino interactions occuring in the drift chamber target (Sec. 6.3.1);

---

[1] The analysis presented here was performed starting from the DST version v7r2 [99].

- second, muon (electron) identification is performed. Events with at least one lepton found are classified into $\mu^\pm$ or $e^\pm$ samples of the candidates for $\overset{(-)}{\nu}_\mu$ CC or $\overset{(-)}{\nu}_e$ CC interactions (Sec. 6.3.2);

- next, a set of conversion rejection cuts is applied to $e^\pm$ sample in order to reduce the non-prompt electron background (Sec. 6.3.3);

- the energy flow and kinematic variables of the event are reconstructed (Sec. 6.4);

- finally, selection criteria based on the kinematics of charged current neutrino interactions are imposed upon both $\mu^\pm$ and $e^\pm$ samples, to further reduce the non-prompt background (Sec. 6.5).

Various Monte Carlo event samples were used to define and to optimize the identification and selection criteria that reduce the non-prompt backgrounds to an acceptable level and yield the high efficiency to charged current neutrino interactions.

To increase the robustness of the analysis with respect to systematic uncertainties, the selection algorithms for ν_μ CC and ν_e CC event candidates are kept as similar as possible. Identical quality and kinematic cuts are imposed upon the muon and the electron samples. No distinction is made between positive and negative leptons until the very end of the selection.

6.3.1 Event quality cuts

At the first step of the analysis, a few pre-selection cuts are applied:

- **Monte Carlo event truncation.** If the MC event was truncated during GENOM processing due to internal program space limitations, there could be a potentially dangerous lack of information (e.g., missing hits of a muon in muon chambers). All the truncated events were rejected.

- **Data-taking problems.** All the events with raw data missing for some detectors (e.g., muon chambers partially off) or serious detector problems (e.g., significant noise in ECAL) were rejected based on the information from NOMAD data-taking log-books.

- **Event consistency.** Data and Monte Carlo events with simulation or reconstruction problems (like zero momentum tracks, no Monte Carlo vertices, etc.) were rejected.

These cuts normally eliminate only a tiny fraction of the events. At the next step, the event quality cuts are imposed. They remove events either not originating from neutrino interactions in the drift chamber target or those poorly reconstructed, both in data and in the Monte Carlo simulated samples. The following cuts were applied:

- **Density cut.** To speed up event processing, an evaluation of the complexity of each event before its full reconstruction is done based on four quantities: the number of hits in the DC veto chamber[1], the average number of hit wires in hit DC planes, the total number of in-time DC hits and the total number of TRD hits. If at least one of the four numbers is above a given threshold, the event is skipped without being fully reconstructed. The values of the thresholds are chosen in such a way that only a few percent of events, in all cases too complicated to be reliably analysed, are rejected, allowing an essential reduction of the processing time. The precise fraction of removed events depends on neutrino interaction type and typically varies between 2% for ν_μ NC and 7% for ν_e CC.

- **Fiducial volume.** To remove events originating from outside the target part of the detector, cosmic and through-going muons, and to ensure an acceptable quality of event reconstruction, cuts on the position of the reconstructed primary vertex[2] were applied.

  The fiducial volume for this analysis was defined as being between -130 and $+130$ cm in x and between -125 and $+135$ cm in y, where x and y are the horizontal and vertical detector axes perpendicular to the beam direction. The fiducial volume along the longitudinal detector axis, z, was defined as ending at 405 cm (at the end of the target, before the first trigger plane) and starting at 5, 115 and 262 cm for the 1996 and 11 module 1995, 8 module 1995, and 4 module 1995 data respectively.

  The reconstructed primary vertex is required to lie within the so-defined fiducial volume. This criterion eliminates about 30% of the initial data samples.

- **Trigger formation.** We require that a Monte Carlo event would give a trigger, namely that there is at least one in-time hit in both trigger planes.

- **Number of primary tracks.** At least two charged tracks originating from the primary vertex are required. This cut removes cosmic and through-going muons still present in the sample after the fiducial volume cut.[3] The number of events in the data is reduced by about 15%. The efficiency of this cut was estimated to be 98% for ν_e CC and 97% for ν_μ CC interactions.

6.3.2 Particle identification

Events surviving the quality cuts are classified into $\mu^\pm$ and $e^\pm$ samples of the candidates for $\overset{(-)}{\nu_\mu}$ CC or $\overset{(-)}{\nu_e}$ CC interactions. For this purpose, at least one lepton candidate (muon or electron) in the event is searched for, based on particle identification algorithms.

---

[1] the first drift chamber in the detector.

[2] If there is more than one vertex reconstructed in an event, the primary vertex is the most upstream vertex with at least one charged track with momentum larger than 0.5 GeV/c.

[3] Neutrino-electron scattering events and quasielastic neutrino interactions where the recoil proton is not reconstructed are also rejected by this requirement.

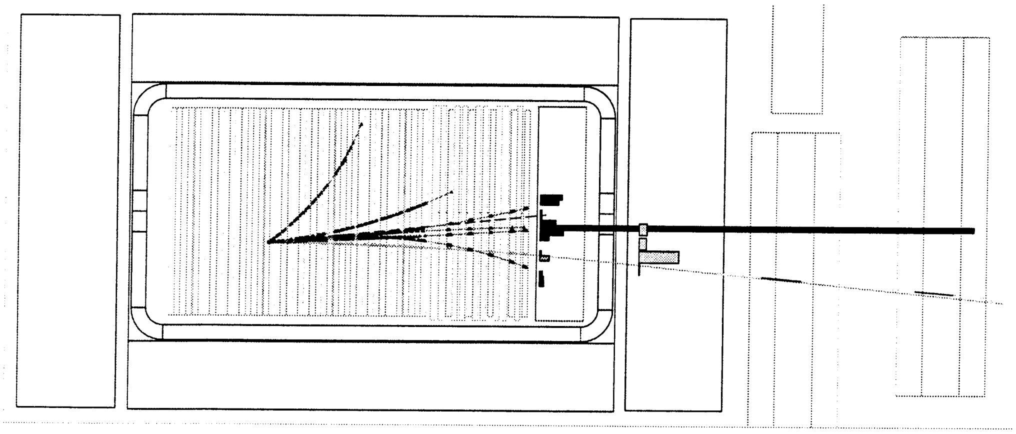

Figure 6.1: A fully reconstructed candidate ν_μ CC event (side view). The longest track is a negatively charged muon matched to the segments in the muon chambers.

We describe first the selection of the $\mu^\pm$ events and then proceed to a more sophisticated search for $e^\pm$ candidates.[1]

Selection of the $\overset{(-)}{\nu_\mu}$ CC candidates

Particles are identified as muons if they penetrate more than 8 interaction lengths (λ_{int}) of absorber material in order to reach muon station 1, or 13 λ_{int} for muon station 2 (see Sec. 3.4.8). Fig. 6.1 shows a candidate ν_μ CC event detected in NOMAD. One energetic particle penetrates to the muon chambers and satisfies all other criteria to be a muon.

Candidates for $\overset{(-)}{\nu_\mu}$ CC interactions are selected by the two following cuts:

- **"Loose" muon identification.** An extrapolated drift chamber track associated with a track reconstructed from the hits in the muon chambers in station 1 (matching distance 40 cm) or muon station 2 (matching distance 50 cm) is required. No additional χ^2 criteria on the quality of the match or DC track extrapolation are imposed.

  The number of ν_μ CC, $\bar{\nu}_\mu$ CC, ν_μ NC Monte Carlo and 1995, 1996 data events which passed this cut (sum of positive and negative candidates), as well as their fraction ϵ with respect to the number of events in the fiducial volume after the event quality cuts, is given in Table 6.1.

  Data samples at this stage of selection consist of ν_μ CC and NC interactions (plus much smaller contributions from other neutrino flavours) with an admixture

---

[1] Though a selection of both $\mu^\pm$ and $e^\pm$ events starts from the same data (and Monte Carlo) samples, there is no overlap between events selected in two categories: we require an identified muon for the $\overset{(-)}{\nu_\mu}$ CC selection and, on the contrary, impose muon veto for the $\overset{(-)}{\nu_e}$ CC search.

	ν_μ CC	$\bar{\nu}_\mu$ CC	ν_μ NC	1995 data	1996 data
# events	702 328	113 825	8 096	172 132	338 296
ϵ, %	86.2	91.8	1.9	61.8	63.5

Table 6.1: ν_μ CC and $\bar{\nu}_\mu$ CC selection: muon identification.

of events other than neutrino interactions in the drift chamber target. Therefore, no accurate comparison of the efficiency of the cut between data and Monte Carlo simulation is possible.

- **Muon momentum cut.** For perpendicular incidence, the momentum thresholds to reach the muon chambers (with 50% probability) are 2.3 GeV/c for station 1, and 3.7 GeV/c for station 2 [55]. We then impose a lower cut on the muon momentum (measured in the drift chambers) of 2.5 GeV/c, to reduce the background due to a missassociation of a drift chamber track with a track segment reconstructed in the muon chambers.

  The effect of the cut on various data and Monte Carlo samples and the fraction of events passing this cut relative to the preceding one are shown in Table 6.2.

	ν_μ CC	$\bar{\nu}_\mu$ CC	ν_μ NC	1995 data	1996 data
# events	699 498	113 484	7 623	171 335	337 005
ϵ, %	99.6	99.7	94.2	99.5	99.6

Table 6.2: ν_μ CC and $\bar{\nu}_\mu$ CC selection: muon momentum cut.

The efficiency of the muon identification (including event quality cuts) with respect to the number of Monte Carlo interactions generated in the fiducial volume of the detector is 78.6% for ν_μ CC (74.5% for $\bar{\nu}_\mu$ CC) events. The ν_μ NC background is suppressed by almost two orders of magnitude. The remaining non-prompt background of the selected $\mu^\pm$ samples is mainly due to $\pi^\pm$ and $K^\pm$ decays and punch-throughs. It represents roughly 0.5% of the selected μ^- events and will be further reduced with the help of the kinematical criteria (Sec. 6.5).

Selection of the $\overset{(-)}{\nu_e}$ CC candidates

Fig. 6.2 shows a candidate ν_e CC event detected in NOMAD. The longest track, identified as an electron by the TRD, deposits a large amount of energy in PRS tubes and ECAL cells, having no associated objects in HCAL and muon chambers.

To select candidates for $\overset{(-)}{\nu_e}$ CC interactions, we apply first a muon veto based on the information from the muon chambers and then an electron identification algorithm which uses information from the DC, TRD, PRS, ECAL and HCAL. The main background to

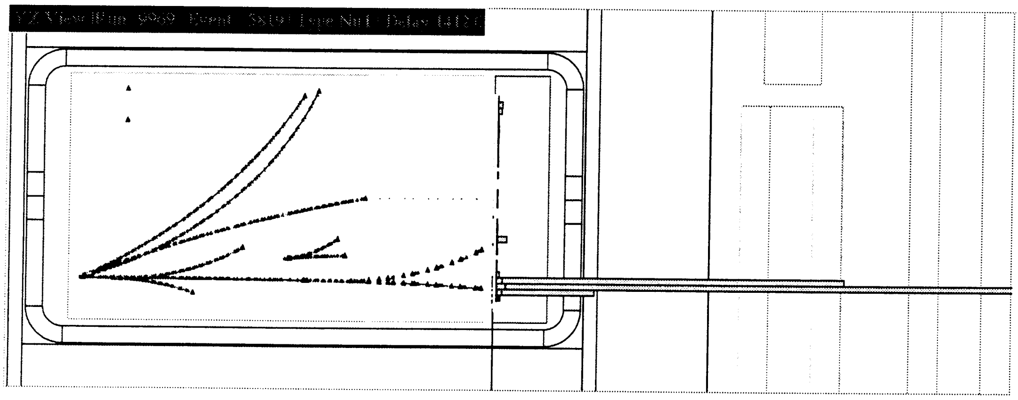

Figure 6.2: A fully reconstructed candidate ν_e CC event (side view). The longest primary track, identified as an electron by the TRD, deposits a large amount of energy in a few electromagnetic calorimeter cells, as indicated by the large "bar". A hadronic jet of charged particles is clearly visible at the primary vertex. Two symmetric photon conversions – one very close to the primary electron track and one far, and an asymmetric conversion – only a positively charged track is reconstructed – are also evident.

be rejected at this stage comes from misidentified hadrons in ν_μ CC and NC interactions. The following selection criteria are imposed:

- **Rejection of events with an identified muon.** We require that there be no drift chamber track associated with track projections reconstructed in muon chambers. The number of ν_μ CC, ν_μ NC (both backgrounds), ν_e CC, $\bar{\nu}_e$ CC (both signals) Monte Carlo and 1995, 1996 data events passing this cut, as well as their fraction ϵ with respect to the number of events in the fiducial volume after the event quality cuts, is given in Table 6.3.

	ν_μ CC	ν_μ NC	ν_e CC	$\bar{\nu}_e$ CC	1995 data	1996 data
# events	102 714	408 585	200 418	104 548	104 369	190 289
ϵ, %	12.6	98.0	97.7	97.9	37.4	35.7

Table 6.3: ν_e CC and $\bar{\nu}_e$ CC selection: muon rejection.

The data sample selected here is complementary to that after the μ identification in $\overset{(-)}{\nu}_\mu$ CC selection. About 13% of ν_μ CC simulated events remain unvetoed because of the geometrical acceptance of the muon chambers or low momentum of a muon.

- **Muon hit veto.** For muons which are well above the momentum threshold to reach the muon chambers and which are inside the muon chamber geometrical acceptance, the efficiency to detect at least 2 hits is about 98%. If the number of muon chamber hits in both the X and Y projections in a ±20 cm road around an extrapolated DC track is greater than two each, the event is rejected.

The effect of this cut on various data and Monte Carlo samples, and the relative number ϵ of events passing this cut with respect to the preceding one, are shown in Table 6.4.

	ν_μ CC	ν_μ NC	ν_e CC	$\bar{\nu}_e$ CC	1995 data	1996 data
# events	98 765	404 464	198 090	104 047	101 350	181 266
ϵ, %	96.2	99.0	98.8	99.5	97.1	95.3

Table 6.4: ν_e CC and $\bar{\nu}_e$ CC selection: muon hit veto.

- **TRD identification of isolated tracks.** We tag as an electron (positron) all the negatively (positively) charged particles with a TRD pion acceptance ε_π (see Sec. 5.3.1) in the range $0 \leq \varepsilon_\pi < 10^{-3}$. If the momentum of the track in the TRD region is greater than 50 GeV/c, the TRD identification of isolated tracks is not applied and the particle is assumed to be an electron.

  The performance of the TRD identification of isolated tracks for the ν_μ CC, ν_μ NC and ν_e CC Monte Carlo events is shown in Table 6.12. This table displays the absolute and relative number of $e^\pm$, $\pi^\pm$+$K^\pm$ and protons identified as electrons at the different stages of the selection, as well as the purity of the samples defined as $N_{e^\pm}/N_{\text{total}}$. At this stage, all the samples are already dominated by real $e^\pm$ with about 15% (30%) admixture of misidentified $\pi^\pm$, $K^\pm$ and protons for ν_e (ν_μ) events.

  The presence of at least one identified electron (or positron) is required for the $\overset{(-)}{\nu_e}$ CC candidate event at all the stages of the analysis. The number of events passing the TRD identification of isolated tracks and their fraction with respect to the preceding cut is given in Table 6.5.

	ν_μ CC	ν_μ NC	ν_e CC	$\bar{\nu}_e$ CC	1995 data	1996 data
# events	39 900	163 246	182 430	97 080	41 041	81 470
ϵ, %	40.4	40.4	92.1	93.3	40.5	44.9

Table 6.5: ν_e CC and $\bar{\nu}_e$ CC selection: TRD identification of isolated tracks.

- **TRD identification of non-isolated tracks.** If a given drift chamber track shares more than three associated TRD hits with another track, the TRD identification algorithm for non-isolated tracks (see Sec. 5.3.2) is applied. The event is rejected only if there are no electron (positron) candidates left. The number of the selected events and the efficiency of the cut is given in Table 6.6.

  The performance of the algorithm is shown in Table 6.12. The number of misidentified $\pi^\pm$ and $K^\pm$ is reduced by about 30% with a ~3% loss in electron efficiency.

	ν_μ CC	ν_μ NC	ν_e CC	$\bar{\nu}_e$ CC	1995 data	1996 data
# events	37 921	154 776	179 655	95 776	39 054	77 811
ϵ, %	95.0	94.8	98.5	98.7	95.2	95.5

Table 6.6: ν_e CC and $\bar{\nu}_e$ CC selection: TRD identification of non-isolated tracks.

- **TRD truncated identification of non-isolated tracks.** If the number of TRD hits shared by a non-isolated track is less than four, the TRD identification is performed on the basis of the non-shared hits only (see Sec. 5.3.2). If truncated identification was applied and the value of pion acceptance ε_π is greater than 10^{-3}, the particle is no longer considered as an electron candidate.

  This procedure reduces the number of remaining misidentified $\pi^\pm$ and $K^\pm$ by about 20% with a ~2% loss of real electrons (see Table 6.12).

	ν_μ CC	ν_μ NC	ν_e CC	$\bar{\nu}_e$ CC	1995 data	1996 data
# events	37 137	151 625	178 714	95 318	38 167	76 292
ϵ, %	97.9	98.0	99.5	99.5	97.7	98.0

Table 6.7: ν_e CC and $\bar{\nu}_e$ CC selection: TRD truncated identification.

- **DC – ECAL match.** Charged energy clusters in the ECAL are formed by summing up the energy deposition in the calorimeter cells pointed to by charged tracks. If there is no energy in the ECAL associated to a given track, it is no longer considered as an electron candidate. This cut rejects mainly low-momentum protons misidentified by the TRD and depositing no energy in the ECAL (more than 80% of misidentified protons are rejected, see Table 6.12) and particles escaping the fiducial volume of the detector through the sides.

	ν_μ CC	ν_μ NC	ν_e CC	$\bar{\nu}_e$ CC	1995 data	1996 data
# events	28 950	116 610	168 987	90 332	27 541	56 260
ϵ, %	78.0	76.9	94.6	94.8	72.2	73.7

Table 6.8: ν_e CC and $\bar{\nu}_e$ CC selection: DC – ECAL match efficiency.

- **Preshower – ECAL π rejection.** A further enhancement in the purity of the $e^\pm$ samples could be obtained by combining the ECAL and the PRS signals. The following consistency between the energy depositions in the PRS and in the ECAL based on test beam measurements [100] is required for an electron candidate:

  ○ $E_x > 1.5$, $E_y > 1.5$;

$$\circ\ E_x + E_y > \begin{cases} 3.2 + 1.35 & \text{if } E < 1 \text{ GeV} \\ 3.2 + 1.35 \times E & \text{if } 1 \text{ GeV} \le E \le 10 \text{ GeV} \\ 3.2 + 13.5 & \text{if } E > 10 \text{ GeV}, \end{cases}$$

where E_x and E_y are the energies measured in the matched preshower clusters in horizontal and vertical planes respectively (in m.i.p.) and E is the energy of the associated calorimeter cluster (in GeV), with angular, non-linearity and preshower corrections applied. With this cut imposed, the purity of all samples gets above 90% (see Table 6.12). The effect of the PRS – ECAL π rejection on the data and Monte Carlo samples is shown in Table 6.9.

	ν_μ CC	ν_μ NC	ν_e CC	$\bar{\nu}_e$ CC	1995 data	1996 data
# events	24 133	98 215	160 958	86 395	22 517	45 162
ϵ, %	83.4	84.2	95.2	95.6	81.8	80.3

Table 6.9: ν_e CC and $\bar{\nu}_e$ CC selection: PRS – ECAL pion rejection efficiency.

- **Consistency between electron momentum and energy.** Two similar quantities are formed for each $e^\pm$ candidate:

  1. $\Delta_1 = (E_e - p_\pi)/(E_e + p_\pi)$, where E_e is the estimated electron energy (its calculation is described in Sec. 6.4.1) and p_π is the momentum at the first hit of the track obtained with the pion track fit.
  2. $\Delta_2 = (E_e - p_e)/(E_e + p_e)$, where p_e is the momentum at the first hit of the track obtained with the electron track fit.

  Pion and electron track fits give significantly different estimates of the electron momentum: on average, it is underestimated in the former case and overestimated in the latter one. The lower cut of -0.1 on Δ_1 and the upper cut of 0.4 on Δ_2 are applied. Such combination of two cuts was empirically found to be the most efficient: while the lower cut rejects mainly isolated protons and pions misidentified by the TRD and PRS (populating the leftmost region of Δ_1 distribution), the upper cut rejects pions overlapping with other particles in the ECAL.

	ν_μ CC	ν_μ NC	ν_e CC	$\bar{\nu}_e$ CC	1995 data	1996 data
# events	20 336	83 005	140 815	75 306	17 094	35 032
ϵ, %	84.3	84.5	87.5	87.2	75.9	77.6

Table 6.10: ν_e CC and $\bar{\nu}_e$ CC selection: $(E_e - p)/(E_e + p)$ cut efficiency.

- **DC – HCAL match.** An electron typically deposits all its energy in the preshower and electromagnetic calorimeter and does not reach the hadronic calorimeter. It is thus required that no HCAL energy be associated with an $e^\pm$ candidate. This cut rejects about 20% of remaining misidentified hadrons with almost no reduction of $e^{\pm}$ sample (see Table 6.12).

	ν_μ CC	ν_μ NC	ν_e CC	$\bar{\nu}_e$ CC	1995 data	1996 data
# events	20 128	82 220	139 479	74 632	16 732	34 488
ϵ, %	99.0	99.0	99.1	99.1	97.9	98.4

Table 6.11: ν_e CC and $\bar{\nu}_e$ CC selection: DC – HCAL match efficiency.

As a result, the total efficiency of the electron identification procedure and event quality cuts (estimated on Monte Carlo samples) is 60.9% for ν_e CC (58.5% for $\bar{\nu}_e$ CC) events, selecting 2.3% of ν_μ CC and 14.1% of ν_μ NC background events generated in the fiducial volume of the detector.

The purity of different samples estimated from Monte Carlo is summarized in Table 6.12. Almost 99% of the particles identified as $e^{\pm}$ in ν_e CC events are real electrons and positrons. The admixture of misidentified hadrons and muons in the surviving ν_μ-induced background events is about 2.5%.

At this stage of analysis, the ratio of the non-prompt background to prompt ν_e CC events in the e^- sample is about 7:1. The non-prompt background is largely dominated by real electrons and positrons.

6.3.3 Rejection of photon conversions

As has been shown, the dominant remaining background for $\overset{(-)}{\nu_e}$ CC interactions after muon veto and electron identification cuts comes from ν_μ CC and ν_μ NC interactions with real electrons in the final state (and not from misidentified charged hadrons). Among the many possible sources of background from real electrons (muon decays, π^0 or η Dalitz decays, Compton scattered photons, decays of K^- and K^0, etc.), the predominant one is converted photons ($\gamma \to e^+e^-$) from $\pi^0 \to \gamma\gamma$ decays. To reduce the non-prompt background in the e^- sample, we apply a set of cuts based on the kinematics and topology of photon conversions.

We tag as conversions all the electrons originating from reconstructed V^0 vertices.[1] In addition, all combinations of identified $e^{\pm}$ with any $e^{\mp}$ or any other track of opposite charge sign to which TRD identification was not applied (low momentum tracks or tracks not matched to TRD hits) are subjected to the following cuts:

- Candidate tracks are linearly extrapolated from their first hits to the point of the minimum distance between them; a cut on the minimum distance (< 1 cm) is applied;

---

[1] V^0 is a secondary vertex due to γ conversion or K^0 or Λ decay, with no incoming and two outgoing oppositely charged tracks.

MC sample	$e^\pm$ # tracks	ϵ, %	$\pi^\pm$, $K^\pm$ # tracks	ϵ, %	protons # tracks	ϵ, %	**Purity,** %
TRD identification of isolated tracks							
ν_μ CC	53 019	25.8	13 888	2.6	10 865	9.3	68.2
ν_μ NC	224 753	26.9	57 056	3.0	46 022	10.1	68.6
ν_e CC	351 060	42.5	37 609	4.3	22 628	10.1	85.4
TRD identification of non-isolated tracks							
ν_μ CC	50 352	95.0	9 207	66.3	9 952	91.6	72.4
ν_μ NC	213 602	95.0	37 307	65.4	42 440	92.2	72.8
ν_e CC	341 172	97.2	25 648	68.2	20 428	90.3	88.1
TRD truncated identification of non-isolated tracks							
ν_μ CC	49 127	97.6	7 482	81.3	9 409	94.5	74.4
ν_μ NC	208 147	97.4	29 433	78.9	40 200	94.7	74.9
ν_e CC	334 013	97.9	20 542	80.1	19 012	93.1	89.4
DC – ECAL match							
ν_μ CC	42 409	86.3	5 853	78.2	1 247	13.3	85.7
ν_μ NC	179 104	86.0	23 885	81.1	5 051	12.6	86.1
ν_e CC	299 247	89.6	16 565	80.6	3 396	17.9	93.7
PRS – ECAL π rejection							
ν_μ CC	35 876	84.6	2 334	39.9	517	41.5	92.6
ν_μ NC	152 705	85.3	9 409	39.4	2 183	43.2	92.9
ν_e CC	272 326	91.0	7 094	42.8	1 521	44.8	96.9
Consistency between electron momentum and energy							
ν_μ CC	27 978	78.0	729	31.2	149	28.9	97.0
ν_μ NC	117 264	76.8	2 966	31.5	573	26.3	97.1
ν_e CC	198 595	72.9	2 258	31.8	407	26.8	98.7
DC – HCAL match							
ν_μ CC	27 752	99.2	594	81.5	131	88.2	97.4
ν_μ NC	116 273	99.2	2 393	80.7	471	82.2	97.6
ν_e CC	196 472	98.9	1 824	80.8	333	81.8	98.9

Table 6.12: Summary of electron identification performance estimated from Monte Carlo simulation. The absolute and relative number of $e^\pm$, $\pi^\pm$+$K^\pm$ and protons identified as electrons at the different stages of the selection is shown for the ν_μ CC, ν_μ NC and ν_e CC Monte Carlo events. The purity of the samples defined as $N_{e^\pm}/N_{\text{total}}$ is also given.

- The cut on the coplanarity *copl* is imposed:

$$copl = \frac{([\vec{p}_1^{\,f} \times \vec{p}_2^{\,f}] \cdot \vec{n}_y)}{|\vec{p}_1^{\,f}| \cdot |\vec{p}_2^{\,f}|} < 0.3 \tag{6.1}$$

  where $\vec{p}_1^{\,f}$, $\vec{p}_2^{\,f}$ are the final momenta of the candidates, $\vec{n}_y$ is a unit vector along the y-axis. The coplanarity cut is motivated by the fact that e^+e^- tracks originating from the photon conversion are produced with zero opening angle and, affected only by magnetic field, should lie in the vertical plane (neglecting multiple scattering effects). Thus, a coplanarity distribution for conversion pairs is peaked at zero, whereas for random pairs it is essentially flat.

- The invariant mass of the pair, taken to be a e^+e^-, should be less than 100 MeV/c^2.

If all three above-mentioned conditions are fulfilled, the pair of tracks is tagged as a photon conversion and removed from the list of prompt electron (positron) candidates. If no other electron (positron) remains in the event, it is rejected. The efficiency of the photon conversion rejection is shown in Table 6.13.

	ν_μ CC	ν_μ NC	ν_e CC	$\bar{\nu}_e$ CC	1995 data	1996 data
# events	7 549	30 658	121 444	66 447	9 251	17 905
ϵ, %	37.5	37.3	87.1	89.0	55.3	51.9

Table 6.13: ν_e CC and $\bar{\nu}_e$ CC selection: rejection of conversion pairs.

The cuts described above can reject neither asymmetric conversions nor those with one of the tracks not reconstructed. To further reduce conversion background, the distance between the reconstructed primary vertex and the first hit of the track of a e$^\pm$ candidate is required to be less than 15 cm. Again, if there are no electron candidates left satisfying this condition, the event is rejected (see Table 6.14).

	ν_μ CC	ν_μ NC	ν_e CC	$\bar{\nu}_e$ CC	1995 data	1996 data
# events	931	3 418	104 175	58 297	2 557	4 718
ϵ, %	12.3	11.1	85.8	87.7	27.6	26.3

Table 6.14: ν_e CC and $\bar{\nu}_e$ CC selection: cut on a distance from the primary vertex.

Due to the changes in the curvature caused by emission of bremsstrahlung photons, an electron track could be reconstructed in several pieces (segments). In this case, only the downstream-most segment of a track (reaching TRD, PRS and ECAL) could be tagged as an electron. Such events could then be rejected by the distance cut. To increase the selection efficiency, a merging algorithm is applied recursively to each electron track segment before the distance cut is imposed. The criteria for the merging depend on the vertex type of the segment and are based on the distance between the first and the last hits of the two segments and the difference in their angles and momenta. When the criteria of the algorithm are met, two segments are considered to be pieces of the same electron track. This procedure increases the efficiency of the distance cut for ν_e CC events by about 40%.

To keep the selection of $\overset{(-)}{\nu_e}$ CC and $\overset{(-)}{\nu_\mu}$ CC interactions as similar as possible, identical conversion rejection and distance cuts are also applied to $\mu^\pm$ candidates. The conversion rejection criteria leave $\mu^\pm$ data and Monte Carlo samples practically intact. The effect of the distance cut on $\overset{(-)}{\nu_\mu}$ CC selection is shown in Table 6.15.

	ν_μ CC	$\bar{\nu}_\mu$ CC	ν_μ NC	1995 data	1996 data
# events	584 732	95 339	5 067	133 714	272 706
ϵ, %	83.6	84.0	66.5	78.0	80.9

Table 6.15: ν_μ CC and $\bar{\nu}_\mu$ CC selection: cut on a distance from the primary vertex.

6.3.4 Choice of a prompt electron

In about 2% of both $\overset{(-)}{\nu_e}$ CC Monte Carlo and data events which passed the electron identification and conversion rejection cuts, there is more than one electron (positron) candidate. Three ways to choose the prompt $e^\pm$ among the candidates were studied on a ν_e CC Monte Carlo sample:

- the one with the largest initial momentum p_{ini};
- the one closest to the reconstructed primary vertex;
- the one with the largest transverse momentum p_T.

The largest p_T hypothesis was found to give better results than the two others (in ~93% of the events the prompt electron was correctly chosen compared to 85% for the largest p_{ini} and 63% for closest electron). Afterwards, all electrons (positrons) save the one with the largest p_T are ascribed either to the hadron jet or to a bremsstrahlung photon conversion (see Sec. 6.4.1).

An additional conversion rejection test is performed after the prompt lepton has been chosen. Its minimum coplanarity partner is selected from any $e^\pm$ or any other track of opposite charge sign to which the TRD identification procedure was not applied. Then, the two-dimensional cut on the distance between the first hits of the two tracks and their invariant mass (taken to be a e^+e^-) is imposed. The effect of this cut on Monte Carlo and data samples is shown in Table 6.16.

6.4 Energy flow algorithm

The remaining non-prompt background in both e^- and μ^- samples can be further suppressed by imposing the kinematical cuts, which require the reconstruction of the event

	ν_μ CC	ν_μ NC	ν_e CC	$\bar{\nu}_e$ CC	1995 data	1996 data
# events	575	1 816	101 190	56 757	2 027	3 858
ϵ, %	61.8	53.1	97.1	97.4	79.3	81.2

Table 6.16: ν_e CC and $\bar{\nu}_e$ CC selection: conversion test on prompt lepton.

kinematics. Furthermore, the $\nu_\mu \to \nu_e$ oscillation search in NOMAD is conducted by comparing the observed and predicted ratios of ν_e/ν_μ events as a function of the neutrino energy. The incident neutrino energy is not known on an event by event basis and in charged current events is approximated by a so-called "total visible energy", which is defined as the sum of the energies of the charged lepton and of the observed hadrons in the final state.[1] In this section we describe the algorithms developed for the reconstruction of the leptonic and the hadronic energy components of the total visible energy of the event.

6.4.1 Estimation of lepton energy

The energy and the direction of a muon is estimated using the fitted track momentum at the first hit. The momentum resolution is limited by multiple scattering and the single-hit resolution of the drift chambers, and is a function of the particle momentum and track length (cf. Sec. 3.4.3). The momentum resolution $\delta P/P = (P_{Rec} - P_{MC})/P_{MC}$ of prompt muons in ν_μ CC Monte Carlo simulated interactions is shown in Fig. 6.3 (left). The muon momentum measurement in the drift chambers in the absence of alignment errors is unbiased; its precision is typically 3% for momenta below 20 GeV/c (where the error is dominated by multiple scattering) and slowly worsens for larger momenta. The muon momentum resolution in the data has additional contributions from systematic uncertainties in the drift chamber alignment and in the knowledge of the magnetic field.

For electrons, however, the energy resolution obtained in this way is poor and has long tails due to the large fluctuations in the energy losses from bremsstrahlung photon emission. The electron energy resolution can be significantly improved by using calorimetric measurements, which are sensitive to the bremsstrahlung photons emitted in the showering process of the electron. The so-called "bremsstrahlung strip" algorithm has been developed [101] for this purpose. It proceeds as follows:

- the energy of the nonet (nine ECAL cells) built around the impact point of the electron candidate on ECAL is used as an initial estimate of the electron energy E_e;
- the (vertical) bremsstrahlung volume of the electron candidate is identified by linearly extrapolating the track momentum vector at the first hit of the track to the

---

[1] This approximation is not valid for neutrino-nucleon neutral current interactions (background to both $\overset{(-)}{\nu_e}$ CC and $\overset{(-)}{\nu_\mu}$ CC selections), where the escaping neutrino carries away a fraction of the energy of the incident neutrino.

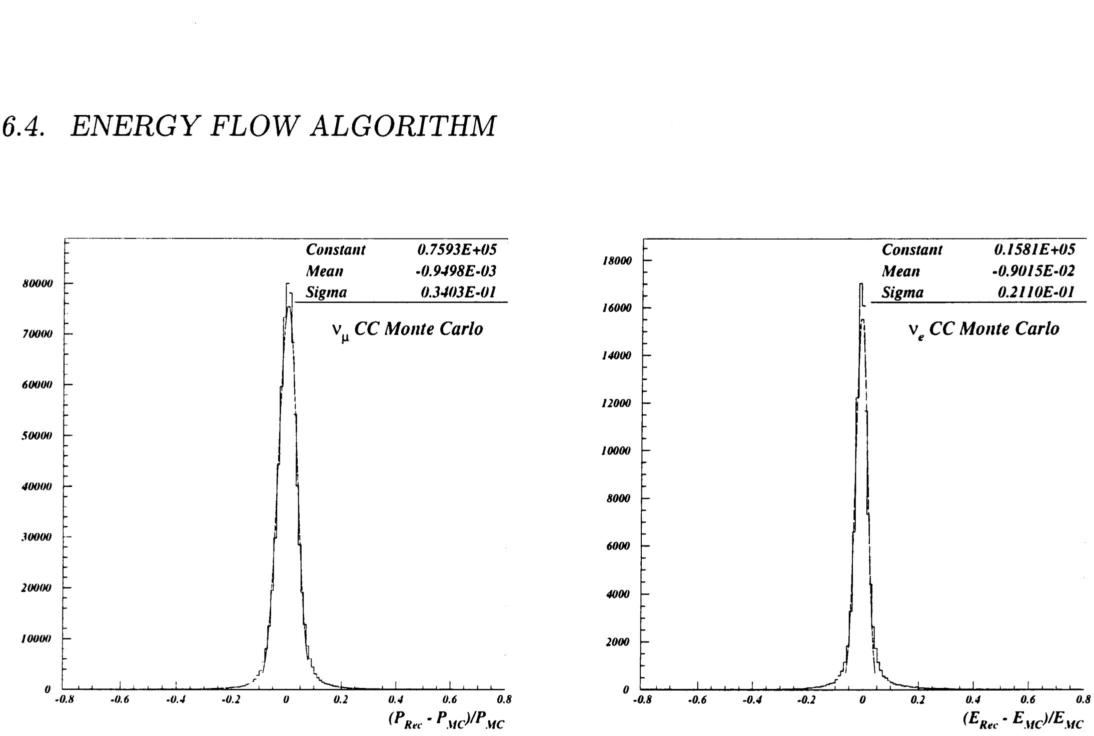

Figure 6.3: Left: momentum resolution of identified prompt muons in ν_μ CC Monte Carlo simulated interactions. Right: energy resolution of identified prompt electrons in ν_e CC Monte Carlo simulated interactions.

ECAL; the energy of the photons[1] located between this point and the impact point of the electron candidate is added to the energy E_e;

- The ECAL associated energy of the gammas[2] converted in the bremsstrahlung volume of the electron candidate is added; in case of overlaps in the ECAL the common cells are not double-counted.

Appropriate impact angle, non-linearity and PRS corrections determined during the calibration runs of the ECAL [101, 102] are applied to the ECAL energy. The performance of the algorithm is much superior to the fitted DC track momentum estimate, reducing both the reconstruction bias and the resolution tails.

The bremsstrahlung strip algorithm described in [101] was used whenever available ($\sim$98% of ν_e CC Monte Carlo events); a simplified version with slightly worse performance was used otherwise. The energy resolution, $\delta E/E = (E_{Rec} - E_{MC})/E_{MC}$, obtained for prompt electrons in ν_e CC Monte Carlo interactions is shown in Fig. 6.3 (right). The bias between the reconstructed (E_{Rec}) and generated (E_{MC}) energy is less than 1%; the Gaussian resolution is about 2% and is 60% better than that of muons.

Although the ECAL energy is used to compute the modulus of the electron momentum, the direction of the electron is determined from the fitted momentum of its track as measured by the drift chambers.

---

[1] neutral ECAL objects built around local maxima in the calorimeter after suppression of energy associated to tracks.

[2] photons converted in the drift chamber volume; one and two prongs are allowed.

In order to eliminate from consideration the mismeasured electrons with bremsstrahlung photons potentially escaping detection, we require that the initial and final directions of the electron track linearly extrapolated to the z-coordinate of the ECAL front face are both contained within the ECAL active volume. This mandatory "quality cut" leads to $\sim$4% loss in the efficiency of ν_e CC selection. To keep geometrical acceptancy of ν_e CC and ν_μ CC events as similar as possible, the same requirement (yielding a very similar efficiency) is also imposed on ν_μ CC candidates.

6.4.2 Estimation of hadronic energy

The reconstruction of the hadronic energy is performed in two steps:

- All drift chamber tracks, neutral electromagnetic clusters and hadronic calorimeter clusters reconstructed in the event are classified into so-called particle objects (PO) [103] and the momentum vector of each PO in the neutrino beam frame[1] is computed. The momentum of a track reconstructed by the drift chambers is defined as its parameters at the first hit, while for electromagnetic and hadronic clusters the momentum components are computed assuming that they originated from the primary vertex.
- A decision on which sub-sample of PO objects should be included in the computation of the hadron momentum vector is made according to an algorithm which was optimized with the Monte Carlo simulation.

In the first step, all reconstructed objects are classified into different PO categories (having a rough correspondance with physical objects) in the following way:

- A primary track is called *Charged* if not identified as a lepton, *Muon* if matched to the muon chambers and *Electron* if identified by the TRD.
- The PO type of a track originating from a secondary vertex is assigned according to its vertex type. It is called *NeutralInteract, Scatter, Conversion* or *Decay* depending on the number of the incoming and outgoing tracks in the vertex to which it is attached. A single (hanging) track is called *CloseAsymConversion* if the distance between the z-coordinate of its first hit and the primary vertex is less than 25 cm and *FarAsymConversion* otherwise. All secondary vertex tracks are called *Secondary-Muon* if matched to the muon chambers and *SecondaryElectron* if identified by the TRD.
- If the track has less than 12 hits, it is labeled *ShortCharged.*
- All tracks with a reconstructed momentum greater than 500 GeV/c are labeled *Ghosts.*
- Electromagnetic clusters with no associated charged track are called *Neutrals.*

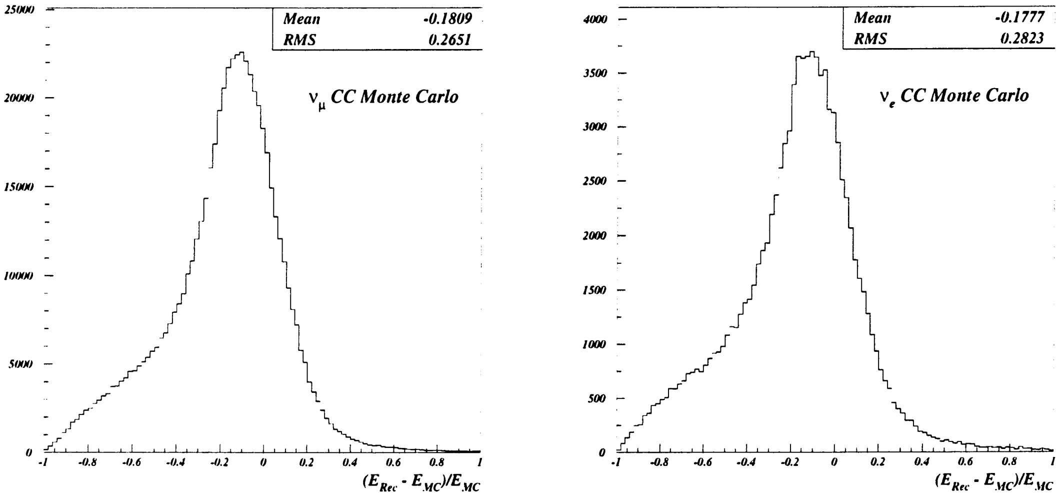

Figure 6.4: Hadronic energy resolution $\delta E^h/E^h = (E^h_{Rec} - E^h_{MC})/E^h_{MC}$ in ν_μ CC (left) and ν_e CC (right) Monte Carlo simulated interactions.

In the second step, a loop over POs is performed and the PO tags are used to make a decision on the inclusion of each PO in the computation of the total hadronic momentum:

- All *Charged*, *Muons* and *Electrons* are used.
- *NeutralInteracts* and *Conversions* are used regardless whether they point or not to the primary vertex. However, it was found necessary to apply an additional veto against the interactions of charged tracks whose products are not attached to their parent track by the vertex reconstruction package. The veto is performed by searching for the track whose last hit is closest to the *NeutralInteract* vertex. If the last hit on this track satisfies dr < 20 cm and $|dz|$ < 20 cm (with $p_z > 0$) criteria, the *NeutralInteract* is re-labeled *Scatter*.
- *Scatters* and *Decays* are used only if their parent tracks are not used. This can occur, e.g., if the parent track is classified as *ShortCharged* and its momentum measurement is unreliable. In such cases the vector sum of all the daughter tracks is used instead.
- *AsymConversions* are included depending on the result of a linear extrapolation (using the error matrix propagation) of the track to the z-plane of the primary vertex. The *AsymConversion* is used if there is a good match between the extrapolated track and the primary vertex in the transverse plane (dr < 8 cm) or if a tight match is obtained in y with a looser constraint in x ($|dy|$ < 2 cm and $|dx|$ < 20 cm).
- *ShortCharged* and *Ghosts* are ignored.

---

[1] The neutrino beam line points upwards, at an angle of 2.4° to the z-axis of the detector [104].

- All *Neutrals* with energy greater than 100 MeV are used. The TDC timing flag of each *Neutral* is also checked. If all the energy of the cluster is not associated to the triggered event, the *Neutral* is ignored.

- All POs already used in the lepton energy calculation by the bremsstrahlung strip algorithm (see Sec. 6.4.1) are ignored.

- HCAL clusters are only used for vetoing purposes. An undetected energetic neutral hadron (e.g., neutron or K_L^0) could spoil a measurement of the energy of the hadronic jet and, consequently, that of the total visible energy of the event, in particular, in the plane transverse to the incident neutrino direction. Since HCAL measurements do not have good energy or spatial resolution, we have chosen to use them as a veto for both $\mu^\pm$ and $e^\pm$ samples. If the total neutral (not associated to extrapolated charged tracks) energy deposited in the HCAL exceeds 5 GeV, the event is rejected. The efficiency of this cut on Monte Carlo and data samples in the selection of ν_e CC candidates is shown in Table 6.17.

	ν_μ CC	ν_μ NC	ν_e CC	$\bar{\nu}_e$ CC	1995 data	1996 data
# events	465	1 461	93 707	53 476	1 804	3 477
ϵ, %	80.9	80.4	92.6	94.2	89.0	90.1

Table 6.17: ν_e CC and $\bar{\nu}_e$ CC selection: efficiency of HCAL veto.

The hadronic energy is computed as the sum of momenta of all the POs included in the calculations. The obtained hadronic energy resolution $\delta E^h/E^h = (E^h_{Rec} - E^h_{MC})/E^h_{MC}$ in ν_μ CC and ν_e CC Monte Carlo events is shown in Fig. 6.4. The fractional difference between the reconstructed (E^h_{Rec}) and generated (E^h_{MC}) energy is ~18% for both samples; the obtained resolutions are also similar for the ν_μ CC and ν_e CC interactions.

The reconstruction of the total visible energy and its uncertainty is further discussed in Sec. 7.7.4.

6.5 Kinematic cuts

The prompt lepton, $\mu^\pm$ or $e^\pm$, in a deep inelastic ν-induced charged current interaction is usually kinematically isolated from the hadronic jet comprising all other particles. This lepton will have a large transverse momentum q_{lep} with respect to the hadron jet (typically above 1 GeV/c in NOMAD) and it will balance the component of the hadron momentum in the plane transverse to the neutrino beam direction. On the other hand, since hadrons are produced in the fragmentation of the hit quark and the nucleon remnants, non-prompt background leptons (such as electrons originating from photon conversions or muons from π/K decays) will have a small q_{lep} value (typically less than ~1 GeV/c) and will not balance the transverse momentum of the rest of the jet.

At the final stage of the event selection kinematic cuts are imposed, with the aim of using the prompt lepton's isolation from the hadron jet to reduce the non-prompt background. The variables used for the kinematic selection are:

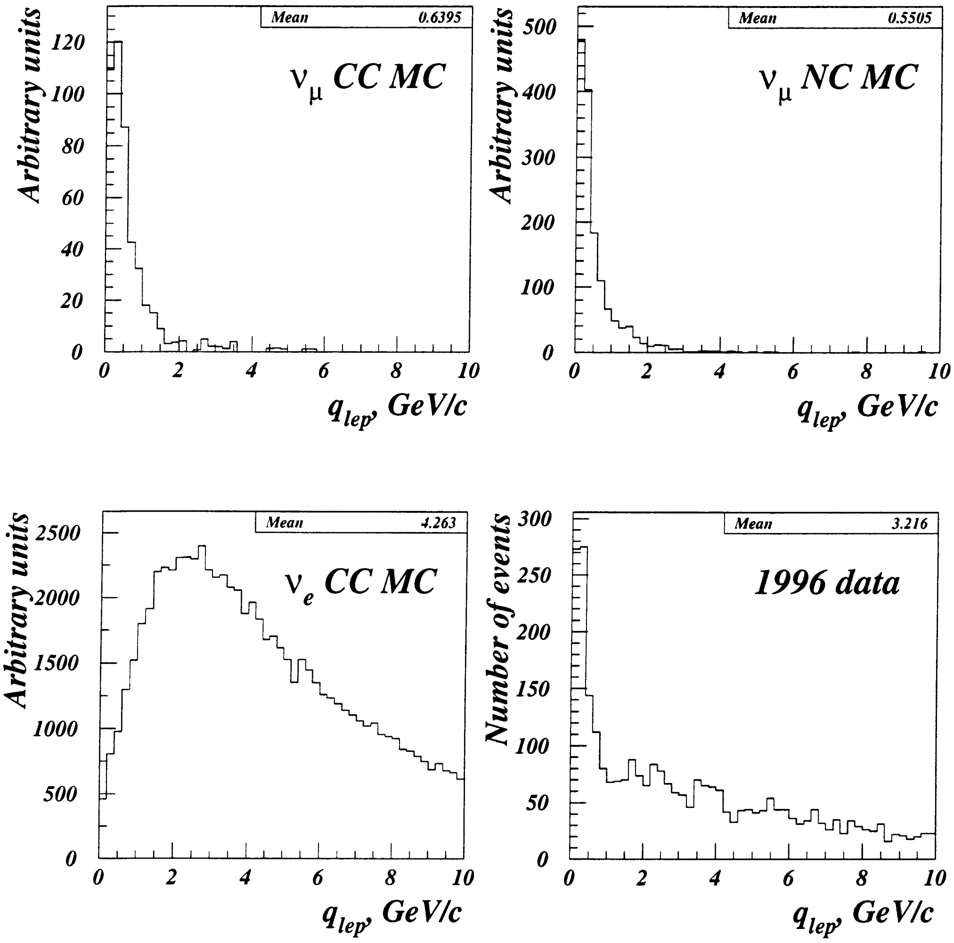

Figure 6.5: The q_{lep} distributions in the selection of ν_e CC candidates, for the ν_μ CC, ν_μ NC (both background), ν_e CC (signal) Monte Carlo and 1996 data events, after electron identification and conversion rejection criteria.

- q_{lep}: the component of lepton momentum $\vec{p}_{lep}$ transverse to the hadron jet direction.[1] The q_{lep} distributions for the MC samples and 1996 data after applying the ν_e CC candidate selection criteria (electron identification and conversion rejection) are shown in Fig. 6.5. The q_{lep} distribution for the data displays two components: a peak at low values due to ν_μ-induced non-prompt background and a long tail due to isolated electrons from ν_e CC interactions.

- ϕ^t_{lh}: the azimuthal angle between the lepton and the hadron jet vectors in the plane

---

[1] Note that the q_{lep} cut implicitly imposes a cut on the lepton momentum of at least the value of q_{lep}.

perpendicular to the incident neutrino direction. The distribution of $\phi^t_{lh} \times q_l$ for ν_μ NC Monte Carlo events is centered at zero (Fig. 6.6) as the sample is dominated by electrons and positrons originating from conversions and imbedded into hadron jet. In contrast, in ν_e CC MC events the $\phi^t_{lh} \times q_l$ distribution peaks at $-\pi$, as the prompt electron's p_T balances that of the hadron jet. The $\phi^t_{lh} \times q_l$ distribution in data clearly shows two main components: conversions from ν_μ NC interactions, symmetrically positioned around zero, and prompt $e^\pm$ from $\overset{(-)}{\nu_e}$ CC interactions, peaked at $\pm\pi$.

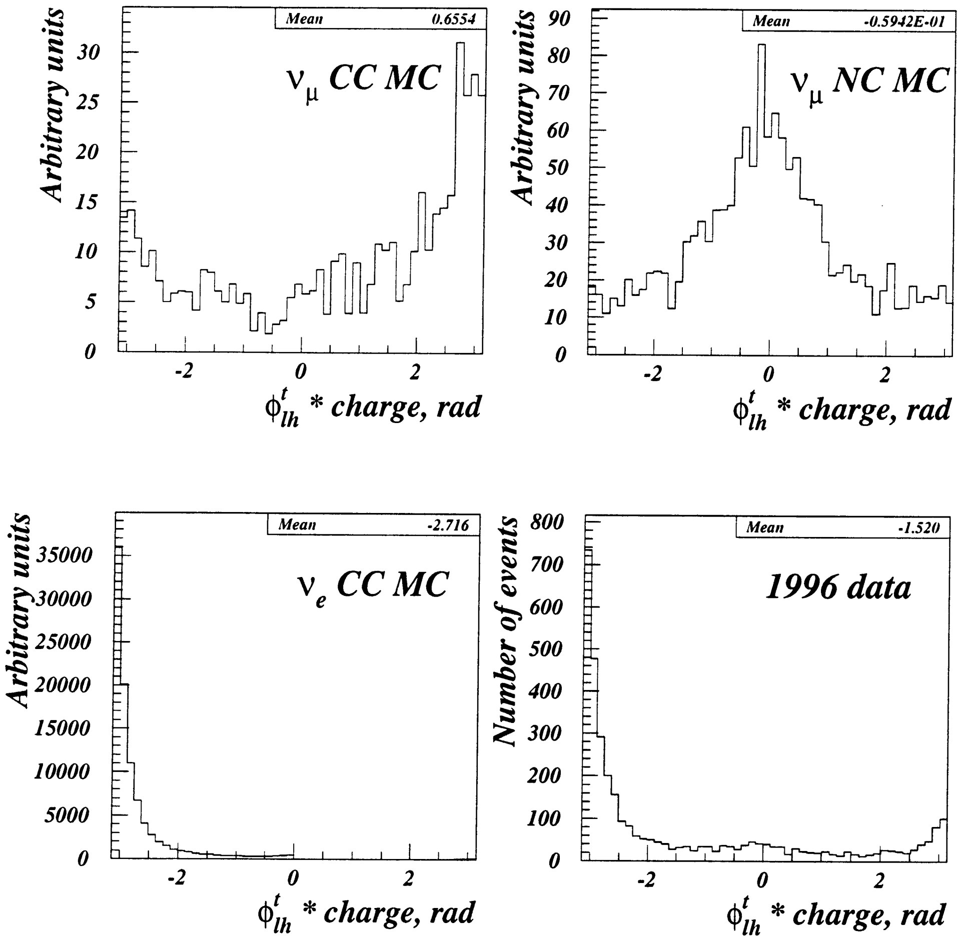

Figure 6.6: The ϕ^t_{lh} distributions, signed by the charge q_l of the prompt electron, for the ν_μ CC, ν_μ NC, ν_e CC Monte Carlo and 1996 data events after application of the electron identification and conversion rejection criteria.

If we first impose a q_{lep} cut (e.g. $q_{lep} > 1.6$ GeV/c), a cut on ϕ^t_{lh} still remains efficient against ν_μ NC background. The requirement $\phi^t_{lh} > \pi/2$, e.g., reduces ν_μ NC background by more than a factor of two while retaining more than 95% of the signal. In practice, we apply a correlated two-dimensional cut in a $q_{lep} - \phi^t_{lh}$ plane, with the parametrization chosen as

$$\phi^t_{lh} > \frac{1\ (\mathrm{GeV}/c)^2}{(q_{lep} - q^0_{lep})^2} + \phi^0_{lh} \quad [\mathrm{rad}]. \tag{6.2}$$

The parameters $q^0_{lep} = 0.1$ GeV/c and $\phi^0_{lh} = 1.9$ were chosen by maximizing the ratio of the signal to the sum of the signal and the expected non-prompt background.

The ϕ^t_{lh} versus q_{lep} distributions and the 2D isolation cut are shown in Fig. 6.7, for the MC samples and 1996 data passing the ν_e CC candidate selection criteria. Identical kinematic cuts are imposed on the $\mu^\pm$ and $e^\pm$ samples. The efficiency of the kinematic cut for $\overset{(-)}{\nu_e}$ CC and $\overset{(-)}{\nu_\mu}$ CC selections is given in Tables 6.18 and 6.19.

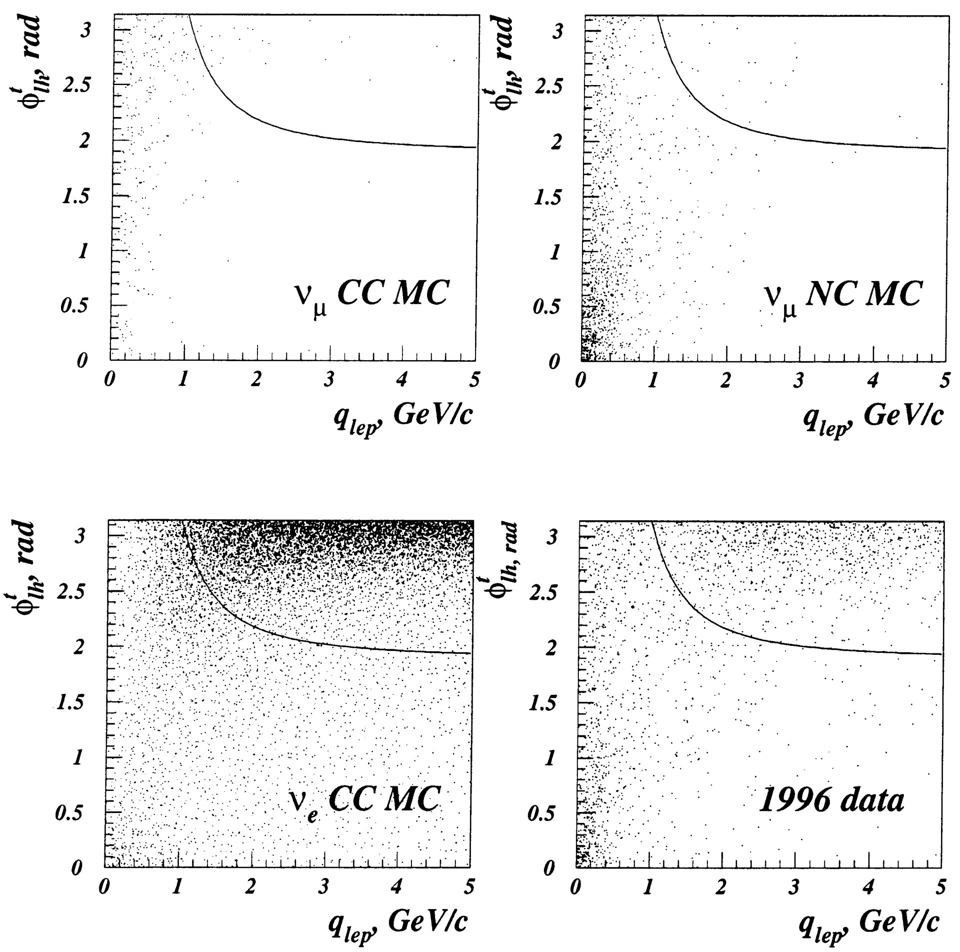

Figure 6.7: The ϕ^t_{lh} (vertical axis) versus q_{lep} (horizontal axis), for the ν_μ CC, ν_μ NC, ν_e CC Monte Carlo and 1996 data events passing the electron identification and conversion rejection criteria. The region selected by the two-dimensional kinematic cut lies to the right of the curve.

In the analysis presented below we use only the deep inelastic neutrino-nucleon interactions. The inclusion of the quasielastic (QE) and resonance (RES) events to the $\nu_\mu \to \nu_e$

	ν_μ CC	ν_μ NC	ν_e CC	$\bar{\nu}_e$ CC	1995 data	1996 data
# events	45	43	81 469	44 487	1 080	2 212
ϵ, %	9.8	2.9	86.9	83.2	59.9	63.6

Table 6.18: ν_e CC and $\bar{\nu}_e$ CC selection: efficiency of kinematic cut.

	ν_μ CC	$\bar{\nu}_\mu$ CC	ν_μ NC	1995 data	1996 data
# events	460 441	72 391	181	94 631	201 442
ϵ, %	78.7	75.9	3.6	70.8	73.9

Table 6.19: ν_μ CC and $\bar{\nu}_\mu$ CC selection: efficiency of kinematic cut.

oscillation search requires an optimization of the selection criteria for low multiplicity and low hadronic energy events, as well as a dedicated simulation of the quasielastic neutrino interactions and resonance production. The work on the QE and RES event generator is in progress at the time of completing this paper [105], making possible the use of the quasielastic and resonance events for the $\nu_\mu \to \nu_e$ oscillation search in the future. In this analysis, however, the QE and RES components of the selected data samples are removed by imposing the cuts on the reconstructed values of an energy transfer $\nu > 1.5$ GeV and momentum transfer $Q^2 > 0.5$ GeV$^2/c^2$. These cuts remove ~11% of events in the μ^- and e^- data samples.

6.6 Signal efficiency and background rejection

The performance of the $\overset{(-)}{\nu_e}$ CC DIS event selection algorithm is shown in Tables 6.20 and 6.21 for the Monte Carlo and data samples. The $e^\pm$ data sample consists of 880 (1 780) electron and 93 (203) positron candidates found in 1995 (1996) data. An energy-averaged ν_e CC selection efficiency of 32% (estimated on Monte Carlo simulated sample) is obtained, while reducing the non-prompt background by $0.7 \cdot 10^{-5}$ for ν_μ CC and by $2.6 \cdot 10^{-5}$ for ν_μ NC samples.[1]

The performance of the $\overset{(-)}{\nu_\mu}$ CC event selection using event quality and kinematical criteria identical to those used for $\overset{(-)}{\nu_e}$ CC selection is shown in Table 6.22 for the Monte Carlo and data samples. The $\mu^\pm$ data sample consists of 81 138 (171 781) μ^- and 1 816 (3 983) μ^+ candidates in 1995 (1996) data respectively. The average ν_μ CC selection efficiency is ~45% with a negligible background.

The event selection efficiency as a function of the simulated (true) neutrino energy is shown in Fig. 6.8 for the ν_e CC (left) and ν_μ CC (right) Monte Carlo samples.

Having selected the $e^\pm$ and $\mu^\pm$ samples – candidates for the $\overset{(-)}{\nu_e}$ CC and $\overset{(-)}{\nu_\mu}$ CC DIS

---

[1] All quoted selection and rejection efficiencies are computed here with respect to the number of events generated in the fiducial area of 260 × 260 × 400 cm^3, representing the complete detector configuration.

Summary of $\overset{(-)}{\nu_e}$ CC selection: MC signal and backgrounds				
	ν_μ CC	ν_μ NC	ν_e CC	$\bar{\nu}_e$ CC
Initial	889 446	582 470	228 980	127 500
e^-	6 **(0.7±0.3)·10^{-5}**	15 **(2.6±0.7)·10^{-5}**	74 182 **(32.4±0.1)%**	114 (8.9±0.8)·10^{-4}
e^+	28 (3.1±0.6)·10^{-5}	16 (2.7±0.7)·10^{-5}	234 (1.0±0.1)·10^{-3}	37 624 **(29.5±0.1)%**

Table 6.20: Summary of $\overset{(-)}{\nu_e}$ CC Monte Carlo selection efficiency and background rejection. The number of Monte Carlo events generated in the fiducial volume, number of selected negative and positive candidates and the average efficiency of the selection are shown for the ν_μ CC, ν_μ NC, ν_e CC and $\bar{\nu}_e$ CC Monte Carlo samples.

Summary of $\overset{(-)}{\nu_e}$ CC selection		
	1995 data	1996 data
Initial	341 222	605 571
e^-	**880**	**1 780**
e^+	**93**	**203**

Table 6.21: Summary of $\overset{(-)}{\nu_e}$ CC selection in 1995 and 1996 data. The number of events reconstructed in the fiducial volume of the detector (after event quality cuts) and the number of negative and positive candidates selected in 1995 and 1996 data are shown.

events – we now proceed to the estimation of the non-prompt background components of the samples and to the comparison of the data with the Monte Carlo predictions.

Summary of $\overset{(-)}{\nu}_\mu$ CC selection: signal and background					
	ν_μ CC MC	$\bar{\nu}_\mu$ CC MC	ν_μ NC MC	1995 data	1996 data
Initial	889 446	152 243	582 470	341 222	605 571
μ^-	403 515 **(45.4±0.1)%**	30 **(2.0±0.4)·10^{-4}**	52 **(8.9±1.2)·10^{-5}**	**81 138**	**171 781**
μ^+	324 (3.6±0.2)·10^{-4}	58 247 **(38.3±0.1)%**	48 **(8.2±1.2)·10^{-5}**	**1 816**	**3 983**

Table 6.22: Summary of $\overset{(-)}{\nu}_\mu$ CC selection efficiency and background rejection. For the ν_μ CC, $\bar{\nu}_\mu$ CC and ν_μ NC Monte Carlo samples, the numbers shown are: events generated in the fiducial volume, selected negative and positive candidates and the average efficiency of the selection. For 1995 and 1996 data, the number of events reconstructed in the fiducial volume of the detector (after event quality cuts) and the number of selected negative and positive candidates are given.

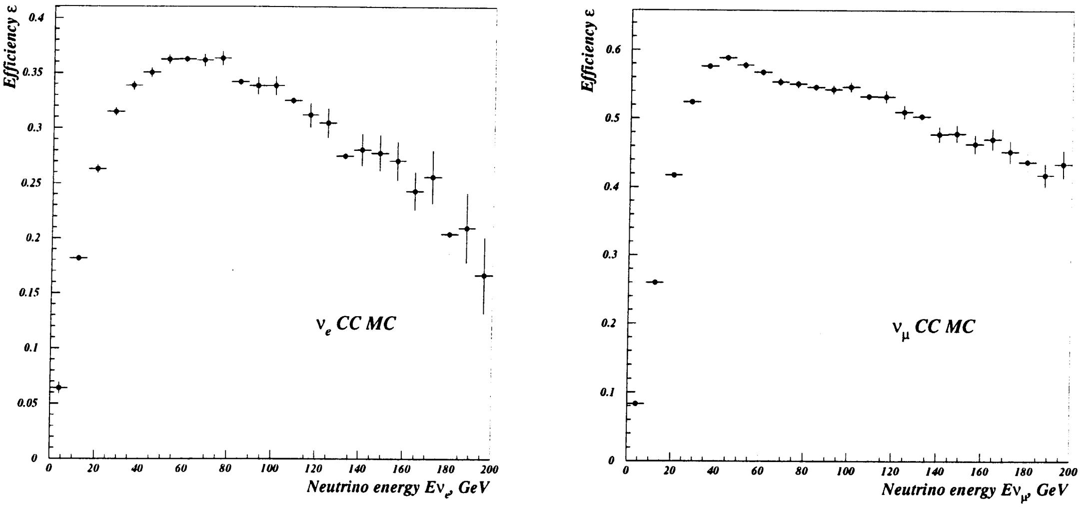

Figure 6.8: Event selection efficiency as a function of the simulated (true) neutrino energy E_ν for the ν_e CC (left) and ν_μ CC (right) Monte Carlo samples.

Chapter 7

Search for $\nu_\mu \rightarrow \nu_e$ oscillations

7.1 The non-prompt background estimates

Let us recall that the $\nu_\mu \rightarrow \nu_e$ oscillation signal would appear as an excess of events in the e^- sample above the predicted background, which consists of 1) prompt electrons from beam ν_e-induced CC events and 2) non-prompt electrons and misidentified hadrons mainly from ν_μ neutral current and charged current interactions. In order to compare data with Monte Carlo predictions, we treat these two background sources separately, estimating the non-prompt background contributions with the help of the Monte Carlo simulation, and adding them appropriately to the prompt ν_e component predicted by the primordial beam simulation packages.

The following algorithm was used for the estimation of non-prompt background contributions:

1. We define the efficiency of ν_μ CC selection as

   $$\varepsilon_{\nu_\mu CC}(E_\nu, E_{vis}) = \frac{N_{MC}^{sel}(E_{vis})}{N_{MC}^{sim}(E_\nu)} \tag{7.1}$$

   where

   - $N_{MC}^{sel}(E_{vis})$ is the number of ν_μ CC Monte Carlo simulated events passing the ν_μ CC selection criteria as a function of the total visible energy E_{vis}.
   - $N_{MC}^{sim}(E_\nu)$ is the number of ν_μ CC Monte Carlo simulated events as a function of the true neutrino energy E_ν.

   Such a definition of the efficiency allows one to account for both the instrumental and selection acceptance and the distortion (smearing) of the neutrino energy due to the finite energy resolution [106].

2. After the kinematic cuts, the non-prompt background contribution to the μ^- sample is negligible (well below 1% level). The unfolded number of ν_μ CC interactions[1]

---

[1] i.e. the number of ν_μ CC interactions which would be observed at 100% selection efficiency.

can be then estimated from the observed number of μ^- events and the Monte Carlo efficiency of ν_μ CC selection using the method of correction factors described in [106]:

$$N^{unf}_{\nu_\mu CC}(E_\nu) = \frac{N^{obs}_{\mu^-}(E_{vis})}{\varepsilon_{\nu_\mu CC}(E_\nu, E_{vis})} \tag{7.2}$$

The number of observed and unfolded ν_μ CC interactions in the 1995 and 1996 data integrated over E_{vis} is shown in Table 7.1. The unfolded number of ν_μ CC events for different target configurations gives an absolute normalization for the background prediction.

The number of observed and unfolded $\overset{(-)}{\nu_\mu}$ CC interactions								
Data sample		ν_μ CC selection			$\bar{\nu}_\mu$ CC selection			
	BCT, p.o.t.	$N^{obs}_{\mu^-}$	ε,%	$N^{unf}_{\nu_\mu CC}$	$N^{obs}_{\mu^+}$	$N^{bckg}_{\mu^+}$	ε,%	$N^{unf}_{\bar{\nu}_\mu CC}$
4 mod	$2.4 \cdot 10^{18}$	11 413	48.3	23 756	290	16	40.0	650
8 mod	$3.1 \cdot 10^{18}$	29 483	47.2	62 704	665	29	39.5	1 686
11 mod	$3.1 \cdot 10^{18}$	40 242	45.4	88 716	861	40	38.3	2 212
1996	$1.3 \cdot 10^{19}$	171 781	45.4	378 943	3 983	155	38.3	10 041

Table 7.1: Summary of ν_μ CC and $\bar{\nu}_\mu$ CC event selection. For each target configuration, the number of observed events N^{obs}_μ, the average selection efficiency ε and the corresponding number of unfolded events $N^{unf}_{\nu CC}$ are given for the ν_μ CC and $\bar{\nu}_\mu$ CC candidates. The exposure measured in protons on target (p.o.t.) by the BCT is quoted for each data taking period. For the μ^+ sample, the total number of expected non-prompt background events $N^{bckg}_{\mu^+}$ from ν_μ CC and ν_μ NC interactions is also shown.

3. The contributions from different sources to the non-prompt background are then obtained by scaling the unfolded number of ν_μ CC events by the Monte Carlo estimated efficiencies of the background rejection computed identically to Eq. (7.1).

The expected number of non-prompt background events for e^- and e^+ samples is shown in Table 7.2. As the acceptance of the prompt and the non-prompt electron backgrounds strongly depends on the z-coordinate of the primary vertex, the selection efficiencies (and, consequently, the estimations of the expected background and signal) are computed separately for the different target configurations, namely for 4, 8 and 11 module data taking periods of 1995 and for the 1996 data. For the estimations of the ν_μ NC background the factor 0.31 for the $\sigma_{\nu_\mu NC}/\sigma_{\nu_\mu CC}$ ratio is used, while the ratio of $\sigma_{\bar{\nu} CC}/\sigma_{\nu CC} = 0.50$ is used to estimate the antineutrino background.

Two sources contribute to both the e^- and e^+ non-prompt backgrounds: ν_μ NC events and ν_μ CC events where the muon escaped detection. The neutral current background is charge symmetric, while the ν_μ CC background for the e^+ sample exceeds that for the

Expected number of background events in $e^{\pm}$ samples					
	Data taking	ν_μ CC	ν_μ NC	ν_e CC	$\bar{\nu}_e$ CC
e$^-$	4 mod	0.3 ± 0.1	0.2 ± 0.1	-	0.0 ± 0.0
	8 mod	0.6 ± 0.2	0.6 ± 0.2	-	0.1 ± 0.0
	11 mod	0.7 ± 0.2	0.7 ± 0.2	-	0.1 ± 0.0
	1996	3.0 ± 1.0	3.0 ± 0.7	-	0.3 ± 0.0
e$^+$	4 mod	1.0 ± 0.3	0.3 ± 0.1	0.6 ± 0.1	-
	8 mod	2.5 ± 0.5	0.7 ± 0.2	1.0 ± 0.1	-
	11 mod	2.8 ± 0.5	0.7 ± 0.2	1.3 ± 0.1	-
	1996	12.3 ± 2.2	3.2 ± 0.8	5.2 ± 0.4	-

Table 7.2: Estimation of various non-prompt background contributions to the e^- and e^+ samples. Only statistical errors are shown.

e^- due to the charge bias of the hadron jet (there are more misidentified positive hadrons than negative) and due to an additional contribution of positrons from charm decays. For the e^+ sample, significant background comes not only from ν_μ CC and NC interactions, but also from the incorrect reconstruction of the charge sign of the prompt electron in ν_e CC events. Backgrounds for the $e^{\pm}$ samples from $\bar{\nu}_\mu$ CC, $\bar{\nu}_\mu$ NC and ν_μ quasielastic interactions were estimated from simulation too and found to be negligible.

The summary of the observed e^-, e^+ and μ^+ events and of the total predicted non-prompt background is given in Table 7.3. The sum of all non-prompt background contributions constitutes less than 0.5% of the e^- and about 11% of the e^+ data samples. The sum of ν_μ CC and ν_μ NC backgrounds amounts to about 4% of the μ^+ sample.

	Year	N^{obs}	N^{bckg} (MC)	N^{obs}-N^{bckg}	N^{bckg}/N^{obs}
e^-	1995	880 ± 30	3.2 ± 0.4	877 ± 30	0.4 %
	1996	1 780 ± 42	6.3 ± 1.2	1 774 ± 42	0.4 %
e^+	1995	93 ± 10	11.1 ± 0.8	82 ± 10	11.9 %
	1996	203 ± 14	20.7 ± 2.4	182 ± 14	10.2 %
μ^+	1995	1 816 ± 43	84.6 ± 2.6	1 731 ± 43	4.7 %
	1996	3 983 ± 63	148.1 ± 7.7	3 835 ± 63	3.7 %

Table 7.3: Predicted composition of the e^-, e^+ and μ^+ samples. The number of observed events N^{obs}, the total predicted non-prompt background N^{bckg}, the estimated number of the beam ν-induced events and the ratio of the non-prompt background to observed events are shown for the 1995 and 1996 data. The errors are only statistical.

Having estimated the various non-prompt backgrounds, the unfolded numbers of ν_e CC, $\bar{\nu}_e$ CC and $\bar{\nu}_\mu$ CC interactions can be evaluated by subtracting the corresponding non-prompt background contributions from the observed e^-, e^+ and μ^+ data samples and dividing by the Monte Carlo efficiencies of the ν_e CC, $\bar{\nu}_e$ CC and $\bar{\nu}_\mu$ CC selections:

$$N^{unf}_{\nu CC}(E_\nu) = \frac{N^{obs}(E_{vis}) - N^{bckg}(E_{vis})}{\varepsilon_{\nu CC}(E_\nu, E_{vis})} \tag{7.3}$$

The number of the observed and unfolded charged current neutrino interactions in the 1995 and 1996 data and the corresponding predicted non-prompt background contributions are shown in Table 7.1 for the $\bar{\nu}_\mu$ CC and in Table 7.4 for the ν_e CC and $\bar{\nu}_e$ CC candidates.

The number of observed and unfolded $\overset{(-)}{\nu}_e$ CC interactions								
Data taking	ν_e CC selection				$\bar{\nu}_e$ CC selection			
	$N^{obs}_{e^-}$	$N^{bckg}_{e^-}$	ε,%	$N^{unf}_{\nu_e CC}$	$N^{obs}_{e^+}$	$N^{bckg}_{e^+}$	ε,%	$N^{unf}_{\bar{\nu}_e CC}$
4 mod	135	0.5	37.4	364	14	1.9	33.6	37
8 mod	315	1.2	35.2	871	30	4.3	31.9	93
11 mod	430	1.5	32.4	1 331	49	4.9	29.5	154
1996	1 780	6.3	32.4	5 433	203	20.7	29.5	622

Table 7.4: Summary of ν_e CC and $\bar{\nu}_e$ CC event selection. For each target configuration, the number of observed events N^{obs}_e, the predicted number of non-prompt background events N^{bckg}_e, the average selection efficiency ε and the corresponding number of unfolded events $N^{unf}_{\nu CC}$ are given for the ν_e CC and $\bar{\nu}_e$ CC candidates.

Apart from the estimations of the non-prompt background contributions, the unfolding procedure described here is used for some of the consistency checks on data samples (presented in the next section) and for the estimation of the systematic uncertainty of the kinematic selection efficiency (Sec. 7.7.2). The data and Monte Carlo distributions *as reconstructed*, appropriately normalized, are used otherwise; in particular, in the determination of the confidence region.

7.2 Consistency checks on 1995 versus 1996 data

An important consistency check is the comparison of the $\mu^\pm$ and $e^\pm$ events and ν_e/ν_μ and $\bar{\nu}_e/\bar{\nu}_\mu$ ratios in the 1995 and 1996 data. Any statistically significant discrepancy between the two data samples would be an indication for a possible data taking or analysis problem, such as unknown instrumental effects, etc.

The set of consistency checks conducted on the 1995 and 1996 data samples is presented below.

1. **Comparison of μ^- samples.** First, we compare the ratio of background-free μ^- events selected in 1995 and 1996 data with that expected from the number of p.o.t.'s of each exposure. We use only the 11 module target configuration sample of 1995

data as it is directly comparable with the 1996 data. From Table 7.1, we find that the ratio of observed μ^- events in 1996 and 11 module 1995 data is

$$\frac{N_{\mu^-}^{11mod}}{N_{\mu^-}^{1996}} = \frac{40\ 242}{171\ 781} = (23.4 \pm 0.1(stat.))\%. \tag{7.4}$$

The ratio of the corresponding number of p.o.t.'s is

$$\frac{N_{p.o.t.}^{11mod}}{N_{p.o.t.}^{1996}} = \frac{3.1 \cdot 10^{18}}{13.0 \cdot 10^{18}} = (23.8 \pm 1.7)\%. \tag{7.5}$$

We assume 5% uncertainty on the BCT measurements of the flux of incident protons during the lifetime of the NOMAD data acquisition system. The μ^- and p.o.t. ratios agree within errors.

2. **Comparison of e^- samples.** The ratio of observed e^- events in 1996 and 11 module 1995 data samples (see Table 7.4) is

$$\frac{N_{e^-}^{11mod}}{N_{e^-}^{1996}} = \frac{430}{1\ 780} = (24.2 \pm 1.3(stat.))\% \tag{7.6}$$

   and agrees within errors with that expected from the number of protons on target (7.5). This test is statistically less precise than that of the μ^- samples; however, it is essential in order to ensure the stability of the electron identification. The estimations of the non-prompt background for 1996 and 11 module 1995 data are identical, so that the above ratio is deduced using the full e^- samples, non-prompt background included.

   The ratio (7.6) of e^- events is also in agreement with that of μ^- from Eq. (7.4), showing the stability of the relative electron/muon identification efficiency within the 5% statistical accuracy of the electron samples.

3. **Comparison of $\mu^\pm$ and $e^\pm$ samples as a function of the visible energy.** The μ^-, μ^+, e^- and e^+ samples selected in 11 module 1995 data are compared to those in 1996 data as a function of the visible energy in Fig. 7.1. Satisfactory agreement between 1995 and 1996 data for all samples is demonstrated.

4. **Consistency of ν_e/ν_μ ratio.** The expected ν_e/ν_μ ratios in 1995 and 1996 data are (from Tables 7.1 and 7.4):

$$\left(\frac{N_{\nu_e CC}^{unf}}{N_{\nu_\mu CC}^{unf}}\right)_{1995} = \frac{2\ 566}{175\ 177} = (1.46 \pm 0.05)\% \tag{7.7}$$

$$\left(\frac{N_{\nu_e CC}^{unf}}{N_{\nu_\mu CC}^{unf}}\right)_{1996} = \frac{5\ 433}{378\ 943} = (1.43 \pm 0.03)\% \tag{7.8}$$

   The ν_e/ν_μ ratios are consistent within errors.

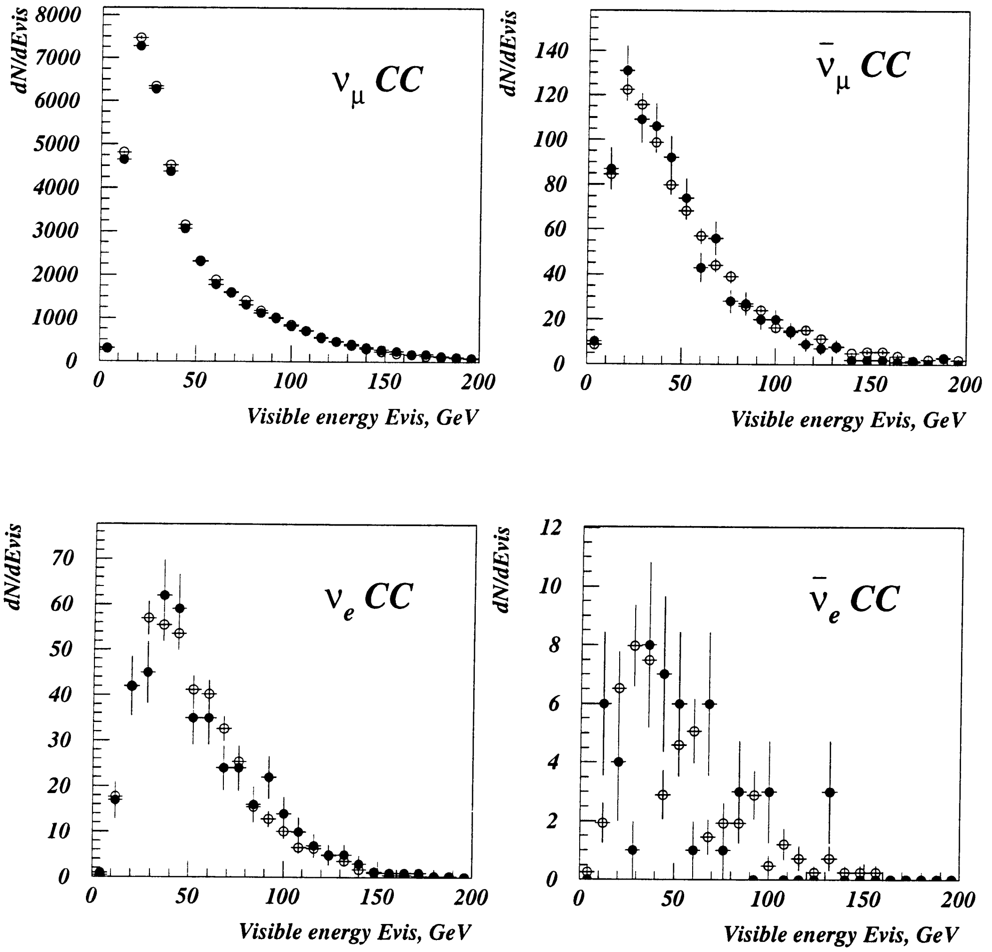

Figure 7.1: Comparison of 1996 and 11 module 1995 data as a function of the visible energy for μ^-, μ^+, e^- and e^+ samples. The 11 module 1995 data are shown in solid circles, the open circles are the 1996 data. All plots are normalized to the μ^- sample in 11 module 1995 data.

5. **Comparison of ν_e/ν_μ ratios as a function of neutrino energy.** A comparison of the unfolded ν_e/ν_μ ratios in 1995 and 1996 data as a function of the neutrino energy is shown in Fig. 7.2. No statistically significant discrepancies between the two data samples are found.

6. **Consistency of $\bar{\nu}_e/\bar{\nu}_\mu$ ratio.** Finally, we compare the $\bar{\nu}_e/\bar{\nu}_\mu$ ratio in 1995 and 1996 data. A deviation in this ratio would imply an error in the analysis most likely arising from different non-prompt background contaminations of the two data samples. The expected $\bar{\nu}_e/\bar{\nu}_\mu$ ratios in 1995 and 1996 data are (from Tables 7.1 and 7.4):

$$\left(\frac{N^{unf}_{\bar{\nu}_e CC}}{N^{unf}_{\bar{\nu}_\mu CC}}\right)_{1995} = \frac{284}{4\ 548} = (6.2 \pm 0.6)\% \qquad (7.9)$$

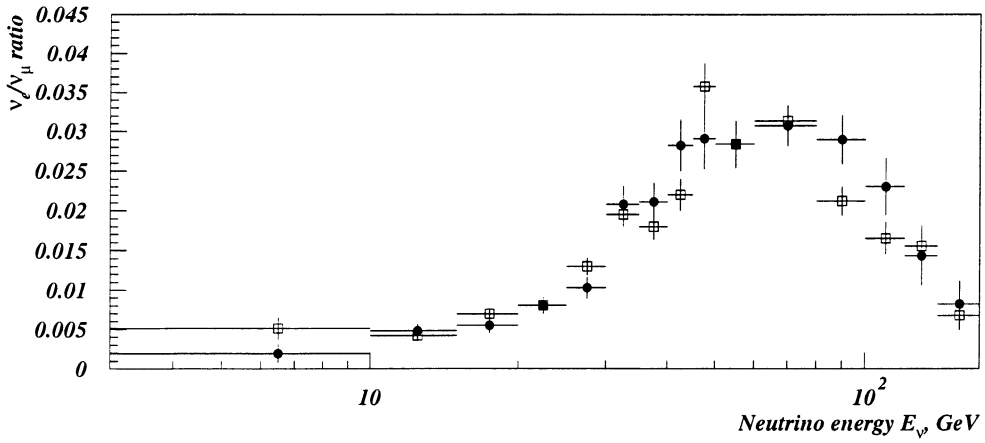

Figure 7.2: Comparison of the unfolded ν_e/ν_μ ratio in 1995 and 1996 data as a function of the neutrino energy. The solid circles are the 1995 data, the open squares are the 1996 data. The non-prompt background contribution to the ν_e CC sample was estimated from MC and appropriately subtracted.

$$\left(\frac{N^{unf}_{\bar{\nu}_e CC}}{N^{unf}_{\bar{\nu}_\mu CC}}\right)_{1996} = \frac{621}{10\ 041} = (6.2 \pm 0.4)\% \tag{7.10}$$

Within ~10% statistical accuracy of the e^+ samples, the two ratios agree, indicating the similarity of the non-prompt background contributions in 1995 and 1996 data.

We conclude that all four samples, $\mu^\pm$ and $e^\pm$, are consistent between 1995 and 1996 data within statistical errors.

7.3 Comparison between data and Monte Carlo predictions

One possible way to search for $\nu_\mu \to \nu_e$ oscillations in NOMAD would be to look for deviations in the ν_e CC energy spectrum from the predictions of the simulation. Such an approach would make the analysis extremely sensitive to the prediction of the absolute neutrino flux. A sensitivity of the oscillation search to the absolute flux predictions can be reduced by considering a relative measurement - the ratio of the ν_e CC over ν_μ CC spectra - the approach we use. However, the knowledge of the relative fluxes - the relative abundance of ν_e to ν_μ neutrinos as a function of energy - is crucial.

High energy neutrinos in the CERN wide-band neutrino beam come from the decays of $\pi^\pm$, $K^\pm$, K^0_L, $\mu^\pm$ and to a lesser extent of charmed mesons and hyperons (see Sec. 3.2). These secondary particles are produced in the interactions of the 450 GeV/c proton beam with a Beryllium target. The positive component of the secondary beam is focused by a system of magnetic lenses (the horn and the reflector) and transported to a vacuum tunnel where the particles decay. The residual charged particles are finally stopped by a shield placed before the experimental site, which only neutrinos can penetrate.

The production of the secondary particles in the pBe interactions is the crucial part of the flux prediction, since the relative fraction of ν_e with respect to ν_μ neutrinos in the beam is determined by the kaon and pion content of the secondary meson flux. Several packages have been developed to simulate secondary particle production:

- **GFLUKA** (or FLUKA92) package [91] computes the differential and total cross-sections of the hadronic processes and simulates hadronic interactions.

- **FLUKA standalone** (or FLUKA95) [107], a modified version of FLUKA92, reproduces the measured differential cross-section $d^2\sigma/d\Omega dp$ [108] with improved accuracy. Further adjustments to the data of the NA56 (SPY) collaboration [109], which in 1996 has measured the yield of the $\pi^\pm$, $K^\pm$ and secondary p with momenta down to 15 GeV/c in pBe interactions, are being implemented.

- **Empirical parametrization** (EP) [53] parametrizes the differential production cross-section of the secondary mesons such that the resultant ν_μ, $\bar{\nu}_\mu$ and $\bar{\nu}_e$ fluxes empirically fit the corresponding measured NOMAD data. The so-called "fixed ν_0 method" (see [53] and references therein) is employed, which follows from the general expression of the neutrino-nucleon differential cross-section. Namely, one makes use of the fact that the number of events in a given energy bin with $E_{had} < \nu_0$ is proportional to the neutrino (antineutrino) flux in that energy bin up to correction factors of the order of $\mathcal{O}(\nu_0/E_\nu)$ or smaller, which are not significant for small values of ν_0 at high energies.[1] The resulting cross-sections are then used to predict the ν_e flux in the absence of oscillations.

All these simulations predict the flux of the four neutrino species as a function of the neutrino energy E_ν and radial position R^2.

The entire beam line is simulated by a Monte Carlo package called NUBEAM [110]. NUBEAM describes the propagation and reinteractions of the secondary particles as they travel through the focussing devices and the rest of the beam line to NOMAD; it makes use of the GEANT [47] library for the apparatus and the material description.[2]

The predicted integrated neutrino fluxes and the average energies at the position of the NOMAD detector are shown in Table 7.5 for FLUKA92, FLUKA95 and EP. As already mentioned, the ν_e/ν_μ ratio predicted by all Monte Carlo simulations is of the order of 1%. The ν_e spectrum is significantly harder than that of ν_μ, which increases the sensitivity of the experiment to the oscillation search.

---

[1] ν_0 is $\sim$5 GeV or less at NOMAD typical energies.

[2] An important check of the quality of the beam line simulation will be provided by the comparison between the measured and predicted $\bar{\nu}_\mu$ spectra for an antineutrino run. Such a run with an exposure of about $2.3 \cdot 10^{18}$ p.o.t. (3 weeks of data taking) has been performed in May, 1998 and is expected to yield about 25 000 $\bar{\nu}_\mu$ CC events – sufficient for such a comparison.

Neutrino flux predictions									
ν	$\Phi(\nu_x)/\Phi(\nu_\mu)$			$\langle E_\nu \rangle$, GeV			$N(\nu_x CC)/N(\nu_\mu CC)$		
type	FL92	FL95	EP	FL92	FL95	EP	FL92	FL95	EP
ν_μ	1.0	1.0	1.0	24.1	22.8	24.5	1.0	1.0	1.0
$\bar{\nu}_\mu$	0.068	0.059	0.055	23.0	22.5	18.7	0.032	0.029	0.021
ν_e	0.0093	0.0090	0.0095	37.7	36.0	39.1	0.015	0.014	0.015
$\bar{\nu}_e$	0.0025	0.0028	0.0025	29.4	31.1	31.5	0.0017	0.0019	0.0016

Table 7.5: Relative flux abundance $\Phi(\nu_x)/\Phi(\nu_\mu)$, average neutrino energy $\langle E_\nu \rangle$ and relative number of CC DIS interactions $N(\nu_x CC)/N(\nu_\mu CC) = \Phi(\nu_x)/\Phi(\nu_\mu) \cdot \langle E_{\nu_x} \rangle / \langle E_{\nu_\mu} \rangle \cdot \sigma(\nu_x)/\sigma(\nu_\mu)$ for four neutrino species at NOMAD, as predicted by FLUKA92 (FL92), FLUKA95 (FL95) and empirical parametrization (EP) [111]. The fiducial area for the FLUKA92 and FLUKA95 predictions is 260×260 cm^2, that for the empirical parametrization is 240×240 cm^2.

7.3.1 Data versus Monte Carlo: comparison of the number of charged current events

First of all, we compare the total number of events observed in the μ^+, e^- and e^+ data samples with that predicted by the simulation. The expected number of events from the different possible sources is based on the neutrino fluxes - predicted by FLUKA92, FLUKA95 and the empirical parametrization - passed through the detector simulation, event reconstruction and the selection criteria. The number of background-free ν_μ CC events observed in the data and the expected relative abundance of ν_x DIS interactions $N(\nu_x)/N(\nu_\mu CC)$ are used to normalize the predicted number of ν_x CC and NC events.

The number of μ^+, e^- and e^+ events expected in 1995 and 1996 data from the different possible sources as predicted by FLUKA92, FLUKA95 and EP simulations is compared to that observed in the data in Table 7.6.

The number of μ^+ events selected in the 1995 and 1996 data differs significantly from those predicted by the Monte Carlo simulations: it is considerably lower than the predictions of FLUKA92 and FLUKA95 (by $\sim$40% and $\sim$20% respectively) and is $\sim$15% higher than that given by the EP. Note also that the Monte Carlo predictions disagree with each other: the number of $\bar{\nu}_\mu$ CC predicted by FLUKA92 is more than 50% higher than that given by the EP. The discrepancy between μ^+ data and predictions, though large, is not, in all probability, due to the errors in the estimations of the non-prompt background in the μ^+ sample, but is most likely due to intrinsic problems in the description of the yield of the negative secondary mesons by the neutrino flux simulation programs. A better description of the $\bar{\nu}_\mu$ yield is expected in the new version of the FLUKA package, FLUKA97 [112], which is being tuned to reproduce the existing measurements of the charged secondary particle production [108, 109].

The data - Monte Carlo agreement in the total number of e^- and e^+ events is good.

The number of observed and expected events									
	Year	Flux	ν_μ CC	$\bar{\nu}_\mu$ CC	ν_μ NC	ν_e CC	$\bar{\nu}_e$ CC	Total	Data
μ^+	1995	FL92	77.1	2 494.3	5.0	0.0	0.0	2 576.4	1 816±43
		FL95	78.7	2 103.3	4.9	0.0	0.0	2 186.8	
		EP	80.0	1 523.8	4.6	0.0	0.0	1 608.5	
	1996	FL92	142.1	5 326.4	10.3	0.0	0.0	5 478.7	3 983±63
		FL95	143.8	4 494.2	10.1	0.0	0.0	4 648.0	
		EP	145.2	3 243.8	9.8	0.0	0.0	3 398.7	
e^-	1995	FL92	1.3	0.0	1.5	888.8	0.2	891.8	880±30
		FL95	1.3	0.0	1.5	856.5	0.2	859.5	
		EP	1.6	0.0	1.5	892.0	0.2	895.2	
	1996	FL92	2.6	0.1	2.9	1 829.9	0.3	1 835.8	1 780±42
		FL95	2.7	0.1	2.8	1 764.4	0.3	1 770.4	
		EP	3.0	0.1	3.0	1 836.6	0.3	1 842.9	
e^+	1995	FL92	6.6	0.2	1.7	3.0	102.0	113.5	93±10
		FL95	6.7	0.2	1.5	3.1	103.4	114.9	
		EP	6.3	0.1	1.7	3.0	90.2	101.4	
	1996	FL92	12.8	0.4	3.0	5.3	211.1	232.5	203±14
		FL95	12.9	0.4	2.8	5.4	214.1	235.9	
		EP	12.3	0.2	3.2	5.2	186.5	207.4	

Table 7.6: Number of μ^+, e^- and e^+ events expected in 1995 and 1996 data from the different possible sources as predicted by FLUKA92, FLUKA95 and EP simulations compared to that measured in the data. The errors shown are only statistical.

A discrepancy between data and simulation in the number of e^- events could indicate an oscillation signal; we see that all three Monte Carlo predictions agree rather well, within statistical errors of the data, with the number of the observed e^- events, both for 1995 and 1996 data. The FLUKA92 and EP predictions are consistent with each other within 1%, FLUKA95 gives 5% lower e^- expected number. The number of e^+ events in the data agrees well with the EP prediction; the almost identical FLUKA92 and FLUKA95 predictions, though somewhat higher than the data, are also consistent within statistical errors. The agreement between data and Monte Carlo for the e^+ events, where the non-prompt background constitutes about 11% of the sample, indicates that our background estimations are correct within the statistical accuracy of the sample.[1]

---

[1] One should note, however, that discrepancies between the e^+ data sample and MC predictions would not necessarily mean that our estimate of the non-prompt background is incorrect. To evaluate the uncertainty of the background independently from the uncertainty of the ν_e and $\bar{\nu}_e$ flux predictions, one should study the data samples completely dominated by the non-prompt background. This issue is discussed in Sec. 7.7.3.

7.3.2 Data versus Monte Carlo: comparison of energy spectra

A comparison of the energy spectra as reconstructed for the μ^-, μ^+, e^- and e^+ samples selected in 1995 and 1996 data with the corresponding DIS Monte Carlo predictions is shown in Fig. 7.3 – 7.6.

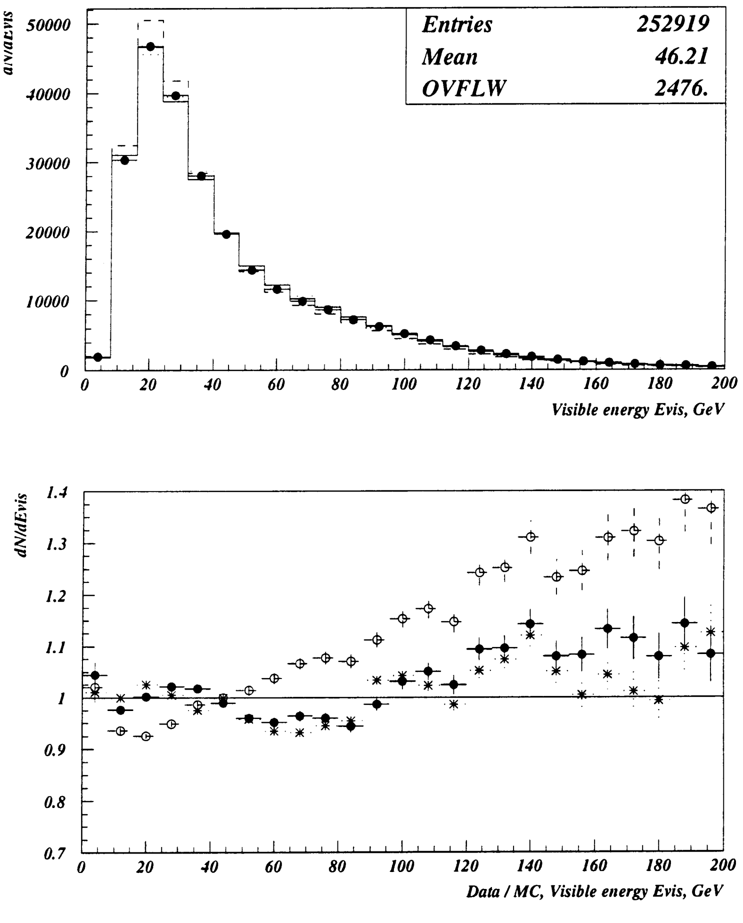

Figure 7.3: Top: comparison of the visible energy spectrum of the μ^- events selected in 1995 and 1996 data with the ν_μ CC DIS Monte Carlo predictions. The solid circles are the sum of 1995 and 1996 data, FLUKA92 predictions are shown in solid line, FLUKA95 - in dashed line, EP - in dotted line. The Monte Carlo predictions are normalized to the number of events in the data. Bottom: ratio of the measured μ^- energy spectrum to those predicted by simulation using FLUKA92 (solid circles), FLUKA95 (open circles) and EP (asterisks). Only statistical errors are shown.

In order to compare ν_μ energy spectrum, the Monte Carlo predictions should be normalized to the number of μ^- events in the data, i.e. only the comparison of the energy shape (and not of the absolute normalization) is possible. None of the three predictions agree very well with the μ^- data in the whole energy range (Fig. 7.3). The discrepan-

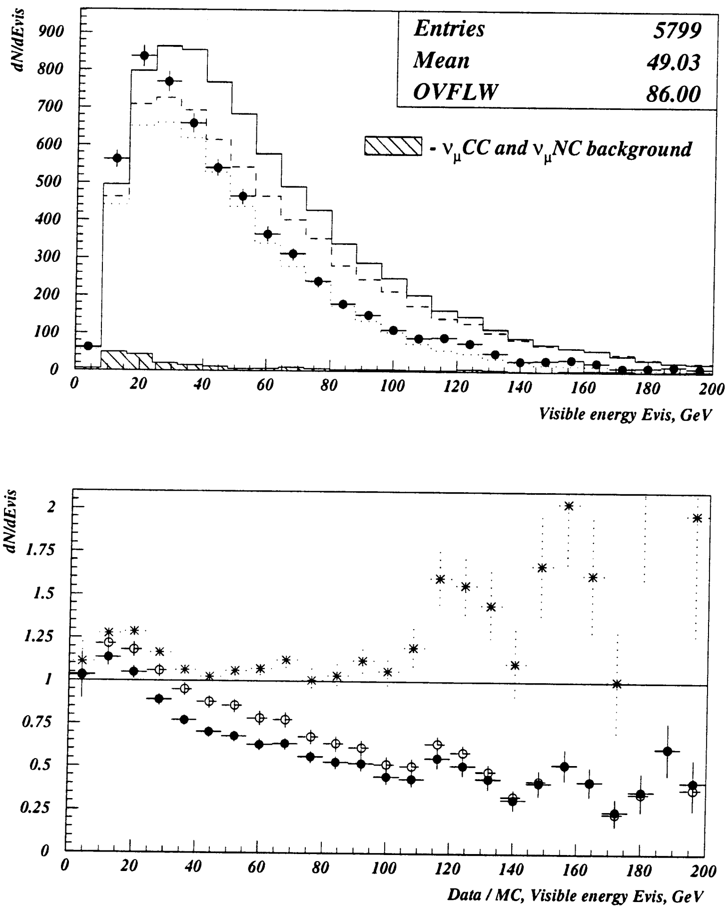

Figure 7.4: Top: comparison of the visible energy spectrum of the μ^+ events selected in 1995 and 1996 data with the $\bar{\nu}_\mu$ CC DIS Monte Carlo predictions. The solid circles are the sum of 1995 and 1996 data, FLUKA92 predictions are shown in solid line, FLUKA95 – in dashed line, EP – in dotted line (non-prompt background component is appropriately added). The sum of the estimated ν_μ CC and ν_μ NC non-prompt backgrounds as predicted by FLUKA92 is shown separately in shaded histogram for comparison. The Monte Carlo predictions are normalized to the μ^- data. Bottom: ratio of the measured μ^+ energy spectrum to those predicted by simulation using FLUKA92 (solid circles), FLUKA95 (open circles) and EP (asterisks). Only statistical errors are shown.

cies are particularly clear (5% and more) in the energy regions between 10–30 GeV for FLUKA95, 60–90 GeV for FLUKA95 and EP and above 120 GeV for FLUKA92 and FLUKA95. The predictions of the various production packages are also not in agreement with each other.

To compare $\bar{\nu}_\mu$, ν_e and $\bar{\nu}_e$ energy spectra in data and Monte Carlo, the number of ν_μ CC events observed in the data and the expected relative number of $\bar{\nu}_\mu/\nu_\mu$ (ν_e/ν_μ, $\bar{\nu}_e/\nu_\mu$) DIS interactions are used to normalize the predicted number of Monte Carlo events.

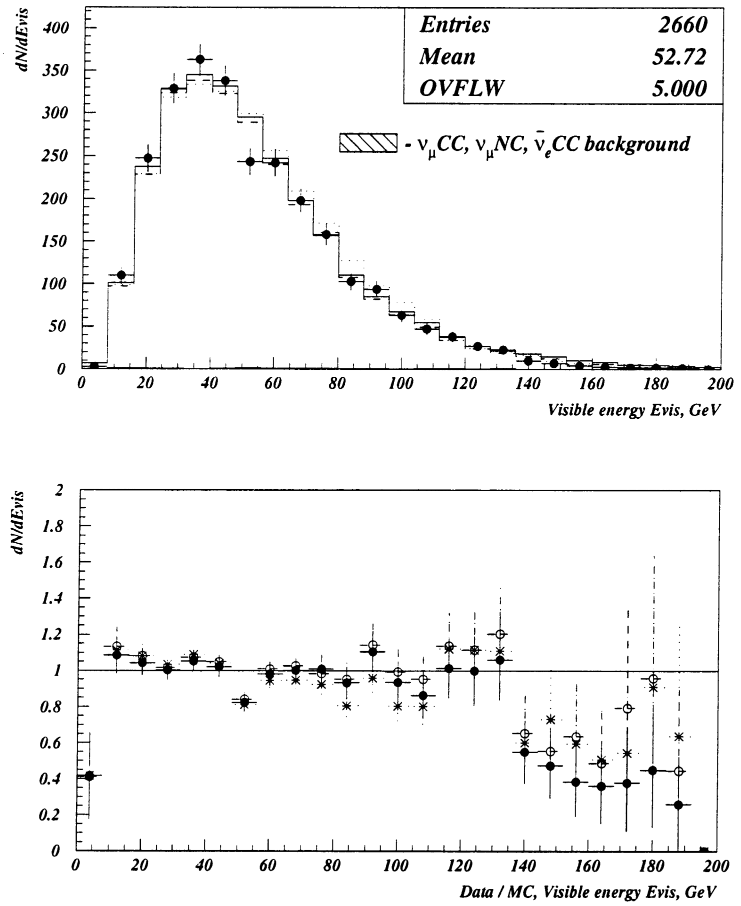

Figure 7.5: Top: comparison of the visible energy spectrum for the e^- events selected in 1995 and 1996 data with the ν_e CC DIS Monte Carlo predictions (assuming no oscillations). The solid circles are the sum of 1995 and 1996 data, FLUKA92 predictions are shown in solid line, FLUKA95 – in dashed line, EP – in dotted line (non-prompt background component is appropriately added). The total estimated non-prompt background as predicted by FLUKA92 is shown separately in shaded histogram for comparison. The Monte Carlo predictions are normalized to the μ^- data. Bottom: ratio of the measured e^- energy spectrum to those predicted by simulation using FLUKA92 (solid circles), FLUKA95 (open circles) and EP (asterisks). Only statistical errors are shown.

The shape of the $\bar{\nu}_\mu$ energy spectrum (Fig. 7.4) predicted by the EP is consistent with that of the μ^+ data sample but the relative $\bar{\nu}_\mu/\nu_\mu$ yield is underestimated, while the FLUKA92 and FLUKA95 predictions for the $\bar{\nu}_\mu$ are particularly poor, both in normalization and in shape. Unlike the case of ν_μ and $\bar{\nu}_\mu$ energy spectra, the ν_e and $\bar{\nu}_e$ predictions from various packages agree well and are consistent with the measurements (with the exception of the high energy tail of the ν_e spectrum), which is illustrated in Fig. 7.5 and 7.6. The most probable explanation of the agreement is that ν_e and $\bar{\nu}_e$ neutrinos emerg-

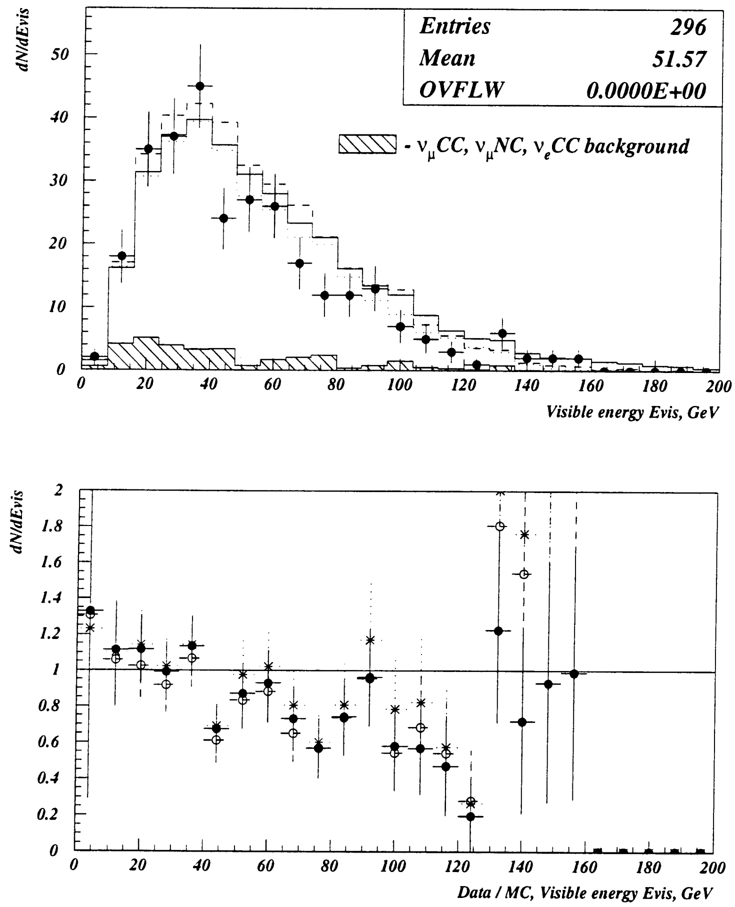

Figure 7.6: Top: comparison of the visible energy spectrum for the e^+ events selected in 1995 and 1996 data with the $\bar{\nu}_e$ CC DIS Monte Carlo predictions. The solid circles are the sum of 1995 and 1996 data, FLUKA92 predictions are shown in solid line, FLUKA95 – in dashed line, EP – in dotted line (non-prompt background component is appropriately added). The total estimated non-prompt background as predicted by FLUKA92 is shown separately in shaded histogram for comparison. The Monte Carlo predictions are normalized to the μ^- data. Bottom: ratio of the measured e^+ energy spectrum to those predicted by simulation using FLUKA92 (solid circles), FLUKA95 (open circles) and EP (asterisks). Only statistical errors are shown.

ing mainly from a three-body K-decays are less sensitive to the details of the production spectra and to the angular divergence of the parent meson beam than ν_μ and $\bar{\nu}_\mu$ neutrinos from two-body π- and K-decays.

As may be expected from the above discussion, the uncertainty in the neutrino flux predictions represents one of the largest contributions to the systematic uncertainties of this analysis. It is discussed in more detail in the following sections.

7.3.3 Data versus Monte Carlo: comparison of radial distributions

A comparison of the distribution of the radial position of neutrino interaction vertices as reconstructed for the μ^- and e^- samples selected in 1995 and 1996 data with the corresponding DIS Monte Carlo predictions is shown in Fig. 7.7.

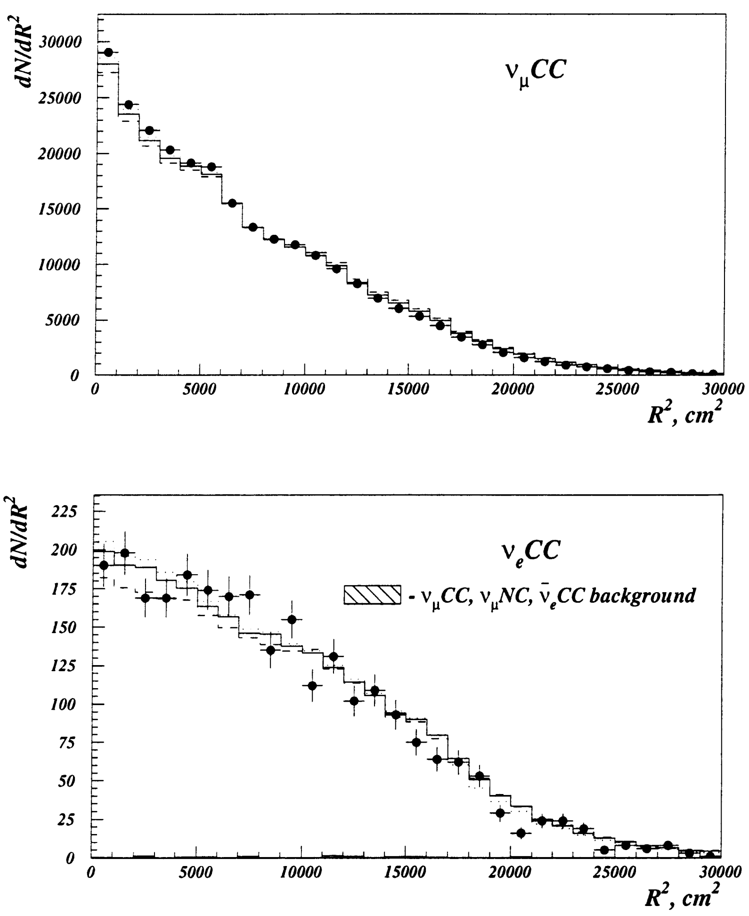

Figure 7.7: Comparison of the radial distribution of neutrino interaction vertex as reconstructed for the μ^- and e^- events selected in 1995 and 1996 data with the ν_μ CC DIS Monte Carlo predictions. The solid circles are the sum of 1995 and 1996 data, FLUKA92 predictions are shown in solid line, FLUKA95 – in dashed line, EP – in dotted line. The total estimated non-prompt background in the e^- sample as predicted by FLUKA92 is shown in shaded histogram. The Monte Carlo predictions are normalized to the number of μ^- events in the data, the errors shown are only statistical.

The predictions agree well with the data. The radial distribution of ν_e emerging from the three-body decay of kaons is, as expected, much broader than that of ν_μ neutrinos from the two-body decays of π^+ and K^+ mesons. In other words, the ν_e/ν_μ ratio in the absence of oscillations is expected to be smaller (i.e. more sensitive to oscillation contribution) at small radii and larger (less sensitive) at the edges of the detector. The radial dependence of the ν_e/ν_μ ratio can be explored in order to possibly increase the sensitivity of the analysis by performing the $\nu_\mu \rightarrow \nu_e$ oscillation search in radial bins (in addition to energy bins).

7.3.4 Data versus Monte Carlo: the $\bar{\nu}_e/\bar{\nu}_\mu$ ratio

As already mentioned, no measurable contribution to the $\bar{\nu}_e$ events from $\bar{\nu}_\mu \rightarrow \bar{\nu}_e$ oscillations is expected, due to the small relative $\bar{\nu}_\mu/\nu_\mu$ fraction in the beam and the small non-excluded probability of the oscillations. Therefore, the observed ratio of $\bar{\nu}_e/\bar{\nu}_\mu$ CC events has to be consistent with predictions; a deviation could indicate an incorrect estimation of the non-prompt background.

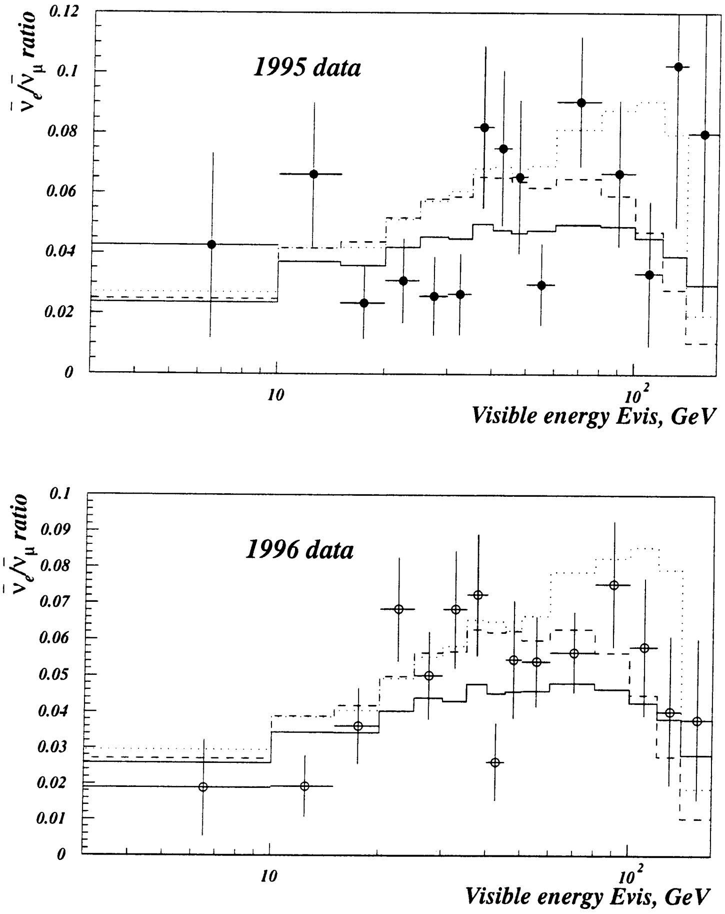

Figure 7.8: The ratio of $\bar{\nu}_e$ CC to $\bar{\nu}_\mu$ CC events as reconstructed in 1995 (top, solid points) and 1996 data (bottom, open points) as a function of the total visible energy E_{vis}, compared to the predictions of the Monte Carlo simulation. FLUKA92 predictions are shown in solid line, FLUKA95 - in dashed line, EP - in dotted line. The total estimated non-prompt background is appropriately added to the Monte Carlo predictions. The errors shown are only statistical.

The ratio of $\bar{\nu}_e$ CC to $\bar{\nu}_\mu$ CC events observed in the 1995 and 1996 data, compared to that predicted by the Monte Carlo simulations, is shown in Fig. 7.8 as a function of the total visible energy E_{vis}. The disagreement between the FLUKA92 prediction and the observation is particularly clear at high energies; it is mainly due to the poor FLUKA92 description of $\bar{\nu}_\mu$ flux (discussed in Sec. 7.3.1 and 7.3.2). The $\bar{\nu}_e/\bar{\nu}_\mu$ predictions of the FLUKA95 and EP agree with the measurement within the statistical accuracy of the positron data sample.

7.3.5 Data versus Monte Carlo: the $R_{e\mu}$ ratio

The next step towards an oscillation search is to compare the ratio $R_{e\mu}$ of ν_e CC to ν_μ CC events to that predicted by the Monte Carlo simulation packages as a function of the neutrino energy. The presence of $\nu_\mu \rightarrow \nu_e$ oscillations would lead to an increase in that ratio. In particular, an enhancement in the low-energy region ($5 < E_\nu < 30$ GeV) is expected, due to the lower average energy of oscillating ν_μ neutrinos compared to that of ν_e (see Table 7.5).

The ratio of ν_e CC to ν_μ CC events observed in the 1995 and 1996 data as a function of the total visible energy E_{vis} is compared to the predictions of the Monte Carlo simulations (assuming no contribution from $\nu_\mu \rightarrow \nu_e$ oscillations) in Fig. 7.9.

The data agree well with the no oscillation hypothesis. The important fact also illustrated by the plot is the consistency of the three Monte Carlo predictions of $R_{e\mu}$ ratio. The Monte Carlo predictions agree especially well in the low energy range (below 30 GeV), the region most sensitive to $\nu_\mu \rightarrow \nu_e$ oscillations.

7.4 Monte Carlo samples and oscillation parameters

To determine an allowed (or exclusion) confidence region of $\nu_\mu \rightarrow \nu_e$ oscillation parameters, the experimental distributions have to be compared with those predicted by the simulation for various sets of oscillation parameters. The standard Monte Carlo simulation of ν_μ CC and ν_e CC events and their reconstruction has been done without the presence of neutrino oscillations. To take into account an oscillation contribution, different distributions (e.g., $R_{e\mu}$ ratio) expected for a given set of oscillation parameters are produced through event by event reweighting of the oscillation-free MC samples.

The calculation of W_{ν_μ} and W_{ν_e} weights for ν_μ and ν_e Monte Carlo events is done in several steps. The starting point is the predicted ν_μ^0 and ν_e^0 flux. The presence of $\nu_\mu \rightarrow \nu_e$ oscillations would yield modified ν_e and ν_μ fluxes:

$$\begin{aligned} \nu_e(E_\nu, R^2) &= \nu_e^0(E_\nu, R^2) \cdot P_{\nu_e \rightarrow \nu_e}(E_\nu, L) + \nu_\mu^0(E_\nu, R^2) \cdot P_{\nu_\mu \rightarrow \nu_e}(E_\nu, L) \\ \nu_\mu(E_\nu, R^2) &= \nu_\mu^0(E_\nu, R^2) \cdot P_{\nu_\mu \rightarrow \nu_\mu}(E_\nu, L) + \nu_e^0(E_\nu, R^2) \cdot P_{\nu_e \rightarrow \nu_\mu}(E_\nu, L) \end{aligned} \tag{7.11}$$

where P are the probabilities of observing the indicated type of oscillations. For two-family

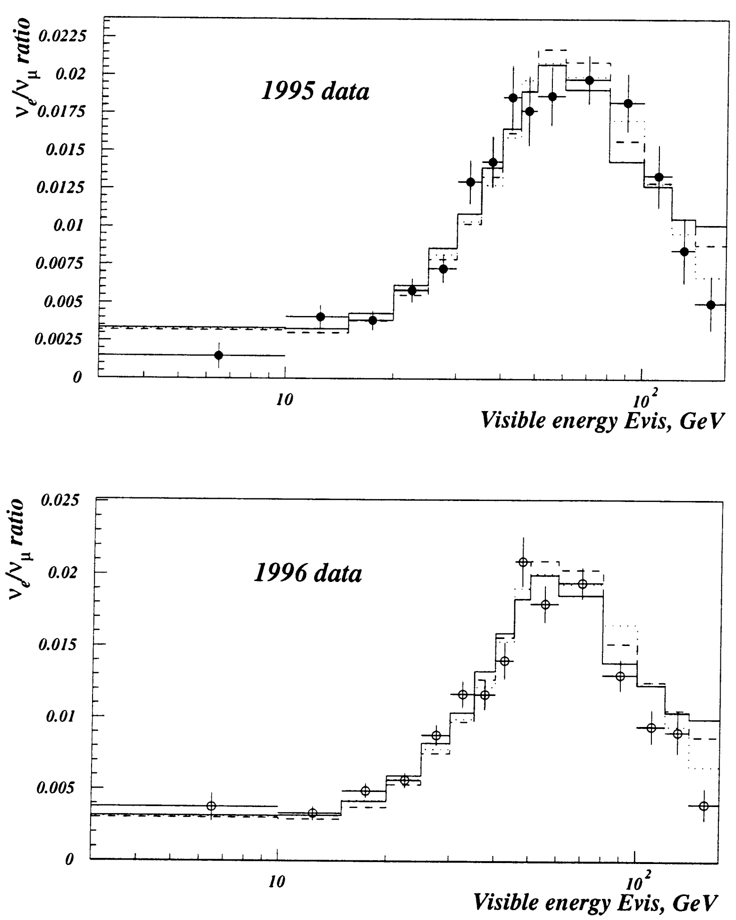

Figure 7.9: The ratio of ν_e CC to ν_μ CC events as reconstructed in 1995 data (top, solid points) and 1996 data (bottom, open points) as a function of the total visible energy E_{vis}, compared to the predictions of the Monte Carlo simulations assuming no contribution from $\nu_\mu \rightarrow \nu_e$ oscillations. FLUKA92 predictions are shown in solid line, FLUKA95 – in dashed line, EP – in dotted line. The total estimated non-prompt background to ν_e CC interactions is appropriately added to the Monte Carlo predictions. The errors shown are only statistical.

mixing, the oscillation probabilities are related:

$$P_{\nu_e \rightarrow \nu_\mu} = P_{\nu_\mu \rightarrow \nu_e} = 1 - P_{\nu_\mu \rightarrow \nu_\mu} = 1 - P_{\nu_e \rightarrow \nu_e} \quad (7.12)$$

Therefore, the weights are

$$\begin{aligned} W_{\nu_e} &= \nu_e/\nu_e^0 = 1 + (\frac{1}{R^0} - 1) \cdot P_{\nu_\mu \rightarrow \nu_e} \\ W_{\nu_\mu} &= \nu_\mu/\nu_\mu^0 = 1 - (1 - R^0) \cdot P_{\nu_\mu \rightarrow \nu_e} \end{aligned} \quad (7.13)$$

where $R^0(E_\nu, R^2)$ is the predicted ν_e^0/ν_μ^0 ratio of neutrino fluxes assuming no contribution from oscillations.

The oscillation probability $P_{\nu_\mu \to \nu_e}$ in the case of two-neutrino mixing is given by

$$P_{\nu_\mu \to \nu_e}(E_\nu, L) = \sin^2 2\theta \cdot \sin^2 \pi \frac{L}{\lambda}; \qquad \lambda(km) = \frac{2.48 E_\nu(GeV)}{\Delta m^2(eV^2)} \tag{7.14}$$

where θ is the mixing angle, L is the distance between the neutrino production point and its observation point, λ is the oscillation length determined by the neutrino energy E_ν and the eigenstate squared mass difference $\Delta m^2 = m_1^2 - m_2^2$. Approximating the probability of π- and K-decays along the decay path length by a uniform distribution, the probability of oscillations in (7.13) can be expressed as

$$P_{\nu_\mu \to \nu_e}(E_\nu, \Delta m^2, \sin^2 2\theta) = \frac{\int\limits_{L_{min}}^{L_{max}} P_{\nu_\mu \to \nu_e}(L)\, dL}{L_{min} - L_{max}} \tag{7.15}$$

where $L_{max} = 835$ m and $L_{min} = 421$ m are the distances from the target and from the end of the decay tunnel to the NOMAD detector. The integration over L can be performed analytically. Therefore, the weights W are computed for a given set of oscillation parameters (Δm^2, $\sin^2 2\theta$) as a function of neutrino energy E_ν and the radial position of the interaction vertex R^2.

7.5 Determination of confidence region

As mentioned previously, the sensitivity of the oscillation search to the absolute flux predictions and to many systematic uncertainties could be reduced by considering the ratio $R_{e\mu}$ of the number of ν_e and ν_μ charged current interactions. It is the $R_{e\mu}$ ratio as a function of the total visible energy and of the radial location of the interaction in the detector that we use for determination of confidence region of oscillation parameters.

We have chosen to use a variable bin size for the $R_{e\mu}$ as a function of the visible energy. The bin width and number of bins have been chosen in such a way that there are at least 10 events in each energy bin for the ν_e CC data sample. The comparison of the $R_{e\mu}$ predicted by the EP Monte Carlo (assuming no oscillations) and that observed in 1995 and 1996 data is shown in Fig. 7.10. The data agree well with the no oscillation hypothesis and disagree with the minimum χ^2 LSND solution ($\Delta m^2 = 19$ eV^2, $\sin^2 2\theta = 0.006$) [34].

As was discussed in Sec. 7.3.3, the sensitivity of the analysis can be increased by splitting the available data into radial bins. We used two radial bins, defined by a requirement that the radius of the reconstructed primary vertex position with respect to the longitudinal beam axis should be smaller (larger) than 70 cm. The ratio of the number of ν_e CC candidate events in inner and outer radial bins is about 1:2, providing reasonable statistical accuracy in each energy bin in both radial samples.

The comparison of the $R_{e\mu}$ predicted by the EP Monte Carlo (assuming no oscillations) with that observed in 1995 and 1996 data in two radial bins is shown in Fig. 7.11 as a

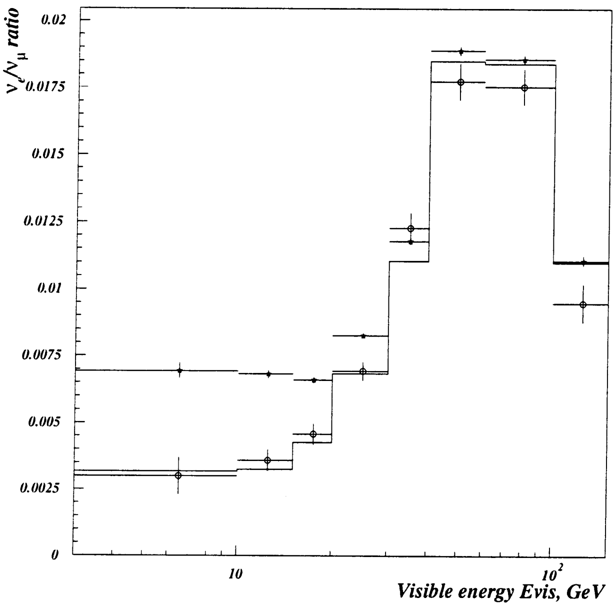

Figure 7.10: Comparison of $R_{e\mu}$ ratio for the sum of 1995 and 1996 data (open circles) with the EP Monte Carlo prediction assuming no contribution from oscillations (histogram), as a function of the visible energy E_{vis}. The signal expected in NOMAD in case of $\nu_\mu \rightarrow \nu_e$ oscillations with the minimum χ^2 LSND solution ($\Delta m^2 = 19$ eV^2, $\sin^2 2\theta = 0.006$) [34] is also shown (asterisks). The total estimated non-prompt background is added to the Monte Carlo predictions. The errors are only statistical.

function of the visible energy E_{vis}. Again, the data agree with the no oscillation hypothesis and disagree with the minimum χ^2 LSND solution in both radial regions.

Two different methods to determine a confidence region – a "global scan" (with both chi-squared and likelihood estimators) and a "unified approach" (technique recently proposed by Feldman and Cousins [113]) – have been used to set a limit on the parameters of $\nu_\mu \rightarrow \nu_e$ oscillations.

7.5.1 Global scan

This method consists of the global (2D) minimization of the $\chi^2(\sin^2 2\theta, \Delta m^2)$ in the $\log(\sin^2 2\theta)$ - $\log(\Delta m^2)$ plane. The point ($\sin^2 2\theta_{min}$, Δm^2_{min}) with $\chi^2 = \chi^2_{min}$ gives the best estimate of the oscillation parameters. The confidence region is then computed as the set of solutions of the inequality

$$\chi^2 > \chi^2_{min} + UP \tag{7.16}$$

where UP is the confidence level for a χ^2 distribution and is equal to 4.61 for a 90% C.L. for two degrees of freedom [114].

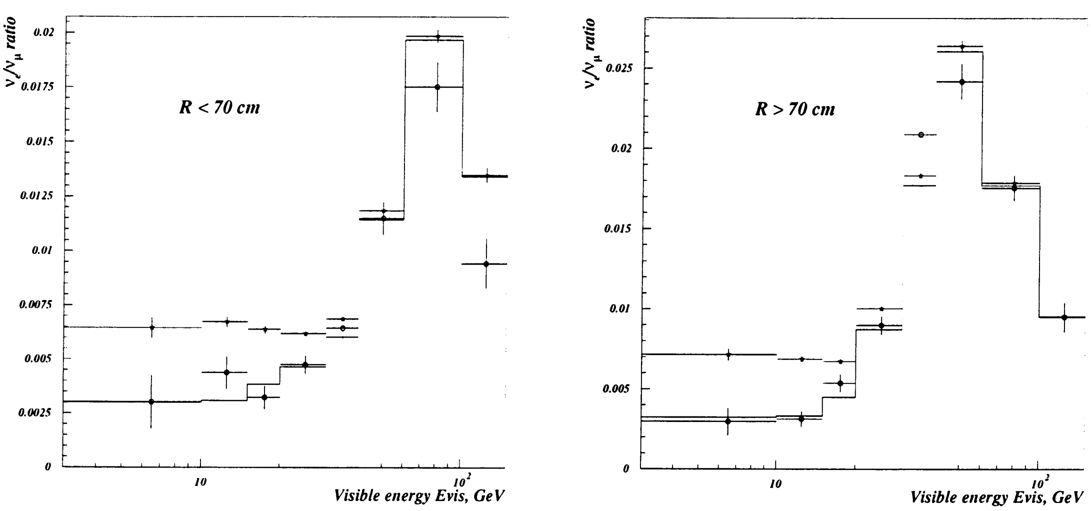

Figure 7.11: Comparison of $R_{e\mu}$ ratio for the sum of 1995 and 1996 data (open circles) with the EP Monte Carlo prediction assuming no contribution from oscillations (histogram) in inner (R < 70 cm, left) and outer (R > 70 cm, right) radial bins as a function of the visible energy E_{vis}. The signal expected in NOMAD in case of $\nu_\mu \to \nu_e$ oscillations with the minimum χ^2 LSND solution ($\Delta m^2 = 19$ eV^2, $\sin^2 2\theta = 0.006$) [34] is shown in asterisks. The total estimated non-prompt background is added to the Monte Carlo predictions. The errors are only statistical.

The χ^2 as a function of two unknown physical parameters – $\sin^2 2\theta$ and Δm^2 – is computed as

$$\chi^2 = \sum_i \sum_j \frac{(R_{ij} - R_{ij}^{MC}(\sin^2 2\theta, \Delta m^2))^2}{\sigma_{stat}^2 + \sigma_{syst}^2} \qquad (7.17)$$

where R_{ij} is the ν_e/ν_μ ratio in the i-th visible energy and j-th radial bin and σ_{stat} is its statistical error. The systematic error of the Monte Carlo prediction σ_{syst} could be estimated as

$$\sigma_{syst} = \varepsilon \cdot R_{ij}^{MC}(\sin^2 2\theta, \Delta m^2) \qquad (7.18)$$

where ε is the relative error independent of the visible energy E_i^{vis} and the radius R_j^2.

Instead of minimizing the χ^2, we can perform the maximization of the log-likelihood function[1]

$$\begin{aligned} ln\mathcal{L} &= \sum_i \sum_j \Big(N_{ij}^{\nu_e} \cdot ln\left(1 + 1 \Big/ R_{ij}^{MC}(\sin^2 2\theta, \Delta m^2)\right) + \\ &\qquad N_{ij}^{\nu_\mu} \cdot ln\left(1 + R_{ij}^{MC}(\sin^2 2\theta, \Delta m^2)\right)\Big) \end{aligned} \qquad (7.19)$$

where $N_{ij}^{\nu_e}, N_{ij}^{\nu_\mu}$ are the numbers of observed ν_e and ν_μ events in the i-th visible energy and j-th radial bin. As for the χ^2 minimization, the point ($\sin^2 2\theta_{max}$, Δm^2_{max}) is the best

---

[1] Both are performed with the help of the MINUIT [114] function minimization package.

estimate of the oscillation parameters. The asymptotic behavior of the function $-2ln\mathcal{L}$ is identical to that of the χ^2-function and the inequality (7.16) holds true.

7.5.2 Unified approach

Another method to calculate the confidence region is given by a unified approach to the classical statistical analysis, described in [113] and recently recommended by the PDG [3]. As shown in [113], the unified approach avoids the difficulties in setting the confidence region which are caused by the non-Gaussian nature of the oscillation probability function, its one-dimensionality in some regions of the $\sin^2 2\theta$ - Δm^2 plane and the proximity to the unphysical region. As a result, unlike the global scan which has regions of undercoverage and overcoverage, the unified approach gives the confidence region with proper coverage.

The χ^2 estimator used by the unified approach takes into account the absolute normalization of the ν_e/ν_μ ratio predicted by the Monte Carlo through an additional parameter r. Then in the χ^2 calculations the MC predicted ratio is scaled by r and an additional term appears:

$$\chi^2 = \sum_i \sum_j \frac{(R_{ij} - r \cdot R_{ij}^{MC}(\sin^2 2\theta, \Delta m^2))^2}{\sigma_{stat}^2 + \sigma_{syst}^2} + \frac{(r-1)^2}{\sigma_r^2} \tag{7.20}$$

where σ_r is the estimation of the overall normalization uncertainty.

Since the unified Feldman – Cousins approach gives the confidence regions with exact coverage, it is used to calculate the final results of our $\nu_\mu \rightarrow \nu_e$ oscillation search. We think it useful to present also the confidence regions set by the global scan method, as they can be compared with those obtained by the neutrino oscillation search experiments conducted in the past.

7.6 Results of the $\nu_\mu \rightarrow \nu_e$ oscillation search

The results of the $\nu_\mu \rightarrow \nu_e$ oscillation search presented in this section are based on the data collected during the 1995 and 1996 NOMAD runs. The measured $R_{e\mu}$ distribution as a function of the total visible energy is compared with the Monte Carlo predictions in two radial bins and the 90% C.L. exclusion limit on the parameters of oscillations is set. The calculations of the confidence region are performed using the two methods described in Sec. 7.5.

Together with the upper limit, the sensitivity of the experiment is computed, which is defined as the average upper limit that would be obtained by an ensemble of experiments with the expected background and no true signal. The sensitivity curve is computed replacing the experimental data by the Monte Carlo prediction assuming no oscillations, with statistical errors of the data sample.

The 90% C.L. exclusion region on $\sin^2 2\theta$ – Δm^2 plane and the sensitivity of the experiment calculated by the global scan method with the likelihood estimator (7.19) are shown in Fig. 7.12 for the EP (left) and FLUKA92 (right) Monte Carlo simulations (only

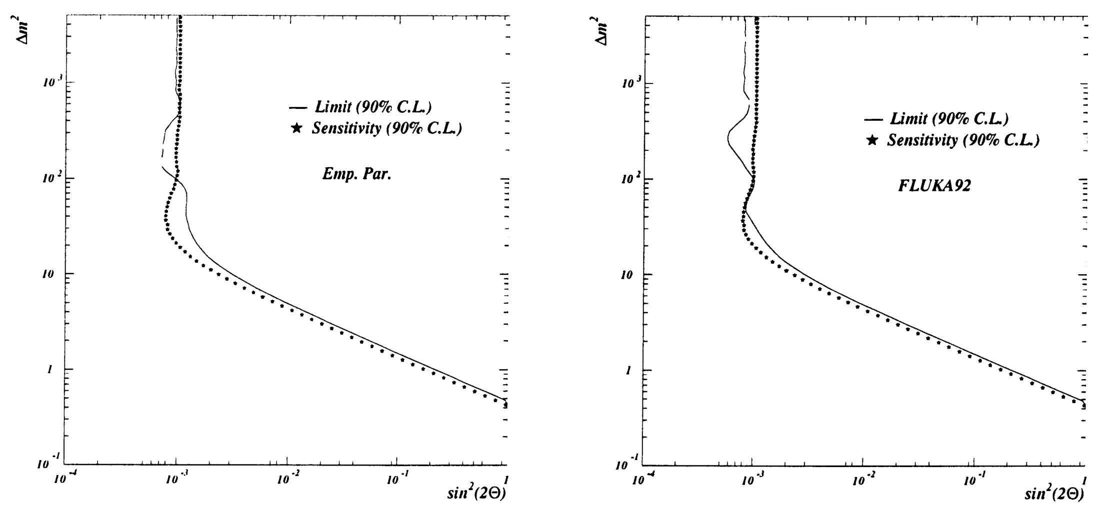

Figure 7.12: The 90% C.L. exclusion region (to the right of the solid line) for the EP (left) and FLUKA92 (right) MC predictions, as determined by the global scan method with the likelihood estimator (7.19). The experimental sensitivity is shown in stars. Only statistical errors are considered.

statistical errors are considered). The region of $\sin^2(2\theta) > 9.6\cdot10^{-4}$ ($> 8.2\cdot10^{-4}$) for the EP (FLUKA92) flux predictions is excluded at large (> 1000 eV^2) Δm^2 at 90% C.L. The experiment is sensitive to the region of $\sin^2(2\theta) > 1.0\cdot10^{-3}$ (at large Δm^2). The limit and sensitivity curves are close to each other as expected. Due to random fluctuations, the upper limit is more stringent than the sensitivity for some values of Δm^2 and less stringent for others.

The χ^2 estimator (7.17) allows the inclusion of systematic errors in the calculations of the confidence region and experimental sensitivity. The 90% C.L. excluded regions obtained by the global scan method with the χ^2 estimator for several values of ε (7.18) are shown in Fig. 7.13 for the EP Monte Carlo predictions. The upper limit on $\sin^2(2\theta)$ varies from $1.1\cdot10^{-3}$ to $1.6\cdot10^{-3}$ for 0% to 10% variation of the absolute uncertainty (at large Δm^2); the corresponding variation in the sensitivity is $1.0\cdot10^{-3}$ to $1.5\cdot10^{-3}$.

The 90% C.L. contours set by the unified approach [113] using the χ^2 estimator given by Eq. (7.20) are shown in Fig. 7.14 for the EP (left) and FLUKA92 (right) Monte Carlo predictions (the errors are only statistical). The region of $\sin^2(2\theta) > 9.7\cdot10^{-4}$ ($> 8.2\cdot10^{-4}$) for the EP (FLUKA92) flux predictions is excluded at large Δm^2, very similar to that ruled out by the global scan method.

7.7 Systematic uncertainties in the prediction of ν_e/ν_μ ratio

In the following sections we discuss the various sources of potential systematic errors and attempt to evaluate their impact on the results of the oscillation search. We start

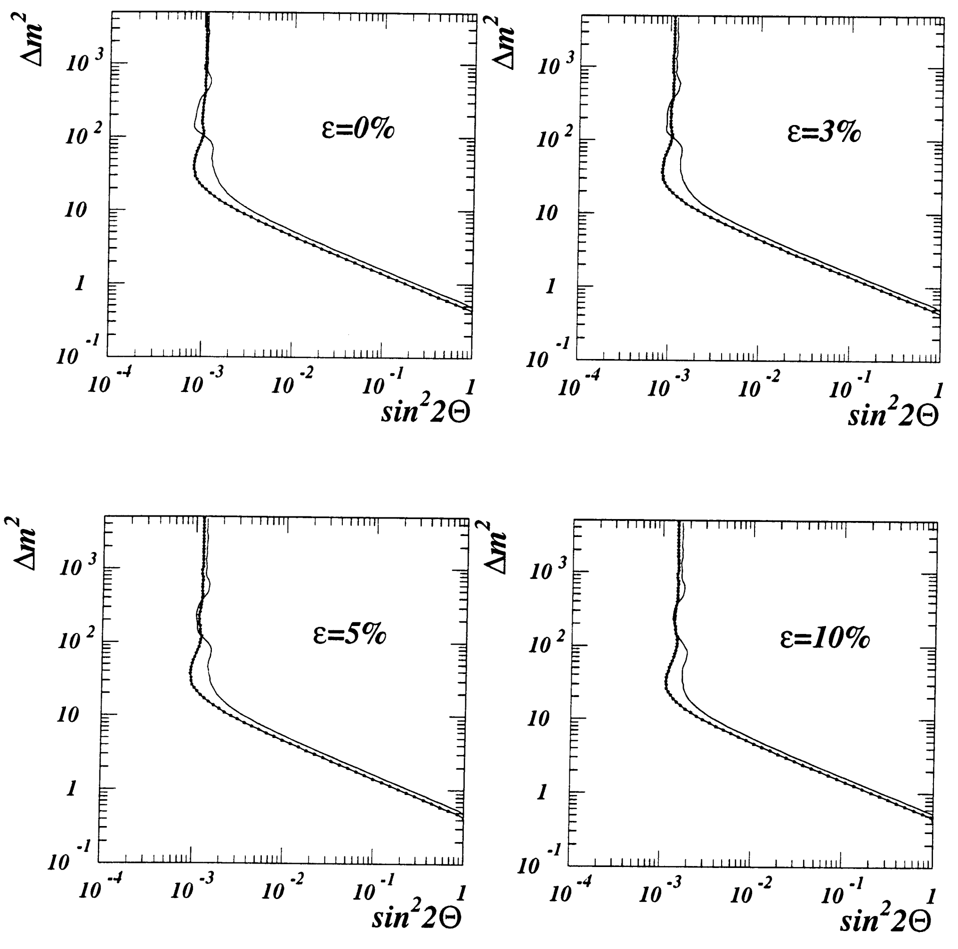

Figure 7.13: The 90% C.L. exclusion region as determined by the global scan method with the χ^2 estimator (7.17), assuming null, 3%, 5% and 10% systematic error independent of the visible energy and the radial position. The sensitivity limit of the experiment is shown in dots. The description of neutrino flux is given by the empirical parametrization.

with a discussion of the uncertainties in the efficiency of the kinematic selection and in the predictions of the non-prompt background.

7.7.1 Uncertainty of kinematic selection efficiency

It is essential to evaluate the accuracy of the non-prompt background estimation, both its content and its dependence on the kinematic variables used to isolate the $e^\pm$ signal. It is equally important to determine the dependence of the relative ν_e/ν_μ efficiency on the isolation variables.

The Monte Carlo simulation of neutrino interactions does not describe equally well all distributions of the observed data. The discrepancies are mostly due to the unprecise hadron jet description in the Monte Carlo. This is particularly clear in the purely trans-

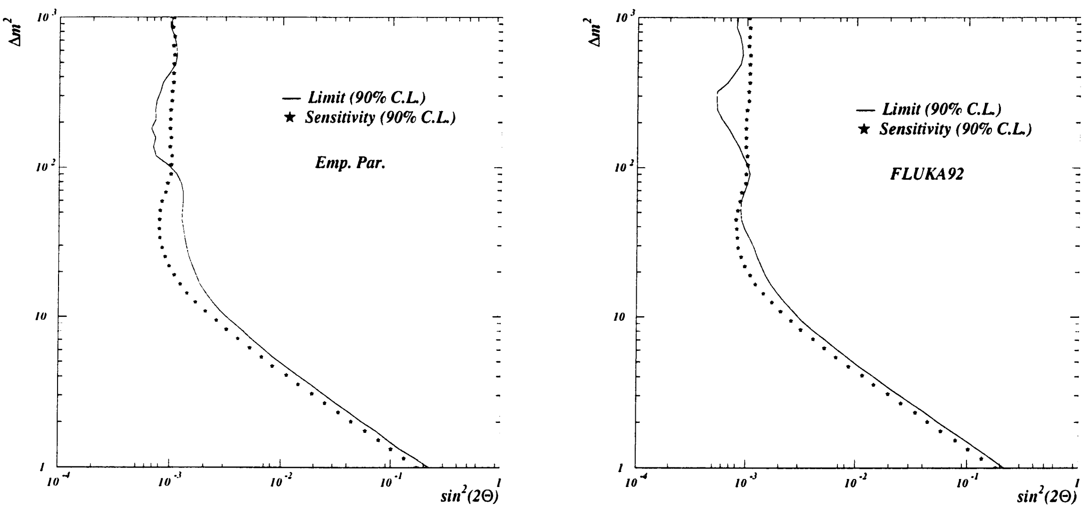

Figure 7.14: The 90% C.L. exclusion region for the EP (left) and FLUKA92 (right) MC predictions, as determined by the unified approach [113] (only statistical errors are considered). The experimental sensitivity is shown in stars.

verse variables, such as the azimuthal angle between the lepton and the hadron jet vectors in the transverse plane ϕ^t_{lh} and the missing transverse momentum $\not{p}_T$. The comparison between the simulated and observed ϕ^t_{lh} and $\not{p}_T$ distributions for e^- and μ^- samples (no kinematic cuts imposed) is shown in Fig. 7.15.

The distributions of ϕ^t_{lh} and q_{lep}, the component of lepton momentum transverse to the hadron jet direction, were used for the kinematic selection of both $\mu^\pm$ and $e^\pm$ events. When the q_{lep} distribution is described by the simulation rather well (Fig. 7.16), the ϕ^t_{lh} is not. Therefore, the efficiency of the kinematic cuts, calculated from the Monte Carlo, would be incorrect, which would give rise to errors when comparing data with absolute Monte Carlo predictions.

However, for the $\nu_\mu \to \nu_e$ oscillation search it is sufficient to determine the relative ν_e/ν_μ efficiency dependence on the isolation variables. For this purpose, instead of comparing the transverse kinematic distributions in the data with the corresponding MC predictions, we compare the e^- data with the μ^- data. To perform the comparison, μ^- data events are reweighted for the relative expected ν_e/ν_μ flux and the ν_e/ν_μ Monte Carlo estimated efficiency.[1] The appropriately normalized non-prompt background contributions are added to reweighted μ^- data events and the resulting prediction (the data simulator) is compared with the e^- sample.

A comparison of ϕ^t_{lh} and $\not{p}_T$ for the e^- sample, without kinematic cuts, with the data simulator is shown in Fig. 7.17. The solid circles are the sum of 1995 and 1996 data, the hatched histogram shows the sum of the estimated ν_μ CC and NC contributions to the

---

[1] It should be noted that the transverse variables are largely insensitive to the relative flux weights.

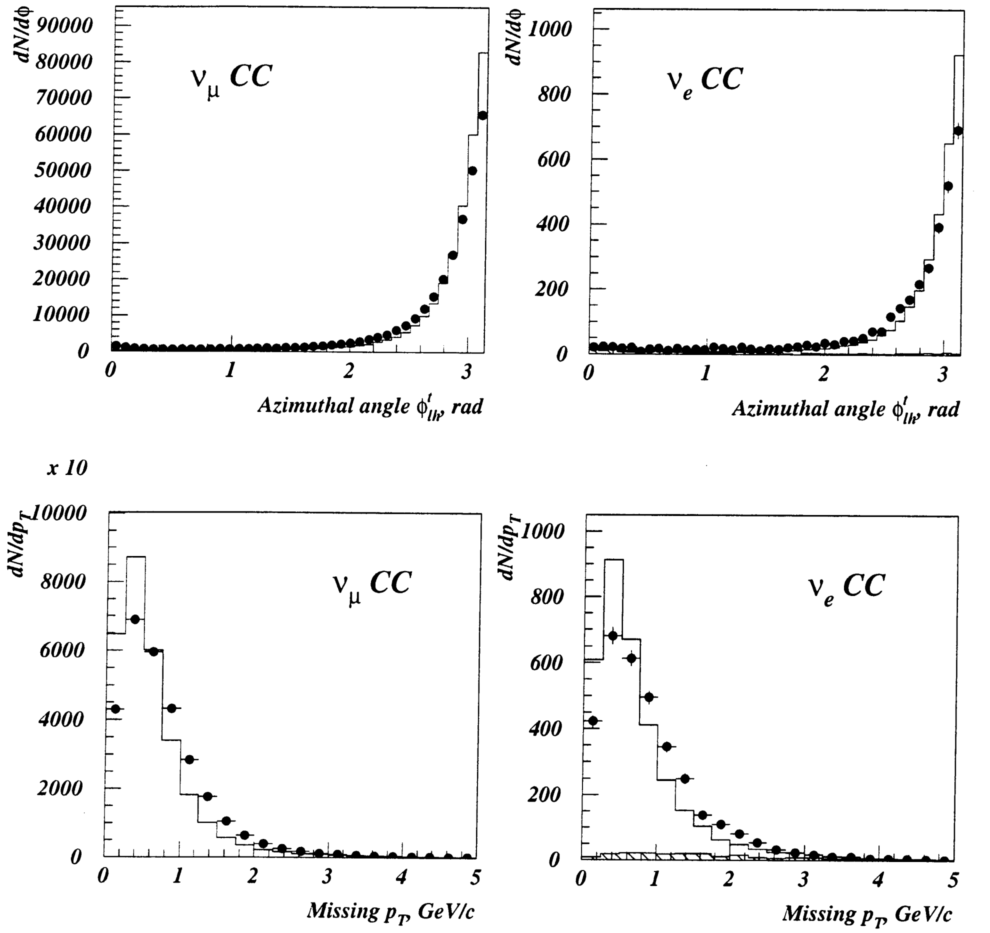

Figure 7.15: Comparison of the azimuthal angle ϕ^t_{lh} (top) and the missing transverse momentum $\not{p}_T$ (bottom) for the observed and Monte Carlo simulated μ^- (left) and e^- (right) events. The solid circles are the sum of 1995 and 1996 data, the solid histogram is the Monte Carlo prediction (including the non-prompt background). The non-prompt background contribution to the e^- sample is shown separately in hatched histogram. No kinematic cuts are imposed.

e^- sample, the solid histogram is the μ^- data simulator (sum of the μ^- reweighted data and the expected non-prompt background). The μ^- data simulator describes the electron data sample very well. It is evident that the ϕ^t_{lh} region below $\pi/2$ for the e^- sample has a significant contribution from the non-prompt background.

Good agreement between e^- sample and data simulator indicates that the relative ν_e/ν_μ selection efficiency is not very sensitive to the choice of the kinematic isolation cuts. A direct estimate of the uncertainty of the ν_e/ν_μ and $\bar{\nu}_e/\bar{\nu}_\mu$ ratios to the kinematic selection criteria is described in the next section.

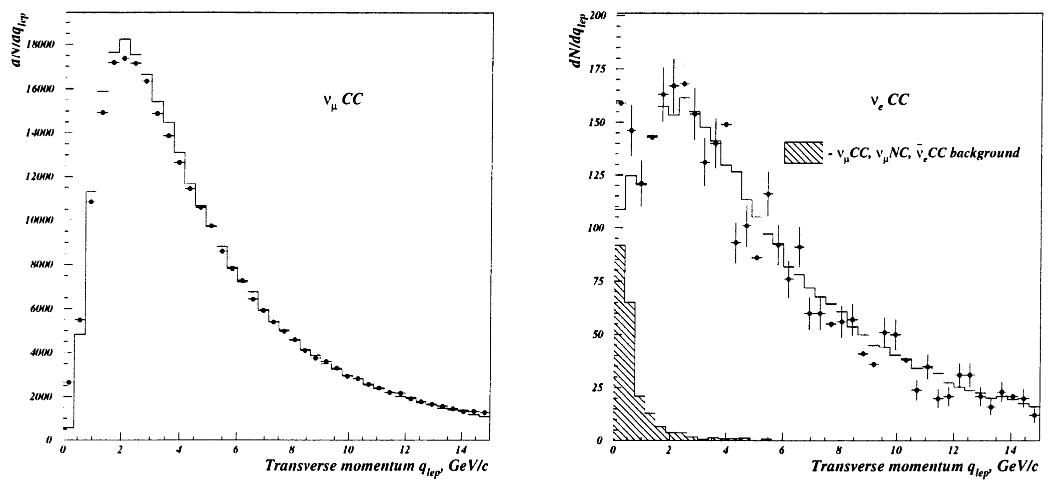

Figure 7.16: Comparison of q_{lep} for the observed and Monte Carlo simulated μ^- (left) and e^- (right) events. The solid circles are the sum of 1995 and 1996 data, the solid histogram is the Monte Carlo (EP) prediction (sum of the prompt and non-prompt components). The non-prompt background contribution to the e^- sample is shown separately in hatched histogram. No kinematic cuts are imposed. Note that for e^- events the q_{lep} region below 1 GeV, normally rejected by kinematic cuts, is largely populated by the non-prompt background and is acceptably described by the sum of the prompt and non-prompt estimates.

7.7.2 Stability of the ν_e/ν_μ ratio with respect to the kinematic cuts

An important check to be performed is to study the stability of $e^\pm$ and $\mu^\pm$ samples and of their ratios under varying kinematic cuts. For this purpose, we compute the unfolded number of events (see Sec. 7.1) under two additional sets of kinematic cuts based upon the q_{lep} and ϕ^t_{lh} variables. These two sets of cuts were chosen to be "tight" and "loose" with respect to the "standard" selection criteria discussed in Sec. 6.5. The choice of loose cuts causes about a 10% increase in the observed number of μ^- and e^- events, while tight cuts reduce the number of the selected events by about 25%, as illustrated in Table 7.7.

For each set of cuts, the total expected non-prompt background was estimated. For the e^- sample, it varies from ~1% of the e^- events for the loose cuts to essentially zero background for the tight cuts. A larger background contribution (between 4 and 20%) is present in the e^+ sample. The parameters of the cuts, the number of the observed $\mu^\pm$ and $e^\pm$ events and the total estimated non-prompt background contribution to each data sample are shown in Table 7.7.

The number of expected beam-induced neutrino charged current interactions, background subtracted and corrected by the efficiency according to Eq. (7.2) and (7.3), is shown in Table 7.8. Also shown are the ν_e/ν_μ and $\bar{\nu}_e/\bar{\nu}_\mu$ ratios and the minimum and maximum deviations from the corresponding numbers obtained for the "standard" selec-

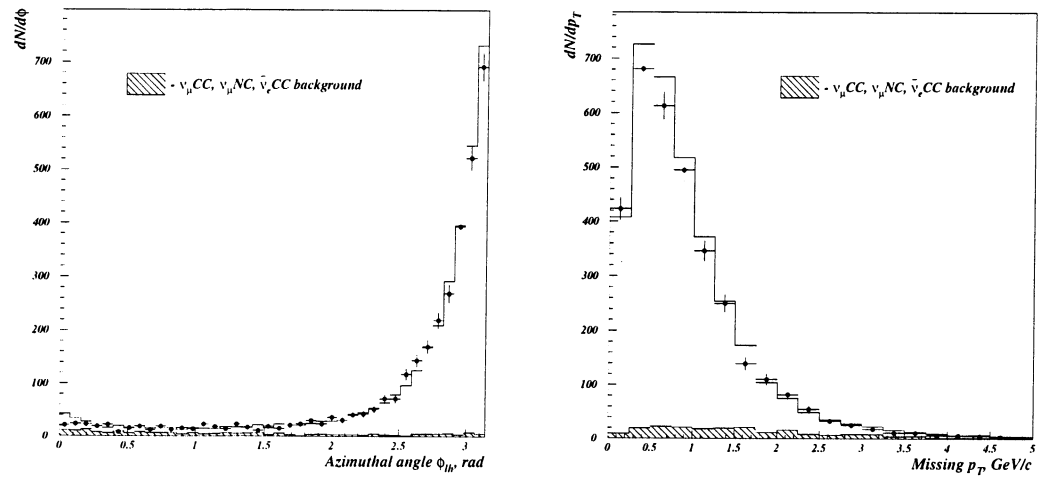

Figure 7.17: Comparison of ϕ^t_{lh} (left) and $\not{p}_T$ (right) for the e^- events with the data simulator. The solid circles are the sum of 1995 and 1996 data, the hatched histogram shows the non-prompt background contribution for e^- events, the solid histogram is the μ^- data simulator prediction (including the non-prompt background). No kinematic cuts are imposed.

tion criteria. The variations in ν_e/ν_μ ($\bar{\nu}_e/\bar{\nu}_\mu$) ratios do not exceed ±5% (±15%) and are within the statistical errors of the prompt e^- (e^+) samples. We conclude that the ν_e/ν_μ and $\bar{\nu}_e/\bar{\nu}_\mu$ ratios are stable with respect to the choice of kinematic cuts within the statistical errors of the data samples. However, we conservatively use the change in the value of the ν_e/ν_μ ratio under variation of the kinematic cuts as an estimate of the systematic uncertainty associated with the kinematic selection efficiency. The fractional difference found in the sum of 1995 and 1996 data is 3.8%.

7.7.3 Uncertainty of non-prompt background estimation

The correctness of our estimation of the absolute amount and the shape of the non-prompt background has already been indirectly verified in the studies of the uncertainties with respect to the choice of the kinematic cuts. As was pointed out in Sec. 7.7.2, any serious discrepancy between the predicted non-prompt background contribution to the $e^\pm$ samples and its actual amount and shape would result in large variations in the fully corrected number of events under various kinematic cuts, which have not been observed.

The uncertainty of the non-prompt background estimation can be evaluated directly by using the data samples consisting mostly of non-prompt induced events and complementary to the selected $e^\pm$ samples dominated by the ν_e and $\bar{\nu}_e$ CC interactions. Two data samples were studied for this purpose:

- $e^\pm$ at the primary vertex that failed the kinematic isolation cuts;

1995 data									
	q^0_{lep}	ϕ^0_{lh}	μ^-	μ^+	*bckg*	e^-	*bckg*	e^+	*bckg*
Loose	0.0	1.0	88 384	2 045	130	965	9	112	21
Standard	0.1	1.9	81 138	1 816	85	880	3	93	11
Tight	1.5	2.3	57 823	1 356	41	645	1	62	3
1996 data									
	q^0_{lep}	ϕ^0_{lh}	μ^-	μ^+	*bckg*	e^-	*bckg*	e^+	*bckg*
Loose	0.0	1.0	186 596	4 380	249	1 930	16	249	35
Standard	0.1	1.9	171 781	3 983	155	1 780	5	203	19
Tight	1.5	2.3	123 673	3 003	66	1 337	2	149	6

Table 7.7: The parameters of the kinematic isolation cuts (defined in Sec. 6.5), the number of the selected events and the total estimated non-prompt background for μ^-, μ^+, e^- and e^+ 1995 and 1996 data samples under various kinematic cuts.

- $e^\pm$ passing the kinematic cuts but failing the distance cut.

The latter sample could not be used for a statistically significant test of the non-prompt background: the $e^\pm$ events in the vicinity of the primary vertex but failing the distance cut (15 cm < ΔZ[1] < 50 cm) are still largely dominated by the prompt ν_e and $\bar{\nu}_e$ components, whereas the sample of $e^\pm$ events observed far from the primary vertex and passing the kinematic selection has poor statistics (18 e^+ events observed and 22.3 events predicted in 1995 and 1996 data with $\Delta Z > 50$ cm and the standard set of identification and isolation cuts).

However, the samples of $e^\pm$ events that failed the kinematic cuts are well suited to estimate the uncertainty in the prediction of the non-prompt background. In particular, the positron sample that fail the kinematic isolation cuts has reasonable statistics and is largely populated by non-prompt background events; the corresponding prompt $\bar{\nu}_e$ contribution to this sample is at the 12% level, as determined from the Monte Carlo simulation.

The number of positron events failing the kinematic cuts, N^{data}_{e+}, found in 1995 and 1996 data samples is:

$$N^{data}_{e+} = 437 \pm 21. \tag{7.21}$$

The estimated ν_μ NC and ν_μ CC contribution to this sample is 344.6 events. A smaller contribution from the $\bar{\nu}_e$ CC events that fail the kinematic cuts is 49.0 events. This estimation is based on the Monte Carlo simulation and uses the relative flux as determined by the empirical parametrization. The total expected number of positron events that fail

---

[1] the distance between the reconstructed primary vertex and the first hit of the $e^\pm$ candidate track; for a discussion on the distance cut see Sec. 6.3.3.

			1995 data			
	ν_μ CC	$\bar{\nu}_\mu$ CC	ν_e CC	$\bar{\nu}_e$ CC	ν_e/ν_μ	$\bar{\nu}_e/\bar{\nu}_\mu$
Loose	179 861	4 704	2 668	296	1.48	6.3
Standard	175 177	4 548	2 566	284	1.46	6.3
Tight	172 866	4 449	2 406	238	1.39	5.3
Variation, %	-1.3 +2.7	-2.2 +3.4	-6.2 +4.0	-16.2 +4.2	-5.0 +1.3	-14.5 +0.1
			1996 data			
	$\nu_\mu CC$	$\bar{\nu}_\mu CC$	$\nu_e CC$	$\bar{\nu}_e CC$	ν_e/ν_μ	$\bar{\nu}_e/\bar{\nu}_\mu$
Loose	387 982	10 171	5 539	702	1.43	6.9
Standard	378 943	10 041	5 433	622	1.43	6.2
Tight	377 566	9 930	5 241	603	1.39	6.1
Variation, %	-0.4 +2.4	-1.1 +1.3	-3.5 +1.9	-3.1 +12.9	-3.2 +0.0	-1.9 +11.5

Table 7.8: The number of unfolded ν_μ, $\bar{\nu}_\mu$, ν_e and $\bar{\nu}_e$ charged current events in 1995 and 1996 data under various kinematic cuts. Also shown are the ν_e/ν_μ and $\bar{\nu}_e/\bar{\nu}_\mu$ ratios and the minimum and maximum deviations (in %) of the fully corrected number of events and their ratios from those for the "standard" selection criteria.

the kinematic cuts, N_{e+}^{MC}, is therefore:

$$N_{e+}^{MC} = 393.6 \pm 10.0. \tag{7.22}$$

The errors quoted above are only statistical. The observation and prediction agree rather well within the statistical accuracy of the samples. However, the fractional difference between the two central values is 11%. If we conservatively attribute all the observed difference to the inaccuracy of the prediction of the non-prompt background contribution by the Monte Carlo simulation, we find that the background could be underestimated by:

$$\frac{N_{e+}^{data} - N_{e+}^{MC}}{N_{bckg}^{MC}} = \frac{437 - 393.6}{344.6} = (12.6 \pm 6.7)\%. \tag{7.23}$$

The electron events that fail the kinematic cuts have a much larger contribution from the ν_e CC interactions: about 60% of the sample are ν_e induced events. The number of electron events in 1995 and 1996 data samples failing the kinematic cuts, N_{e-}^{data}, is:

$$N_{e-}^{data} = 680 \pm 26. \tag{7.24}$$

The Monte Carlo estimated ν_μ NC and ν_μ CC contribution to this sample is 299.6 events, that from the ν_e CC events that fail the kinematic cuts is 440.4 events. The total expected number of electron events that fail the kinematic cuts, N_{e-}^{MC}, is therefore:

$$N_{e-}^{MC} = 740.0 \pm 9.1. \tag{7.25}$$

Again, only statistical errors are quoted. The fractional difference between the central values of the observation and prediction is about 8%. If once again we assume that all the observed difference is due to the error in the prediction of the non-prompt background by the Monte Carlo simulation, we find that the estimation of the background contribution could be erroneous by:

$$\frac{N_{e^-}^{data} - N_{e^-}^{MC}}{N_{bckg}^{MC}} = \frac{680 - 740.0}{299.6} = (-20.0 \pm 9.3)\%. \tag{7.26}$$

The two checks on the background evaluation presented above indicate that the error in the Monte Carlo estimation of the absolute amount of non-prompt background does not exceed 25%. Therefore, we conservatively assign a 25% systematic error on the non-prompt background estimate.

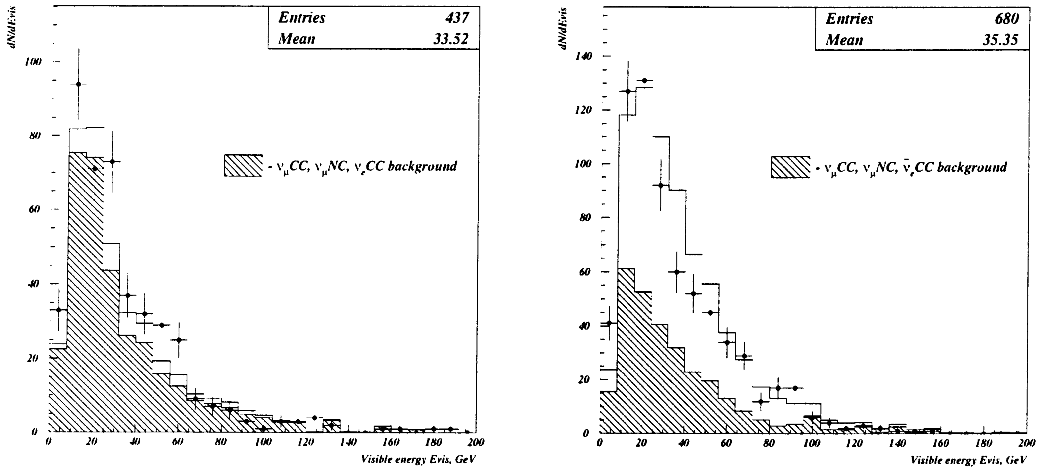

Figure 7.18: Comparison of the observed and predicted energy spectra for the e^+ (left) and e^- (right) events that failed the kinematic cuts. The solid circles are the sum of 1995 and 1996 data, the hatched histogram shows the total non-prompt background contribution, the solid histogram is the sum of the non-prompt and prompt components as predicted by the Monte Carlo (EP) simulation.

Since it is expected that the non-prompt background will populate the region of the energy spectrum below ~25 GeV – the most sensitive to the $\nu_\mu \rightarrow \nu_e$ oscillation induced signal, the accurate description of the background energy shape is also important. A comparison of the observed and predicted energy spectra for the e^+ and e^- events that failed the kinematic cuts is shown in Fig. 7.18. As was already mentioned, the e^+ sample is largely dominated by the non-prompt background component (hatched histogram), whereas the e^- sample contains a large fraction of the beam-induced ν_e events. The energy spectrum of the non-prompt sources indeed peaks at energies about 15–20 GeV. The shape of the sum of the non-prompt and prompt contributions as predicted by the Monte Carlo simulation agrees well with the measured energy spectrum for both e^+ and e^- samples. We conclude that within the present statistical error no additional systematic uncertainty needs to be added to account for the differences in the shape of the non-prompt background in the data and MC.

To study the impact of the systematic uncertainty in the non-prompt background estimation on the excluded region of the oscillation parameters, the 90% C.L. upper limit was recalculated varying the non-prompt background contribution to the e^- event sample by ±25% and ±50%. The non-prompt background component was scaled proportionally to its predicted amount in a given energy bin. The maximum change in the value of $\sin^2(2\theta)$ produced by these variations is at the level of $\pm 2 \cdot 10^{-5}$ for large Δm^2, regardless the flux prediction and the method of upper limit calculation. Such stability of the excluded region of oscillation parameters under varying a non-prompt background contribution could probably be explained by a very small ($\approx$0.4%) contamination of the selected e^- sample by the non-prompt sources.

The result obtained in this section leads us to neglect the systematic uncertainty on the non-prompt background estimate in the calculations of the systematic error on the oscillation parameters.

7.7.4 Uncertainty of total visible energy scale

The search for $\nu_\mu \to \nu_e$ oscillations presented here is performed by comparing the observed ν_e/ν_μ ratio with that predicted by the Monte Carlo simulation as a function of the total visible energy. If the total visible energy scale were different in the data from that predicted by the simulation, it would induce a shift in the observed ratio as a function of energy with respect to the prediction. Therefore, it is important to estimate the uncertainty of the energy scale and energy resolution and their impact on the systematic error of our analysis.

The total visible energy E_{vis} was computed as the sum of the leptonic and hadronic energies (see Sec. 6.4). A comparison of the leptonic and hadronic components of the total visible energy for the observed and Monte Carlo simulated μ^- and e^- events is shown in Fig. 7.19. The leptonic energy scale (Fig. 7.19, top) is described well by the Monte Carlo predictions. The average energy of the hadronic jet, however, is overestimated by the Monte Carlo simulation by about 6%, both in ν_μ CC and ν_e CC events (Fig. 7.19, bottom). This difference could introduce a discrepant shift in the total visible energy scale which would result in an additional error on the oscillation parameters.

Basing analysis on the $R_{e\mu}$ ratio should reduce the impact of the difference in the visible energy scale, as long as the discrepancy is similar in ν_μ CC and ν_e CC events. In order to study how significant the effect of the energy mismatch on the oscillation parameters could be, we estimate neutrino energy E_ν by several methods independent from our standard approach and compare the resulting confidence regions.

The following alternative methods for E_ν estimation have been used:

- the so-called "double-angle" method uses the relatively well-measured lepton energy

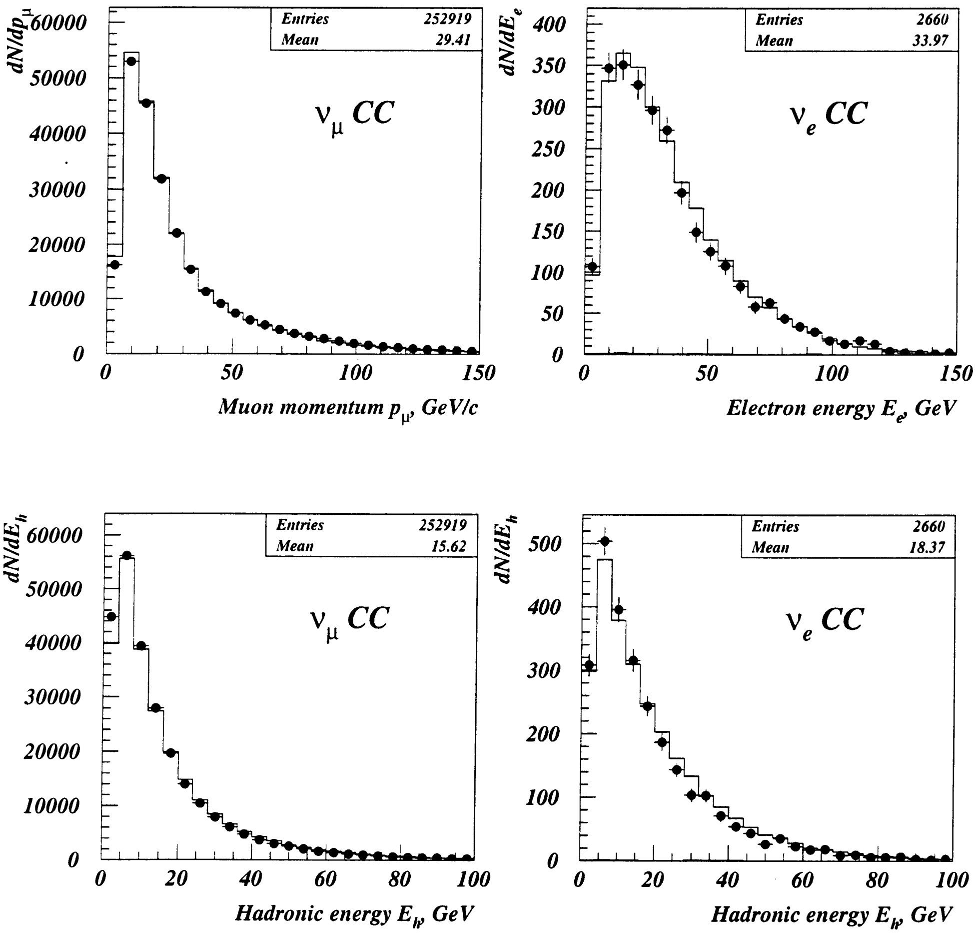

Figure 7.19: Comparison of the leptonic energy (top) and the hadronic energy (bottom) for the observed and Monte Carlo simulated ν_μ CC (left) and ν_e CC (right) events. The solid circles are the sum of 1995 and 1996 data, the solid histogram is the EP Monte Carlo prediction (including non-prompt background). The non-prompt background contribution for e^- events is also shown separately in hatched histogram.

and direction, only the direction of the hadron jet, and energy and momentum conservation for the energy calculation:

$$E_{da} = E_{lep}\frac{\sin\gamma + \sin\theta + \sin(\gamma+\theta)}{2\sin\gamma} \tag{7.27}$$

where γ, θ are defined in Fig. 7.20.

- in the so-called Myatt kinematics [116] extensively used in the bubble chamber experiments, the measured energy of the hadron jet, E_h, is rescaled by the ratio of the transverse components of the momentum of the lepton, p^T_{lep}, and of the jet, p^T_{had}, to

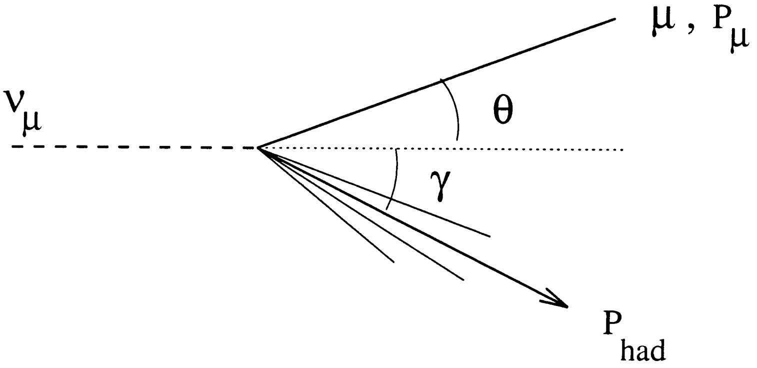

Figure 7.20: Definition of the angles used for the "double-angle" method of calculating E_{vis} [115].

account for the losses in the hadron jet reconstruction:

$$E_{Myatt} = E_{lep} + E_h \frac{p^T_{lep}}{p^T_{had}} \tag{7.28}$$

- the total momentum estimate

$$P_{tot} = |\sum_i \vec{p_i}| = |\vec{p_{lep}} + \vec{p_h}| \tag{7.29}$$

is based on the fact that $E_\nu = |\vec{P_\nu}| = |\vec{P_{tot}}|$, neglecting the Fermi momentum of the nucleon.

The momenta, energies and angles used in the above-mentioned equations are computed according to the energy flow reconstruction algorithm described in Sec. 6.4.

A comparison of the resolution $\delta E_\nu / E_\nu = (E - E_\nu^{MC})/E_\nu^{MC}$ for the neutrino energy E_ν reconstructed by the "standard" ($E_{vis} = \sum |\vec{p_i}|$) and by the alternative methods described above is shown in Fig. 7.21 for the ν_μ CC Monte Carlo simulated events (after all selection criteria applied). The four independent approaches yield different biases and R.M.S.: both standard and P_{tot} methods underestimate E_ν on average (by 2.8% and 4.3% respectively) and have a relatively small R.M.S. (≈11%), whereas E_{da} and E_{Myatt} are E_ν overestimates (by 1.2% and 1.7%) with a larger R.M.S. (≈15%).

In order to estimate the impact of the energy scale uncertainty on the excluded region of oscillation parameters, we compare the upper limits on $\sin^2(2\theta)$ obtained with the alternative methods of E_ν calculation with that of our standard energy flow algorithm. The exclusion regions corresponding to different methods of neutrino energy reconstruction are shown in Fig. 7.22. All the four methods give consistent results. The maximum variation produced in the value of $\sin^2(2\theta)$ does not exceed $\pm 1.5 \cdot 10^{-4}$ for large Δm^2. We conclude

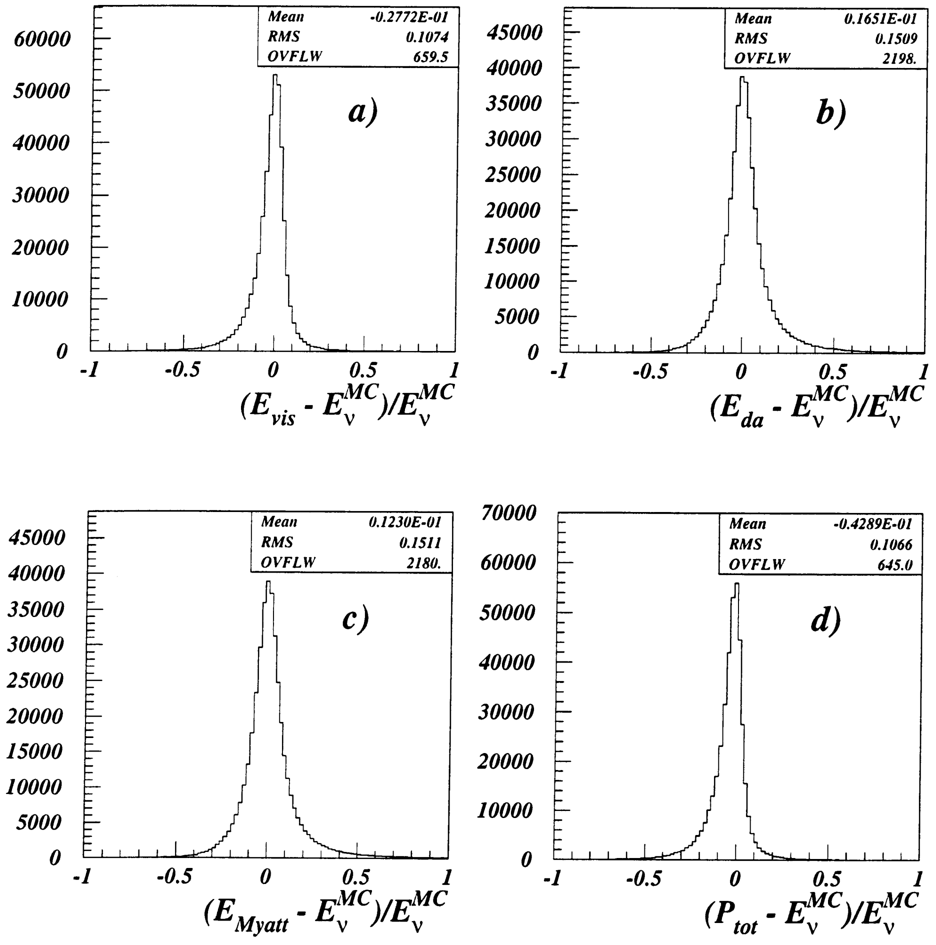

Figure 7.21: Resolution of the neutrino energy $\delta E_\nu/E_\nu = (E - E_\nu^{MC})/E_\nu^{MC}$ for the ν_μ CC Monte Carlo simulated events: a) standard method reconstruction; b) "double-angle" method reconstruction; c) Myatt kinematics; d) total momentum estimation.

that the uncertainty of the energy scale, conservatively estimated in our analysis, does not produce any significant impact on the result of the oscillation search.

An additional error could also arise from the uncertainty of the energy resolution. The width and tails of the energy resolution, if not well described by the simulation, could create the discrepancies between data and Monte Carlo, particularly in the low-energy region where the ν_μ CC and ν_e CC spectra are falling rapidly. An indication that the effect of the energy resolution uncertainty on the result is small has already been obtained by using the alternative methods of E_ν estimation which have worse resolution compared to the standard method. Another way to evaluate energy resolution effects is to introduce an additional energy smearing to the Monte Carlo events. The variation of the 90% C.L. upper limit on $\sin^2(2\theta)$ (at large Δm^2) and of the experimental sensitivity as a function of

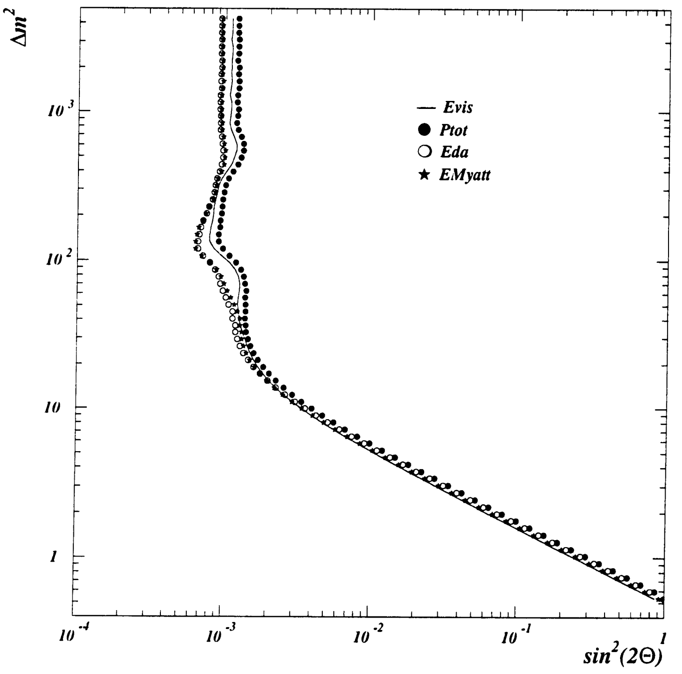

Figure 7.22: The 90% C.L. confidence regions corresponding to different methods of neutrino energy reconstruction: standard method (solid line), total momentum estimation (closed circles), "double-angle" method (open circles), Myatt kinematics (asterisks). The exclusion regions are determined by the global scan method, for the EP description of neutrino fluxes.

an additional gaussian-like smearing, σ, of 5%, 7.5%, 10% and 15% is shown in Fig. 7.23. A 15% smearing, which doubles the width of the expected energy resolution and is, in all probability, a significant overestimate, leads to a variation of $4.5{\cdot}10^{-5}$ in the value of $\sin^2(2\theta)$ for large Δm^2, which is negligibly small.

Based on the studies described in this section we conclude that no significant impact of the uncertainty in the energy scale or in the energy resolution upon the results of our analysis is expected.

7.7.5 Lepton identification uncertainty

The relative lepton identification efficiency, i.e. the efficiency to identify an electron with respect to a muon, can introduce systematic errors into the analysis. The relative e/μ identification uncertainty is dominated by that of an electron, more difficult to reconstruct and to identify than a muon. If the electron identification or reconstruction efficiency were incorrectly described by the Monte Carlo simulation, this error would not cancel considering $R_{e\mu}$ ratio and would affect the results of the analysis.

Due to the impossibility of an in-situ calibration of the detector by an electron beam,

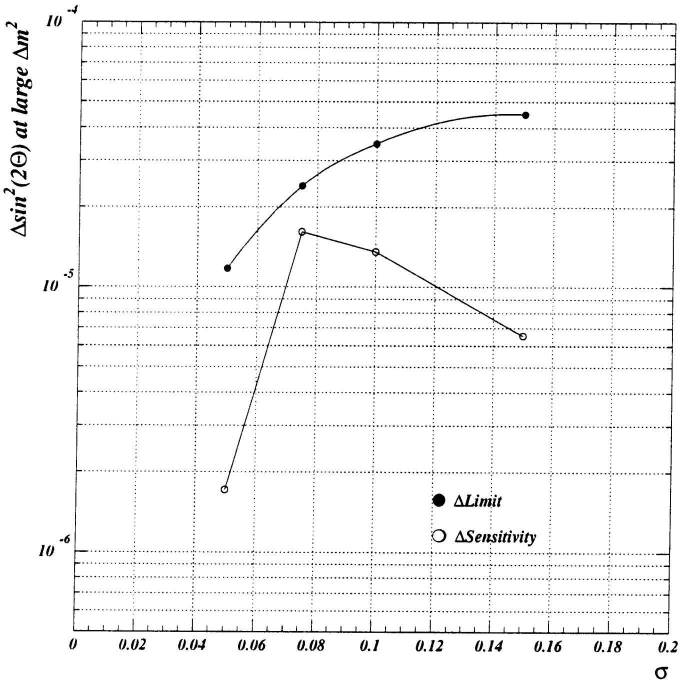

Figure 7.23: The variation of the 90% C.L. upper limit on $\sin^2(2\theta)$ (solid circles) and of the experimental sensitivity (open circles) at large Δm^2 as a function of an additional gaussian-like smearing σ (see text). The exclusion regions are computed by the global scan method, for the EP description of neutrino fluxes.

the choice of measurements which could be performed in NOMAD to demonstrate that the electron identification error is small is rather limited. One such measurement, the study of the TRD electron identification performance on a sample of δ electrons produced by through-going muons, was described in chapter 5. The measured value of the TRD electron identification efficiency, ε_e=(88.4±0.9)%, agreed well with the (89.9±1.1)% expected for the electrons in the energy range of 0.5–5 GeV (for a 10^3 pion rejection factor). The identification of electrons in the PRS and ECAL was based on the test-beam measurements [100]. A number of studies to estimate the systematic uncertainty of the electron identification and reconstruction from NOMAD data is under way at present:

- An increase in statistics of the accumulated sample of δ-ray electrons (including the 1995 and 1996 muon "flat-top" data) is being used to assess the TRD and ECAL electron identification error. The preliminary results of these studies show the consistency of the data with the Monte Carlo predictions and indicate that a possible discrepancy, if any, does not exceed the level of 2–3% [117].
- The absolute $e^{\pm}$ reconstruction efficiency is being examined on the 1996 data sample by matching TRD tracks to ECAL clusters, performing TRD identification, and looking for the existence of the matched DC tracks for the electron candidates. The pre-

liminary results yield the measured electron reconstruction efficiency of (97.7±0.4)%, to be compared with the 99.8% expected [118].

All these results indicate that the relative lepton identification uncertainty in NOMAD does not exceed the level of ~3-4%.

As a additional consistency check, we study the stability of the e^- sample under varying electron identification and conversion rejection cuts. As was described in the previous chapter, the basic electron identification is performed by the TRD, and the crucial cut for the conversion rejection is on the distance from the primary vertex. The values of the TRD identification and distance cuts were varied to study their impact on the exclusion region. The 90% C.L. upper limit on $\sin^2(2\theta)$ (at large Δm^2) and the experimental sensitivity are shown in Fig. 7.24 as a function of the TRD pion acceptance cut (left) and the distance cut (right). The following conclusions could be drawn:

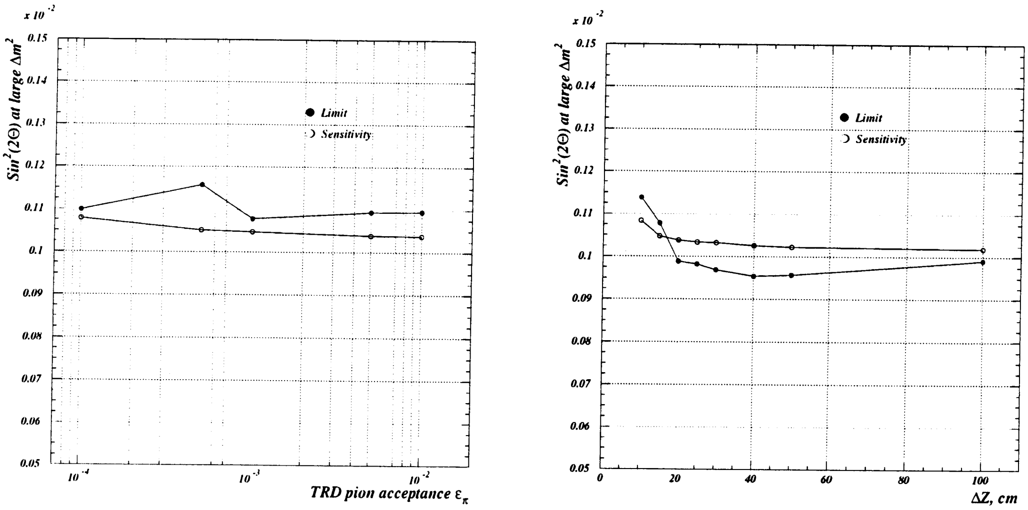

Figure 7.24: The 90% C.L. upper limit (solid circles) on $\sin^2(2\theta)$ (at large Δm^2) and the experimental sensitivity (open circles) as a function of the TRD pion acceptance cut (left) and the distance cut (right). The exclusion regions are computed by the global scan method, for the EP description of neutrino fluxes.

- The value of the TRD pion acceptance cut, ε_π, was varied by two orders of magnitude (from $\varepsilon_\pi = 10^{-4}$ to 10^{-2} with a standard cut at 10^{-3}) which results in a ±5% variation in the observed e^- sample. The corresponding variation in the upper limit on $\sin^2(2\theta)$ (Fig. 7.24, left) is remarkably small ($<1 \cdot 10^{-4}$).

- The distance cut was varied in the range of 10–100 cm (the standard value of the cut is 15 cm), which lead to a ±7.5% variation in the observed e^- sample. The corresponding variation in the upper limit is again at the level of $1 \cdot 10^{-4}$ (see Fig. 7.24, right).

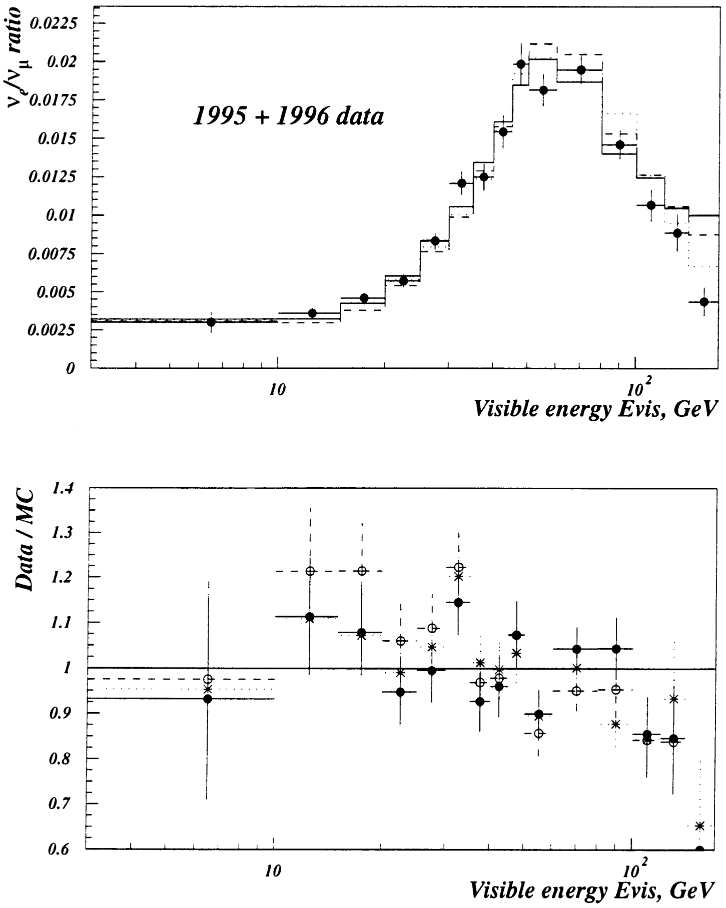

Figure 7.25: Top: the ratio of ν_e CC to ν_μ CC events as reconstructed in 1995 and 1996 data (solid points) compared to the predictions of the different Monte Carlo simulations as a function of the total visible energy E_{vis} (assuming no contribution from $\nu_\mu \rightarrow \nu_e$ oscillations). FLUKA92 predictions are shown in solid line, FLUKA95 – in dashed line, EP – in dotted line. Bottom: the ratio of $R_{e\mu}$ in 1995 and 1996 data to those predicted by FLUKA92 (solid circles), FLUKA95 (open circles) and EP (asterisks) simulations. The total estimated non-prompt background to ν_e CC interactions is appropriately added to the Monte Carlo predictions. Only statistical errors are shown.

Based on the results described in this section, we assign a 4.0% systematic error on the relative lepton efficiency.

7.7.6 Neutrino flux uncertainty

The uncertainty in the relative ν_e/ν_μ neutrino flux prediction is one of the largest contributions to the systematic uncertainties of the analysis (and probably the ultimate limitation of its sensitivity in the future). Bearing this in mind, the data distributions were deliberately compared throughout this chapter to the predictions of the three different flux simulation programs – FLUKA92, FLUKA95 and EP.

The scale of the variations in the ν_e/ν_μ ratio prediction could indicate the size of the uncertainties in the relative flux description. The ratio of ν_e CC to ν_μ CC events in 1995 and 1996 data is compared to the predictions of the different flux simulations as a function of the total visible energy in Fig. 7.25. The independent methods of the relative neutrino flux description give consistent predictions – the fluxes given by FLUKA and EP are in a good agreement as a function of E_{vis}.

The data – Monte Carlo comparison described in Sec. 7.3 leads us to conclude that at present the best description of the energy spectra and of the total number of events in the μ^-, μ^+ and e^+ samples – where no oscillation contribution is expected – is given by the empirical parametrization [53]. In addition, the EP is the only flux prediction for which the evaluation of systematic errors in the ν_e flux relative to ν_μ has been performed. The quoted overall normalization error in the ratio is 2.7%, arising mainly from 2.45% uncertainty in the K^+/π^+ prediction. An additional energy-dependent error was obtained as a 1σ spread in the ν_e/ν_μ prediction for consistent EP predictions. The energy-dependent error is small for neutrino energies below 30 GeV, but is comparable to the normalization error for energies greater than 75 GeV. It is reproduced in Table 7.9 (from ref. [53]).

Energy, GeV	Fractional error on ν_e/ν_μ, %
2.5 - 5	0.27
5 - 7.5	0.08
7.5 - 10	1.60
10 - 15	0.90
15 - 20	0.75
20 - 25	1.33
25 - 30	1.71
30 - 40	1.50
40 - 50	0.60
50 - 75	0.90
75 - 100	1.90
100 - 150	2.26
150 - 200	5.50
200 - 300	10.0

Table 7.9: Energy-dependent systematic error in the ν_e/ν_μ flux prediction in 14 energy bins, as given by the EP [53].

To set a limit on the parameters of $\nu_\mu \to \nu_e$ oscillations, we use the EP prediction of the relative ν_e/ν_μ neutrino flux together with the normalization and energy-dependent systematic errors on the EP flux prediction quoted above.

7.8 An upper limit on the $\nu_\mu \rightarrow \nu_e$ oscillations

The summary of the non-negligible systematic errors in the $R_{e\mu}$ ratio discussed in the previous section is given in Table 7.10. The total energy-independent systematic uncertainty is 6.2%, to which the energy-dependent error on the flux prediction from Table 7.9 is added in quadrature.

Source of systematic error	Fractional error on ν_e/ν_μ
Lepton efficiency (identification and reconstruction)	4.0%
Relative kinematic selection efficiency	3.8%
Relative flux:	
– overall error	2.7%
– energy-dependent error	see Table 7.9

Table 7.10: Summary of systematic errors in $R_{e\mu}$ ratio prediction. The numbers shown are fractional errors, i.e. the central value of the ν_e/ν_μ ratio multiplied by these numbers gives the error.

The 90% C.L. exclusion region of $\sin^2(2\theta)$ and Δm^2 for $\nu_\mu \rightarrow \nu_e$ oscillations and the experimental sensitivity, both including the effects of all systematic errors, are shown in Fig. 7.26. The upper limit and the sensitivity are computed by the unified approach method [113] using the EP description of neutrino fluxes [53]. The limit on the mixing angle for large (> 1000 eV^2) Δm^2 is[1]

$$\sin^2(2\theta) < 1.3 \cdot 10^{-3} \quad (90\% \text{ C.L.}) \tag{7.30}$$

The values of $\Delta m^2 > 0.5$ eV^2 at full mixing are excluded. The limit obtained is close (and typically less stringent) than the expected experimental sensitivity for the 1995 and 1996 NOMAD data sample.

---

[1] Computed by the global scan method, the limit of $\sin^2(2\theta) < 1.4 \cdot 10^{-3}$ for large Δm^2 at 90% C.L. is obtained.

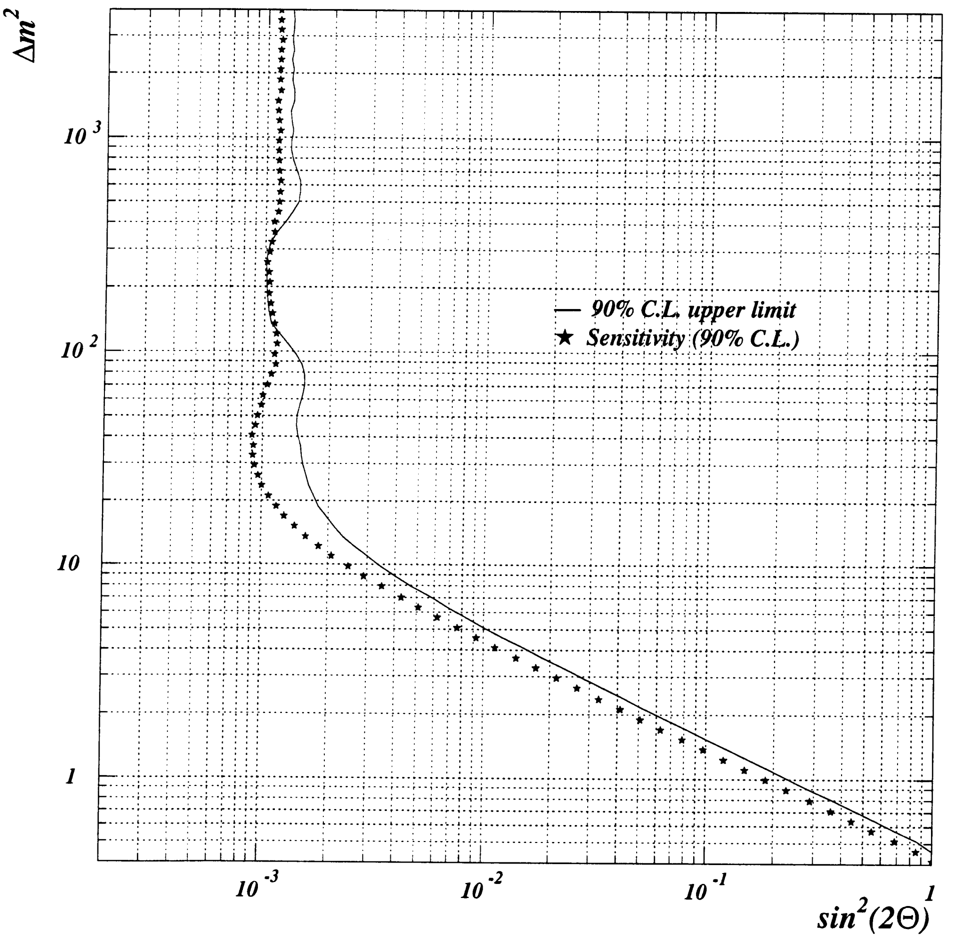

Figure 7.26: The 90% C.L. exclusion region (to the right of the solid line) and the expected experimental sensitivity (shown in asterisks) determined with this analysis for the 1995 and 1996 data, considering both statistical and systematic errors. The upper limit and the sensitivity are computed by the unified approach method [113] using the EP description of neutrino fluxes [53].

Chapter 8

Conclusion

The search for $\nu_\mu \to \nu_e$ oscillations based on the 1995 and 1996 NOMAD data has given a negative result. The observed ratio of ν_e to ν_μ charged current events as a function of neutrino energy is consistent with the hypothesis of no neutrino oscillation.

Our analysis enables us to set an upper limit on the $\nu_\mu \to \nu_e$ oscillation probability taking into account both the statistical and systematic uncertainties. The limit on the mixing angle for large (> 1000 eV^2) Δm^2 is

$$\sin^2(2\theta) \; < \; 1.3 \cdot 10^{-3} \quad (90\% \text{ C.L.})$$

The values of $\Delta m^2 > 0.5$ eV^2 at full mixing are excluded.

The 90% C.L. exclusion region of $\sin^2(2\theta)$ and Δm^2 for $\nu_\mu \to \nu_e$ oscillations obtained in our analysis is shown in Fig. 8.1, superimposed with the LSND 90% and 99% C.L. allowed regions [34] and with the most stringent limits set by other neutrino oscillation experiments. Our result fully excludes the LSND allowed region of oscillation parameters with $\Delta m^2 > 15$ eV^2. It gives the most stringest limit in the world on $\sin^2(2\theta)$ at $\Delta m^2 > 20$ eV^2.

The results presented here are based on only two first years of NOMAD data taking. The incorporation of the 1997 and 1998 data and quasielastic-like events, yielding more than a twofold increase in the statistics, will enlarge the region of NOMAD sensitivity. The larger statistical sample should also provide stronger constraints on the beam uncertainties. The quality of event simulation, reconstruction and identification has been gradually improving, and there is an ongoing work on better understanding of lepton efficiency uncertainty, which is promising. Though the estimation of the systematic errors in the $\nu_\mu \to \nu_e$ oscillation search in NOMAD is not an easy issue, there is a hope that these uncertainties could be reduced.

Smaller statistical and systematic errors would allow NOMAD to explore more space of oscillation parameters at large Δm^2 and to reinforce the disproval of the LSND claim for evidence for $\bar{\nu}_\mu \to \bar{\nu}_e$ oscillations in this region. However, NOMAD is not sensitive to the small Δm^2 range of the LSND allowed oscillation parameter space. The sensitivity of the NOMAD experiment to small Δm^2 region is limited by its small L/E ratio (high

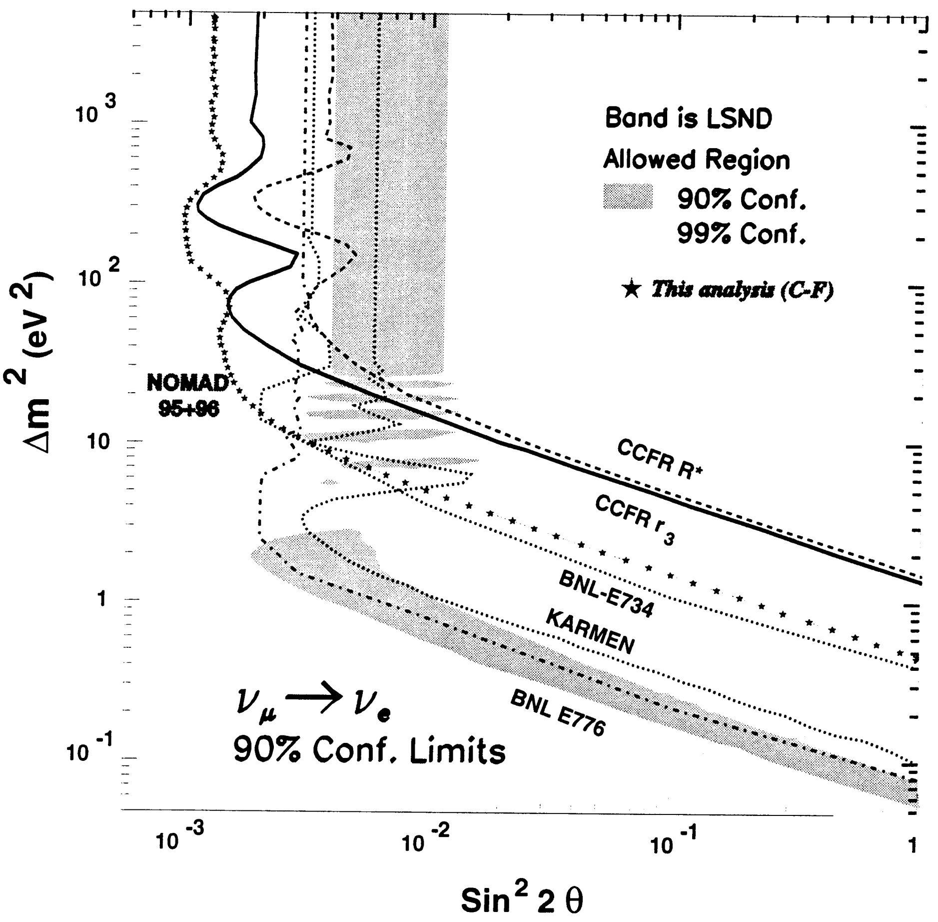

Figure 8.1: The 90% C.L. exclusion region for $\nu_\mu \to \nu_e$ oscillations determined with this analysis, superimposed with the LSND muon decay at rest 90% and 99% C.L. allowed regions and with the most stringent limits set by other experiments.

neutrino energies and relatively small source-detector distance). Therefore, NOMAD will never be able to fully exclude the LSND claim for evidence for $\bar{\nu}_\mu \to \bar{\nu}_e$ oscillations, nor to confirm the LSND positive result if the $\nu_\mu \to \nu_e$ oscillations with Δm^2 less than a few eV^2 do exist.

The only running experiment potentially able to completely disprove or confirm the LSND claim for oscillations is KARMEN. Hovewer, the expected sensitivity of KARMEN just barely covers the LSND allowed region of oscillation parameters (see Fig. 2.7). Even more importantly, the KARMEN experiment uses a method of the oscillation search which is too similar to that of LSND to provide an independent check of systematic uncertainties. A truly convincing test would be that performed by an experiment at the same L/E as LSND but using a different technique.

A number of papers have been recently submitted proposing such experiments:

- **Experiment at Jura** [119]. A neutrino detector, located at the position where the existing CERN SPS neutrino beam emerges from the Jura mountain at 17 km from the source [120], would offer two fundamental advantages with respect to any other existing or planned facilities:

  - the energy of the beam could be lowered by perhaps as much as an order of magnitude, still allowing reasonable counting rates in the $\nu_\mu \to \nu_e$ channel. It would then be possible to extend the search to higher L/E region;
  - the neutrino beam energy is above the τ production threshold, which would allow a simultaneous study of the $\nu_\mu \to \nu_e$ and $\nu_\mu \to \nu_\tau$ channels.

  The ICARUS-CERN-Milano group has proposed to use a 600 t module of the ICARUS liquid argon TPC for the Jura experiment [121]. Given the possible improved performances of the CERN neutrino beam, even a fiducial mass of 100 t and probably a conventional fine-grained calorimetric detector would be sufficient to fully test the LSND solution.

- **Experiment at CERN PS** [122]. Another possibility has been proposed at CERN to search for $\nu_\mu \to \nu_e$ oscillations at the reactivated low energy ($\langle E_\nu \rangle \sim 1.5$ GeV) CERN PS neutrino beam. The ν_e appearance search would be performed with the close and far fine-grained calorimetric detectors. A comparison of the ν_e/ν_μ ratios in two detectors would allow to explore the region of oscillation parameters down to $\sin^2(2\theta) \approx 10^{-3}$ for $\Delta m^2_{e\mu} \sim 1$ eV^2.

- **MiniBooNE** [123]. The Booster Neutrino Experiment has been proposed at FNAL as a relatively inexpensive way to test the LSND result in a short time scale. The detector would be located at 0.5 km from the neutrino source, constructed using the 8 GeV proton booster at FNAL and yielding neutrinos of E_ν between 0.1 and 1 GeV. The detector would be similar to that of the LSND experiment and would consist of a spherical tank filled with 769 t of mineral oil and viewed by the 1220 8" phototubes. Due to a high proton beam intensity and a very low ν_e background ($\approx$0.3% of ν_μ), a sensitivity at the level of $\sin^2(2\theta) < 4{\cdot}10^{-4}$ at large Δm^2 and $\Delta m^2 < 0.02$ eV^2 at full mixing is expected after only one year of running.

With the decision pending at CERN and the recent approval of the MiniBooNE experiment at FNAL, it is quite possible that the next significant results in the $\nu_\mu \to \nu_e$ oscillation search will come from the MiniBooNE collaboration in 4-5 years from now.

Bibliography

[1] W. Pauli, Letter to the Physical Society of Tubingen (1930) (unpublished); reproduced in Neutrino Physics, ed. K. Winter, Cambridge (1991) 4.

[2] C. L. Cowan, Jr. *et al.*, Science **124** (1956) 103.

[3] Particle Data Group, C. Caso *et al.*, Eur. Phys. J. **C3** (1998).

[4] G. Gelmini and E. Roulet, CERN-TH/7541 (1994).

[5] For a recent review see, for instance, M. Nakahata, Neutrino Masses and Oscillations, Plenary talk at the International Europhysics Conference on High Energy Physics, Jerusalem, Israel, 19-26 August 1997.

[6] B. Pontecorvo, Zh. Eksp. and Teor. Fiz. **33** (1957) 549, **34** (1958) 247.

[7] Z. Maki *et al.*, Progr. Theor. Phys. **28** (1962) 870.

[8] M. Gell-Mann, P. Ramond and R. Slansky, in Supergravity, eds. P. van Nieuwenhuizen and D. Freedman, North Holland, Amsterdam (1979) 315.

[9] V. A. Lubimov *et al.*, Phys. Lett. **B94** (1980) 266.

[10] J. Blietschau *et al.*, Nucl. Phys. **B133** (1978) 205.

[11] N. Armenise *et al.*, Phys. Lett. **B100** (1981) 182.

[12] O. Erriquez *et al.*, Phys. Lett. **B102** (1981) 73.

[13] C. Angelini *et al.*, Phys. Lett. **B179** (1986) 307.

[14] N. J. Baker *et al.*, Phys. Rev. Lett. **47** (1981) 1576.

[15] V. V. Ammosov *et al.*, Z. Phys. **C40** (1988) 487.

[16] F. Bergsma *et al.*, Z. Phys. **C40** (1988) 171.

[17] A. N. Diddens *et al.*, Nucl. Instr. and Meth. **176** (1980) 189, **178** (1980) 27.

[18] F. Dydak *et al.*, Phys. Lett. **B134** (1984) 281.

[19] M. Holder *et al.*, Nucl. Instr. and Meth. **148** (1978) 235.

[20] I. E. Stockdale *et al.*, Phys. Rev. Lett. **52** (1984) 1384, Z. Phys. **C27** (1985) 53.

[21] P. Vilain *et al.*, Z. Phys. **C64** (1994) 539.

[22] K. Winter *et al.*, Nucl. Instr. and Meth. **A278** (1989) 670.

[23] P. F. Loverre, Phys. Lett. **B370** (1996) 156.

[24] L. A. Ahrens *et al.*, Phys. Rev. **D31** (1985) 2732.

[25] P. Astier *et al.*, Nucl. Phys. **B335** (1990) 517.

[26] L. Borodovsky *et al.*, Phys. Rev. Lett. **68** (1992) 274.

[27] L. A. Ahrens *et al.*, Phys. Rev. Lett. **51** (1983) 1514.

[28] L. A. Ahrens *et al.*, Phys. Rev. **D36** (1987) 702.

[29] Ch. Berger *et al.*, Nucl. Instr. and Meth. **A262** (1987) 463.

[30] B. Blumenfeld *et al.*, Phys. Rev. Lett. **62** (1989) 2237.

[31] C. Athanassopoulos *et al.*, Nucl. Instr. and Meth. **A388** (1997) 149.

[32] C. Athanassopoulos *et al.*, Phys. Rev. **C54** (1996) 2685.

[33] R. L. Burman, M. E. Potter and E. S. Smith, Nucl. Instr. and Meth. **A291** (1990) 621;
R. L. Burman, A. C. Dodd and P. Plischke, Nucl. Instr. and Meth. **A368** (1996) 416.

[34] C. Athanassopoulos *et al.*, Phys. Rev. Lett. **77** (1996) 3082.

[35] http://www.neutrino.lanl.gov/LSND/papers.html, Preliminary 1993-1997 LSND $\bar{\nu}_\mu \to \bar{\nu}_e$ Results, September 1997.

[36] C. Athanassopoulos *et al.*, **nucl-ex/9706006**, submitted to Phys. Rev. **C**.

[37] E. Kolbe, K. Langanke and S. Krewald, Phys. Rev. **C49** (1994) 1122.

[38] C. Athanassopoulos *et al.*, Phys. Rev. Lett. **81** (1998) 1774.

[39] G. Drexlin *et al.*, Nucl. Instr. and Meth. **A289** (1990) 490.

[40] B. Armbruster *et al.*, contributed paper to the International Europhysics Conference on High Energy Physics, Jerusalem, Israel, 19-26 August 1997, to be published.

[41] A. Rubbia, contributed paper to LP97, Hamburg, Germany, 28 July – August 1 1997, to be published.

[42] K. Eitel, Results from the ν Oscillation Search with KARMEN, CERN Particle Physics Seminar, 17 February 1998.

[43] S. J. Freedman *et al.*, Phys. Rev. **D47** (1993) 811.

[44] K. S. McFarland *et al.*, Phys. Rev. Lett. **75** (1995) 3993.

[45] A. Romosan *et al.*, Phys. Rev. Lett. **78** (1997) 2912.

[46] C. G. Arroyo *et al.*, Phys. Rev. Lett. **72** (1994) 3452.

[47] R. Brun and F. Carminati, GEANT Detector Description and Simulation Tool, CERN Program Library, Long Writeup W5013, 1993.

[48] B. Achkar *et al.*, Nucl. Phys. **B434** (1995) 503.

[49] P. Astier *et al.*, CERN-SPSLC/91-21 (1991); Add. 1, CERN-SPSLC/91-48 (1991); Add. 2, CERN-SPSLC/91-53 (1991); CERN-SPSLC/93-31 (1993).

[50] M. C. Gonzalez-Garcia and J. J. Gomez-Cadenas, Phys. Rev. **D55** (1997), 1297; B. Van de Vyver, Nucl. Instr. and Meth. **A385** (1997), 91.

[51] G. Acquistapace *et al.*, CERN-ECP/95-14 (1995).

[52] L. Casagrande *et al.*, CERN Report 96-06 (1996).

[53] R. Das and S. R. Mishra, Measurement of Neutrino Flux in NOMAD, NOMAD Internal Note #97-038, 1997.

[54] C. Albright *et al.*, Phys. Lett. **B84** (1979) 123.

[55] J. Altegoer *et al.*, Nucl. Instr. and Meth. **A404** (1998) 96.

[56] The magnet was previously used in the UA1 experiment: M. Barranco-Luque *et al.*, Nucl. Instr. and Meth. **A176** (1980) 175.

[57] A. Cavestro *et al.*, Nucl. Instr. and Meth. **A305** (1991) 488.

[58] J. Altegoer *et al.*, Instrumenting the Front 'I's of NOMAD, NOMAD Internal Note #95-011, 1995.

[59] M. Holder *et al.*, Nucl. Instr. and Meth. **148** (1978) 235.

[60] W. K. Sakumoto *et al.*, Nucl. Instr. and Meth. **A294** (1990) 179.

[61] D. Autiero *et al.*, Nucl. Instr. and Meth. **A373** (1996) 358.

[62] D. Autiero *et al.*, Nucl. Instr. and Meth. **A387** (1997) 352.

[63] K. Eggert *et al.*, Nucl. Instr. and Meth. **A176** (1980) 217.

[64] Y. Perrin *et al.*, CASCADE: a Toolkit for the Construction of Distributed, Real-Time, Data-Acquisition Systems, CERN-ECP/93-13 (1993).

[65] LabVIEW User Manual for Sun (1994 Edition), National Instruments Corporation, Austin, TX, 1994.

[66] B. Schmidt, Study of ν_μ Charged Current Interactions and Search for $\nu_\mu \leftrightarrow \nu_\tau$ Oscillations in the Channel $\tau^- \to \mu^- \bar{\nu}_\mu \nu_\tau$ with the NOMAD Detector at the CERN Wideband Neutrino Beam, Dissertation zur Erlangung des akademischen Grades eines Doktors der Naturwissenschaften der Abteilung Physik an der Universität Dortmund, 1997.

[67] J. Altegoer *et al.*, Phys. Lett. **B431** (1998) 219.

[68] V. Valuev, Proc. of the International Europhysics Conference on High Energy Physics, Jerusalem, Israel, 19-26 August 1997, to be published.

[69] V. L. Ginzburg and I. M. Frank, Z. Eksper. Teor. Fiz. **16** (1946) 15;
G. M. Garibian, JETP **6** (1958) 1079; **10** (1960) 372;
K. A. Barsukov, JETP **10** (1960) 787;
L. Durand, Phys. Rev. **D11** (1975) 89.

[70] See e.g. B. Dolgoshein, Nucl. Instr. and Meth. **A252** (1986) 137; **A326** (1993) 434;
S. Paul, Particle Identification Using Transition Radiation Detectors, CERN Report 91-199 (1991).

[71] See e.g. X. Artru *et al.*, Phys. Rev. **D12** (1975) 1289.

[72] G. M. Garibian *et al.*, Nucl. Instr. and Meth. **125** (1975) 133.

[73] T. Fazio, Le détecteur à rayonnement de transition de l'expérience NOMAD pour l'identification du τ dans le canal $\tau^- \to e^- \bar{\nu}_e \nu_\tau$, thèse pour obtenir le titre de Docteur de l'Université Joseph Fourier - Grenoble 1, LAPP-T-95/01, Annecy, 1995.

[74] T. Fazio, P. Nédélec, S. Valuev, TRDSM: TRD Simulation Package, NOMAD Internal Software Note, 1994.

[75] V. C. Ermilova, L. P. Kotenko and G. I. Merzon, Nucl. Instr. and Meth. **145** (1977) 555.

[76] J. E. Bateman *et al.*, Nucl. Instr. and Meth. **135** (1976) 235.

[77] T. Fazio, S. Valuev, Some Results of TRD Simulation, NOMAD Internal Note #49, 1994.

[78] G. Grgic, Efficiency of NOMAD TRD Planes, NOMAD Internal Note #79, 1994.

[79] T. Ludlam *et al.*, Nucl. Instr. and Meth. **180** (1981) 413;
C. W. Fabjan *et al.*, Nucl. Instr. and Meth. **185** (1981) 119.

[80] A. Peisert and F. Sauli, Drift and Difusion of Electrons in Gases: a Compilation, CERN Report 84-08 (1984);
L. G. Christophorou *et al.*, Nucl. Instr. and Meth. **171** (1980) 491.

[81] G. Bassompierre *et al.*, Nucl. Instr. and Meth. **A403** (1998) 363.

[82] C. Engster *et al.*, The Front-end Electronics and the Monitoring System of the NOMAD Transition Radiation Detector, NOMAD Internal Note #78, 1994.

[83] HEPDB Database Management Package, CERN Program Library, Long Writeup Q180, 1993;
B. Khomenko, DBNOM: NOMAD Offline Database Software, NOMAD Internal Note #74, 1994.

[84] S. Valuev, P. Nedelec, M. Gouanère, TRD Calibration, NOMAD Internal Note #81, 1995.

[85] J.-P. Mendiburu, D. Sillou, S. Valuev, TRD Slow Control, NOMAD Internal Note #95-021, 1995.

[86] Atomic Data and Nuclear Data Tables, vol. 54, no. 2, 1993.

[87] T. Fazio, J-P. Mendiburu, P. Nédélec, D. Sillou, S. Valuev, NOMAD TRD Electron Identification: Method and First Results, NOMAD Internal Note #95-041, 1995.

[88] P. Nédélec, D. Sillou, S. Valuev, NOMAD TRD Identification of Overlapping Tracks, NOMAD Internal Note #96-005, 1996.

[89] G. M. Garibian *et al.*, JETP **6** (1960) 1306;
J. C. Ashley, Phys. Rev. **155** (1967) 208.

[90] F. Sauli, Principles of Operation of Multiwire Proportional and Drift Chambers, CERN Report 77-09 (1977).

[91] P. A. Aarnio *et al.*, Fluka User's Guide, Technical Report TIS-RP-190, CERN (1990).
A. Ferrari and P. R. Sala, Proc. of MC93 Int. Conf. on Monte-Carlo Simulation in High-Energy and Nuclear Physics, Tallahassee, Florida, 1993.

[92] J.-P. Meyer and A. Rubbia, NOMAD Event Generator Off-Line Manual, NOMAD Internal Software Note, 1994.

[93] G. Ingelman, The LUND MC for Deep Inelastic Lepton-Nucleon Scattering, CERN Program Library, Long Writeup W5046, 1989;
T. Sjöstrand, Computer Phys. Commun. **39** (1986) 347.

[94] T. Sjöstrand and M. Bengtsson, Jet Fragmentation and e^+e^- Annihilation, CERN Program Library, Long Writeup W5035, 1993;
T. Sjöstrand and M. Bengtsson, Computer Phys. Commun. **43** (1987) 367.

[95] J. Altegoer *et al.*, NOMAD GEANT Off-Line Manual, NOMAD Internal Software Note, 1995.

[96] R. Frühwirth, Nucl. Instr. and Meth. **A262** (1987) 444, and references therein.

[97] P. Astier *et al.*, Subdetector Matching Package, NOMAD Internal Software Note, 1995.

[98] Overview of the ZEBRA System, CERN Program Library, Long Writeups Q100/Q101, 1995.

[99] K. Varvell, NOMAD DST Package, Version v7r2, NOMAD Internal Note #97-034, 1997.

[100] M. Mezzetto, D. Gibin, A. Guglielmi, M. Laveder, π/e Rejection with CALO and PRS Modules at T9 Test Beam, NOMAD Internal Note #95-010, 1995.

[101] M. Contalbrigo, D. Gibin and S. Lacaprara, A Bremsstrahlung Algorithm Implemented within the NOMAD Software, NOMAD Internal Note #97-010, 1997.

[102] A. Guglielmi *et al.*, The Electromagnetic Calorimeter Response as a Function of Position and Angle of Incidence of Electrons, NOMAD Internal Note #95-034, 1995; M. Baldo-Ceolin *et al.*, On the e^- and γ Energy Reconstruction from the ECAL and PRS Signals, NOMAD Internal Note #95-039, 1995.

[103] See, e.g., A. Rubbia, Missing P_T Studies, in the minutes of the NOMAD meeting, September 1996.

[104] A. Geiser *et al.*, Conventions for NOMAD Coordinate System, NOMAD Internal Note #80, 1995.

[105] See, e.g., D. Autiero, Status of the $\tau^- \rightarrow e^-\nu_\tau\bar{\nu}_e$ Quasielastic Analysis, in the minutes of the NOMAD meeting, July 1998.

[106] V. B. Anikeev and V. P. Zhigunov, **vol. 24 p. 4** (1993) 989;
V. B. Anikeev *et al.*, Nucl. Instr. and Methods **A322** (1992) 280.

[107] A. Fassò *et al.*, Proc. of 2nd Workshop on Simulating Accelerator Radiation Environments, CERN, Geneva, 1995.

[108] H. W. Atherton *et al.*, CERN Report 80-07 (1980).

[109] G. Ambrosini *et al.*, SPY Proposal, CERN-SPSLC/96-01, SPSLC/P294 (1996).

[110] T. Weisse, Ph.D. Thesis, Dortmund University, 1997.

[111] F. Weber *et al.*, The Construction and Use of the Flux Reweighting Tables, NOMAD Internal Note #97-037, 1997.

[112] G. Collozuol and A. Guglielmi, From NUBEAM 4.00 to NUBEAM 5.00 + FLUKA97.5, in the minutes of the NOMAD meeting, May 1998.

[113] G. J. Feldman, R. D. Cousins, Phys. Rev. **D57** (1998) 3873.

[114] F. James, Function Minimization and Error Analysis, CERN Program Library, Long Writeup D506, 1994.

[115] F. F. Wilson, F. V. Weber, Comparison of Kinematic Reconstruction Variables, NOMAD Internal Note #96-030, 1996.

[116] G. Myatt, CERN/ECFA **72-4**, Vol.II (1973) 117.

[117] A. Krasnoperov, Test of Electron Identification on δ-ray Sample, in the minutes of the NOMAD meeting, July 1998;
V. Flaminio, C. Lazzeroni and R. Renò, Electron Identification Efficiency from δ-rays, NOMAD Internal Note #98-014, 1998.

[118] P. Hurst, Electron Efficiency from Data, in the minutes of the NOMAD meeting, May 1998.

[119] D. Autiero *et al.*, CERN-SPSC/97-23, SPSC/I 217 (1997).

[120] F. Vannucci *et al.*, CERN-SPSLC/P178, SPSLC/82-20 (1982).

[121] ICARUS-CERN-Milano collaboration, CERN-SPSLC/96-58, SPCLC/P304 (1996);
J. P. Revol *et al.*, ICARUS-TM-97/01 (1997).

[122] N. Armenize *et al.*, CERN-SPSC/97-21 (1997).

[123] E. Church *et al.*, Fermilab Proposal (1997).

Résumé

L'expérience NOMAD est une expérience de recherche d'oscillations de neutrinos, auprès du faisceau de neutrinos à large bande du SPS au CERN, dans les deux modes d'oscillations: neutrino-muonique (ν_μ) vers neutrino-tauïque (ν_τ) et neutrino-muonique vers neutrino-electronique (ν_e).

Cette thèse présente les résultats obtenus dans la recherche des oscillations $\nu_\mu \to \nu_e$ dans les données 1995 et 1996 de NOMAD.

Les deux premiers chapitres présentent une brève esquisse de la phénomènologie des oscillations de neutrinos, ainsi qu'une revue de la situation expérimentale concernant les recherches d'oscillations $\nu_\mu \to \nu_e$ auprès d'accélérateurs, qui montre l'interêt d'effectuer cette recherche dans NOMAD.

Le troisième chapitre décrit le dispositif expérimental utilisé et montre que le faisceau de neutrinos du CERN et le détecteur NOMAD ont des caractéristiques adaptées à la recherche des oscillations $\nu_\mu \to \nu_e$. Celle-ci est rendue possible, en particulier, par les excellentes performances du détecteur NOMAD dans l'identification des interactions de ν_e par courant chargé, principalement grâce au détecteur à rayonnement de transition (DRT). Le DRT a été conçu pour séparer les électrons des pions, avec un facteur de rejet supérieur à 1000 pour une efficacité aux électrons de 90%, dans la région d'énergie 1–50 GeV. La conception, l'optimisation et la procédure de calibration du DRT sont résumées au quatrième chapitre. Le cinqiéme chapitre présente et discute les algorithmes de séparation électron-pion ainsi que leurs performances.

Les deux derniers chapitres (six et sept) présentent l'analyse $\nu_\mu \to \nu_e$ des données 1995 et 1996 et les résultats obtenus.

L'algorithme de mesure de l'énergie, les critères de sélection des interactions des neutrinos et anti-neutrinos electroniques et muoniques par courant chargé (CC) sont décrits au chapitre six. L'efficacité de selection des événements ν_e CC s'éléve à 32%, tandis que la contamination du bruit de fond estimée est infériere à 0.4%, ce qui correspond à un facteur de rejet de l'ordre de 10^{-5} pour le bruit de fond provenant des événement ν_μ CC et ν_μ NC.

Plusieurs tests démontrent la compatibilité des differents échantillons de données entre eux. Sur la base de nombreux comparaisons effectuées entre les données et les simulations il apparait que les données sont compatibles avec l'absence d'oscillations.

Enfin, l'évaluation des erreurs systématiques est décrite, avec une attention particulière concernant les prédictions du flux de neutrinos incidents. En conclusion de ces études, les incertitudes systématiques totales sont estimées à 6.2%, auquelles vient s'ajouter un terme concernant le flux de neutrino, dépendant de l'énergie.

En conclusion, il n'y a pas d'évidence des oscillations $\nu_\mu \to \nu_e$ dans les données 1995 et 1996 de NOMAD. La limite obtenue sur l'angle de mélange à grand (> 1000 eV^2) Δm^2 est

$$\sin^2(2\theta) \ < \ 1.3 \cdot 10^{-3} \quad (90\% \text{ C.L.})$$

Cette résultat exclut complètement la région d'oscillations de LSND pour $\Delta m^2 > 15$ eV^2 et donne la limite mondiale la plus contraignante sur $\sin^2(2\theta)$ pour $\Delta m^2 > 20$ eV^2.

Les mots clefs: neutrino, oscillations, masse de neutrino, radiation transition.